

Finite Element Analysis of Ultra-High Performance Concrete: Modeling Structural Performance of an AASHTO Type II Girder and a 2nd Generation Pi-Girder

October 2010

NTIS Accession No. PB2011-100864

FHWA Publication No. FHWA-HRT-11-020



**U.S. Department of Transportation
Federal Highway Administration**

FOREWORD

With the ever increasing congestion and deterioration of our nation's highway system, a need exists to develop highly durable and rapidly constructed infrastructure systems. Durable bridge structures that would require less intrusive maintenance and would exhibit longer life spans thus maximizing the use of the facility are highly desirable. Expediting bridge construction can minimize traffic flow disruptions. Ultra-high performance concrete (UHPC) is an advanced construction material which affords new opportunities to envision the future of the highway infrastructure. The Federal Highway Administration has been engaged in research into the optimal uses of UHPC in the highway bridge infrastructure since 2001 through its Bridge of the Future Initiative. This report presents the results of a research effort aimed at engaging the finite element method as a means to facilitate the development of UHPC structural systems. In this study, a commercial finite element analysis package is used to model the structural performance of a series of UHPC components. Each of these components had been previously tested, thus allowing for the comparison of physical and numerical results and the calibration of the computational model.

This report corresponds to the TechBrief titled, "Finite Element Analysis of Ultra-High Performance Concrete: Modeling Structural Performance of an AASHTO Type II Girder and a 2nd Generation Pi-Girder" (FHWA-HRT-10-079). This report is being distributed through the National Technical Information Service for informational purposes. The content in this report is being distributed "as is" and may contain editorial or grammatical errors.

Notice

This document is disseminated under the sponsorship of the U.S. Department of Transportation in the interest of information exchange. The U.S. Government assumes no liability for the use of the information contained in this document.

The U.S. Government does not endorse products or manufacturers. Trademarks or manufacturers' names appear in this report only because they are considered essential to the objective of the document.

Quality Assurance Statement

The Federal Highway Administration (FHWA) provides high-quality information to serve Government, industry, and the public in a manner that promotes public understanding. Standards and policies are used to ensure and maximize the quality, objectivity, utility, and integrity of its information. FHWA periodically reviews quality issues and adjusts its programs and processes to ensure continuous quality improvement.

TECHNICAL REPORT DOCUMENTATION PAGE

1. Report No. FHWA-HRT-11-020	2. Government Accession No. NTIS PB2011-100864	3. Recipient's Catalog No.	
4. Title and Subtitle Finite Element Analysis of Ultra-High Performance Concrete: Modeling Structural Performance of an AASHTO Type II Girder and a 2 nd Generation Pi-Girder		5. Report Date October 2010	6. Performing Organization Code:
		8. Performing Organization Report No.	
7. Author(s) Linfeng Chen & Benjamin A. Graybeal		10. Work Unit No.	
9. Performing Organization Name and Address Office of Infrastructure Research & Development Federal Highway Administration 6300 Georgetown Pike McLean, VA 22101-2296		11. Contract or Grant No.	
		13. Type of Report and Period Covered Final Report: 2008-2010	
12. Sponsoring Agency Name and Address Office of Infrastructure Research & Development Federal Highway Administration 6300 Georgetown Pike McLean, VA 22101-2296		14. Sponsoring Agency Code HRDI-06	
		15. Supplementary Notes	
<p>16. Abstract</p> <p>Ultra-high performance concrete (UHPC) is an advanced cementitious composite material which has been developed in recent decades. When compared to more conventional cement-based concrete materials, UHPC tends to exhibit superior properties such as increased durability, strength, and long-term stability. This computational investigation focused on modeling the behaviors of existing UHPC structural components including a prestressed UHPC AASHTO Type II girder and a prestressed UHPC 2nd generation pi-girder. Both a concrete smeared cracking model and a concrete damaged plasticity model were tailored to model UHPC within a commercially available finite element analysis package. The concrete damaged plasticity model using three types of tension stiffening definitions can replicate both linear and nonlinear structural responses of both girders reasonably well. A set of UHPC constitutive properties were developed that facilitate the model replication of the local and global responses observed in the series of physical tests. The finite element analysis modeling techniques developed herein are intended to be applicable to other UHPC structural components.</p> <p>This report corresponds to the TechBrief titled "Finite Element Analysis of Ultra-High Performance Concrete: Modeling Structural Performance of an AASHTO Type II Girder and a 2nd Generation Pi-Girder" (FHWA-HRT-10-079).</p>			
17. Key Words Ultra-high performance concrete, UHPC, finite element analysis, FEA, ABAQUS, concrete smeared cracking, concrete damaged plasticity		18. Distribution Statement No restrictions. This document is available through the National Technical Information Service, Springfield, VA 22161.	
19. Security Classif. (of this report) Unclassified	20. Security Classif. (of this page) Unclassified	21. No. of Pages 177	22. Price N/A

SI* (MODERN METRIC) CONVERSION FACTORS

APPROXIMATE CONVERSIONS TO SI UNITS

Symbol	When You Know	Multiply By	To Find	Symbol
LENGTH				
in	inches	25.4	millimeters	mm
ft	feet	0.305	meters	m
yd	yards	0.914	meters	m
mi	miles	1.61	kilometers	km
AREA				
in ²	square inches	645.2	square millimeters	mm ²
ft ²	square feet	0.093	square meters	m ²
yd ²	square yard	0.836	square meters	m ²
ac	acres	0.405	hectares	ha
mi ²	square miles	2.59	square kilometers	km ²
VOLUME				
fl oz	fluid ounces	29.57	milliliters	mL
gal	gallons	3.785	liters	L
ft ³	cubic feet	0.028	cubic meters	m ³
yd ³	cubic yards	0.765	cubic meters	m ³
NOTE: volumes greater than 1000 L shall be shown in m ³				
MASS				
oz	ounces	28.35	grams	g
lb	pounds	0.454	kilograms	kg
T	short tons (2000 lb)	0.907	megagrams (or "metric ton")	Mg (or "t")
TEMPERATURE (exact degrees)				
°F	Fahrenheit	5 (F-32)/9 or (F-32)/1.8	Celsius	°C
ILLUMINATION				
fc	foot-candles	10.76	lux	lx
fl	foot-Lamberts	3.426	candela/m ²	cd/m ²
FORCE and PRESSURE or STRESS				
lbf	poundforce	4.45	newtons	N
lbf/in ²	poundforce per square inch	6.89	kilopascals	kPa

APPROXIMATE CONVERSIONS FROM SI UNITS

Symbol	When You Know	Multiply By	To Find	Symbol
LENGTH				
mm	millimeters	0.039	inches	in
m	meters	3.28	feet	ft
m	meters	1.09	yards	yd
km	kilometers	0.621	miles	mi
AREA				
mm ²	square millimeters	0.0016	square inches	in ²
m ²	square meters	10.764	square feet	ft ²
m ²	square meters	1.195	square yards	yd ²
ha	hectares	2.47	acres	ac
km ²	square kilometers	0.386	square miles	mi ²
VOLUME				
mL	milliliters	0.034	fluid ounces	fl oz
L	liters	0.264	gallons	gal
m ³	cubic meters	35.314	cubic feet	ft ³
m ³	cubic meters	1.307	cubic yards	yd ³
MASS				
g	grams	0.035	ounces	oz
kg	kilograms	2.202	pounds	lb
Mg (or "t")	megagrams (or "metric ton")	1.103	short tons (2000 lb)	T
TEMPERATURE (exact degrees)				
°C	Celsius	1.8C+32	Fahrenheit	°F
ILLUMINATION				
lx	lux	0.0929	foot-candles	fc
cd/m ²	candela/m ²	0.2919	foot-Lamberts	fl
FORCE and PRESSURE or STRESS				
N	newtons	0.225	poundforce	lbf
kPa	kilopascals	0.145	poundforce per square inch	lbf/in ²

*SI is the symbol for the International System of Units. Appropriate rounding should be made to comply with Section 4 of ASTM E380. (Revised March 2003)

TABLE OF CONTENTS

CHAPTER 1. INTRODUCTION	1
INTRODUCTION	1
OBJECTIVE	1
SUMMARY OF APPROACH	1
OUTLINE OF REPORT	1
CHAPTER 2. FINITE ELEMENT METHOD	2
A BRIEF HISTORY	2
ABAQUS	3
BASIC THEORY	3
WHY FEM.....	4
CONSTITUTIVE MODELS FOR CONCRETE	4
<i>Concrete smeared cracking model.....</i>	<i>5</i>
<i>Concrete damaged plasticity model.....</i>	<i>8</i>
CHAPTER 3. EXPERIMENTAL WORK	11
INTRODUCTION	11
I-GIRDER 80F DESCRIPTION.....	11
I-GIRDERS 24S AND 14S DESCRIPTION.....	11
PI-GIRDER DESCRIPTION.....	12
PI-GIRDER WITH JOINT DESCRIPTION	20
CHAPTER 4. I-GIRDER 80F	25
FINITE ELEMENT MODEL.....	25
CONSTITUTIVE MODELS FOR UHPC.....	27
ABAQUS RESULTS.....	29
PARAMETRIC STUDIES	33
<i>Mesh sensitivity.....</i>	<i>33</i>
<i>CDP vs. CSC.....</i>	<i>35</i>
<i>Concrete tension stiffening of CDP</i>	<i>38</i>
<i>Tension Damage of CDP</i>	<i>44</i>
CONCLUSIONS	46
CHAPTER 5. I-GIRDERS 24S AND 14S.....	47
FINITE ELEMENT MODELS.....	47
ABAQUS RESULTS.....	48
<i>I-girder 24S.....</i>	<i>48</i>
<i>I-girder 14S.....</i>	<i>65</i>
CONCLUSIONS	81
CHAPTER 6. PI-GIRDER.....	82
FINITE ELEMENT MODEL.....	82
CONSTITUTIVE MODELS FOR UHPC.....	82
DIAPHRAGMS	85

ELASTOMERIC PADS	86
ABAQUS RESULTS.....	87
PARAMETRIC STUDIES	100
<i>Mesh sensitivity</i>	100
<i>CDP vs. CSC</i>	104
<i>Young's modulus</i>	104
<i>Concrete tension stiffening of CDP</i>	109
<i>Diaphragms</i>	121
<i>Transverse #5 reinforcement in the deck</i>	126
CONCLUSIONS	130
CHAPTER 7. PI-GIRDER WITH JOINT	132
FINITE ELEMENT MODEL.....	132
DIAPHRAGMS	135
ELASTOMERIC PADS	137
ABAQUS RESULTS.....	137
PARAMETRIC STUDIES	155
<i>Stabilization</i>	155
<i>Joint</i>	159
<i>Contact</i>	164
<i>Diaphragms</i>	168
CONCLUSIONS	173
CHAPTER 8. CONCLUSIONS.....	174
INTRODUCTION	174
CONCLUSIONS	174
ONGOING AND FUTURE RESEARCH.....	175
REFERENCES.....	176

LIST OF FIGURES

Figure 1. Equation. Element stiffness equation.	3
Figure 2. Equation. Global stiffness equation.....	4
Figure 3. Graph. Tension stiffening model (from ABAQUS manual).	6
Figure 4. Graph. Fracture energy cracking model (from ABAQUS manual).	6
Figure 5. Graph. Compression hardening model (from ABAQUS manual).	7
Figure 6. Yield surface in plane stress (from ABAQUS manual).	7
Figure 7. Post-failure stress-displacement curve (from ABAQUS manual).....	9
Figure 8. Post-failure stress-fracture energy curve (from ABAQUS manual).	9
Figure 9. Illustration. Test setup of the I-girder Test 80F.....	13
Figure 10. Illustration. Instrumentation plan for the I-girder Test 80F.	13
Figure 11. Illustration. AASHTO Type II cross section and strand pattern.	14
Figure 12. Illustration. Instrumentation plan for the I-girder Test 24S.	15
Figure 13. Illustration. Instrumentation plan for the I-girder Test 14S.	15
Figure 14. Illustration. Pi-girder cross section and strand pattern.	16
Figure 15. Illustration. Elevation view of diaphragms (unit in inch).....	16
Figure 16. Illustration. End view of diaphragm end plate (unit in inch).	16
Figure 17. Illustration. Test plan for the pi-girder.	17
Figure 18. Photo. Setup for the pi-girder.	18
Figure 19. Photo. West end for the pi-girder test.....	18
Figure 20. Illustration. Midspan strain gage locations for the pi-girder test.....	19
Figure 21. Illustration. Midspan potentiometer locations for the pi-girder test.....	19
Figure 22. Illustration. Abutment LVDT locations for the pi-girder test.	20
Figure 23. Illustration. Plan view (above) and elevation view (below) of longitudinal grouted joint detail between pi-girders.	21
Figure 24. Photo. Setup for the pi-girder with joint.....	22
Figure 25. Photo. East end of the pi-girder with joint test.....	22
Figure 26. Illustration. Midspan strain gage locations for the pi-girder with joint test.	23
Figure 27. Illustration. Midspan potentiometer locations for the pi-girder with joint test.	23
Figure 28. Illustration. Midspan LVDT locations for the pi-girder with joint test.	24
Figure 29. Illustration. Abutment LVDT locations for the pi-girder with joint test.	24
Figure 30. Illustration. I-girder 80F model.	25
Figure 31. Graph. Prestressing strand, A36 steel, and reinforcing rebar steel uniaxial stress-strain relationships.....	26
Figure 32. Equation. Assumed stress-strain response of 270 ksi (1862 MPa) prestressing strand.	26
Figure 33. Illustration. Equivalent shape of prestressing strand.	27
Figure 34. Illustration. I-Girder model with (a) a 4-inch (102-mm) seeded mesh (b) a 2-inch (51-mm) seeded mesh.....	27
Figure 35. Graph. Assumed UHPC uniaxial stress-strain relationship.....	28
Figure 36. Graph. FEM vs. experimentally observed vertical deflection at midspan.	31

Figure 37. Graph. FEM vs. experimentally observed longitudinal strain on the top and bottom surfaces of the girder at midspan.....	31
Figure 38. Graph. FEM vs. experimentally observed longitudinal strain along girder depth at midspan.....	32
Figure 39. Graph. FEM predicted (a) longitudinal strain and (b) longitudinal normal stress at midspan under an applied load of 179 kips (796 kN).	33
Figure 40. Graph. Effect of mesh density on the vertical deflection of the girder at midspan.	34
Figure 41. Graph. Effect of mesh density on the longitudinal strains on the top and bottom surfaces of the girder at midspan.....	34
Figure 42. Graph. CDP vs. CSC in the vertical deflection of the girder at midspan.	35
Figure 43. Graph. CDP vs. CSC in the longitudinal strains on the top and bottom surfaces of the I-girder at midspan.	36
Figure 44. Graph. Effect of maximum tensile stress of the CSC model on the vertical deflection of the girder at midspan.....	36
Figure 45. Graph. Effect of maximum tensile stress of the CSC model on the longitudinal strains on the top and bottom surfaces of the girder at midspan.....	37
Figure 46. Graph. Effect of CSC tension stiffening based on fracture energy cracking criterion on the vertical deflection of the girder at midspan.	37
Figure 47. Graph. Effect of CSC tension stiffening based on fracture energy cracking criterion on the longitudinal strains on the top and bottom surfaces of the girder at midspan.	38
Figure 48. Graph. Effect of maximum tensile stress on the vertical deflection of the girder at midspan.....	39
Figure 49. Graph. Effect of maximum tensile stress on the longitudinal strains on the top and bottom surfaces of the girder at midspan.	39
Figure 50. Graph. Effect of ultimate tensile plastic strain on the vertical deflection of the girder at midspan.....	40
Figure 51. Graph. Effect of ultimate tensile plastic strain on the longitudinal strains on the top and bottom surfaces of the girder at midspan.....	40
Figure 52. Graph. Effect of cracking displacement on the vertical deflection of the girder at midspan.....	42
Figure 53. Graph. Effect of cracking displacement on the longitudinal strains on the top and bottom surfaces of the girder at midspan.	43
Figure 54. Graph. Effect of fracture energy on the vertical deflection of the girder at midspan..	43
Figure 55. Graph. Effect of fracture energy on the longitudinal strains on the top and bottom surfaces of the girder at midspan.....	44
Figure 56. Graph. Assumed tension damage.	45
Figure 57. Graph. Effect of tension damage on the vertical deflection of the girder at midspan with an unloading from an applied load of 129.5 kips (576 kN) and reloading to the ultimate load.	45
Figure 58. Illustration. I-girder 24S model.	47
Figure 59. Illustration. I-girder 14S model.	48
Figure 60. Illustration. I-Girder 24S or 14S with a 2-inch (51-mm) seeded mesh.	48

Figure 61. Graph. Predicted versus observed deflection of the girder 24S along Instrumentation Lines 1, 2, and 3.	49
Figure 62. Graph. Predicted versus observed deflection of the girder 24S along Instrumentation Lines 4, 5, and 6.	50
Figure 63. Graph. Assumed vertical rigid body movement of the girder 24S.....	50
Figure 64. Graph. Predicted versus observed (modified) deflection of the girder 24S along Instrumentation Lines 1, 2, and 3.	51
Figure 65. Graph. Predicted versus observed (modified) deflection of the girder 24S along Instrumentation Lines 4, 5, and 6.	51
Figure 66. Graph. Predicted versus observed longitudinal strain on the top and bottom surfaces of the girder 24S along Instrumentation Line 1.....	53
Figure 67. Graph. Predicted versus observed longitudinal strain on the top and bottom surfaces of the girder 24S along Instrumentation Line 2.....	54
Figure 68. Graph. Predicted versus observed longitudinal strain on the top and bottom surfaces of the girder 24S along Instrumentation Line 3.....	54
Figure 69. Graph. Predicted versus observed longitudinal strain on the top and bottom surfaces of the girder 24S along Instrumentation Line 4.....	55
Figure 70. Graph. Predicted versus observed longitudinal strain on the top and bottom surfaces of the girder 24S along Instrumentation Line 5.....	55
Figure 71. Graph. Predicted versus observed longitudinal strain on the top and bottom surfaces of the girder 24S along Instrumentation Line 6.....	56
Figure 72. Graph. Predicted versus observed longitudinal strain on the side face of the girder 24S along Instrumentation Line 1.	56
Figure 73. Graph. Predicted versus observed longitudinal strain on the side face of the girder 24S along Instrumentation Line 2.	57
Figure 74. Graph. Predicted versus observed longitudinal strain on the side face of the girder 24S along Instrumentation Line 3.	57
Figure 75. Graph. Predicted versus observed longitudinal strain on the side face of the girder 24S along Instrumentation Line 4.	58
Figure 76. Graph. Predicted versus observed longitudinal strain on the side face of the girder 24S along Instrumentation Line 5.	58
Figure 77. Graph. Predicted versus observed longitudinal strain on the side face of the girder 24S along Instrumentation Line 6.	59
Figure 78. Graph. Predicted versus observed principal strains on the side face of the girder 24S along Instrumentation Line 1.	59
Figure 79. Graph. Predicted versus observed principal strains on the side face of the girder 24S along Instrumentation Line 2.	60
Figure 80. Graph. Predicted versus observed principal strains on the side face of the girder 24S along Instrumentation Line 3.	60
Figure 81. Graph. Predicted versus observed principal strains on the side face of the girder 24S along Instrumentation Line 4.	61

Figure 82. Graph. Predicted versus observed principal strains on the side face of the girder 24S along Instrumentation Line 5.	61
Figure 83. Graph. Predicted versus observed principal strains on the side face of the girder 24S along Instrumentation Line 6.	62
Figure 84. Graph. Predicted versus observed strain components from rosette strain gage at Instrumentation Line 1.	62
Figure 85. Graph. Predicted versus observed strain components from rosette strain gage at Instrumentation Line 2.	63
Figure 86. Graph. Predicted versus observed strain components from rosette strain gage at Instrumentation Line 3.	63
Figure 87. Graph. Predicted versus observed strain components from rosette strain gage at Instrumentation Line 4.	64
Figure 88. Graph. Predicted versus observed strain components from rosette strain gage at Instrumentation Line 5.	64
Figure 89. Graph. Predicted versus observed strain components from rosette strain gage at Instrumentation Line 6.	65
Figure 90. Graph. Predicted versus observed deflection of the girder 14S along Instrumentation Lines 1, 2, and 3.	66
Figure 91. Graph. Predicted versus observed deflection of the girder 14S along Instrumentation Lines 4, 5, and 6.	66
Figure 92. Graph. Assumed vertical rigid body movement of the girder 14S.	67
Figure 93. Graph. Predicted versus observed (modified) deflection of the girder 14S along Instrumentation Lines 1, 2, and 3.	67
Figure 94. Graph. Predicted versus observed (modified) deflection of the girder 14S along Instrumentation Lines 4, 5, and 6.	68
Figure 95. Graph. Predicted versus observed longitudinal strain on the top and bottom surfaces of the girder 14S along Instrumentation Line 1.	69
Figure 96. Graph. Predicted versus observed longitudinal strain on the top and bottom surfaces of the girder 14S along Instrumentation Line 2.	69
Figure 97. Graph. Predicted versus observed longitudinal strain on the top and bottom surfaces of the girder 14S along Instrumentation Line 3.	70
Figure 98. Graph. Predicted versus observed longitudinal strain on the top and bottom surfaces of the girder 14S along Instrumentation Line 4.	70
Figure 99. Graph. Predicted versus observed longitudinal strain on the top and bottom surfaces of the girder 14S along Instrumentation Line 5.	71
Figure 100. Graph. Predicted versus observed longitudinal strain on the top and bottom surfaces of the girder 14S along Instrumentation Line 6.	71
Figure 101. Graph. Predicted versus observed longitudinal strain on the side face of the girder 14S along Instrumentation Line 1.	72
Figure 102. Graph. Predicted versus observed longitudinal strain on the side face of the girder 14S along Instrumentation Line 2.	72

Figure 103. Graph. Predicted versus observed longitudinal strain on the side face of the girder 14S along Instrumentation Line 3.	73
Figure 104. Graph. Predicted versus observed longitudinal strain on the side face of the girder 14S along Instrumentation Line 4.	73
Figure 105. Graph. Predicted versus observed longitudinal strain on the side face of the girder 14S along Instrumentation Line 5.	74
Figure 106. Graph. Predicted versus observed longitudinal strain on the side face of the girder 14S along Instrumentation Line 6.	74
Figure 107. Graph. Predicted versus observed principal strains on the side face of the girder 14S along Instrumentation Line 1.	75
Figure 108. Graph. Predicted versus observed principal strains on the side face of the girder 14S along Instrumentation Line 2.	75
Figure 109. Graph. Predicted versus observed principal strains on the side face of the girder 14S along Instrumentation Line 3.	76
Figure 110. Graph. Predicted versus observed principal strains on the side face of the girder 14S along Instrumentation Line 4.	76
Figure 111. Graph Predicted versus observed principal strains on the side face of the girder 14S along Instrumentation Line 5.	77
Figure 112. Graph. Predicted versus observed principal strains on the side face of the girder 14S along Instrumentation Line 6.	77
Figure 113. Graph. Predicted versus observed strain components from rosette strain gage at Instrumentation Line 1.	78
Figure 114. Graph. Predicted versus observed strain components from rosette strain gage at Instrumentation Line 2.	78
Figure 115. Graph. Predicted versus observed strain components from rosette strain gage at Instrumentation Line 3.	79
Figure 116. Graph. Predicted versus observed strain components from rosette strain gage at Instrumentation Line 4.	79
Figure 117. Graph. Predicted versus observed strain components from rosette strain gage at Instrumentation Line 5.	80
Figure 118. Graph. Predicted versus observed strain components from rosette strain gage at Instrumentation Line 6.	80
Figure 119. Illustration. (a) Full pi-girder model, and (b) hidden rebar and strands embedded in UHPC.	83
Figure 120. Illustration. Pi-girder model with a 2-inch (51-mm) seeded mesh.	84
Figure 121. Photo. Prying of end plates at peak applied load in Test T2D.	85
Figure 122. Graph. Behaviors of diaphragm subcomponents and assumed nonlinear spring for the diaphragms in the pi-girder T2D.	86
Figure 123. Graph. Vertical deformation of an elastomeric pad support in the experiment and its approximation using a linear spring.	87
Figure 124. Graph. FEM vs. experimentally observed vertical deflection of the bulbs at midspan.	91

Figure 125. Graph. FEM vs. experimentally observed vertical deflection at the midspan middeck position.	91
Figure 126. Graph. FEM vs. experimentally observed diaphragm force.....	92
Figure 127. FEM vs. experimentally observed bulb lateral spreading at midspan.....	92
Figure 128. FEM vs. experimentally observed bulb lateral spreading at support.	93
Figure 129. FEM vs. experimentally observed longitudinal strain on the bottom surface of the north bulb at midspan.	93
Figure 130. Graph. FEM vs. experimentally observed longitudinal strain on the deck immediately above the north web at midspan.	94
Figure 131. Graph. FEM vs. experimentally observed transverse strains on the top and bottom surfaces of the deck at the midspan middeck location.	94
Figure 132. Graph. FEM predicted maximum principal stress on the surface of the girder as viewed from (a) above, (b) below, and (c) beside the girder.....	95
Figure 133. Photo. Underside deck cracking map of T2D after conclusion of test (reproduced from reference (14)).	96
Figure 134. Graph. FEM predicted minimum principal stress on the surface of the girder as viewed from (a) above, (b) below, and (c) beside the girder.....	97
Figure 135. Graph. FEM predicted maximum principal plastic strain on the surface of the girder as viewed from (a) above, (b) below, and (c) beside the girder.....	98
Figure 136. Graph. FEM predicted maximum principal stress at the (a) midspan, and (b) center of loading patch cross sections (Note: deformation scale factor = 5).	99
Figure 137. Graph. FEM predicted maximum principal plastic strain at the (a) midspan, and (b) center of loading patch cross sections (Note: deformation scale factor = 5).	100
Figure 138. Graph. Effect of mesh density on the vertical deflection of the bulbs at midspan..	101
Figure 139. Graph. Effect of mesh density on the vertical deflection at the midspan middeck location.	101
Figure 140. Graph. Effect of mesh density on the diaphragm force.....	102
Figure 141. Graph. Effect of mesh density on the bulb lateral spreading at midspan.....	102
Figure 142. Graph. Effect of mesh density on the bulb lateral spreading at support.....	103
Figure 143. Graph. Effect of mesh density on the longitudinal strain on the bottom surface of the north bulb at midspan.	103
Figure 144. Graph. Effect of mesh density on the longitudinal strain on the deck immediately above the north web at midspan.	104
Figure 145. Graph. CDP vs. CSC in the vertical deflection of the bulbs at midspan.....	105
Figure 146. Graph. CDP vs. CSC in the vertical deflection at the midspan middeck position. .	105
Figure 147. Graph. CDP vs. CSC in the diaphragm force.....	106
Figure 148. Graph. CDP vs. CSC in the bulb lateral spreading at midspan.	106
Figure 149. Graph. CDP vs. CSC in the bulb lateral spreading at support.....	107
Figure 150. Graph. CDP vs. CSC in the longitudinal strain on the bottom surface of the north bulb at midspan.	107
Figure 151. Graph. CDP vs. CSC in the longitudinal strain on the deck immediately above the web at midspan.	108

Figure 152. Graph. Effect of Young’s modulus on the longitudinal strain on the bottom surface of the north bulb at midspan.	108
Figure 153. Graph. Effect of Young’s modulus on the longitudinal strain on the surface of the deck immediately above the web at midspan.	109
Figure 154. Graph. Effect of maximum tensile stress on the vertical deflection of the bulbs at midspan.	110
Figure 155. Graph. Effect of maximum tensile stress on the vertical deflection at the midspan middeck location.	111
Figure 156. Graph. Effect of maximum tensile stress on the diaphragm force.	111
Figure 157. Graph. Effect of maximum tensile stress on the bulb lateral spreading at midspan.	112
Figure 158. Graph. Effect of maximum tensile stress on the bulb lateral spreading at the support.	112
Figure 159. Graph. Effect of maximum tensile stress on the longitudinal strain on the bottom surface of the bulb at midspan.	113
Figure 160. Graph. Effect of maximum tensile stress on the longitudinal strain on the deck immediately above the web at midspan.	113
Figure 161. Graph. Effect of ultimate tensile plastic strain on the vertical deflection of the bulbs at midspan.	114
Figure 162. Graph. Effect of ultimate tensile plastic strain on the vertical deflection at the midspan middeck location.	114
Figure 163. Graph. Effect of the ultimate tensile plastic strain on the diaphragm force.	115
Figure 164. Graph. Effect of the ultimate tensile plastic strain on the bulb lateral spreading at midspan.	115
Figure 165. Graph. Effect of the ultimate tensile plastic strain on the bulb lateral spreading at support.	116
Figure 166. Graph. Effect of the ultimate tensile plastic strain on the longitudinal strain on the bottom surface of the north bulb at midspan.	116
Figure 167. Graph. Effect of the ultimate tensile plastic strain on the longitudinal strain on the deck immediately above the web at midspan.	117
Figure 168. Graph. Effect of fracture energy criterion on the vertical deflection of the bulbs at midspan.	117
Figure 169. Graph. Effect of fracture energy criterion on the vertical deflection at the midspan middeck location.	118
Figure 170. Graph. Effect of fracture energy criterion on the diaphragm force.	118
Figure 171. Graph. Effect of fracture energy criterion on the bulb lateral spreading at midspan.	119
Figure 172. Graph. Effect of fracture energy criterion on the bulb lateral spreading at support.	119
Figure 173. Graph. Effect of fracture energy criterion on the longitudinal strain on the bottom surface of the north bulb at midspan.	120
Figure 174. Graph. Effect of fracture energy criterion on the longitudinal strain on the deck immediately above the web at midspan.	120

Figure 175. Graph. Effect of rigid and no diaphragms on the vertical deflection of the bulbs at midspan.....	121
Figure 176. Graph. Effect of rigid and no diaphragms on the vertical deflection at the midspan middeck location.	122
Figure 177. Graph. Effect of rigid diaphragms on the diaphragm force.....	122
Figure 178. Graph. Effect of rigid and no diaphragms on the bulb lateral spreading at midspan.	123
Figure 179. Graph. Effect of rigid and no diaphragms on the bulb lateral spreading at support.	123
Figure 180. Graph. Effect of rigid and no diaphragms on the longitudinal strain on the bottom surface of the north bulb at midspan.	124
Figure 181. Graph. Effect of rigid and no diaphragms on the longitudinal strain on the deck immediately above the web at midspan.....	124
Figure 182. Graph. FEM predicted maximum principal stress as viewed from (a) above, (b) below and (c) beside the girder for the rigid-diaphragm case.	125
Figure 183. FEM predicted maximum principal stress as viewed from (a) above, (b) below, and (c) beside the girder for the no-diaphragm case at an ultimate load of 215 kips (954 kN).....	126
Figure 184. Graph. Effect of deck transverse reinforcement on the vertical deflection of the bulbs at midspan.	127
Figure 185. Graph. Effect of deck transverse reinforcement on the vertical deflection at the midspan middeck location.	127
Figure 186. Graph. Effect of deck transverse reinforcement on the diaphragm force.....	128
Figure 187. Graph. Effect of deck transverse reinforcement on the bulb lateral spreading at midspan.....	128
Figure 188. Graph. Effect of deck transverse reinforcement on the bulb lateral spreading at support.	129
Figure 189. Graph. Effect of deck transverse reinforcement on the longitudinal strain on the bottom surface of the north bulb at midspan.	129
Figure 190. Graph. Effect of deck transverse reinforcement on the longitudinal strain on the deck immediately above the web at midspan.	130
Figure 191. Graph. FEM predicted stress and deformation in the transverse deck reinforcement (Note: deformation scale factor = 20).	130
Figure 192. Illustration. (a) Full pi-girder with joint model, and (b) hidden rebar and strands embedded in UHPC.	133
Figure 193. Illustration. Pi-girder with joint model with a 2-inch (51-mm) seeded mesh.	134
Figure 194. Graph. Behaviors of diaphragm subcomponents and assumed nonlinear spring for the diaphragms in the pi-girder with joint tests.	136
Figure 195. Graph. FEM vs. experimentally observed vertical deflection of the bulbs at midspan in Test T2J.....	139
Figure 196. Graph. FEM vs. experimentally observed vertical deflection of the deck near the joint at midspan in Test T2J.	139
Figure 197. Graph. FEM vs. experimentally observed diaphragm force in Test T2J.....	140

Figure 198. Graph. FEM vs. experimentally observed bulb lateral spreading at midspan in Test T2J.	140
Figure 199. Graph. FEM vs. experimentally observed longitudinal strain on the bottom surfaces of the bulbs at midspan in Test T2J.	141
Figure 200. Graph. FEM vs. experimentally observed longitudinal strain on the deck immediately above the webs at midspan in Test T2J.	141
Figure 201. Graph. FEM vs. experimentally observed transverse deformation of the joint at midspan in Test T2J.	142
Figure 202. Graph. FEM vs. experimentally observed axial strains in the dowel bars at the midspan and quarterspan in Test T2J.	142
Figure 203. Graph. FEM predicted minimum principal stress in the UHPC girder and MP-Joint in Test T2J (ultimate load = 302 kips).	143
Figure 204. Graph. FEM vs. experimentally observed vertical deflection of the bulbs at midspan in Test T1J.	144
Figure 205. Graph. FEM vs. experimentally observed vertical deflection of the deck near the joint at midspan in Test T1J.	145
Figure 206. Graph. FEM vs. experimentally observed diaphragm force in Test T1J.	145
Figure 207. Graph. FEM vs. experimentally observed bulb lateral spreading at midspan in Test T1J.	146
Figure 208. Graph. FEM vs. experimentally observed longitudinal strain on the bottom surfaces of the bulbs at midspan in Test T1J.	146
Figure 209. Graph. FEM vs. experimentally observed longitudinal strain on the deck immediately above the webs at midspan in Test T1J.	147
Figure 210. Graph. FEM vs. experimentally observed transverse deformation of the joint at midspan in Test T1J.	147
Figure 211. Graph. FEM vs. experimentally observed axial strains in the dowel bars at midspan and quarterspan in Test T1J.	148
Figure 212. Graph. FEM predicted maximum principal stress on the surface of the girder as reviewed from (a) above, (b) below, (c) the north side of, and (d) the south side of the girder in Test T1J (ultimate load = 428 kips or 1904 kN).	150
Figure 213. Graph. FEM predicted maximum principal plastic strain on the surface of the girder as reviewed from (a) above, (b) below, (c) the north side of, and (d) the south side of the girder in Test T1J (ultimate load = 428 kips or 1904 kN).	151
Figure 214. Photo. Underside of deck from midspan to east end after the conclusion of Test T1J with an ultimate applied load of 422 kips (1877 kN), (reproduced from reference (14)).	152
Figure 215. Photo. (a) North face of north web, and (b) south face of south web after the conclusion of Test T1J with an ultimate applied load of 422 kips (1877 kN), (reproduced from reference (14)).	153
Figure 216. Illustration. FEM predicted maximum principal stress at the (a) midspan, and (b) center of loading patch cross sections in Test T1J (Note: deformation scale factor = 5 and ultimate load = 428 kips (1904 kN)).	154

Figure 217. Illustration. FEM predicted maximum principal plastic strain at the (a) midspan, and (b) center of loading patch cross sections in Test T1J (Note: deformation scale factor = 5 and ultimate load = 428 kips (1904 kN)).	155
Figure 218. Graph. Effect of stabilization on the vertical deflection of the bulbs at midspan. ..	156
Figure 219. Graph. Effect of stabilization on the vertical deflection of the deck near the joint at midspan.	156
Figure 220. Graph. Effect of stabilization on the diaphragm force.	157
Figure 221. Graph. Effect of stabilization on the bulb lateral spreading at midspan.	157
Figure 222. Graph. Effect of stabilization on the longitudinal strain on the bottom surfaces of the bulbs at midspan.	158
Figure 223. Graph. Effect of stabilization on the longitudinal strain on the deck immediately above the webs at midspan.	158
Figure 224. Graph. Effect of stabilization on the transverse deformation of the joint at midspan.	159
Figure 225. Illustration. Pi-girder model with continuous deck and a 2-inch (51-mm) seeded mesh.	159
Figure 226. Graph. Joint vs. full bond in the vertical deflection of the bulbs at midspan.	160
Figure 227. Graph. Joint vs. full bond in the vertical deflection of the deck near the joint at midspan.	161
Figure 228. Graph. Joint vs. full bond in the diaphragm force.	161
Figure 229. Graph. Joint vs. full bond in the bulb lateral spreading at midspan.	162
Figure 230. Graph. Joint vs. full bond in the longitudinal strain on the bottom surfaces of the bulbs at midspan.	162
Figure 231. Graph. Joint vs. full bond in the longitudinal strain on the deck immediately above the webs at midspan.	163
Figure 232. Graph. Joint vs. full bond in the transverse deformation of the joint at midspan. ..	163
Figure 233. Graph. Joint vs. full bond in the axial strains in the dowel bars at the midspan and quarterspan.	164
Figure 234. Graph. Effect of coefficient of friction on the vertical deflection of the bulbs at midspan.	165
Figure 235. Graph. Effect of coefficient of friction on the vertical deflection of the deck near the joint at midspan.	165
Figure 236. Graph. Effect of coefficient of friction on the diaphragm force.	166
Figure 237. Graph. Effect of coefficient of friction on the bulb lateral spreading at midspan. ..	166
Figure 238. Graph. Effect of coefficient of friction on the longitudinal strain on the bottom surfaces of the bulbs at midspan.	167
Figure 239. Graph. Effect of coefficient of friction on the longitudinal strain on the deck immediately above the webs at midspan.	167
Figure 240. Graph. Effect of coefficient of friction on the transverse deformation of the joint at midspan.	168
Figure 241. Graph. Effect of diaphragm on the vertical deflection of the bulbs at midspan.	169

Figure 242. Graph. Effect of diaphragm on the vertical deflection of the deck near the joint at midspan.....	169
Figure 243. Graph. Effect of diaphragm on the diaphragm force.....	170
Figure 244. Graph. Effect of diaphragm on the bulb lateral spreading at midspan.....	170
Figure 245. Graph. Effect of diaphragm on the longitudinal strain on the bottom surfaces of the bulbs at midspan.	171
Figure 246. Graph. Effect of diaphragm on the longitudinal strain on the deck immediately above the webs at midspan.	171
Figure 247. Graph. Effect of diaphragm on the transverse deformation of the joint at midspan.	172
Figure 248. Graph. Effect of diaphragm on axial strains in the dowel bars at midspan and quarterspan.	172

LIST OF TABLES

Table 1. Commercially FEM software packages.....	2
Table 2. Material parameters for the CSC & CDP models of the UHPC used in the I-girder test.....	29
Table 3. Concrete tension stiffening in the CDP models of the UHPC in the I-girder.....	41
Table 4. Material parameters for the CSC & CDP models of the UHPC used in the pi-girder tests.	84
Table 5. Properties of the nonlinear springs which replicate the diaphragms in the pi-girder tests.	86
Table 6. Concrete tension stiffening in the CDP models of the UHPC in the pi-girder.....	109
Table 7. Material parameters for the CDP model of the magnesium phosphate grout used in Test T2J.	134
Table 8. Material parameters for the CDP model of the field-cast UHPC used in Test T1J.....	135
Table 9. Properties of the nonlinear springs which replicate the diaphragms in the pi-girder with joint tests.....	136

CHAPTER 1. INTRODUCTION

INTRODUCTION

Ultra-high performance concrete (UHPC) is an advanced cementitious composite material. When compared to more conventional cement-based concrete materials, UHPC tends to exhibit superior properties such as exceptional durability, increased strength, and better long-term stability (reference (1)).

This computational investigation focused on modeling the behaviors of existing UHPC structural components, including a prestressed UHPC AASHTO Type II girder (or I-girder) and a prestressed UHPC 2nd generation pi-girder. Both a concrete smeared cracking model and a concrete damaged plasticity model were tailored to model UHPC within a commercially available finite element analysis package.

OBJECTIVE

The objective of this research program is to develop finite element analysis modeling techniques applicable to UHPC structural components. The modeling was completed by engaging existing functionalities within a commercially available finite element analysis package. Comparisons to full-scale physical test results allowed for calibration of the models.

SUMMARY OF APPROACH

The research discussed herein steps through the development of five progressively more sophisticated finite element models which correspond to physical tests completed within two experimental testing programs. The first program focused on the flexural and shear response of a UHPC I-girder. The second program focused on the structural response of a 2nd generation pi-girder component experiencing relatively complex bending in both longitudinal and transverse directions. The concrete damaged plasticity model is primarily employed and is demonstrated to be superior to the concrete smeared cracking model in terms of replicating physical test results. Nonlinear springs replaced actual diaphragms and linear springs replaced elastomeric pads in order to facilitate modeling. Some idealized scenarios were also investigated to complement the experimental results and to suggest potential future optimizations.

OUTLINE OF REPORT

This report is divided into eight chapters. Chapters 1, 2, and 3 provide an introduction to the study, discuss relevant finite element method concepts, and present experimental work necessary in understanding the study's results. Chapters 4, 5, 6, and 7 present the finite element models and related parametric studies for the flexural testing of I-girder 80F, the shear testing of I-girders 24S and 14S, the 2nd generation pi-girder, and the 2nd generation pi-girder with a longitudinal joint, respectively. Finally, Chapter 8 presents the conclusions and future work of this research program.

CHAPTER 2. FINITE ELEMENT METHOD

A BRIEF HISTORY

The finite element analysis (FEA) or finite element method (FEM) originated from the need for solving complex structural analysis problems in aeronautical and civil engineering. In 1943, Richard Courant first used the principle of potential energy and piecewise polynomial interpolation over triangular subregions to study a torsion problem. In the 1950s in parallel to advances in computers, FEM's development gained momentum for airplane and structural analysis in civil engineering. The term "finite element" was first coined by Ray W. Clough in 1960. The key concepts of stiffness matrix and element assembly took place by late 1960s. Large general-purpose finite element software packages emerged during the late 1960s and 70s. Gradually the method has evolved into a branch of applied mathematics for numerical modeling of physical systems in a wide variety of engineering disciplines.

After decades of development, a large number of FEM commercial software packages with different application emphases are now available for solving a wide range of problems in solid and structural mechanics, heat and mass transfer, fluid mechanics, acoustics and multiphysics. Table 1 lists a few of these packages, including ABAQUS, the package used in this research program.

Table 1. Commercially FEM software packages.

Software Packages	Company	Applications
ABAQUS	Dassault Systèmes Simulia	Structural analysis, acoustics, thermal analysis, multi-physics, etc.
NASTRAN	MSC software corporation	
ANSYS	ANSYS, Inc.	
MARC	MSC software corporation	
LS-DYNA	Livermore Software Technology Corp.	Structural dynamics, computational fluid dynamics, fluid-structural interaction, etc.
ADINA	ADINA R & D, Inc.	
MSC-DYTRAN	MSC software corporation	
SAP2000	Computers and Structures, Inc.	Civil structural analysis and design

ABAQUS

ABAQUS was initially developed by Hibbitt, Karlsson & Sorenson Inc. of Rhode Island, a company founded in 1978 and acquired by Dassault Systèmes Simulia in 2005. The package is popular with academic and research institutions because it has an extensive range of material models and strong capabilities in nonlinear problems. The ABAQUS suite consists of three products: ABAQUS/Standard, ABAQUS/Explicit, and ABAQUS/CAE. ABAQUS/Standard is a general-purpose solver using a traditional implicit integration scheme to solve finite element analysis. ABAQUS/Explicit uses an explicit integration scheme to solve highly nonlinear transient dynamic and quasi-static analysis. ABAQUS/CAE provides an interactive preprocessing and postprocessing environment. In this research program, ABAQUS/CAE was used to create finite element models and the associated input files for ABAQUS/Standard, and to view the results obtained from ABAQUS/Standard solver.

There are extensive manuals covering commands, procedures, and techniques in CAE as well as analysis, examples, benchmarks, tutorials, and theory. The user support section of the Dassault Systèmes Simulia website, <http://www.simulia.com/>, offers additional technical support for both general and specific questions.

BASIC THEORY

The FEM is a numerical technique for finding approximate solutions of partial differential equations (PDE) through a discretization of a complex problem domain into small simple parts (elements) and an assemblage of simple element equations in each element into a set of global finite element equations. The global finite element equations govern the whole domain by applying nodal continuity conditions and boundary conditions. This method eliminates the partial differential equations by transforming them into a set of approximate ordinary differential equations (ODE) which can be solved by standard numerical techniques for simultaneous linear algebraic equations.

The typical FEM procedure in the implicit integration scheme used for solid mechanics problems can be summarized as follows

1. Discretize domain – A solid body is divided into elements by meshing with elements connected to each other by nodes.
2. Determine element stiffness equation in local coordinates – The relationship between an element and its nodes, shown in Figure 1, is derived from an assumed polynomial representation of the displacement field in the element and the material properties.

$$[k]_e \{u\}_e = \{f\}_e$$

Figure 1. Equation. Element stiffness equation.

In this equation, $[k]_e$ is the element stiffness matrix, $\{f\}_e$ is a load vector describing forces on the element, and $\{u\}_e$ is a displacement vector describing the nodal movement due to applied force.

3. Determine global stiffness equation in global coordinates – The element stiffness matrices are assembled into a global stiffness matrix governing the overall structure through local-global coordinate transformation and nodal displacement continuity. This is reflected in Figure 2.

$$[K]\{U\}=\{F\}$$

Figure 2. Equation. Global stiffness equation.

In this equation, $[K]$ is the global stiffness matrix, $\{F\}$ is a load vector describing forces on the structure, and $\{U\}$ is a displacement vector describing the nodal movement due to applied force.

4. Apply boundary conditions – Remove rows and columns in constrained degrees of freedom from the global matrix equations and specify values of applied force at nodes.
5. Invert the modified global stiffness matrix equation to determine the unknown nodal displacements.
6. Calculate element strains and stresses from the nodal displacements and displacement field interpolation.

The comprehensive theories and applications of FEM can be found in classical references (2) through (6).

WHY FEM

In structural simulation, FEM can allow detailed visualization of structures, estimate distribution of stresses and displacements, identify critical components and facilitate the completion of parametric studies. FEM allows entire designs to be constructed, refined, and optimized before the final product is fabricated and standardized. The introduction of FEM can substantially decrease the time to take products from concept to production. At the same time FEM offers benefits including increased accuracy, enhanced design, and better insight into critical design parameters, virtual prototyping, fewer hardware prototypes, less physical testing, and a faster yet less expensive design cycle.

CONSTITUTIVE MODELS FOR CONCRETE

The relationship between strain and displacement, referred as a constitutive model in a general sense, is a key ingredient in the formulation of finite element solutions for structural analysis

problems. This is especially true in the current study as reinforced concrete has a very complex behavior resulting from inelasticity, cracking, and the interaction between concrete and discrete reinforcement.

A significant amount of literature regarding constitutive modeling of reinforced concrete exists. Reference (7) summarized concrete plasticity models into four main groups: (1) using curve-fitting methods, interpolation, or mathematical functions to represent given stress-strain curves; (2) using linear- and nonlinear-elasticity theories; (3) using perfect- and work-hardening-plasticity theories; and (4) using endochronic, or intrinsic, theory of plasticity. Endochronic plasticity is an incremental-flow theory coupled with a hardening rule. Such a plasticity model includes three aspects: the yield surface (initial and evolved yield surfaces), the flow rule, and the hardening rule. The yield surface specifies when plastic deformation starts, the flow rule gives the direction of plastic deformation, and the hardening rule determines how the yield surface evolves. Two concrete constitutive models are readily available in ABAQUS/Standard version 6.9, reference (8): the concrete smeared cracking (CSC) model and the concrete damaged plasticity (CDP) model based on the work of references (9) through (11). (The third model available in this software package, the brittle cracking model (BCM), is only used in ABAQUS/Explicit.) Both models are based on the endochronic theory of plasticity and provide a general capability for modeling concrete in all type of structures and can be used for both plain and reinforced concrete. Both models also assume two failure mechanisms, namely, tensile cracking and compressive crushing of the concrete material.

Concrete smeared cracking model

The CSC model is intended for essentially monotonic straining at low confining pressures. An isotropically hardening yield surface is activated when the stress is dominantly compressive and an independent “crack detection surface” detects if a point in concrete fails by cracking. In this model, associated flow is assumed and cracks are considered to be irrecoverable once formed. The smeared crack model does not track individual “macro” cracks and instead modifies the stress and material stiffness associated with each integration point when stress reaches the “crack detection surface”.

The CSC model requires tension stiffening and compression hardening to define strain softening behavior of concrete under tensile cracking and compressive crushing. Tension stiffening can be defined by the post-failure stress-strain relationship in Figure 3 or by applying the fracture energy cracking criterion in Figure 4. Concrete is assumed to be linear elastic before its tensile stress reaches the ultimate tensile strength and then strain softening behavior occurs after the failure. The post-failure stress is specified as a function of strain across the crack. A total strain is decomposed into elastic strain and cracking (or inelastic) strain. The definition of tension stiffening in a CSC model requires pairs of cracking strain and post-failure stress. Tension stiffening also can be defined in a stress-displacement response, i.e., fracture energy cracking criterion. Basically it assumes that tensile stress is linearly removed as any crack opens up and eventually vanishes at a characteristic length u_{t0} of crack opening, as illustrated in Figure 4. In simulations of plain concrete or lightly reinforcement concrete, the post-failure stress-displacement tension stiffening model is recommended by the ABAQUS manual. Figure 5 presents a typical compressive stress-strain curve beyond a compressive ultimate stress into

strain-softening area. Similar to tension stiffening, compressive strength used in a CSC model is provided as a tabular function of decomposed plastic strain.

With the inputs from uniaxial tensile and compressive response of concrete and relationship between uniaxial and multiaxial stress states, a failure surface can be formed to govern the plastic response of the concrete. A yield surface in plane stress is illustrated in Figure 6.

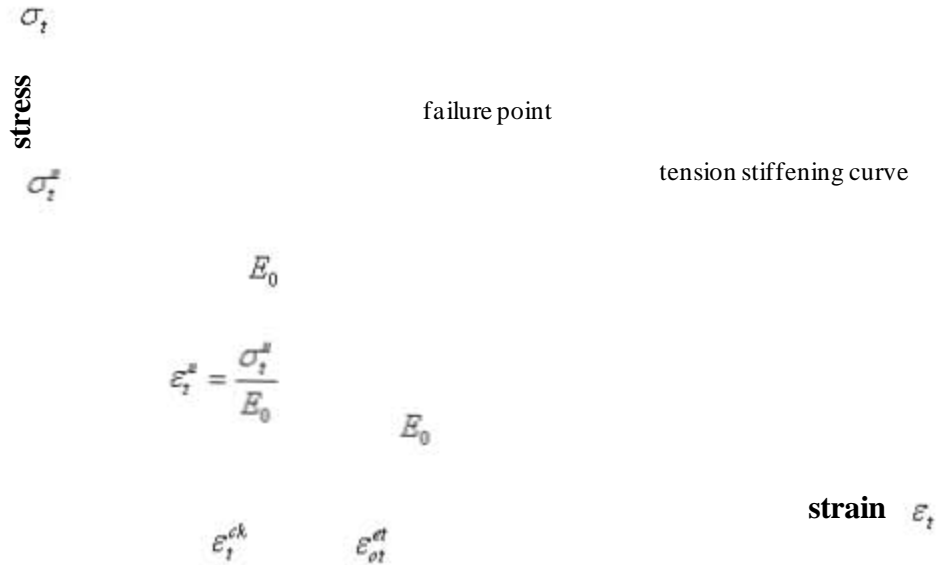


Figure 3. Graph. Tension stiffening model (from ABAQUS manual).

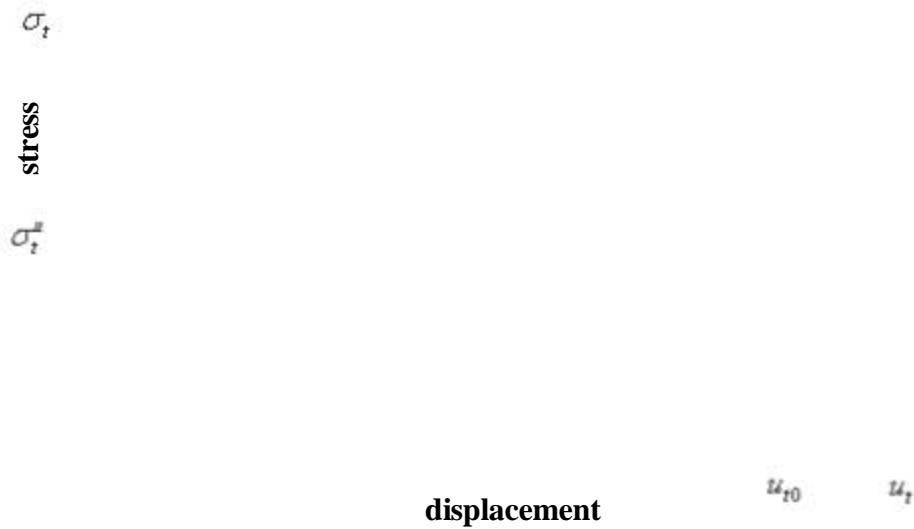


Figure 4. Graph. Fracture energy cracking model (from ABAQUS manual).

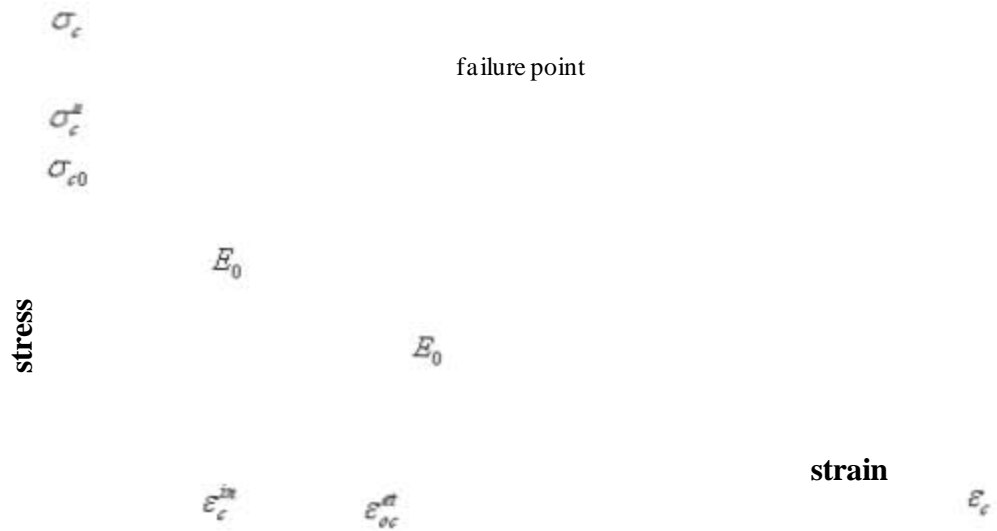


Figure 5. Graph. Compression hardening model (from ABAQUS manual).

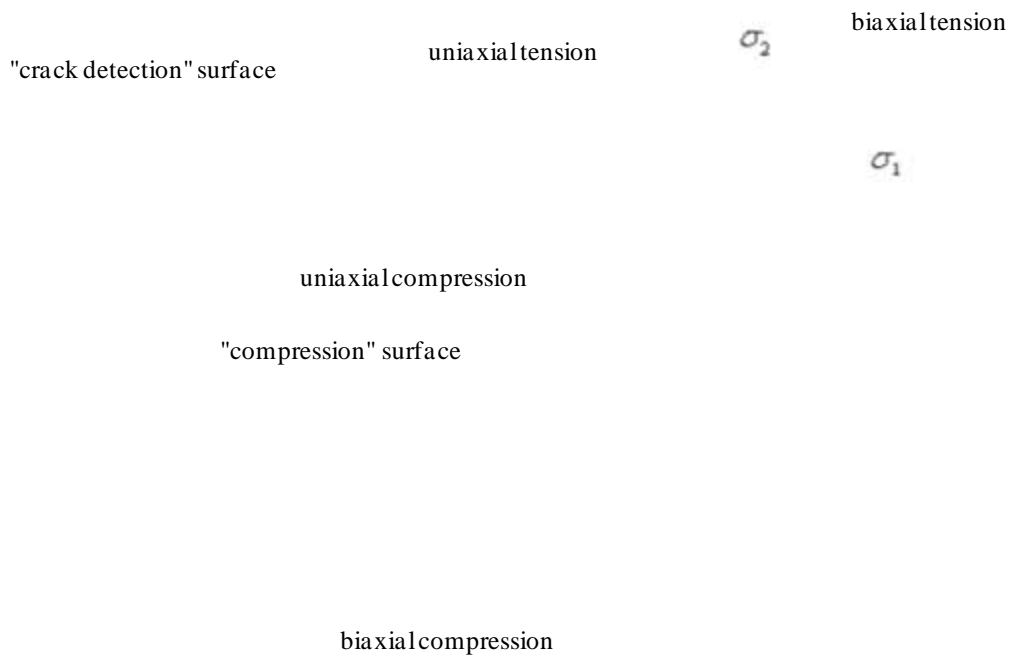


Figure 6. Yield surface in plane stress (from ABAQUS manual).

In order to define a CSC model, a set of parameters regarding compression hardening, tension stiffening and other CSC specific parameters should be supplied in addition to density and elastic modulus. Density, elastic modulus, and compression hardening are straightforward and can be obtained from experimental test data. The tension stiffening may be less readily available, yet is crucial to concrete cracking behavior and should be calibrated to a particular case.

Six additional parameters in the CSC model fall into two categories: failure ratios and shear retention. Failure ratios define the shape of the failure surface. There are four ratios including 1) the ratio of the ultimate biaxial compressive stress to the uniaxial compressive ultimate stress (named as ratio 1, default value is 1.16), 2) the absolute value of the ratio of uniaxial tensile stress at failure to the uniaxial compressive stress at failure (named as ratio 2, default value is 0.09), 3) the ratio of the magnitude of a principal component of plastic strain at ultimate stress in biaxial compression to the plastic strain at ultimate stress in uniaxial compression (named as ratio 3, its default value is 1.28), and 4) the ratio of the tensile principal stress value at cracking in plane stress, when the other nonzero principal stress is at the ultimate compressive stress value, to the tensile cracking stress under uniaxial tension (named as ratio 4, its default value is 1/3). In this study, only ratio 2 has been modified from the default value. For shear retention, it is assumed that shear response is unaffected by cracking. E_{ps_max} defines the maximum strain across the crack and is usually set to 0.1, which is a very large value. The variable ρ_{close} defines the shear retention ratio. With ρ_{close} set to 1, there is full shear retention when strain across the crack is less 0.1.

Concrete damaged plasticity model

The CDP model assumes scalar (isotropic) damage elasticity in combination with isotropic tensile and compressive plasticity to represent the inelastic behavior of concrete. It can handle concrete structures subjected to arbitrary loading conditions including cyclic and/or dynamic loading. It also allows stiffness recovery effects during cyclic load reversals. This model assumes nonassociated potential plastic flow. Formation of tensile micro-cracks is represented macroscopically with a softening stress-strain relationship and similarly its compressive plastic response is typically represented by stress hardening followed by strain softening beyond the ultimate compressive stress. These relationships without cyclic loading are similar to those presented in Figure 3 and Figure 5 in a CSC model. If needed, damage variables can be included in a CDP model to predict damage and stiffness recovery during cyclic load reversals. Although yield function is different between the CDP and CSC models, the yield surface in plane stress for CDP looks schematically similar to the one shown in Figure 6. The schematic yield surface in three-dimensional stress space can be found on page 41 of reference (7). The yield surface can expand or shrink from the initial and subsequent yield surfaces following the hardening or softening rule.

Similar to the CSC model, density, elastic modulus, and compression hardening can be obtained from experimental test data. However, defining tension stiffening accurately is less straightforward. There are three ways: post-failure stress-strain relationship (similar to CSC in Figure 3), post-failure stress-displacement relationship (similar to CSC in Figure 4 but allows more than one value) as depicted in Figure 7, and post-failure stress-fracture energy relationship as shown in Figure 8. The post-failure stress-displacement relationship of a material can be converted into its post-failure stress-fracture energy relationship because the area under a stress-

displacement response is fracture energy, G_f . In ABAQUS, direct definition of fracture energy is always assumed to have a linear loss of strength after cracking as illustrated in Figure 8. Different material response may be observed between these two forms of fracture energy cracking criterion even with the same fracture energy unless the stress-displacement criterion is also defined exactly as a linear loss of strength after cracking.

The five additional parameters required to fully describe a CDP model include dilation angle in degrees, flow potential eccentricity, ratio of initial equibiaxial compressive yield stress to initial uniaxial compressive yield stress, ratio of the second stress invariant on the tensile meridian to that on the compressive meridian, and a viscosity parameter that defines visco-plastic regularization. These default values are set to 15° , 0.1, 1.16, $2/3$ and 0.0, respectively.

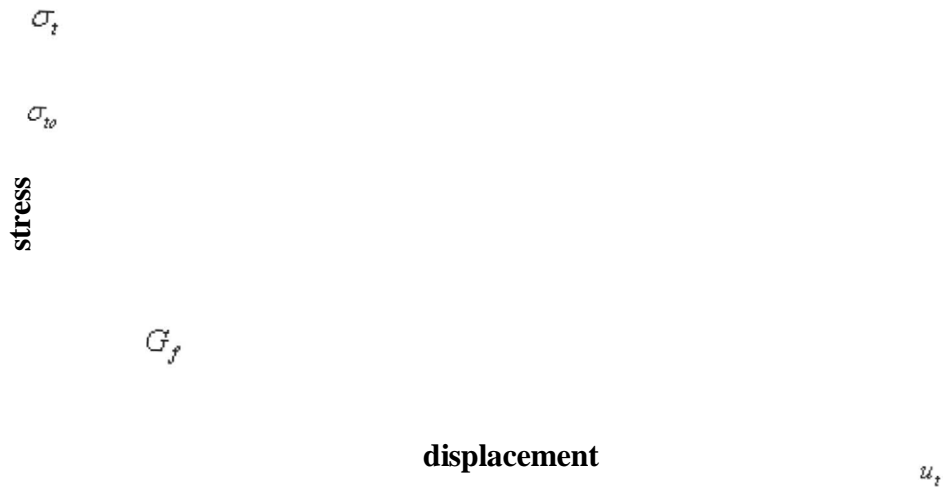


Figure 7. Post-failure stress-displacement curve (from ABAQUS manual).

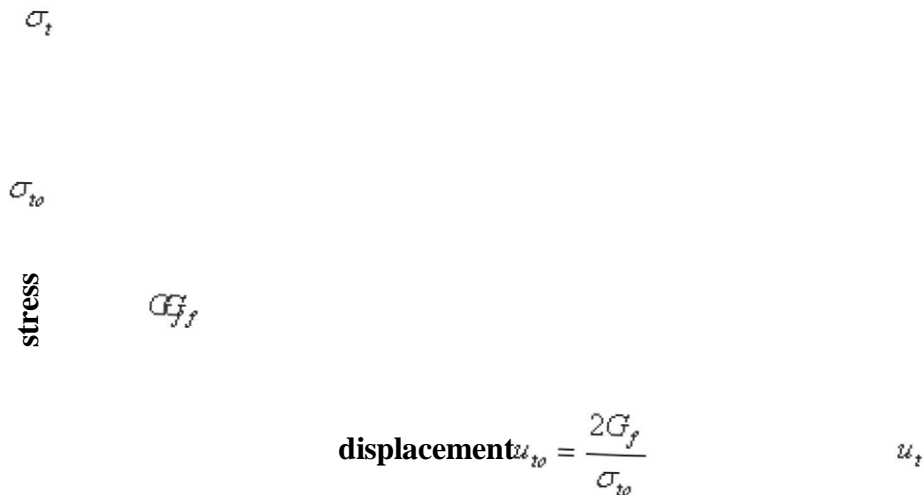


Figure 8. Post-failure stress-fracture energy curve (from ABAQUS manual).

The modeling completed in this study only focuses monotonic loading and therefore both compression and tension damage parameters for damage and stiffness recovery are not provided.

References (7) through (11) provide additional details for the concrete plasticity, CSC, and CDP models used herein.

Since ultra-high performance concrete is significantly different from conventional concrete, the parameters of these constitutive models must be carefully calibrated based on available experimental mechanical testing data. Typical values for a normal concrete may not accurately reflect the behaviors of UHPC.

CHAPTER 3. EXPERIMENTAL WORK

INTRODUCTION

The finite element models proposed in this report were generated in an attempt to reproduce the response of the I-girder 80F reported in references (12) and (13), the responses of the I-girders 24S and 14S reported in reference (12), and the responses of the 2nd generation pi-girders reported in reference (14). Specifically, I-girder Tests 80F, 24S, 14S, and 2nd generation pi-girder Tests T1D, T2D, T1J, and T2J are considered. Since these references cover the detailed information of girder geometries and test plans, only a brief summary of the relevant information is supplied below.

I-GIRDER 80F DESCRIPTION

An overview of the test setup and instrumentation plan is provided in Figure 9 and Figure 10. The test fixture was assembled such that the 80-ft (24.4-m) long girder could be considered as a simply supported flexure member with the bearings centered 9 inch (229 mm) from the ends of the girder. The girder was loaded symmetrically by two point loads each located 3 ft (0.91 m) from midspan. The girder used the AASHTO Type II girder shape, whose cross section is illustrated in Figure 11. This AASHTO shape is 36-inch (0.91-m) deep and has a 12-inch (305-mm) wide top and an 18-inch (457-mm) wide bottom flange. The girder web is 15-inch (381-mm) deep and is 6-inch (152-mm) thick. The girder contained twenty-six 0.5-inch (12.7-mm) diameter, 270 ksi (1862 MPa), low-relaxation prestressing strands. Twenty-four of these strands are located in the bottom flange, spaced in a grid pattern on 2-inch (51-mm) spacing.

The girder contained no mild steel reinforcement. It was designed to carry tensile flexural forces via the combined action of prestressing strand and the UHPC tensile resistance, and was designed to carry tensile shear forces via the UHPC tensile resistance.

I-GIRDERS 24S AND 14S DESCRIPTION

Two additional tests, namely Tests 24S and 14S, focused on shear response of the same AASHTO shape and strand reinforcement as the I-girder 80F illustrated in Figure 11. The test setup and instrumentation plan for Test 24S is provided in Figure 12. The I-girder 24S specimen with a span of 24 ft (7.3 m) is obtained from the east portion of the tested I-girder 80F specimen after the conclusion of Test 80F. Most instrumentation included seven potentiometers to capture the vertical deflection of the girder. Strain gages were installed on the side face, the top and bottom surfaces of the girder along seven instrumentation lines to capture longitudinal deformation. Six 45° strain rosettes were installed on the side face, centered 17 inch (432 mm) from the top of the girder, to capture shear response. The test setup and instrumentation plan for Test 14S is provided in Figure 13. The I-girder 14S specimen was part of a 30-ft (9.2-m) long girder, and was tested on a span of 14 ft (4.3 m). Its instrumentation plan is similar to that implemented for Test 24S.

PI-GIRDER DESCRIPTION

The 2nd generation pi-girder is the result of a research program aimed at developing an optimized prestressed girder that efficiently utilizes the advanced material properties of UHPC. It is a direct descendent of the prototype described in references (15) through (20). Its cross section is shown in Figure 14. The girder is 33-inch (0.84-m) deep, 8.33-ft (2.54-m) wide, 25-ft (7.6-m) long and can contain up to 16 prestressing strands in each bulb. The integral deck of the girder is 4.1-inch (104-mm) thick, and webs range from 3.2- to 3.5-inch (81- to 89-mm) thick. A 5.2-inch (132-mm) deep shear key runs the length of each flange tip to allow for connection of the modular components. The girder was prestressed through the use of 0.6-inch (15.2-mm) diameter, 270 ksi (1862 MPa), low-relaxation prestressing strands. The girder contained 22 strands, with 9 in each of the two bulbs and 2 in the deck above each web. The strands in the bulbs were all stressed to 42.5 kips (189 kN) and the strands in the deck were each pulled to 5 kips (22 kN).

These pi-girder test specimens each included two steel diaphragms within the span. The diaphragms are each located 6.33 ft (1.93 m) from midspan. Figure 15 and Figure 16 show the details of the diaphragms. Figure 15 shows the two different diaphragms configurations with one designed for the space between legs of an individual girder and the other designed to span the transverse distance between the bulbs of two adjacent girders. Figure 16 shows the details of the end plates welded onto the end of the steel tubes that comprise the length of the diaphragms. However, during the installation of the longer diaphragms into the space between the girder legs in Tests T1D and T2D, the end plates were milled from a designed thickness of 0.5 inch (12.7 mm) to a thickness between 0.31 and 0.35 inch (8 and 9 mm) to fit the diaphragms into the space between girder legs.

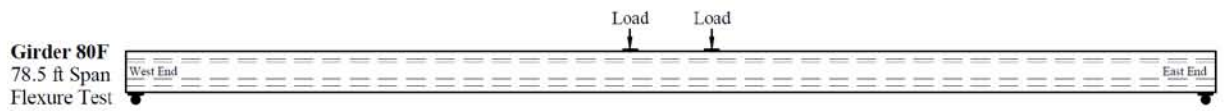


Figure 9. Illustration. Test setup of the I-girder Test 80F.

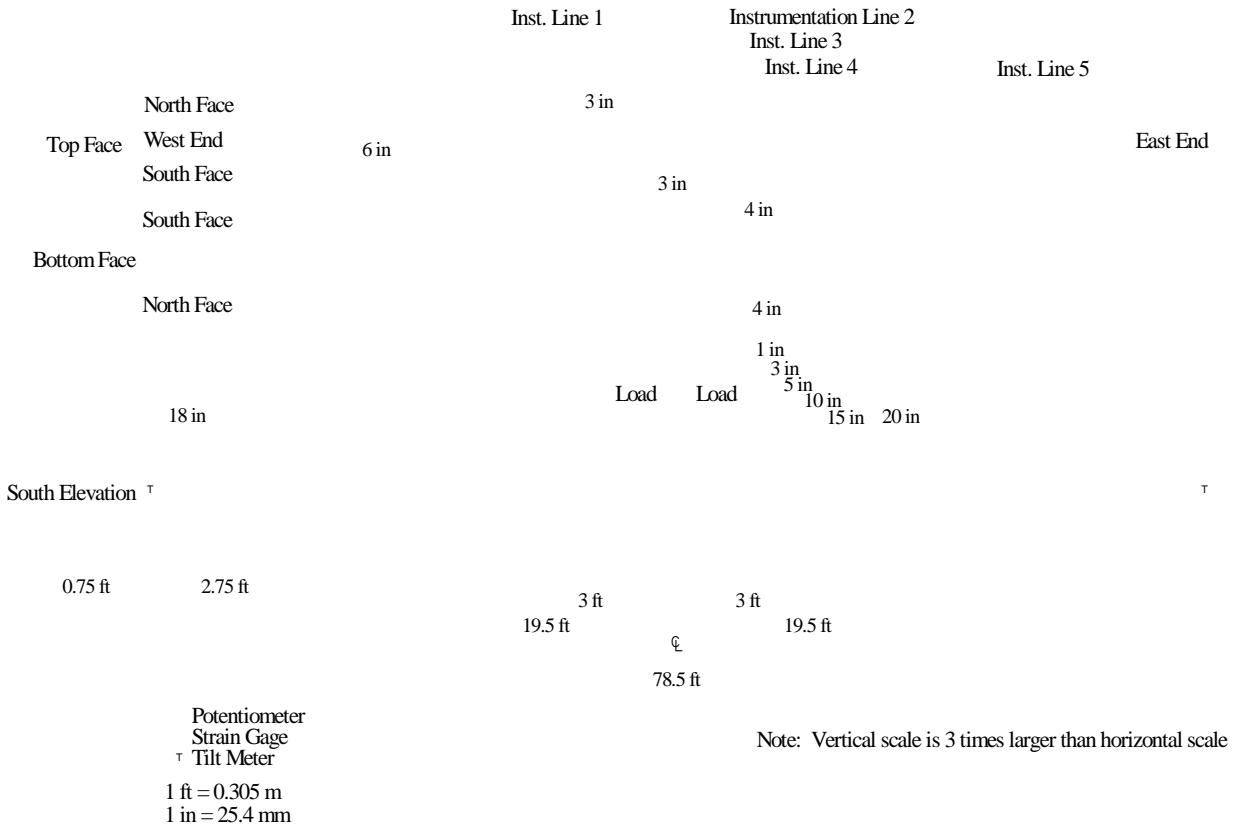


Figure 10. Illustration. Instrumentation plan for the I-girder Test 80F.

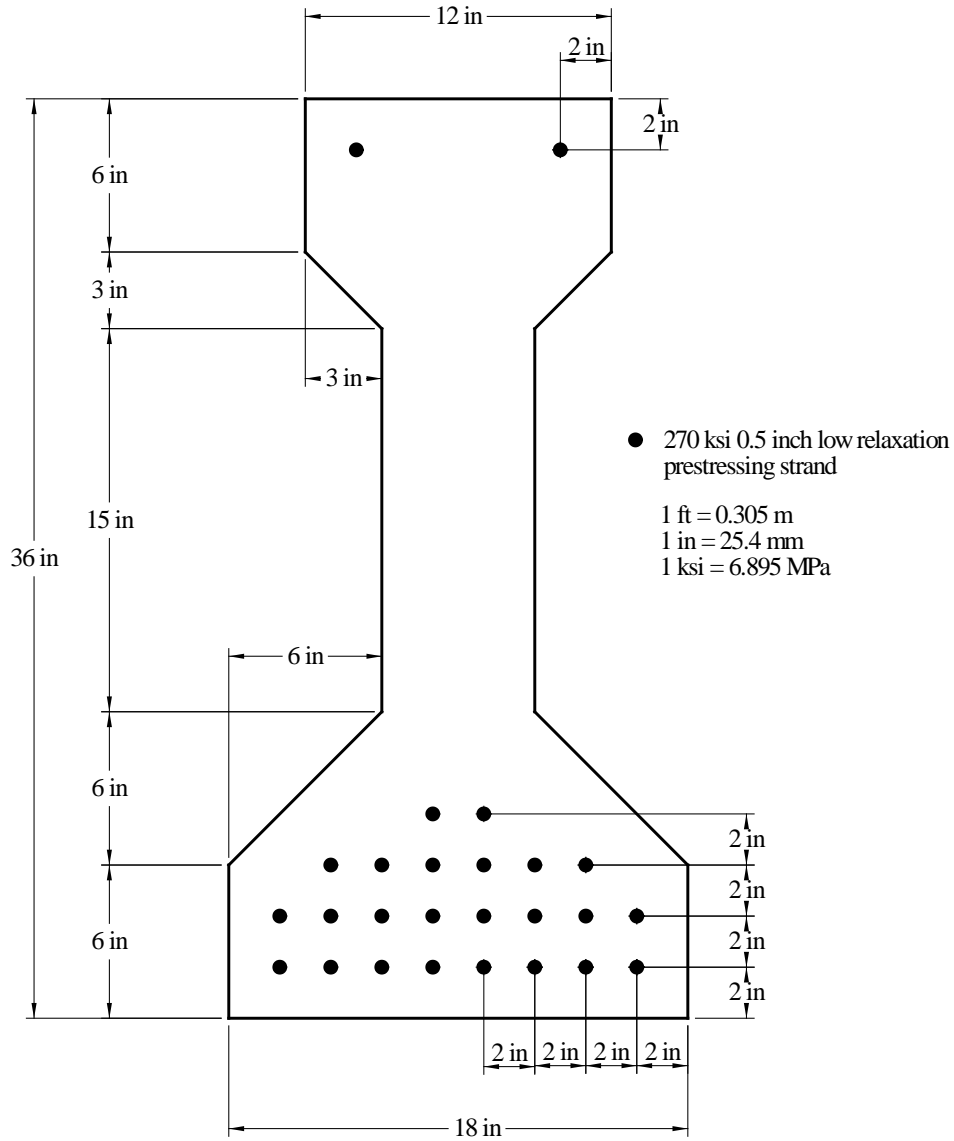


Figure 11. Illustration. AASHTO Type II cross section and strand pattern.

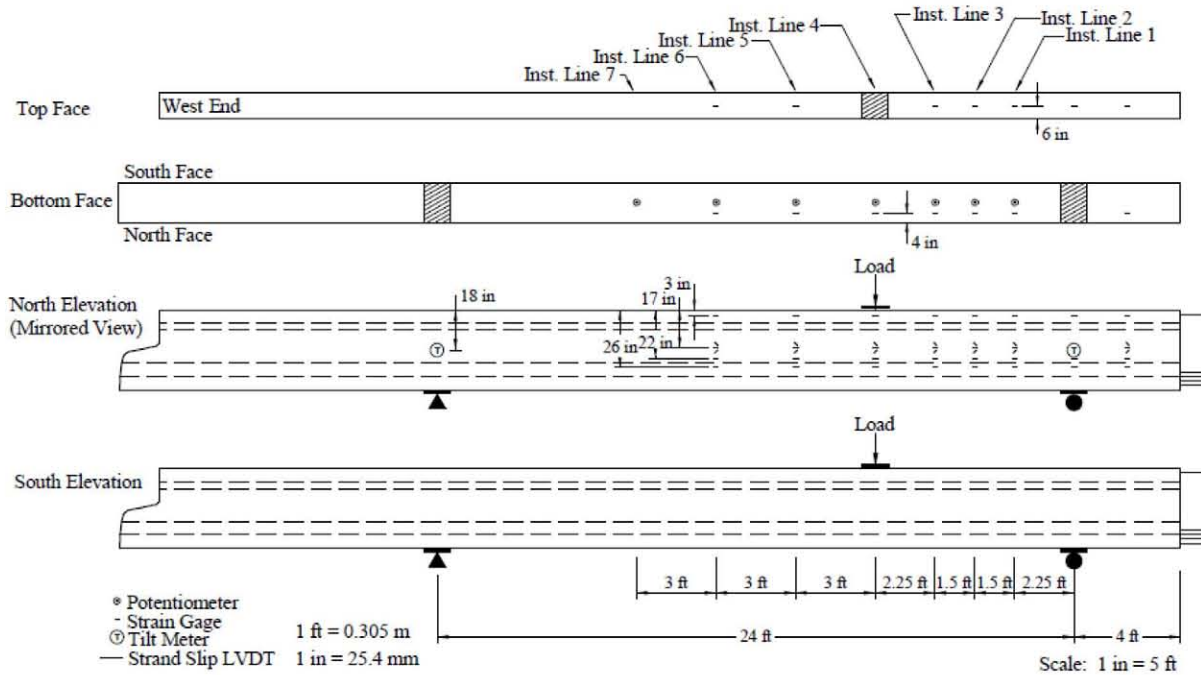


Figure 12. Illustration. Instrumentation plan for the I-girder Test 24S.

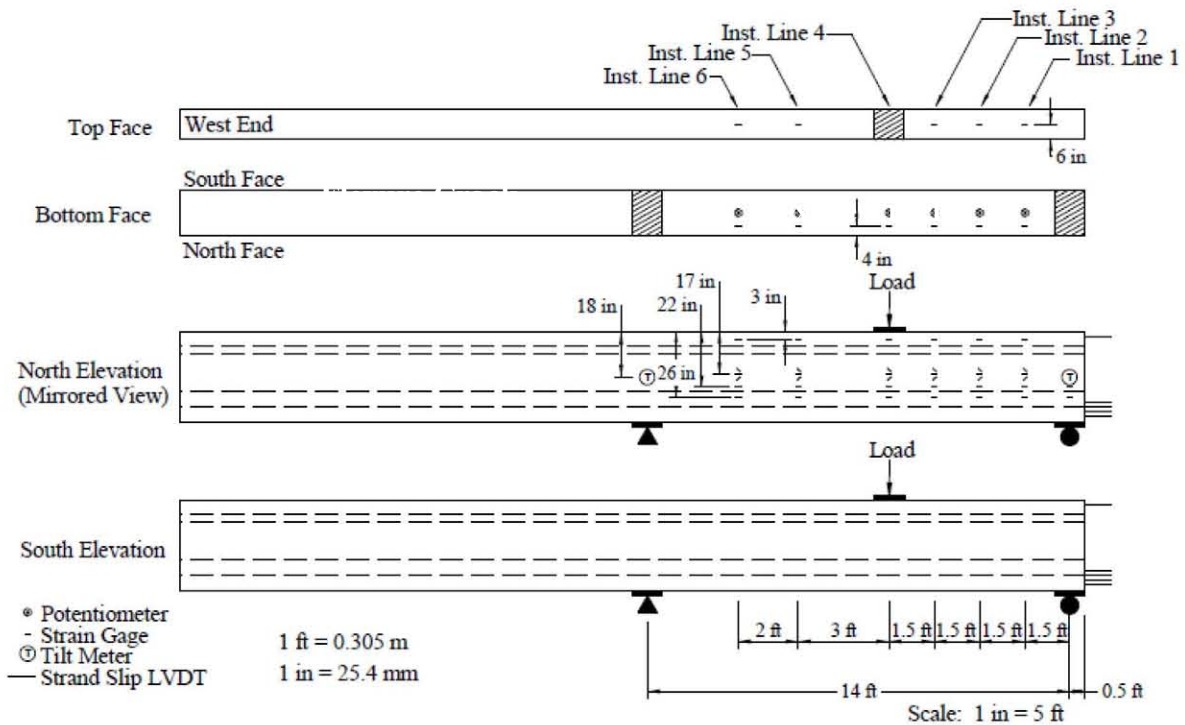


Figure 13. Illustration. Instrumentation plan for the I-girder Test 14S.

5.2 in
 100.0 in
 4.1 in
 33.0 in
 3.2 in
 50.5 in
 1 in = 25.4 mm

Figure 14. Illustration. Pi-girder cross section and strand pattern.

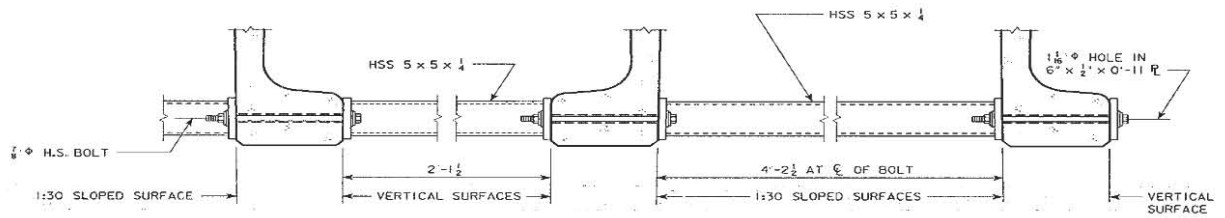


Figure 15. Illustration. Elevation view of diaphragms (unit in inch).

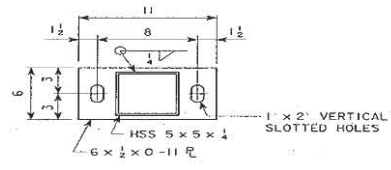


Figure 16. Illustration. End view of diaphragm end plate (unit in inch).

Figure 17 illustrates the loading set up of Test T2D, which focused on transverse flexure behavior of the pi-girder when subjected to loads applied between the girder's legs. Figure 18 and Figure 19 provide photographs of the setup. A peak total load of 340 kips (1512 kN) was applied vertically downward through two hydraulic jacks situated near midspan. In the test, loads were transmitted to the deck through two 10 inch by 20 inch (0.25 m by 0.51 m) elastomeric pads located along the centerline of the girder and situated 2 ft (0.61 m) on either side of midspan. These 1-inch (25-mm) thick elastomeric pads were backed by 1-inch (25-mm) thick steel plates. In the FEM model, two 10 inch by 20 inch (0.25 m by 0.51 m) surfaces replaced the elastomeric pads and assume ultimate uniform pressure of 0.85 ksi (5.86 MPa) on each of them. The girder bulbs rested on four 6 inch by 12 inch (0.15 m by 0.30 m) elastomeric pads at each of the four abutment locations. The elastomeric pads were also 1-inch (25-mm) thick. Although elastomers usually use a hyperelastic material model, two types of linear springs were instead defined to mimic the vertical and horizontal resistances provided to the pi-girder legs. The spring property in the vertical direction can be estimated from measurements captured by an LVDT at one support as shown in Figure 22. The spring in the horizontal direction was defined to exhibit a negligible stiffness of 1 lb/in (0.18 N/mm) to prevent large rigid body movement of the pi-girder.

Figure 20 through Figure 22 illustrate the locations of strain gages, potentiometers, and LVDTs in Test T2D. Test T1D is identical to Test T2D except that the T1D specimen does not have transverse #5 rebar in the deck.

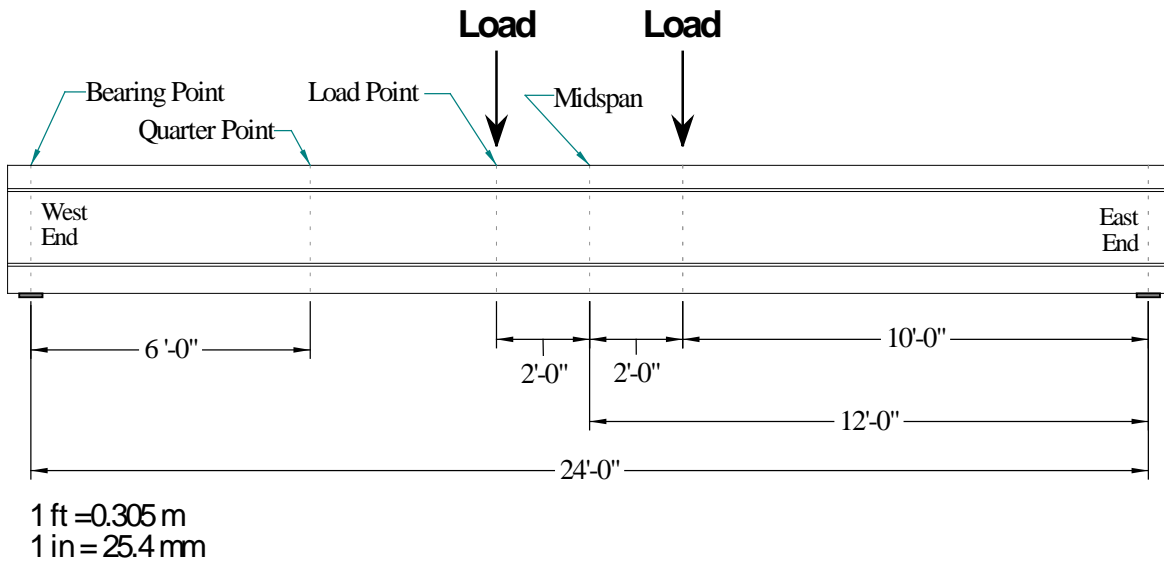


Figure 17. Illustration. Test plan for the pi-girder.



Figure 18. Photo. Setup for the pi-girder.



Figure 19. Photo. West end for the pi-girder test.

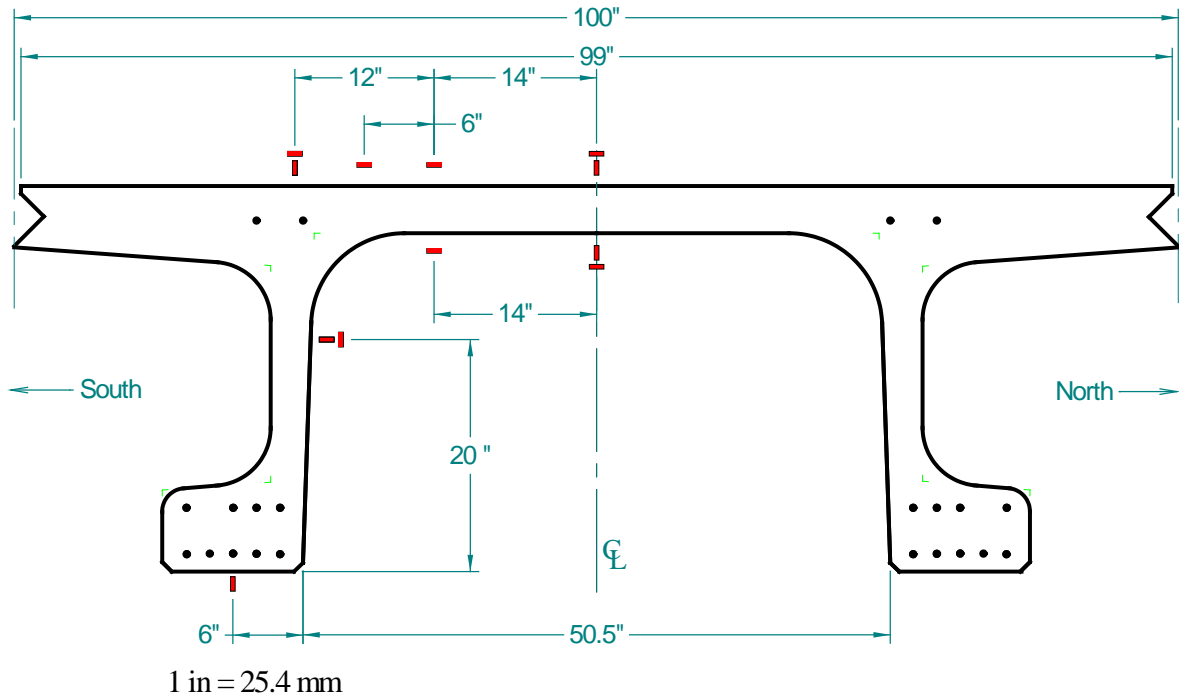


Figure 20. Illustration. Midspan strain gage locations for the pi-girder test.

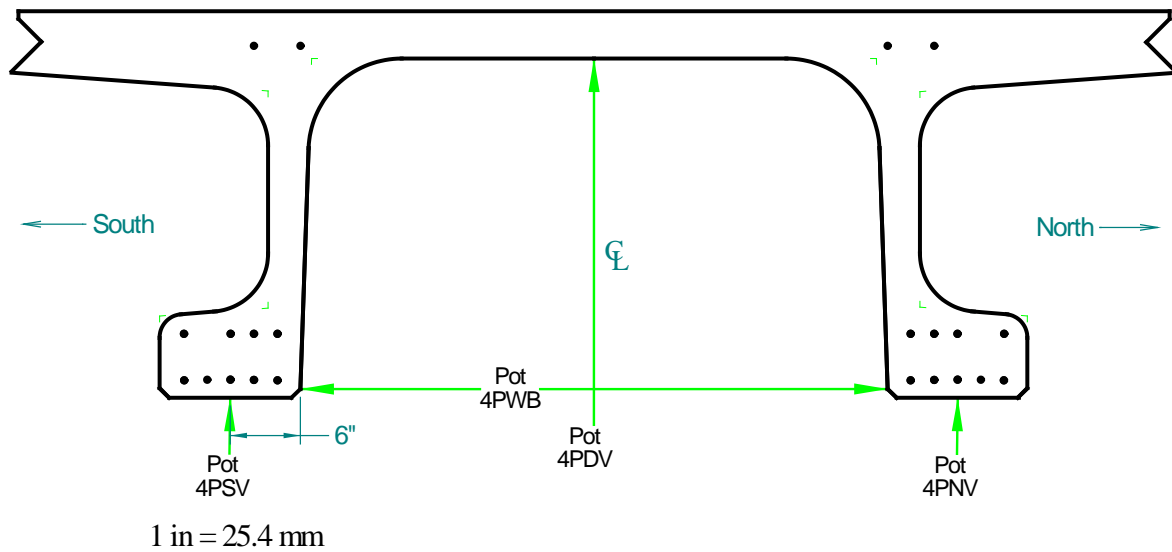


Figure 21. Illustration. Midspan potentiometer locations for the pi-girder test.

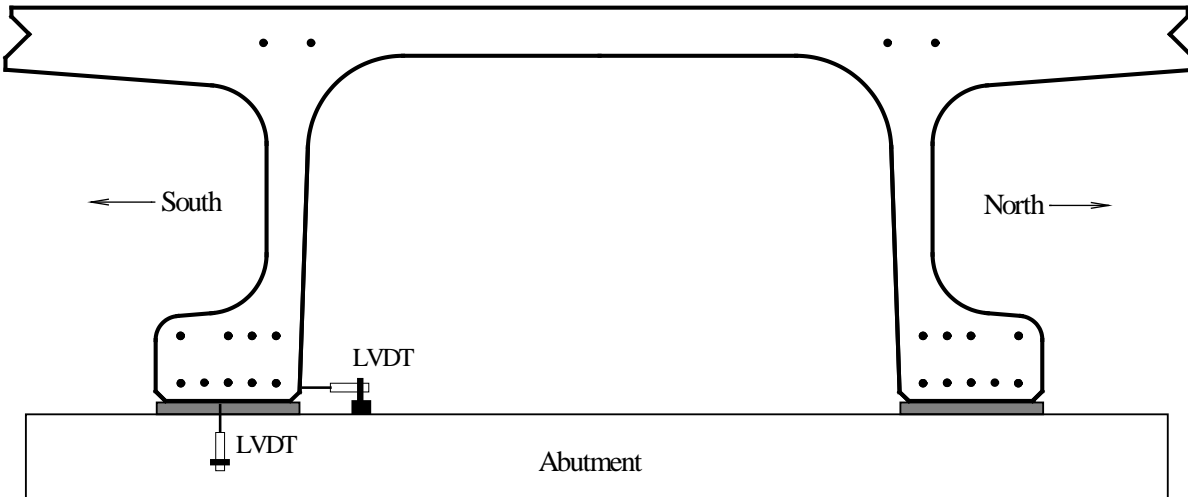


Figure 22. Illustration. Abutment LVDT locations for the pi-girder test.

PI-GIRDER WITH JOINT DESCRIPTION

Test T2J, a test on the pi-girder with a longitudinal joint, was in many ways similar to Test T2D. The T2J test specimen was created by saw-cutting specimen T2D along the longitudinal center line after the conclusion of Test T2D. A high performance magnesium phosphate grout, Eucospeed MP, was used to fill the longitudinal joint between the half-girders. Test T2J focused on transverse flexural and shear behaviors of the pi-girder in presence of the longitudinal joint, a joint which would repeat itself between adjacent pi-girders in a bridge structure. Figure 23 illustrates this joint connection detail, which includes a longitudinal shear key and periodic mild-steel reinforced grout pockets. The diamond-shaped shear key is 3.5-inch (89-mm) deep and has a 1-inch (25-mm) opening along the top to allow for grouting. The periodic grout pockets extended 14 inch (356 mm) into each adjacent girder and were 4-inch (102-mm) wide and deep. Each pocket was intersected by two #5 reinforcing bars. A 26-inch (660-mm) long #8 reinforcing bar was installed in each pocket, with the pockets spaced at 18 inch (457 mm) along the length of the girder. To avoid the complexity of the pocket detail in the FEM model, the model assumed that continuous UHPC material covers the pockets. The diamond-shape shear key filled with grout material and the #8 reinforcing bars were modeled in the study.

Similar to Test T2D, the specimens in Tests T1J and T2J included two diaphragms within the span. These diaphragms were located 6.33 ft (1.93 m) from midspan. The diaphragm configuration is also illustrated in Figure 15 for two adjacent girders. Unlike Test T2D, the end plates were installed with the as-fabricated end plate thickness of 0.5 inch (12.7 mm).

The loading setup of Test T2J is also illustrated in Figure 17 and is similar to Test T2D. The primary modification is that the applied loads were offset 5-inch (127-mm) north of the joint centerline as depicted by the photographs of the loading setup in Figure 24 and Figure 25.

Figure 26 through Figure 29 illustrate the locations of strain gages, potentiometers and LVDTs in Test T2J. Because of unsymmetrical loading along joint centerline, many of the gages are installed on both north and south half girders. There were additional gages provided for measuring the behavior of the longitudinal joint.

The T1J test specimen was created by saw-cutting specimen T1D along transverse center line after the conclusion of Test T1D. Therefore Test T1J is almost the same as Test T2J except that its specimen does not have transverse #5 rebar in the deck and the grouting material for the longitudinal joint is field-cast UHPC.

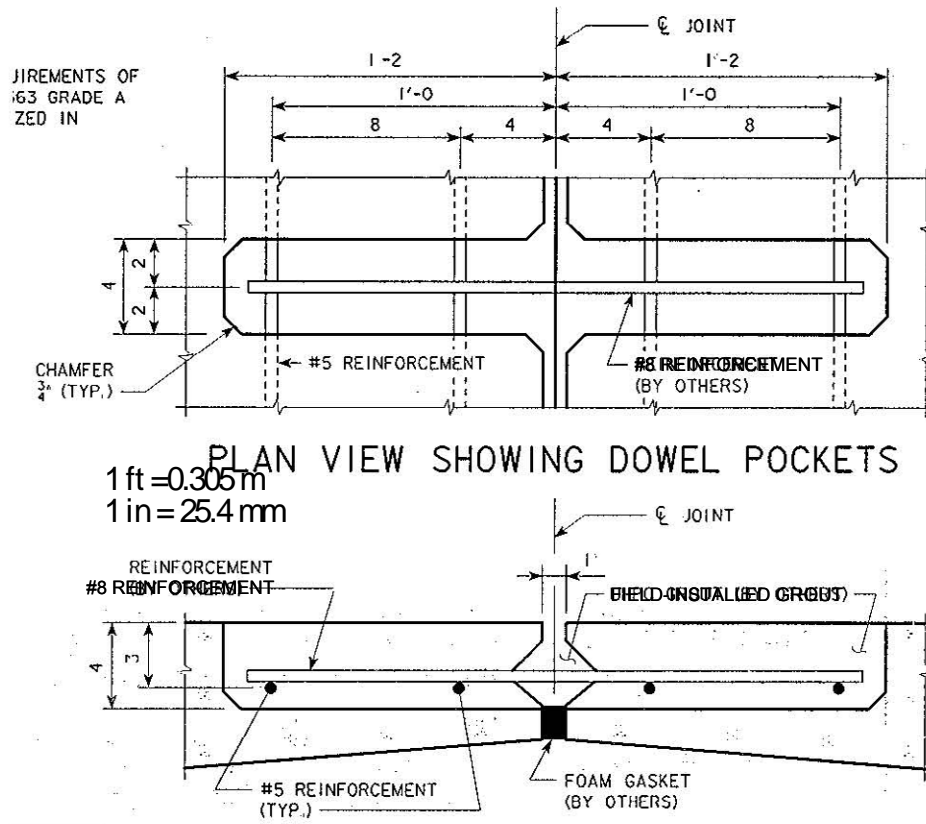


Figure 23. Illustration. Plan view (above) and elevation view (below) of longitudinal grouted joint detail between pi-girders.



Figure 24. Photo. Setup for the pi-girder with joint.



Figure 25. Photo. East end of the pi-girder with joint test.

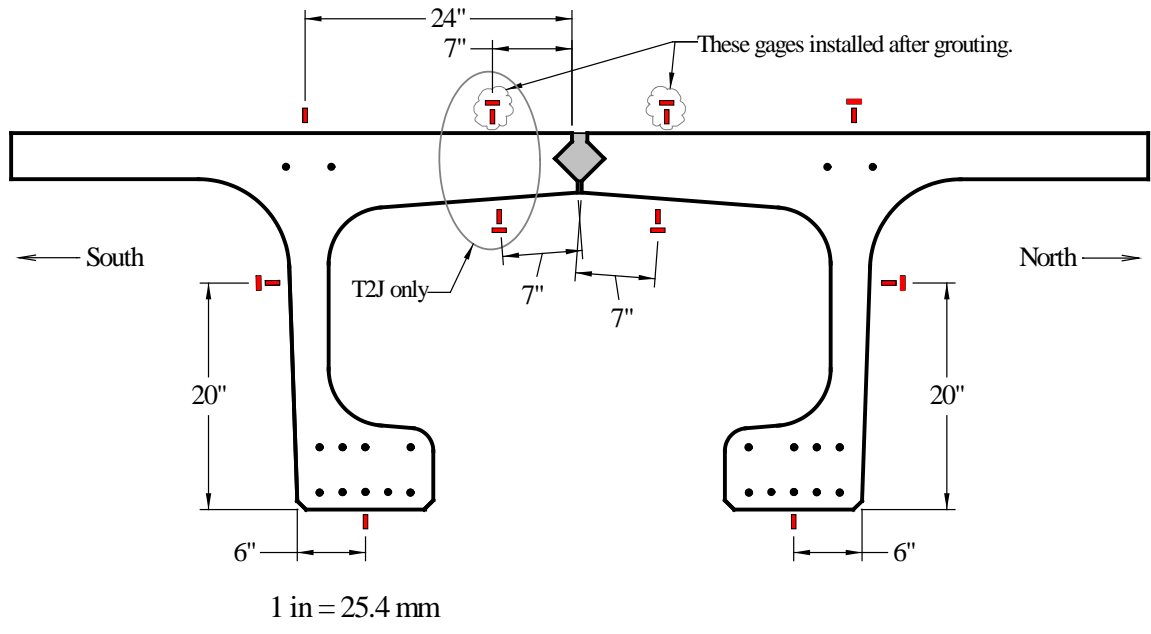


Figure 26. Illustration. Midspan strain gage locations for the pi-girder with joint test.

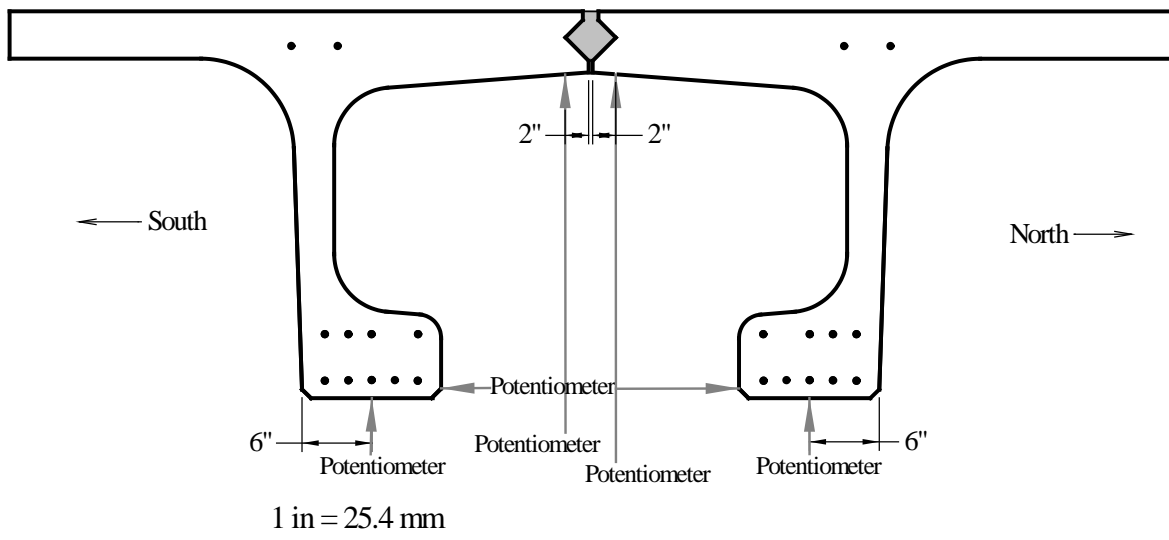


Figure 27. Illustration. Midspan potentiometer locations for the pi-girder with joint test.

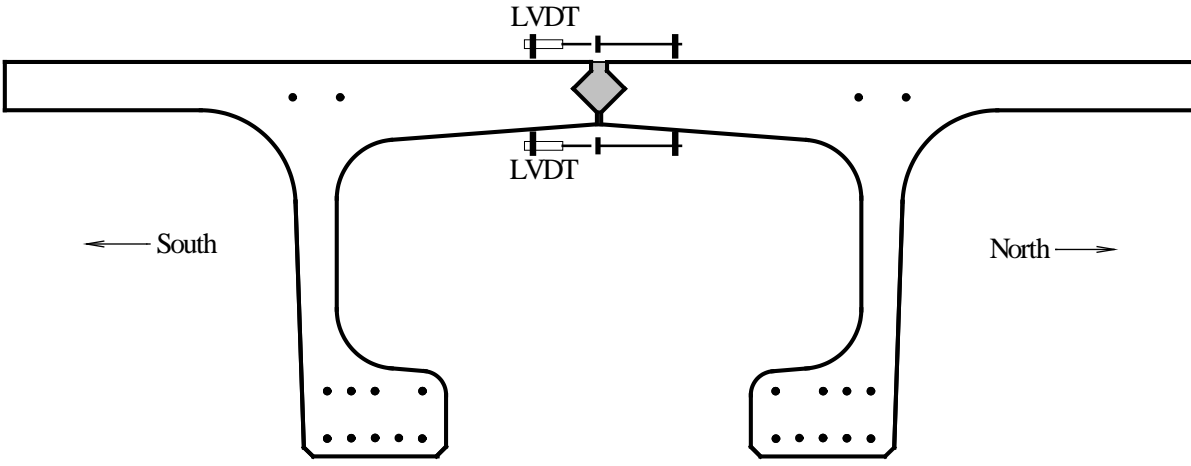


Figure 28. Illustration. Midspan LVDT locations for the pi-girder with joint test.

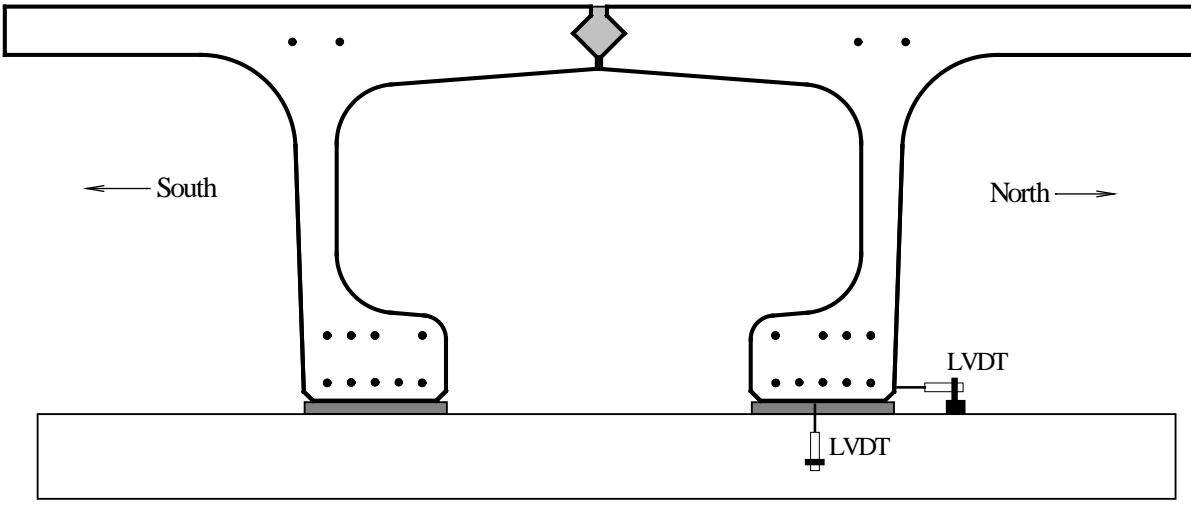


Figure 29. Illustration. Abutment LVDT locations for the pi-girder with joint test.

CHAPTER 4. I-GIRDER 80F

FINITE ELEMENT MODEL

ABAQUS/Standard version 6.9 (reference (8)) was used to perform the three dimensional, static modeling of the girder tested in the full-scale experimental investigation referred to as Test 80F. This effort was undertaken primarily to provide a means to calibrate UHPC mechanical properties within the software package. The test was particularly useful as it represents a relatively simple case wherein the structural behaviors are dominated by flexural response along the strong axis of a beam.

Figure 30 depicts the three dimensional I-girder model. The I-girder was supported on two steel plates which were modeled in 3D continuum shell element SC8R. The steel plates were pinned in the vertical direction along transverse center line in order to simulate roller bearings. Additional nodal restrictions prevented girder rigid body movement while allowing for longitudinal deformation. Vertical downward surface pressure peaking at a total of 180 kips (801 kN) force was applied via 1-inch (25.4-mm) wide strips of two steel plates which sit on the top of the girder near midspan. The plates imparted the pressure to the girder top flange across a frictionless “hard” surface-to-surface contact interaction.

Figure 31 plots the assumed uniaxial stress-strain responses for 270 ksi (1862 MPa) strands, A36 steel and reinforcing rebar steel in the finite element models presented in this report. The stress-strain relationship for 270 ksi (1862 MPa) strand is expressed by the equation in Figure 32. Its Young’s modulus is 28500 ksi (197 GPa) and Poisson’s ratio is 0.3. When the prestressing steel strain is less 0.0086, the strand is assumed to be elastic. However, as the strain exceeds 0.0086, the strand begins yielding and exhibits a reduced stiffness until it fails at its ultimate capacity of 270 ksi (1862 MPa).

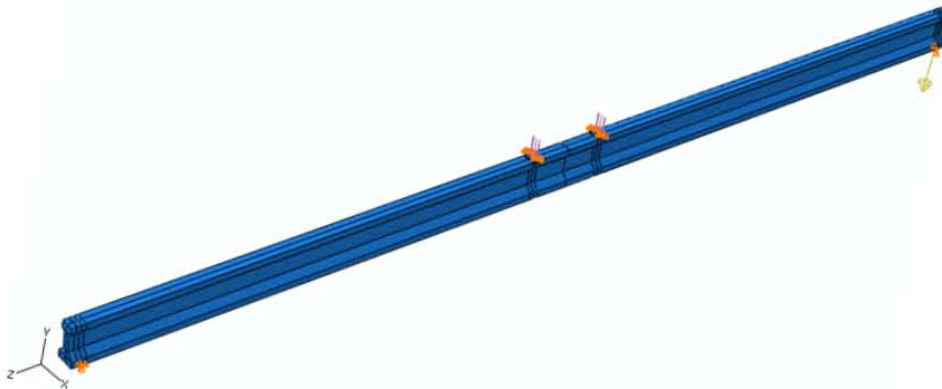


Figure 30. Illustration. I-girder 80F model.

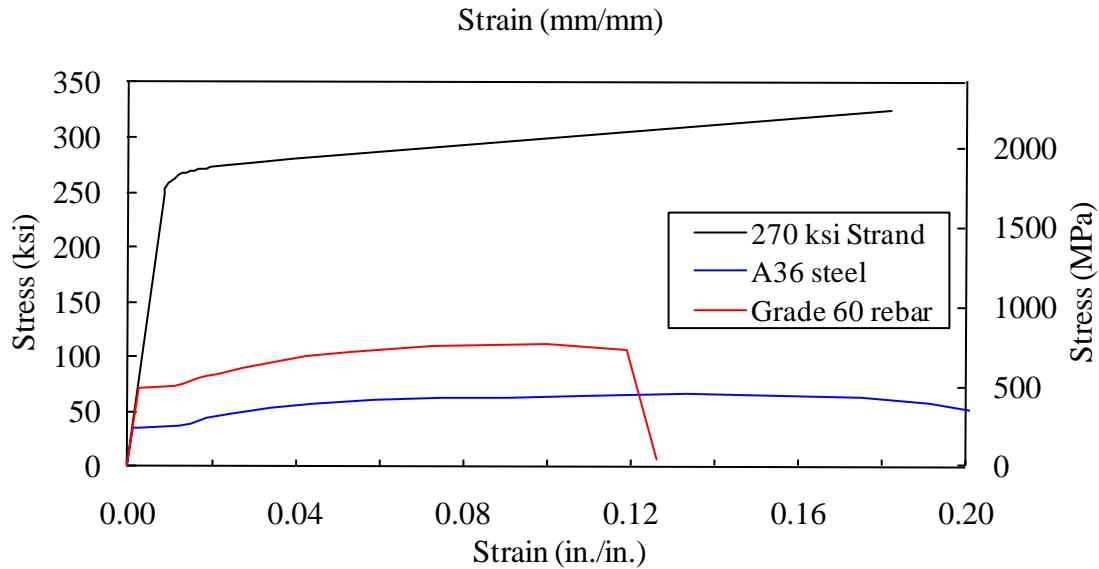


Figure 31. Graph. Prestressing strand, A36 steel, and reinforcing rebar steel uniaxial stress-strain relationships.

$$\begin{aligned}
 f_{ps,270} &= E_p \varepsilon_{ps} && \text{if } \varepsilon_{ps} \leq 0.0086 \\
 &= 270 \text{ksi} - \frac{0.04 \text{ksi}}{\varepsilon_{ps} - 0.007} && \text{if } \varepsilon_{ps} > 0.0086
 \end{aligned}$$

Figure 32. Equation. Assumed stress-strain response of 270 ksi (1862 MPa) prestressing strand.

The strands are pretensioned to 55% of 270 ksi (1862 MPa) for initial prestressing. A 20.2-ksi (139-MPa) loss excluding elastic shortening was assumed. A magnitude of 128.3 ksi (885 MPa) prestressing in the longitudinal z-direction using a stress-type initial condition was applied to all twenty-six strands. Elastic shortening was automatically calculated in the first step. In order to reduce mesh density to model strands, a square of equivalent steel area 0.153 in^2 (98.7 mm^2) replaces the original 7-wire bundle as shown in Figure 33.

Deformation under gravity loads was calculated in the first step according to the given material densities: 160 lb/ft^3 (2565 kg/m^3) for UHPC and 490 lb/ft^3 (7856 kg/m^3) for steel.

D

D'

Figure 33. Illustration. Equivalent shape of prestressing strand.

For strands and concrete, continuous solid element with reduced integration C3D8R was used. Figure 34 illustrates two different meshes with 4 inch (102 mm) and 2 inch (51 mm) global seeds used to check mesh sensitivity.

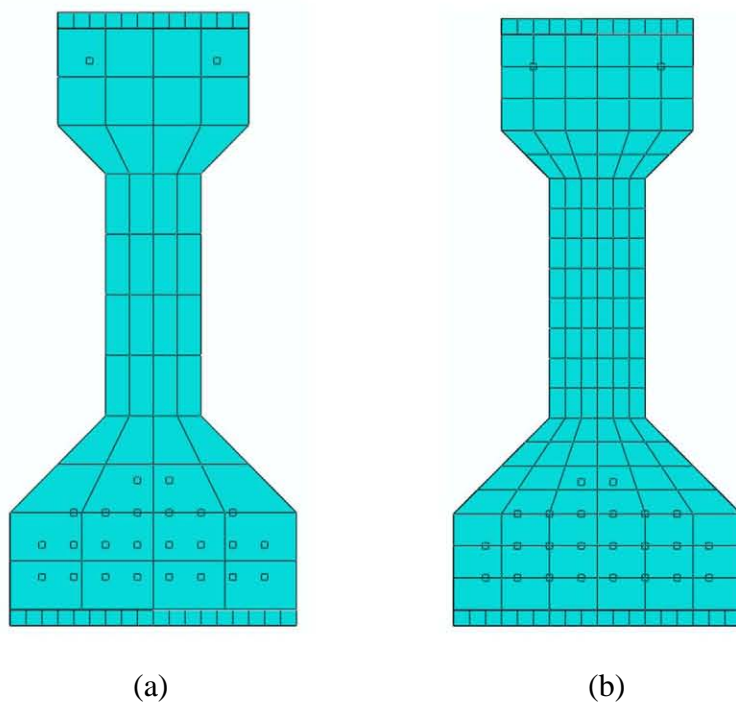


Figure 34. Illustration. I-Girder model with (a) a 4-inch (102-mm) seeded mesh (b) a 2-inch (51-mm) seeded mesh.

CONSTITUTIVE MODELS FOR UHPC

Both CDP and CSC models are frequently used for conventional concrete. Their parameters for UHPC may be significantly different from conventional concrete and must be carefully calibrated based on available experimental tension and compression data. UHPC material

assumptions on the density, elastic modulus, compression hardening, tension stiffening, and other CDP and CSC parameters are listed in Table 2. Unit weight of the UHPC was taken as 160 lb/ft³ (2565 kg/m³) and elastic properties were defined by a Poisson’s ratio of 0.18 and a Young’s modulus of 8000 ksi (55 GPa) per reference (21). Figure 35 depicts the assumed uniaxial stress-strain relationship of UHPC. Its concrete compression hardening is extracted from compression test cylinder response results presented in reference (21). Since the maximum compressive stress estimated to have been observed in Test 80F is approximately 24 ksi (166 MPa) and the I-girder did not reach compressive failure stress, the parameters greater than 27.5 ksi (190 MPa) were never activated and the definition of these parameters are irrelevant to this model. For concrete tension stiffening, a simple elastic perfectly plastic stress-strain relationship is assumed. Two tension stiffening parameters, namely maximum tensile stress and ultimate plastic strain, are very important as tensile failure of the UHPC via fiber pullout across a critical crack location led to the failure of the I-girder.

Beside the parameters for concrete compression hardening and concrete tension stiffening shared by both CDP and CSC models, there are five additional parameters required to fully describe the CDP model and six additional parameters for the CSC model. Those values in the CDP model were set to default values given in Chapter 2, as recommended by ABAQUS/Standard version 6.9 (8).

The parameters defined for failure ratios and shear retention in the CSC model use default values given in Chapter 2 except ratio 2, where the defined value is 2.3 ksi/27.5 ksi=0.0836 and not the default value of 0.09.

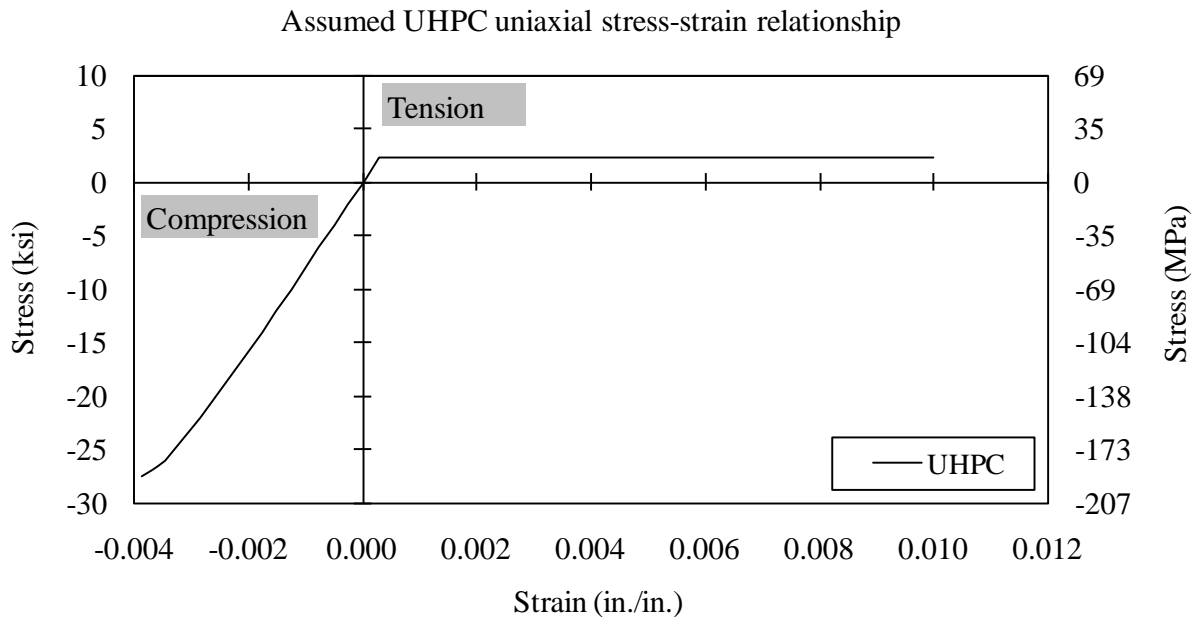


Figure 35. Graph. Assumed UHPC uniaxial stress-strain relationship.

Table 2. Material parameters for the CSC & CDP models of the UHPC used in the I-girder test.

Density, lb/ft ³ (kg/m ³)	160 (2565)	
Concrete elasticity		
E, ksi (GPa)	8000 (55)	
ν	0.18	
Concrete compression hardening		
Compressive stress, ksi (MPa)	Plastic strain (-)	
14.0 (96.5)	0.0000000	
16.0 (110.3)	0.0000284	
20.0 (137.9)	0.0000720	
24.0 (165.5)	0.0001410	
27.5 (189.6)	0.0004140	
Concrete tension stiffening		
Maximum tensile stress, ksi (MPa)	Plastic strain (+)	
2.3 (15.9)	0.00000	
2.3 (15.9)	0.00836	
0.0 (0.0)	0.00900	
The parameters of CDP model		
Dilation angle	15°	
Eccentricity	0.1	
fb0/fc0	1.16	
K	2/3	
Viscosity parameter	0	
The parameters of CSC model		
Failure ratio	Ratio 1	1.16
	Ratio 2	0.0836
	Ratio 3	1.28
	Ratio 4	1/3
Shear retention	Rho_close	1
	Eps_max	0.1

ABAQUS RESULTS

The following results are based on the CDP model using the material parameters in Table 2. Its mesh is illustrated in Figure 34(a). Figure 36 demonstrates that the FEM model accurately replicates the experimental response for the midspan vertical displacement of the I-girder in both elastic and plastic regions. Figure 37 demonstrates the comparison between the FEM and experimental observed longitudinal strain on the top and bottom surfaces of the I-girder at midspan. The longitudinal strains are corresponding to maximum tensile strain on the bottom

surface and maximum compressive strain on the top surface of the girder. Tensile strain is well predicted by the FEM model in both elastic and plastic regions although the experimental data has some fluctuation during loading and unloading processes. The experimental result demonstrated that the UHPC exhibits a tensile strain capacity in the vicinity of 8,000 to 10,000 microstrain. The ultimate tensile plastic strain in the FEM models is deliberately set to a value slightly larger than 0.0083 in order to facilitate the model's convergence. The ultimate tensile strain of the strands generated by prestressing, gravity load, and jack load is approximately 0.013 under the peak load of 178 kips (792 kN). The agreement is reasonably good in the compression strain on the top surface of the girder. The experiment tends to be slightly more compliant than the model after the applied load surpasses 150 kips (667 kN). However, there could be many factors that contribute to this difference, not the least of which is that local strains measured at discrete locations can be biased by local disturbed regions in the structure.

Figure 38 illustrates the strain profile along girder depth at midspan with increased loading. Because cracking on the bottom surface of the I-girder disabled some gages measuring tensile strains along the loading process, those experimental data were extrapolated from other gages located higher on the cross section based on the assumption of the girder midspan cross section remaining plane during bending. It can be observed that the strain profile between FEM and experiment agrees well with each other until the applied load surpasses 108 kips (480 kN). With even higher loading, FEM predicts nonlinear strain distributions which are similar, but not identical, to the extrapolated experimental results. This behavior is more apparent at higher loads and in the tensile zone. However, the discrepancy may be caused by the factors, such as the unavoidable variation of experimental data during the loading (see Figure 37), extrapolation on the strain, and the dramatic strain increment near the failure load. In the compression area, it is noted that the FEM strain is initially slightly smaller than the experiment result on the top surface of the girder but becomes slightly larger along the depth. This behavior also helps to explain the difference in the compressive strain illustrated in Figure 37.

Figure 39 shows the contour plots of longitudinal strain and stress in UHPC at midspan. Both of them stay uniform cross the section in the horizontal direction. The strain smoothly changes from compressive zone to tensile zone. This figure demonstrates that more than 60% of the cross section of the I-girder reaches the assumed maximum uniaxial tensile stress of 2.3 ksi (15.9 MPa).

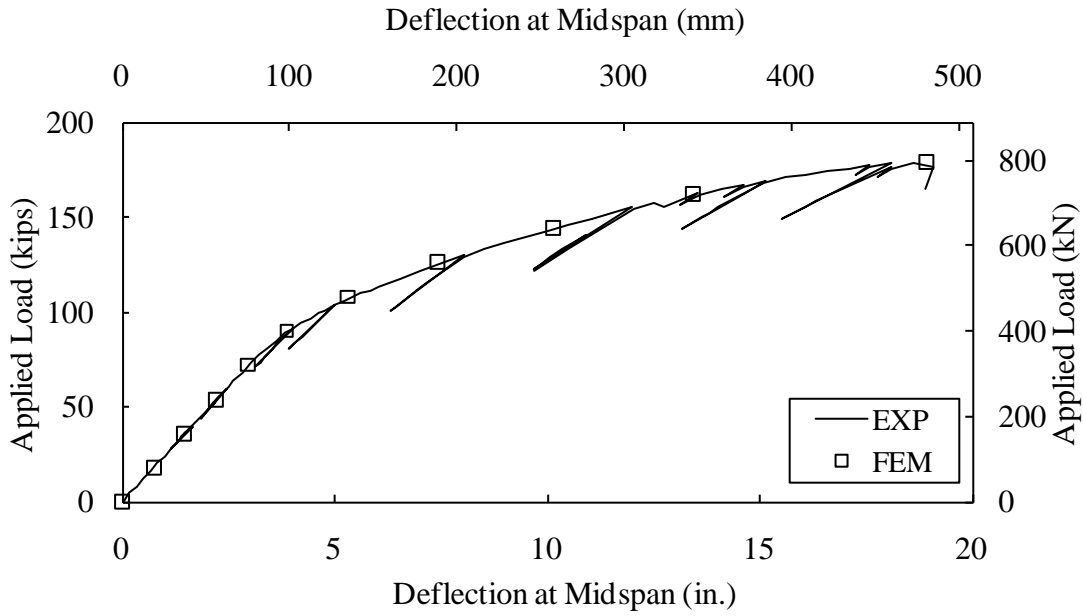


Figure 36. Graph. FEM vs. experimentally observed vertical deflection at midspan.

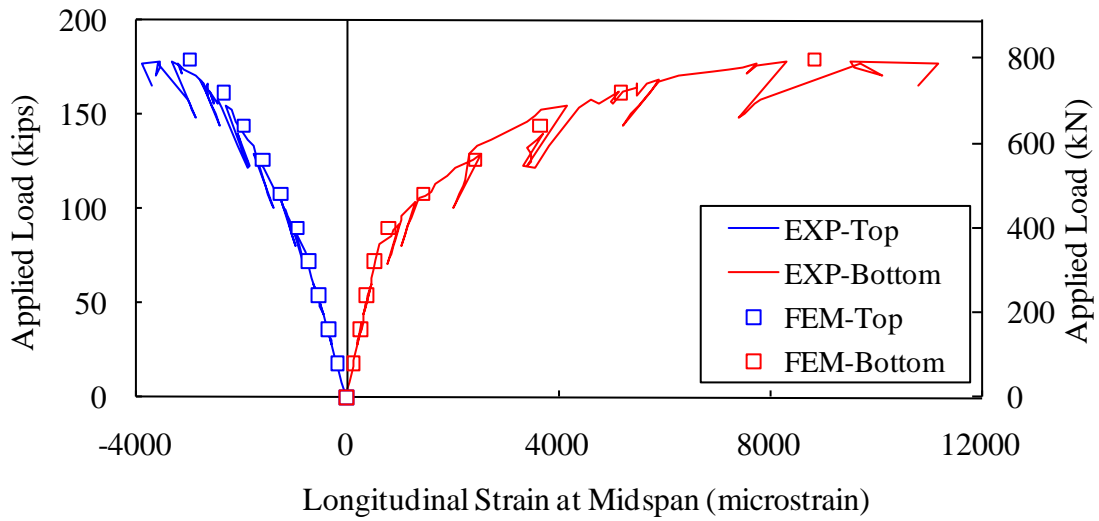


Figure 37. Graph. FEM vs. experimentally observed longitudinal strain on the top and bottom surfaces of the girder at midspan.

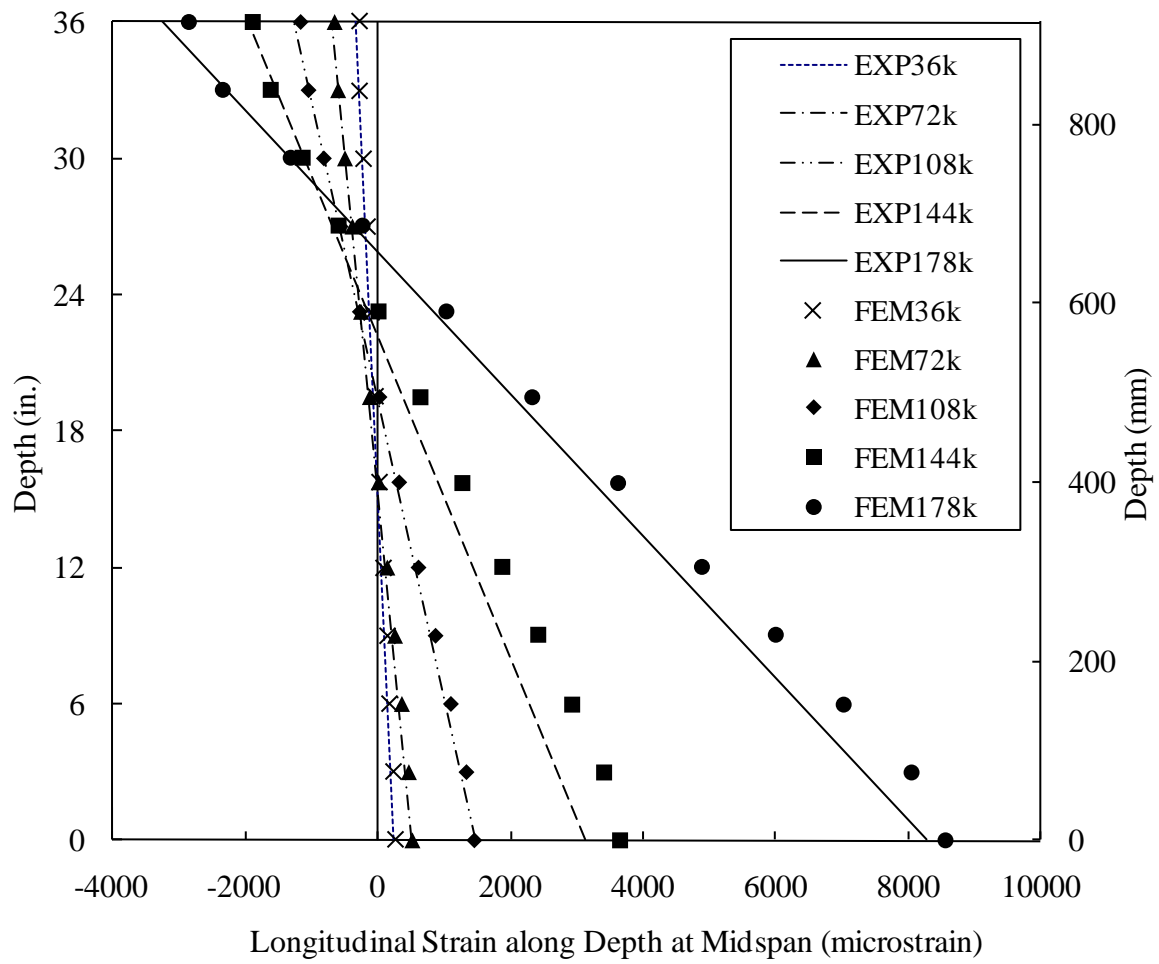


Figure 38. Graph. FEM vs. experimentally observed longitudinal strain along girder depth at midspan.

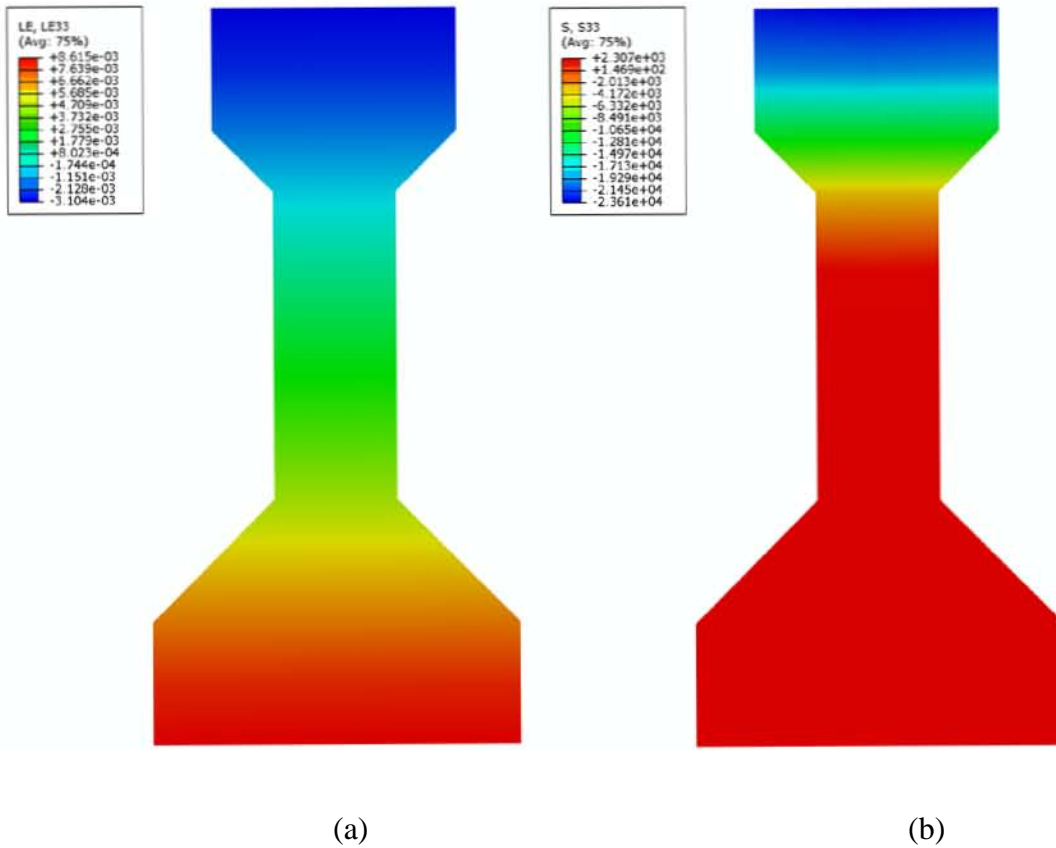


Figure 39. Graph. FEM predicted (a) longitudinal strain and (b) longitudinal normal stress at midspan under an applied load of 179 kips (796 kN).

PARAMETRIC STUDIES

The above model was calibrated through a series of parametric studies. The model sensitivity has been analyzed below. The above model with a 4-inch (102-mm) seeded mesh and the CDP material parameters specified in Table 2 serves as a benchmark in the following comparisons.

Mesh sensitivity

Both 4-inch (102-mm) and 2-inch (51-mm) global seeds were used to mesh UHPC and strands. Figure 40 and Figure 41 demonstrate that both meshes predict almost the same result, even in the plastic region. At the same time, the 4-inch (102-mm) seeded model only required 11% the execution time of the 2-inch (51-mm) seeded model using the same computer.

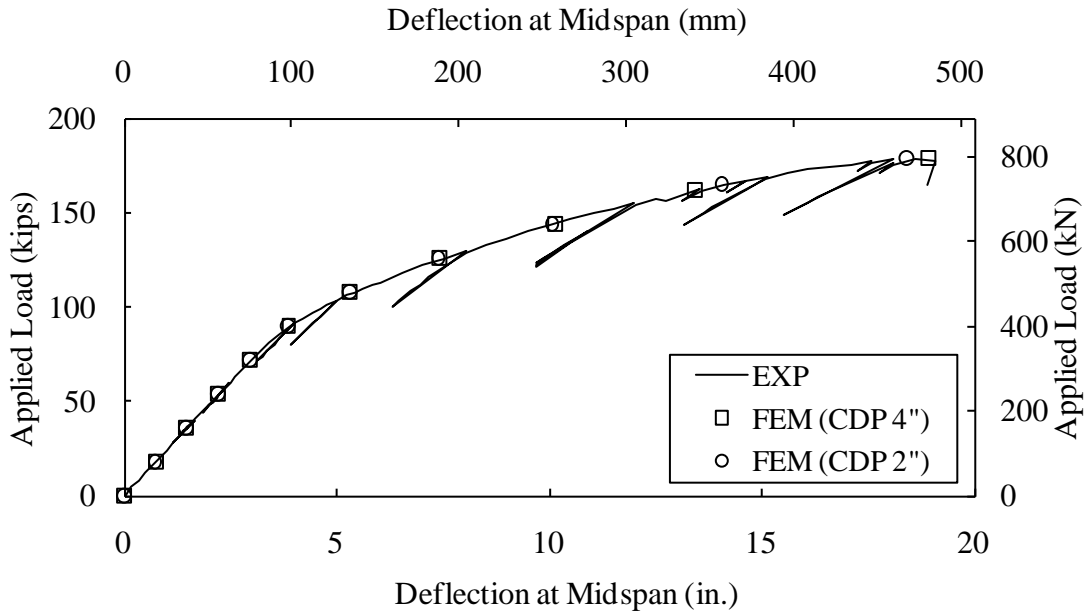


Figure 40. Graph. Effect of mesh density on the vertical deflection of the girder at midspan.

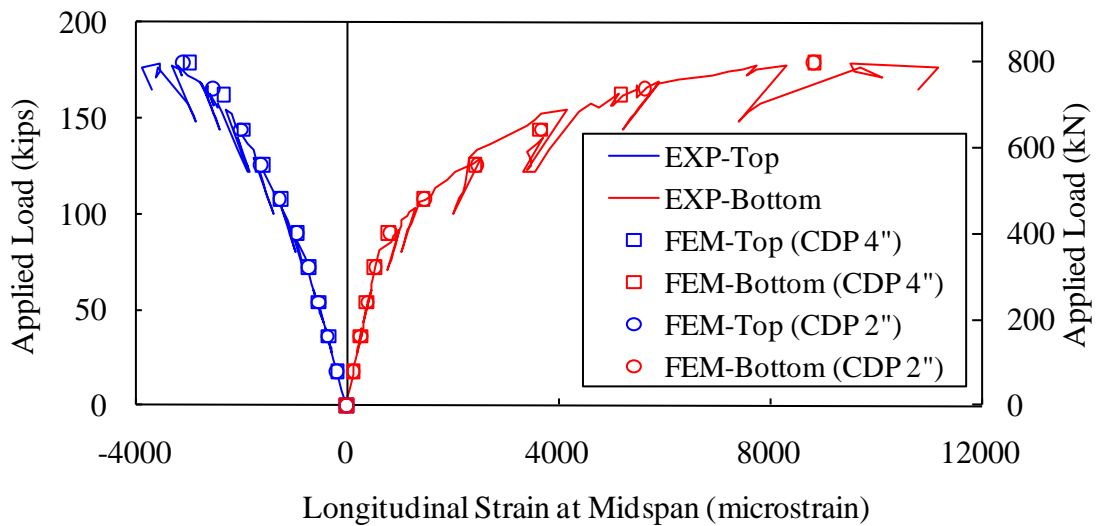


Figure 41. Graph. Effect of mesh density on the longitudinal strains on the top and bottom surfaces of the girder at midspan.

CDP vs. CSC

Figure 42 and Figure 43 demonstrate that both CDP and CSC models capture the experimental result very well in elastic stage simply because their different concrete plasticity models are not activated yet. However, in contrast to the CDP model, the CSC model increasingly deviates from the experiment with increasing load after 90 kips (400 kN) and tends to exhibit greater stiffness than was observed experimentally.

Even when the failure ratio 2 is changed from 0.0836, which defined the maximum uniaxial tensile stress at 2.3 ksi (15.9 MPa), to 0.0655 indicating a maximum tensile stress of 1.8 ksi (12.4 MPa), the CSC model still exhibits stiffer behavior in plastic stage and a significant deviation from the experiment persists as shown in Figure 44 and Figure 45. A maximum uniaxial tensile stress of 1.8 ksi (12.4 MPa) appears to underestimate the tensile response due to the early initiation of nonlinear flexural response.

In a CSC model, there is another way to define tension stiffening: fracture energy cracking criterion, as described in Chapter 2. Tension stiffening is characterized by a stress-displacement response rather than a stress-strain response. The ultimate displacement is set to 0.08 inch (2 mm) for UHPC as compared to 0.003 inch (0.076 mm) for a regular high strength concrete provided by ABAQUS manual. A larger ultimate displacement, say 0.1 inch (2.54 mm), makes the I-girder model stiffer while a lower value than 0.08 inch (2 mm) stops it before the ultimate load is reached. (For example, a case of 0.06 inch (1.5 mm) stops at 131 kips (583 kN)). Figure 46 and Figure 47 show that the CSC model with the fracture energy cracking criterion of ultimate displacement equal to 0.08 inch (2 mm) works better than stress-strain criterion, but still not as well as the CDP models.

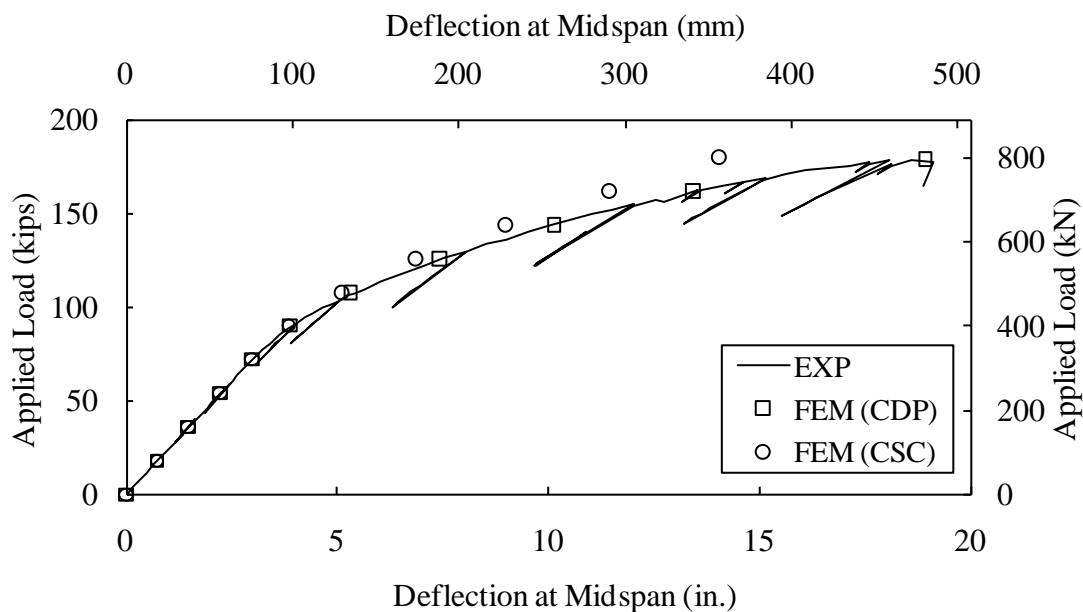


Figure 42. Graph. CDP vs. CSC in the vertical deflection of the girder at midspan.

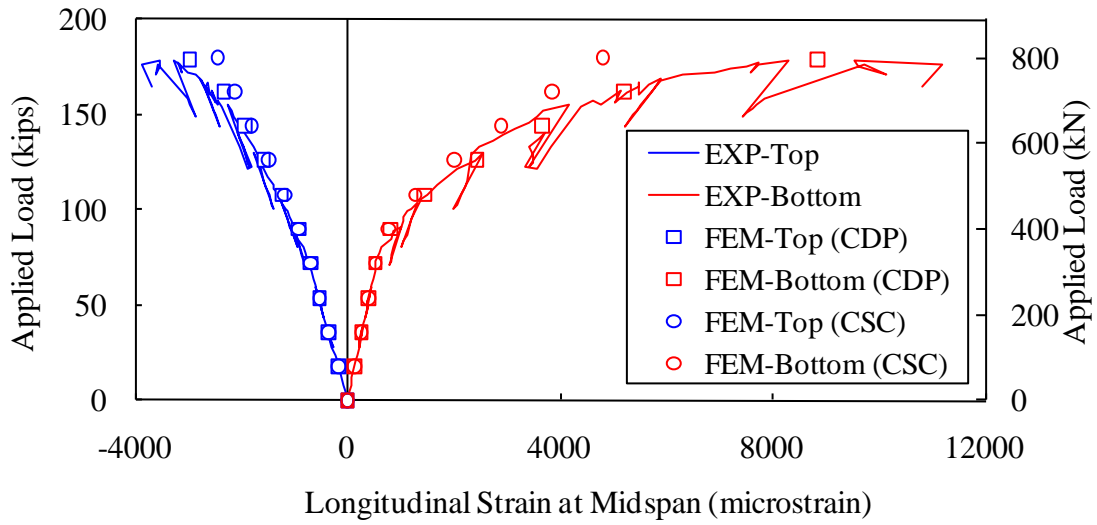


Figure 43. Graph. CDP vs. CSC in the longitudinal strains on the top and bottom surfaces of the I-girder at midspan.

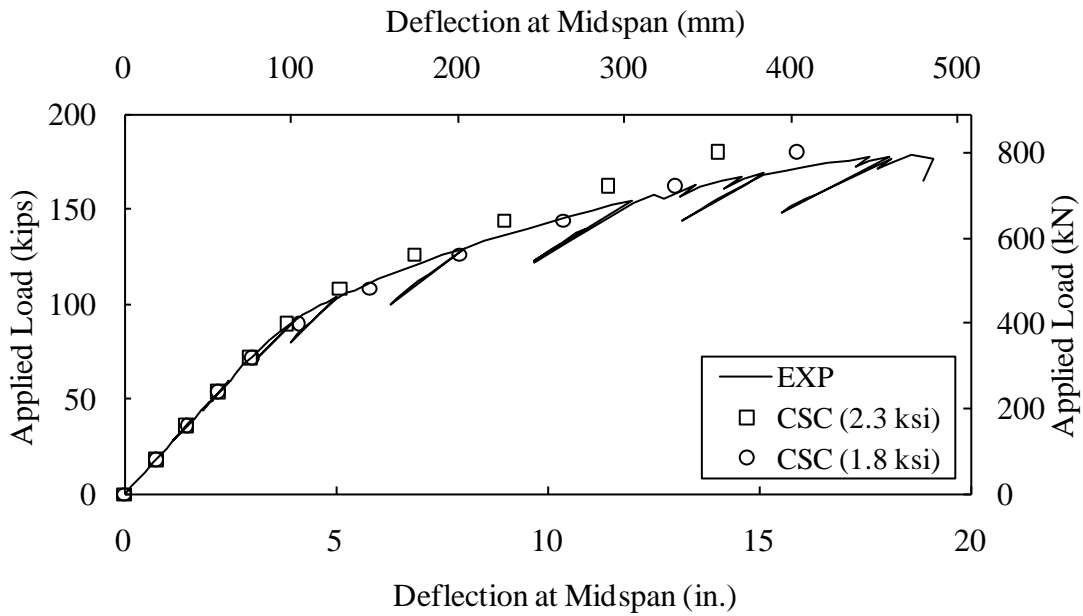


Figure 44. Graph. Effect of maximum tensile stress of the CSC model on the vertical deflection of the girder at midspan.

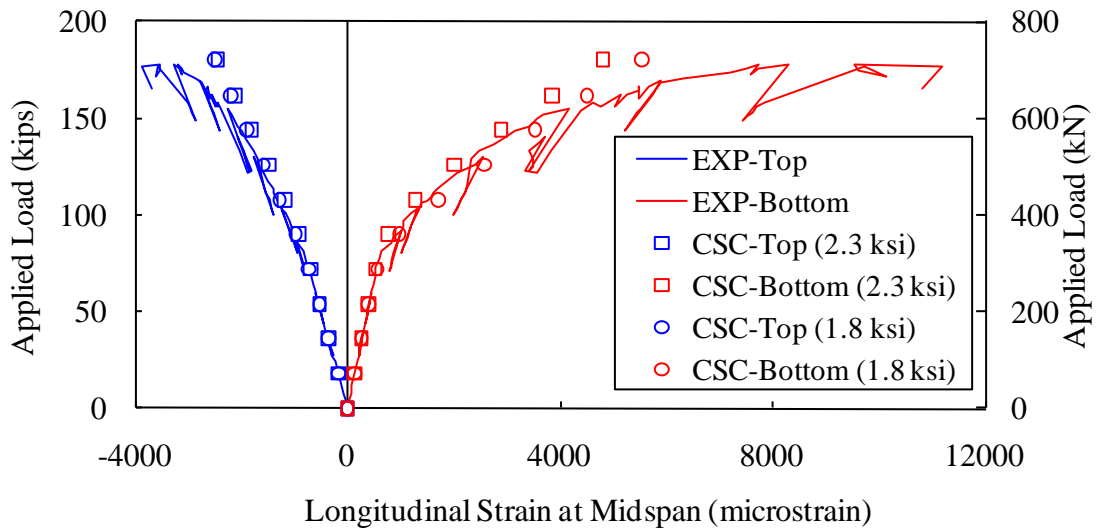


Figure 45. Graph. Effect of maximum tensile stress of the CSC model on the longitudinal strains on the top and bottom surfaces of the girder at midspan.

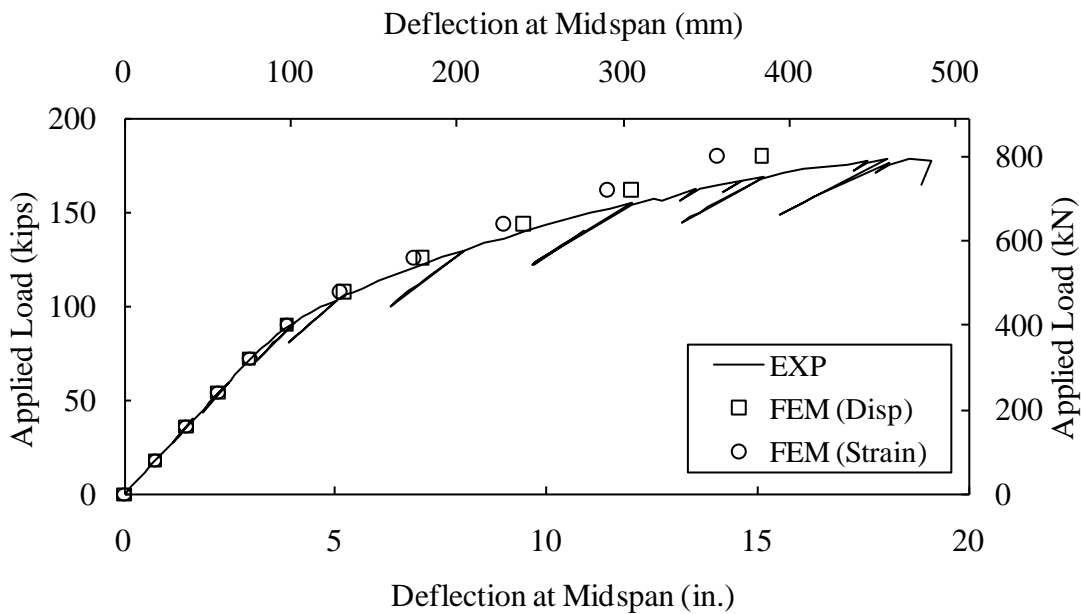


Figure 46. Graph. Effect of CSC tension stiffening based on fracture energy cracking criterion on the vertical deflection of the girder at midspan.

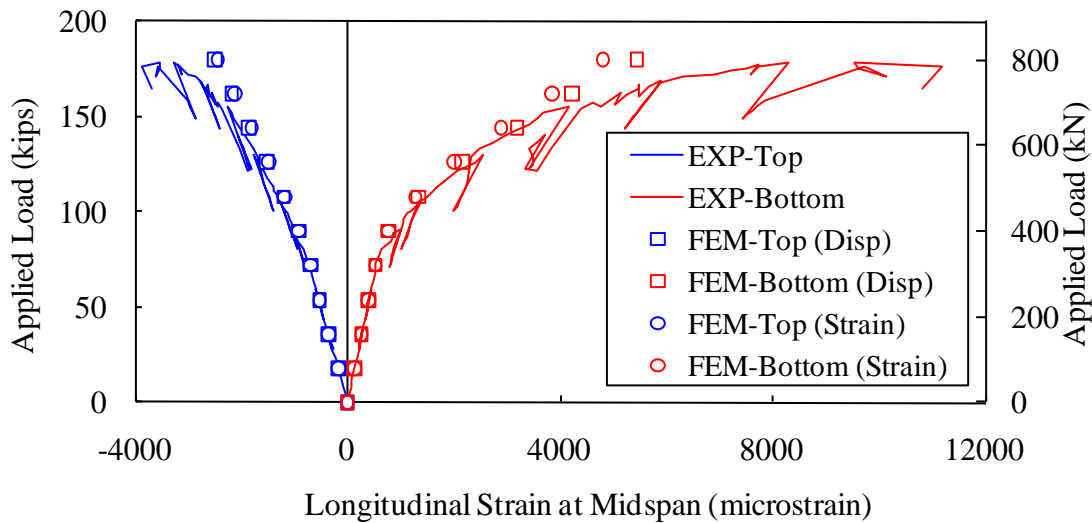


Figure 47. Graph. Effect of CSC tension stiffening based on fracture energy cracking criterion on the longitudinal strains on the top and bottom surfaces of the girder at midspan.

Concrete tension stiffening of CDP

Concrete tension stiffening can be defined by post-failure stress-strain relationship, which in this UHPC material includes two parameters: maximum tensile stress and ultimate tensile plastic strain. Their effects are examined below, respectively.

Figure 48 and Figure 49 illustrate the midspan vertical displacement and longitudinal strain on top and bottom surfaces of the girder with the maximum tensile stress equal to 2.6 ksi (18 MPa) and 2.0 ksi (13.8 MPa), respectively. Magnitude of maximum tensile stress has a significant effect on the structural behavior. It is evident that the experimental result falls between them in both figures. Recall that a value of 2.3 ksi (15.9 MPa), an average of the two assumed maximum tensile stresses, was previously demonstrated to correlate better with the experimental result.

Figure 50 and Figure 51 illustrate the midspan vertical displacement and longitudinal strain on the top and bottom surfaces of the girder with the ultimate tensile plastic strains equal to 0.008 and 0.01, respectively. Neither figures shows much noticeable difference between two cases, aside from the fact that the 0.008-case experienced convergence difficulty and stopped at 178 kips (792 kN) while the 0.01-case easily finished at 180 kips (801 kN). From a convergence standpoint, selecting an ultimate tensile plastic strain slightly larger than that experimentally observed is recommended.

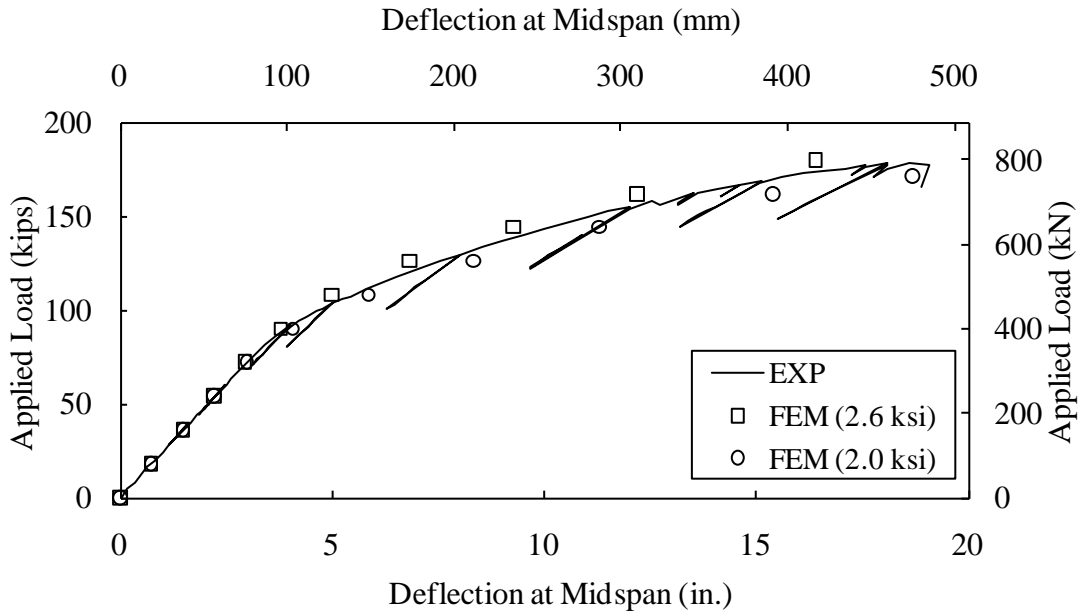


Figure 48. Graph. Effect of maximum tensile stress on the vertical deflection of the girder at midspan.

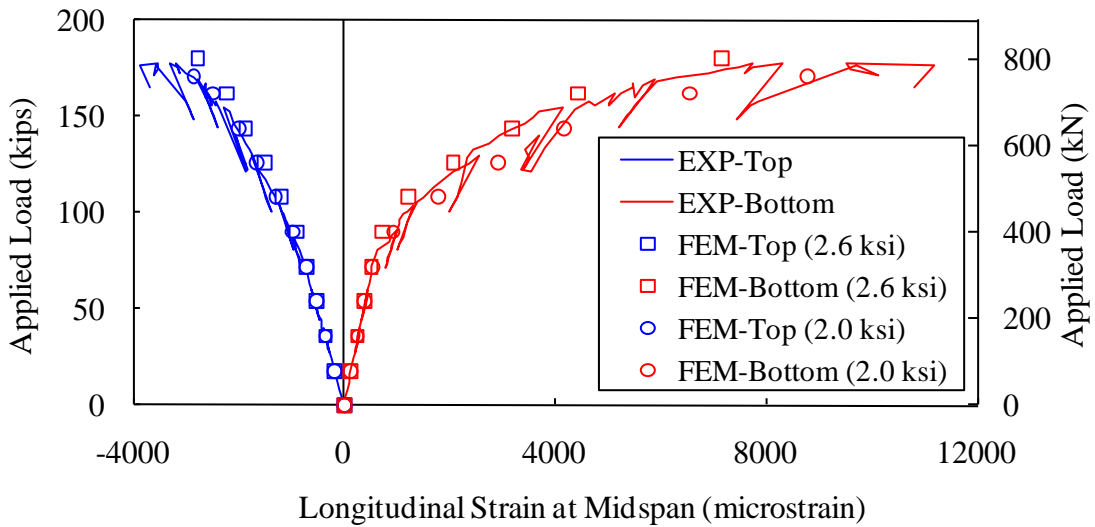


Figure 49. Graph. Effect of maximum tensile stress on the longitudinal strains on the top and bottom surfaces of the girder at midspan.

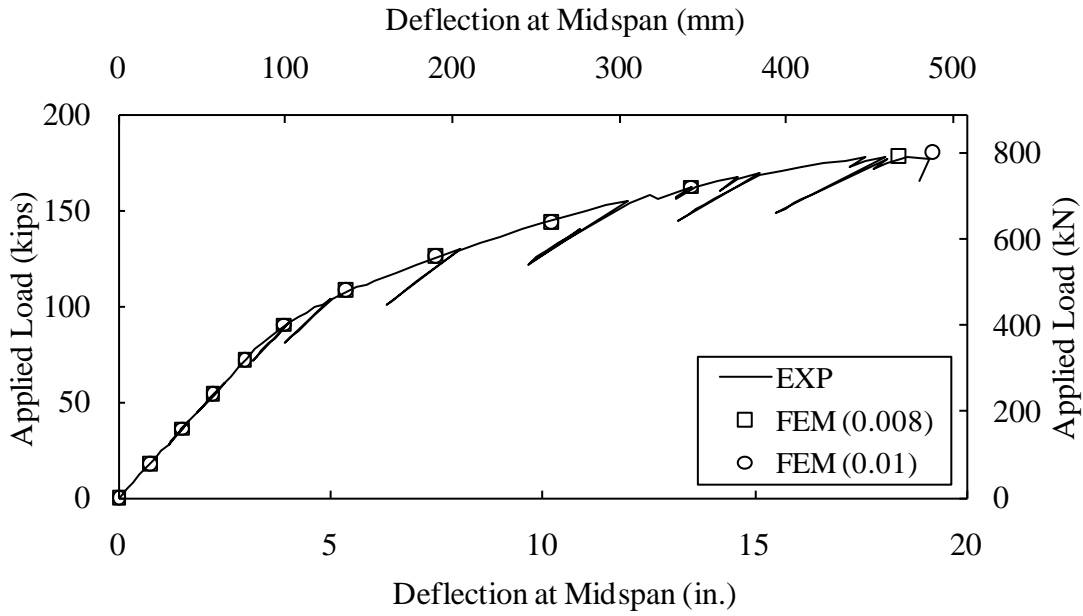


Figure 50. Graph. Effect of ultimate tensile plastic strain on the vertical deflection of the girder at midspan.

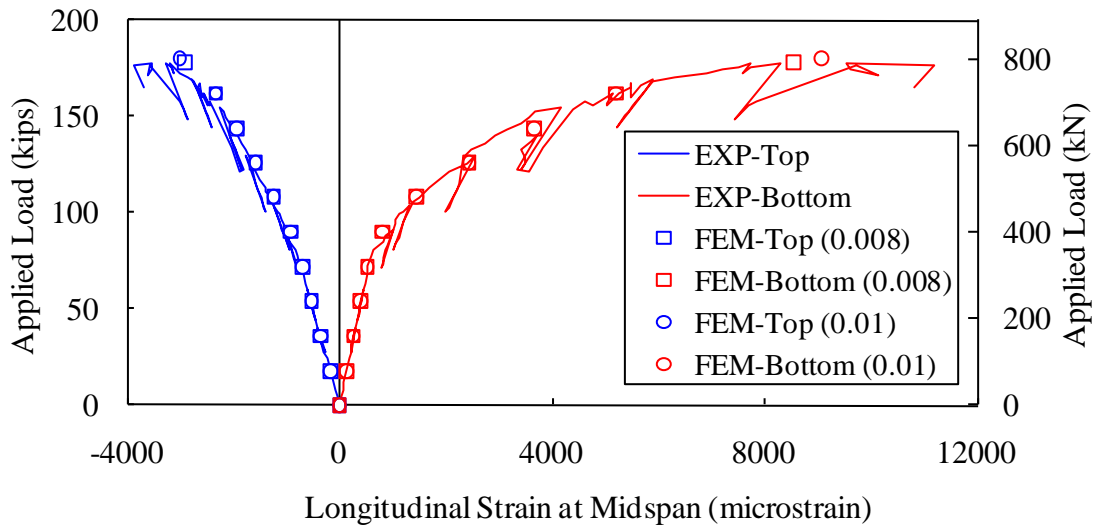


Figure 51. Graph. Effect of ultimate tensile plastic strain on the longitudinal strains on the top and bottom surfaces of the girder at midspan.

ABAQUS also provides two additional ways to define concrete tension stiffening: post-failure stress-displacement relationship and post-failure stress-fracture energy relationship. Both of them belong to fracture energy cracking criterion. Four sets of concrete tension stiffening parameters for the UHPC CDP models are shown in Table 3. The post-failure stress-displacement relationship takes two simple forms: constant and linear loss of strength after cracking.

Table 3. Concrete tension stiffening in the CDP models of the UHPC in the I-girder.

Post-failure stress-strain relationship	
Maximum tensile stress ksi (MPa)	Plastic strain (+)
2.3 (15.9)	0.00000
2.3 (15.9)	0.00836
0.0 (0.0)	0.00900
Post-failure stress-displacement relationship (constant)	
Maximum tensile stress ksi (MPa)	Cracking displacement inch (mm)
2.3 (15.9)	0.00 (0.00)
2.3 (15.9)	0.10 (2.54)
0.0 (0.0)	0.11 (2.79)
Post-failure stress-displacement relationship (linear loss)	
Maximum tensile stress ksi (MPa)	Cracking displacement inch (mm)
2.3 (15.9)	0.00 (0.00)
0.0 (0.0)	0.26 (6.60)
Post-failure stress-fracture energy relationship	
Maximum tensile stress ksi (MPa)	Fracture energy lb/inch (N/m)
2.3 (15.9)	500 (87560)

The post-failure stress-displacement relationship is defined similarly to the post-failure stress-strain relationship. When the maximum cracking stress reaches 2.3 ksi (15.9 MPa), tensile stress provided by steel fibers bridging crack is kept constant until maximum cracking displacement is reached. Figure 52 and Figure 53 illustrate midspan vertical displacement and longitudinal strain on the top and bottom surfaces of the girder with the maximum cracking displacement set to 0.1 inch (2.54 mm) and 0.01 inch (0.254 mm), respectively. The case with maximum cracking displacement equal to 0.1 inch (2.54 mm) fits the experimental results as well as the given parameters defined in post-failure stress-strain relationship. It easily converges to the ultimate applied load. The case with maximum cracking displacement equal to 0.01 inch (0.254 mm) fails to converge at applied loads greater than 136 kips (605 kN), indicating that this value is too small.

The post-failure stress-fracture energy relationship is assumed to have a linear loss of strength after cracking. Therefore only two parameters are needed. Figure 54 and Figure 55 show effect of fracture energy on the midspan vertical displacement and longitudinal strain on the top and bottom surfaces of the girder. Fracture energy with 300 lb/inch (52540 N/m) makes the model slightly more compliant and converges more slowly than a value of 500 lb/inch (87560 N/m),

which seems closer to the experimental data. The stress-fracture energy relationship can be converted into the post-failure stress-displacement relationship. The corresponding ultimate cracking displacement is equal to $2 \times G_f / \sigma_t = 2 \times 300 \text{ lb/inch} / 2.3 \text{ ksi} = 0.26 \text{ inch}$ (6.60 mm) per the formulas in Figure 8. The defined post-failure stress-displacement relationship with linear loss produced an identical result as the post-failure stress-fracture energy relationship. According to ABAQUS, a typical high-strength concrete (with a compressive strength of approximately 5.7 ksi (39 MPa)) has a typical value of fracture energy around 0.67 lb/inch (117 N/m), which is far less than 500 lb/inch (87560 N/m) used for the UHPC here.

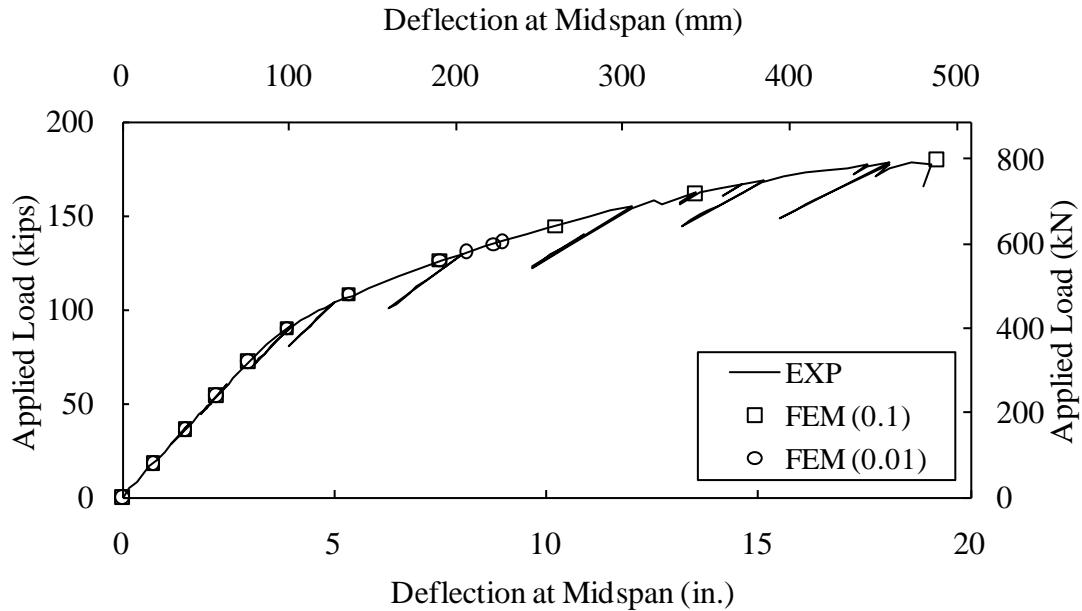


Figure 52. Graph. Effect of cracking displacement on the vertical deflection of the girder at midspan.

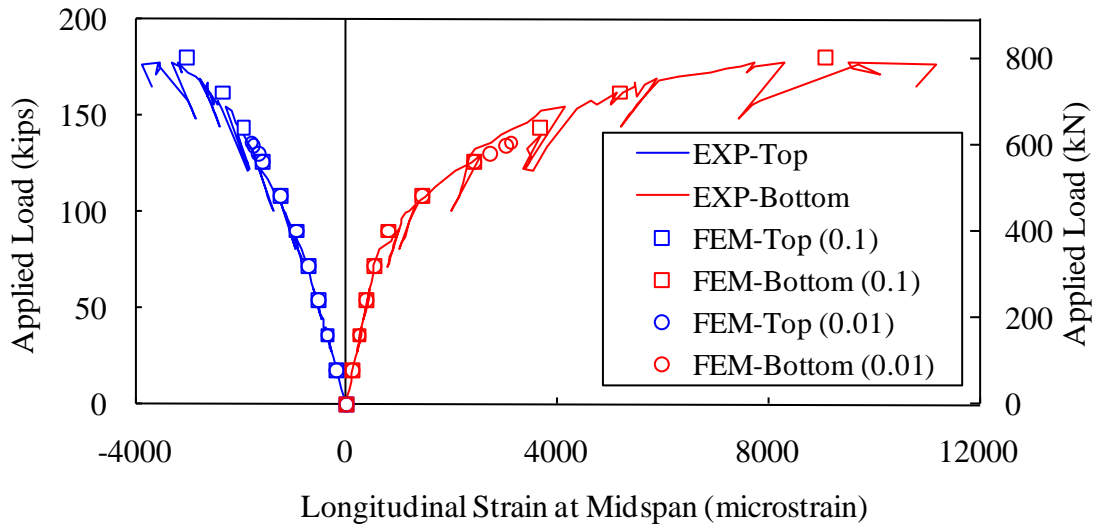


Figure 53. Graph. Effect of cracking displacement on the longitudinal strains on the top and bottom surfaces of the girder at midspan.

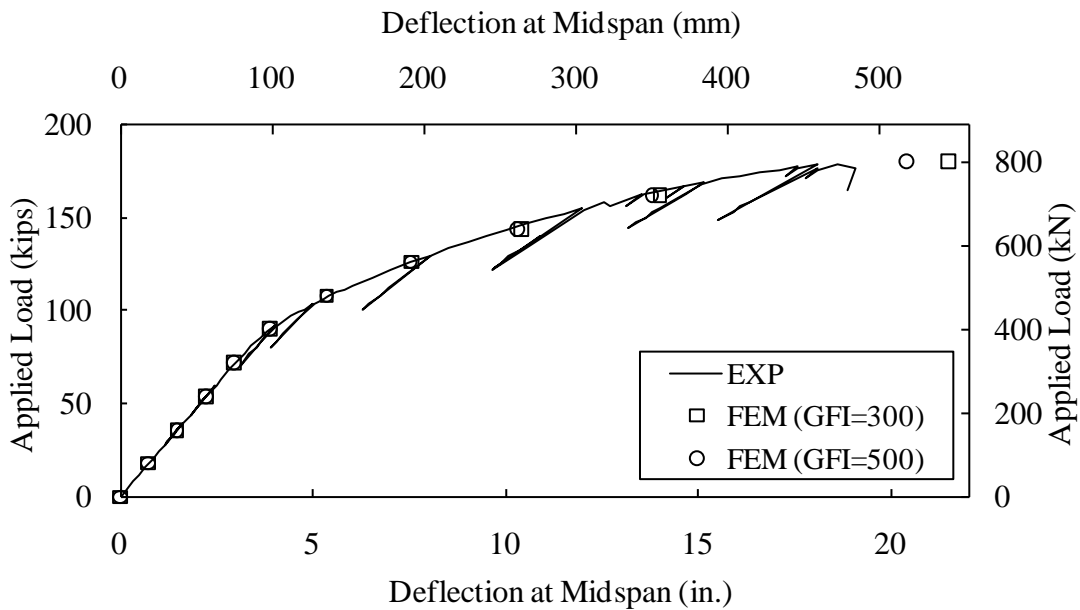


Figure 54. Graph. Effect of fracture energy on the vertical deflection of the girder at midspan.

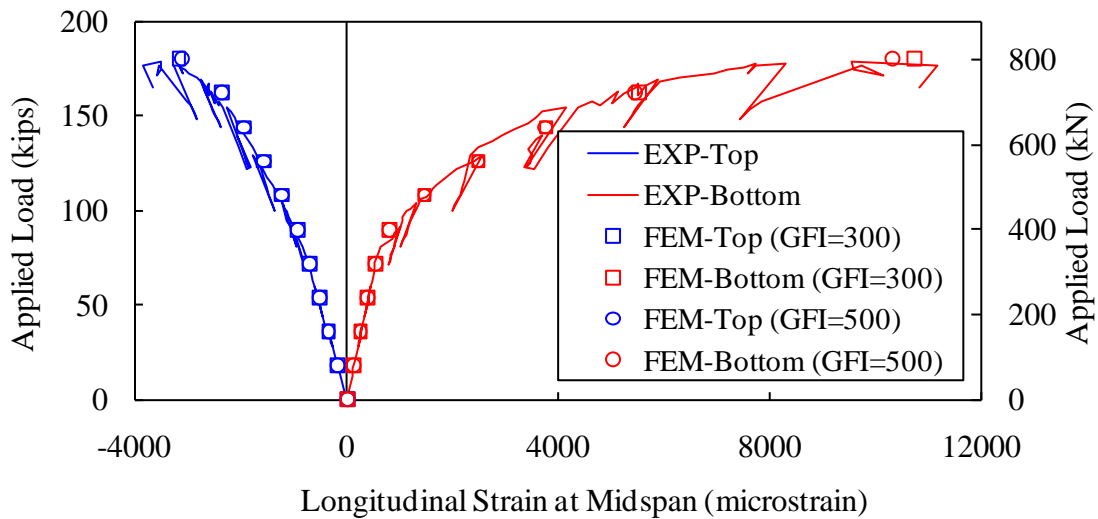


Figure 55. Graph. Effect of fracture energy on the longitudinal strains on the top and bottom surfaces of the girder at midspan.

Tension Damage of CDP

The CDP model is capable of modeling damage and stiffness recovery during cyclic load reversals. Test 80F had six unloads which can be used to estimate the residual stiffness in the UHPC component, and thus the tension damage parameters in the CDP model. This experimental test demonstrated that, at tensile cracking, UHPC experiences a loss of local stiffness caused by the local loss of cement matrix load carrying capacity. However, the subsequent engagement and elastic straining of the fiber reinforcement results in a member response that exhibits an enhanced ability to recover applied deformations during an unloading process.

As observed from the experiment, the failure of the girder was initiated on the tensile side of the flexural member. The UHPC has a nearly linear response up to the compressive strength of 28 ksi (193 MPa), so the compression damage should be minimal given that the modeled girder 80F at failure has a maximum compressive stress of 24 ksi (166 MPa). Therefore, here only tension damage is assumed within the model. Figure 56 shows two assumed types of tension damage and Figure 57 shows their effect on the vertical deflection of the girder at midspan with an unloading from 129.5 kips (576 kN) and reloading to the ultimate load. The linear tension damage assumes that the tension damage variable is a linear function of the plastic strain with no damage at zero plastic strain and 90% damage at the ultimate plastic strain of 0.01. The nonlinear tension damage assigned more damage to the initial plastic straining.

The results in Figure 57 show that the experimental residual deflection of the girder was less than that predicted by the tension damage models, indicating that the chosen damage parameters within these models do not accurately predict the behavior of the UHPC components during the unloading process. In addition, incorporation of tension damage to a model may impact convergence. The CDP model with tension damage is not yet able to replicate the experimental results in an unloading process and thus requires further parametric and experimental study.

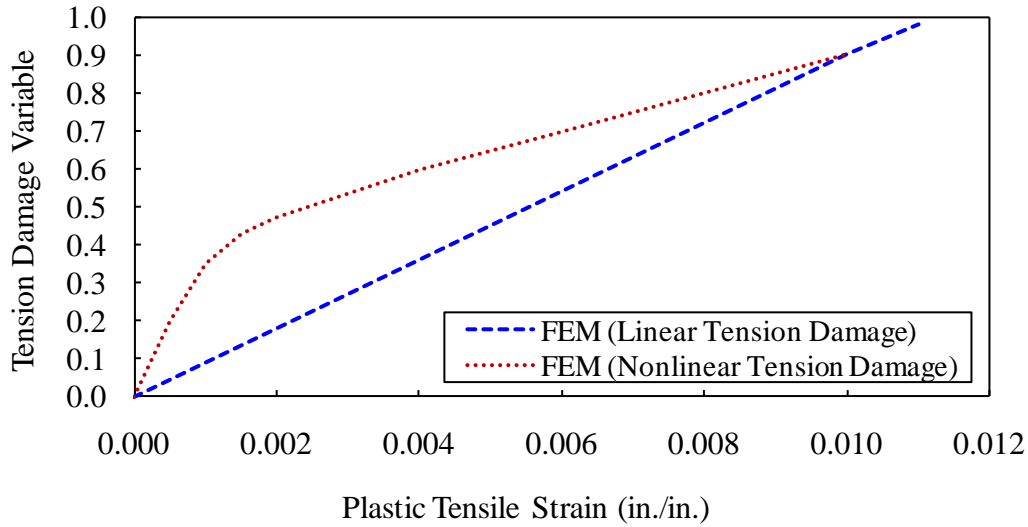


Figure 56. Graph. Assumed tension damage.

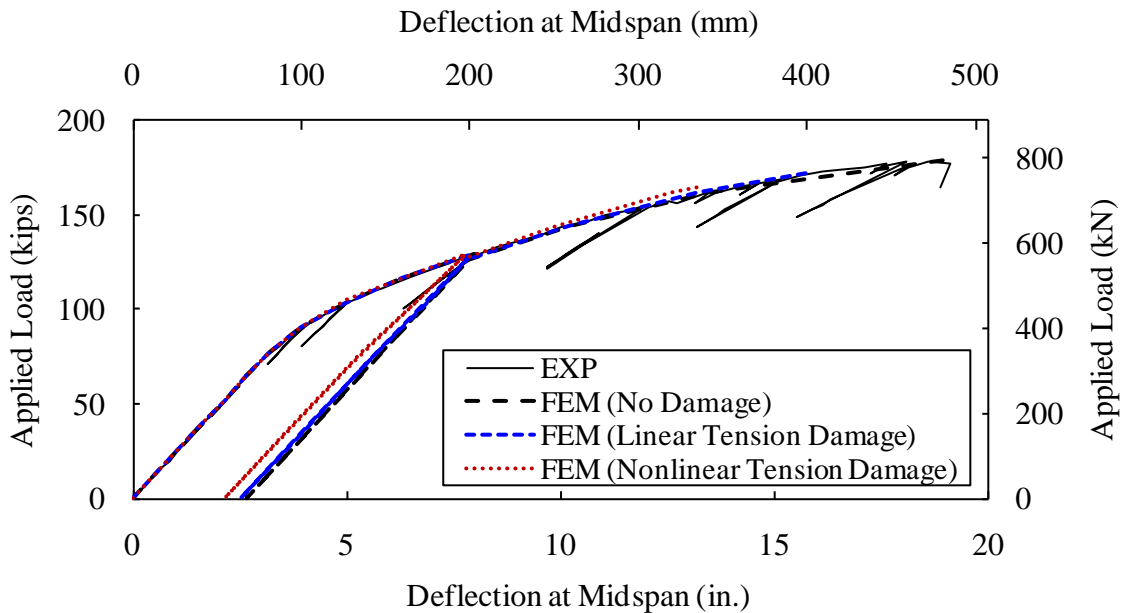


Figure 57. Graph. Effect of tension damage on the vertical deflection of the girder at midspan with an unloading from an applied load of 129.5 kips (576 kN) and reloading to the ultimate load.

CONCLUSIONS

Based on the results of the above parametric studies compared to the experimentally observed flexural response of a UHPC I-girder, the following conclusions are presented.

1. The concrete damaged plasticity model replicates the observed strain and deflection responses of the UHPC I-girder better than the concrete smeared cracking model.
2. The mesh sensitivity of this model is quite low. A coarse 4-inch (102-mm) seeded mesh can capture the I-girder behavior reasonably well. There is minimal difference between the results of 4-inch (102-mm) and 2-inch (51-mm) seeded meshes.
3. Maximum tensile stress of UHPC plays a significant role in the predicted finite element model response. A value of 2.3 ksi (15.9 MPa) produces reasonable results. The selection of the UHPC ultimate tensile strain between 0.008 and 0.010 does not significantly affect the result.
4. All three types of tension stiffening definitions with proper parameters for CDP models can predict almost the same result. However, their sensitivity and convergence may be different.
5. The tension damage model was not capable of accurately modeling the unloading response observed in the experimental girder test at the current modeling stage. The damage prediction functionality of the CDP model requires further study of stiffness reduction mechanism in UHPC during load reversal and sufficient testing data prior to applying it to unloading or cyclic loading scenarios.

CHAPTER 5. I-GIRDERS 24S AND 14S

FINITE ELEMENT MODELS

Two finite element models were developed to replicate the responses of the I-girders 24S and 14S specimens tested in the full-scale experimental investigation with the focus on the UHPC shear behavior.

Most modeling aspects such as material properties of UHPC and strand, mesh, and element types are very similar to that implemented for the I-girder 80F and have been detailed in Chapter 4. The prestressing strand uniaxial stress-strain relationship is plotted in Figure 31 and the UHPC material properties are listed in Table 2. The magnitude of the strand prestressing in the longitudinal z-direction is still assumed to be 128.3 ksi (885 MPa), which was applied using a stress-type initial condition.

The two finite element models originated from the previous I-girder 80F model and were revised to reflect the shear test plans as illustrated in Figure 12 and Figure 13. The shear tests were under three-point loading and the loading point in each test was closer to the east end support. The girders were partitioned so that the loading and support areas, the instrumentation lines and the gage locations were easily defined at various locations on the surfaces of the girders. Figure 58 and Figure 59 show the 3D finite element models for the I-girders 24S and 14S, respectively. There was one additional membrane layer tied to the side face of each girder. The membrane layer provide a means to output maximum and minimum principal strains oriented on the girder side face and compared with the values obtained from the corresponding rosette strain gages installed on the same locations. Figure 60 shows a 2-inch (50.8-mm) seeded mesh shared by both I-girder 24S and 14S models. The mesh is similar to that employed in the I-girder 80F model presented in Figure 34(b).

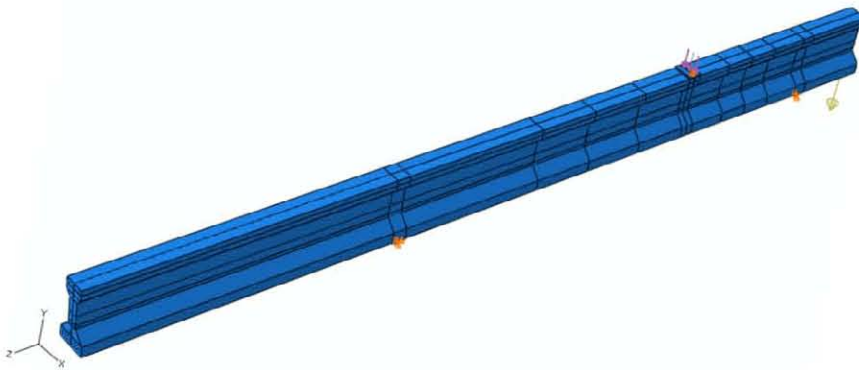


Figure 58. Illustration. I-girder 24S model.

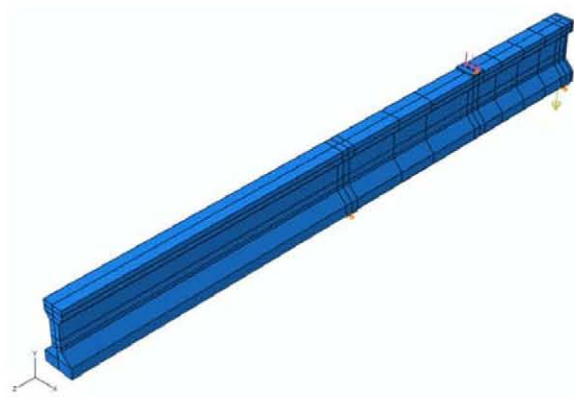


Figure 59. Illustration. I-girder 14S model.

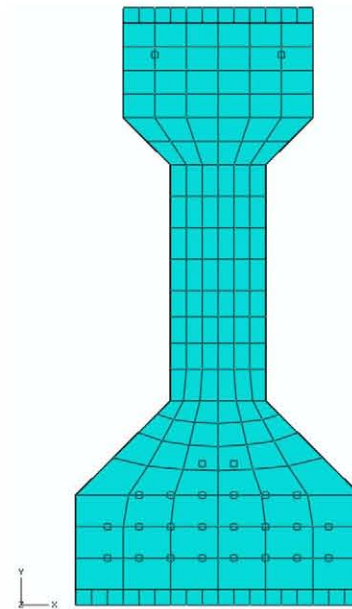


Figure 60. Illustration. I-Girder 24S or 14S with a 2-inch (51-mm) seeded mesh.

ABAQUS RESULTS

The following results are based on the CDP models using the material parameters in Table 2 and are presented in the following two groups for the I-girder 24S and the I-girder 14S respectively.

I-girder 24S

Figure 61 and Figure 62 presented the predicted and observed vertical deflection of the girder along the six instrumentation lines. It appears that the finite element predictions are offset from the experimental measurements at all lines in a nearly uniform fashion. It must be noted that both spans in the shear tests are much smaller and the applied loads are significantly larger than those

in Test 80F which focused on flexural behavior. As were observed from the experiments, the maximum deflection in Test 24S is less than 3 percent of the midspan deflection in Test 80F in terms of a normalized ultimate applied load while the maximum deflection in Test 14S is less than 1 percent of the one in Test 80F. The vertical deformation of the supporting system appears no longer negligible as was in the case of Test 80F. If such a deformation exists on both seats, the girders would have rigid body movement in a form of uniform vertical displacement, rotation, or combination of both. A uniform vertical displacement is assumed to be the primary rigid body movement although slight rotation due to different reaction force on the supporting system and/or different rigidity of the supporting system of each end is possible. At the same time, a uniform vertical displacement is relatively easy to identify and compensate compared to any rotation.

The deflection difference between the finite element and experimental results at Instrumentation Line 4 is named as “Delta” and is plotted in Figure 63. The “Delta” appears almost linear with respect to the applied load and is thought to be elastic response of the seats. It is idealized as exactly linear offset as shown in the same figure. The proposed offset is subtracted from all experimental vertical deflection results in order to exclude the assumed vertical uniform rigid body movement of the girder from the deformation associated from shear response. Figure 64 and Figure 65 show the modified experimental results, which agree with the finite element results significantly better, especially along the Instrumentation Lines 3, 4, 5 and 6. There might be some rigid body rotation and therefore increasing discrepancy is observed as it moves away from the benchmark Instrumentation Line 4 to Instrumentation Line 1.

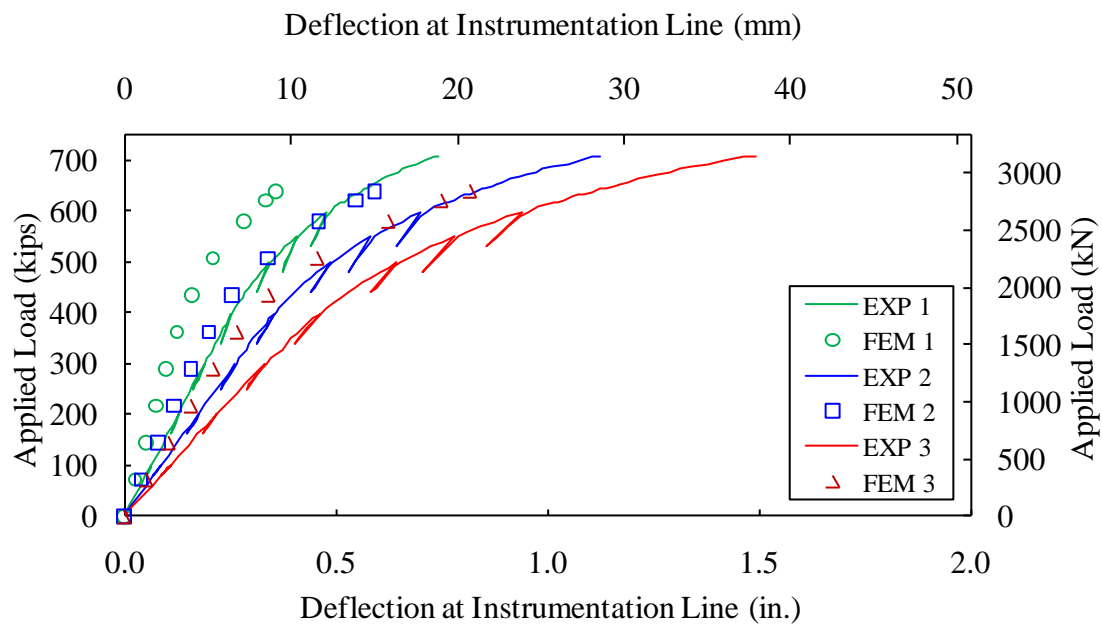


Figure 61. Graph. Predicted versus observed deflection of the girder 24S along Instrumentation Lines 1, 2, and 3.

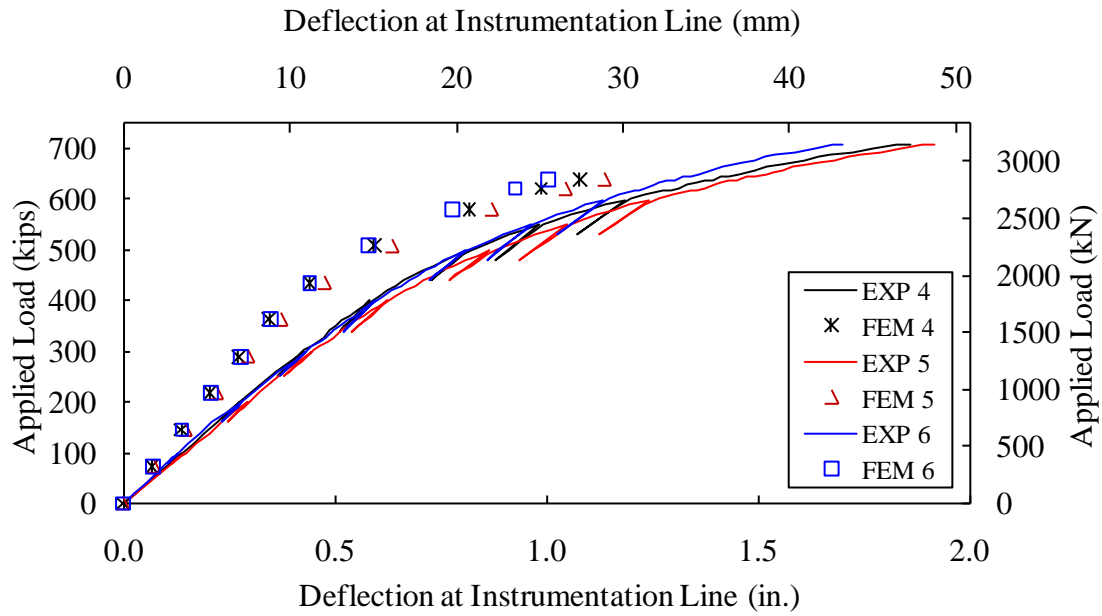


Figure 62. Graph. Predicted versus observed deflection of the girder 24S along Instrumentation Lines 4, 5, and 6.

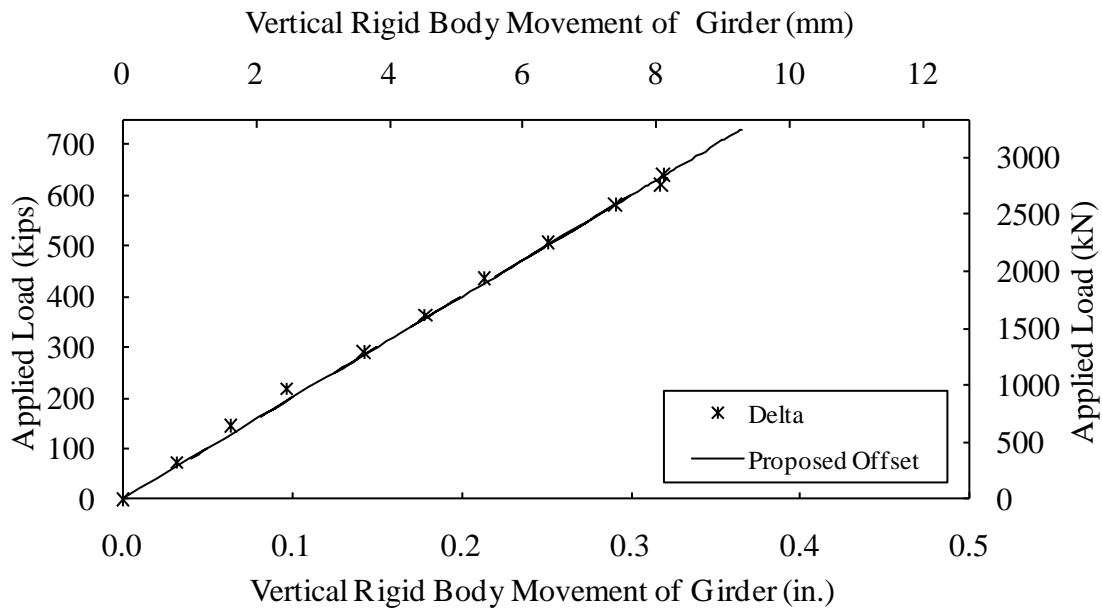


Figure 63. Graph. Assumed vertical rigid body movement of the girder 24S.

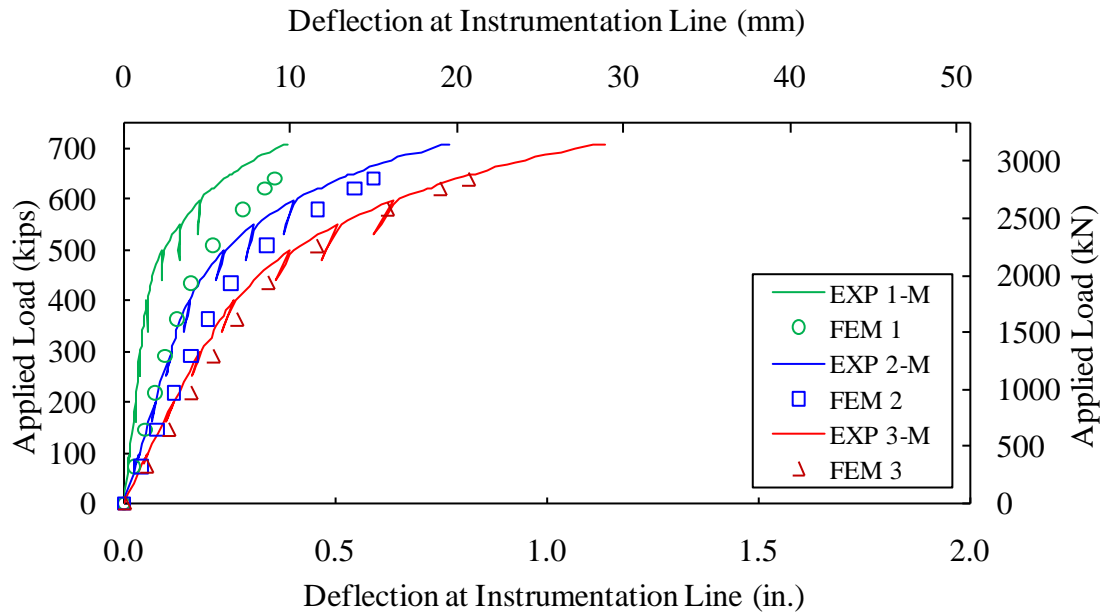


Figure 64. Graph. Predicted versus observed (modified) deflection of the girder 24S along Instrumentation Lines 1, 2, and 3.

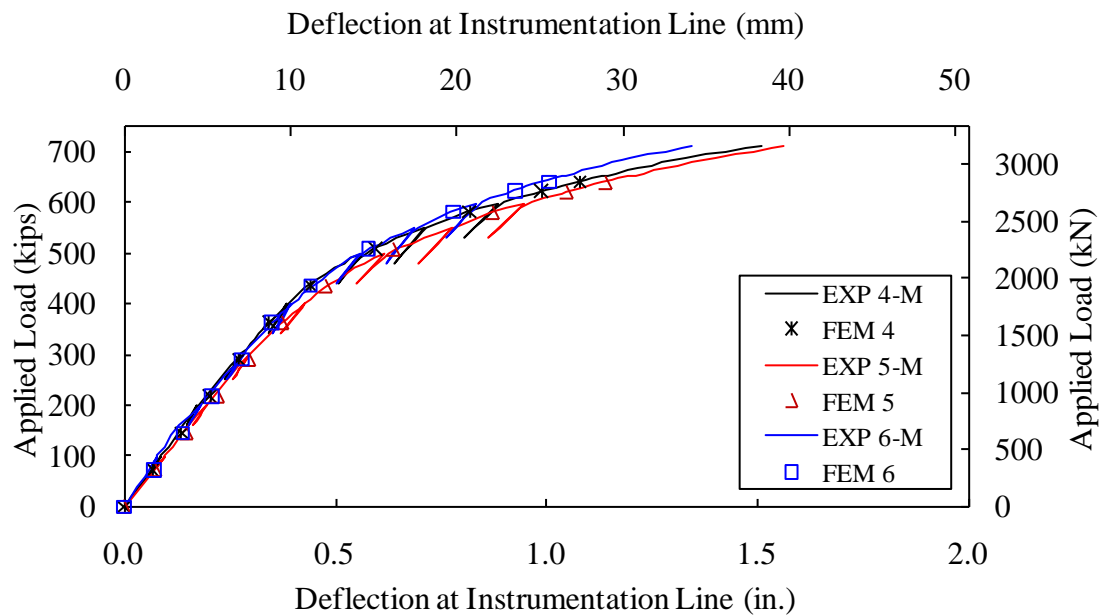


Figure 65. Graph. Predicted versus observed (modified) deflection of the girder 24S along Instrumentation Lines 4, 5, and 6.

Figure 66 through Figure 71 present the comparison on the longitudinal strain on the top and bottom surfaces of the girder along all the instrumentation lines. The tensile strain on the bottom surface of the girder generally expresses reasonable agreement between the model and the experiment at all the instrumentation lines although the difference increases as the loading enters nonlinear stage. Especially at Instrumentation Line 4, the yielding point is closely predicted and the whole process is replicated very well. Figure 70 and Figure 71 illustrate that the nonlinear stage initiates much earlier in the experiment than in the model from the observations at Instrumentation Lines 5 and 6. The compression strain on the top surface of the girder is consistently stiffer in the model with respect to increasing loading except at Instrumentation Line 6. Figure 71 shows that the experimental compressive strain is observed disproportionately larger than the tensile strain at Instrumentation Line 6. It is thought to be a result of partial damage on the girder from the previous flexural test. The experimental measure of compressive strain does not appear to be valid at Instrumentation Line 1, either. No strain gage was installed on the top surface of the girder at Instrumentation Line 4 because of the presence of a loading pad.

Figure 72 through Figure 77 present the longitudinal strain on the side face of the girder with 3 inch (76.2 mm), 17 inch (432 mm), and 22 inch (559 mm) below the girder top surface. The longitudinal strain with 22 inch (559 mm) below the girder top surface is relatively small and does not vary dramatically unless the girder approaches failure. In terms of the longitudinal strain with 3 inch (76.2 mm) and 17 inch (432 mm) below the girder top surface, excellent agreement is observed at Instrumentation Line 1, 2, and 3. At Instrumentation Line 4, the compression zone is just under the loading pad and is expected to have a complicated stress state. Significant difference was observed at Instrumentation Lines 5 and 6. The results increasingly diverge at lower applied loads, and become more consistent after an applied load above approximately 400 kips (1779 kN). The effect of seating on the experimental data is more apparent at Instrumentation Lines 5 and 6. This also provides additional evidence that the west end of the girder may be partially damaged from the previous test.

Figure 78 through Figure 83 present the maximum and minimum principal strains at the rosette strain locations as indicated in Figure 12. The 45° rosette strain gages were installed 17 inch (432 mm) below the girder top surface along the six instrumentation lines and orientated with the 45° diagonal gage component in a horizontal direction and two other gage components in $\pm 45^\circ$ from the horizontal direction. The horizontal strain component has been presented as longitudinal strain on the girder side face, i.e. EXP NX-17, in Figure 72 though Figure 77. Maximum and minimum principal strains are computed from three independent measurements in three directions on a single rosette. It also means that all three strain components have to be accurate in order to get an accurate computed principal strain.

Figure 78 through Figure 80 demonstrate a decent agreement achieved between the experiment and the finite element model at Instrumentation Lines 1, 2, and 3 although the model is slightly stiffer in a consistent way. However, no such agreement exist at Lines 4, 5, and 6. It must be noted that the experimental data at Instrumentation Lines 4, 5, and 6 do not appear linear under the initial loading. Their discrepancy may be originated from the difference in the horizontal

strain component as indicated in Figure 75 through Figure 77. In order to sort out the contributions from two other strain components, Figure 84 through Figure 89 present the direct measurements from the remaining two rosette strain gage components which were oriented 45° upward and downward with respect to the horizontal direction. Figure 84 through Figure 86 demonstrate the good agreement between the experimental and finite element results at Instrumentation Lines 1, 2, and 3. However, there is significant deviation at Instrumentation Lines 4 and 5, possibly because of the complex stress state. The plotted experimental data at Instrumentation Line 6 share the similar trend as those at Instrumentation Lines 1, 2, and 3 and the agreement improves significantly compared to that in Figure 83. Considering the magnitude of contributions from three strain components, the horizontal strain component is the one that mainly caused the observed discrepancy shown in Figure 83. This further supports the idea that the flexure response of the west end of the girder 24S may have been affected by damage imparted during the previously completed Test 80F.

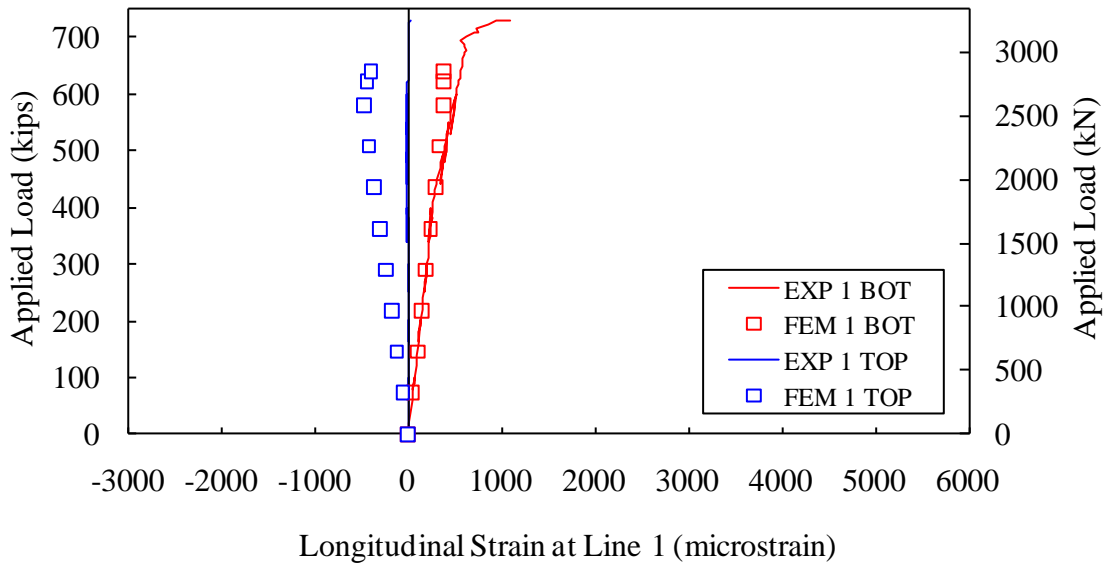


Figure 66. Graph. Predicted versus observed longitudinal strain on the top and bottom surfaces of the girder 24S along Instrumentation Line 1.

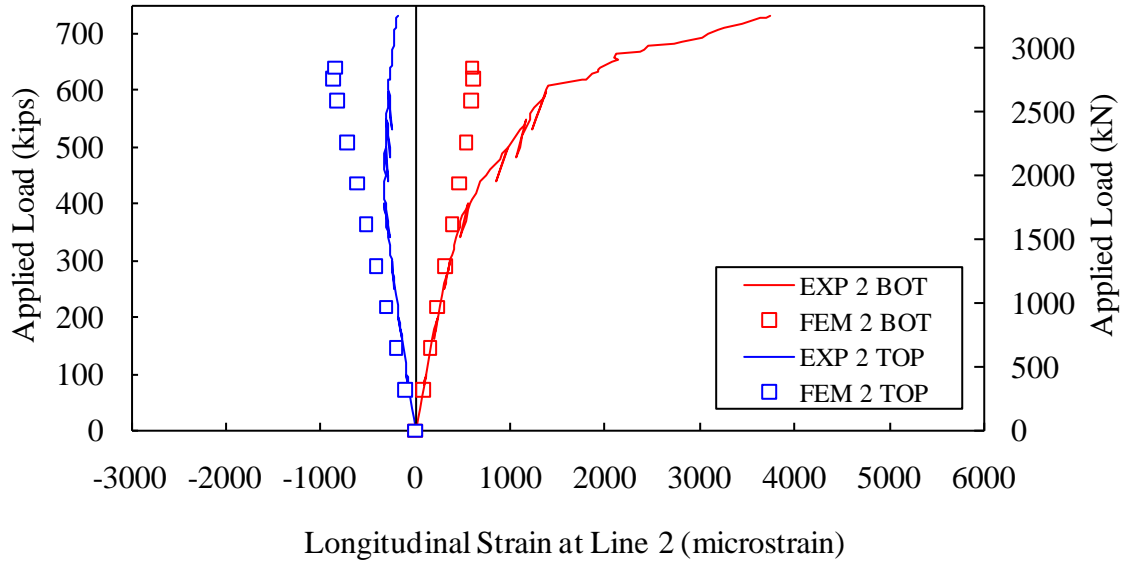


Figure 67. Graph. Predicted versus observed longitudinal strain on the top and bottom surfaces of the girder 24S along Instrumentation Line 2.

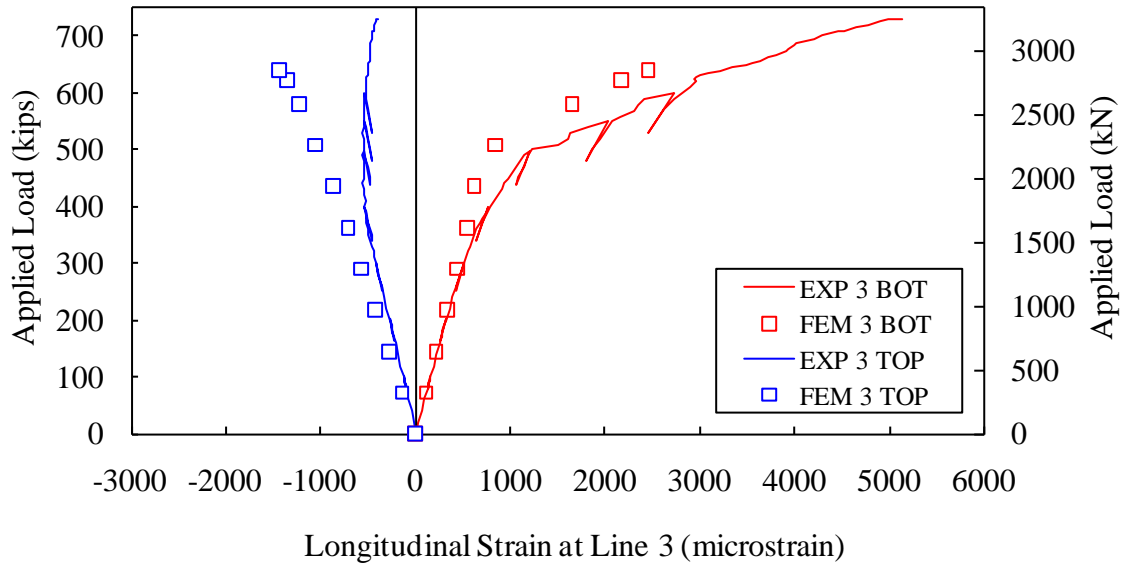


Figure 68. Graph. Predicted versus observed longitudinal strain on the top and bottom surfaces of the girder 24S along Instrumentation Line 3.

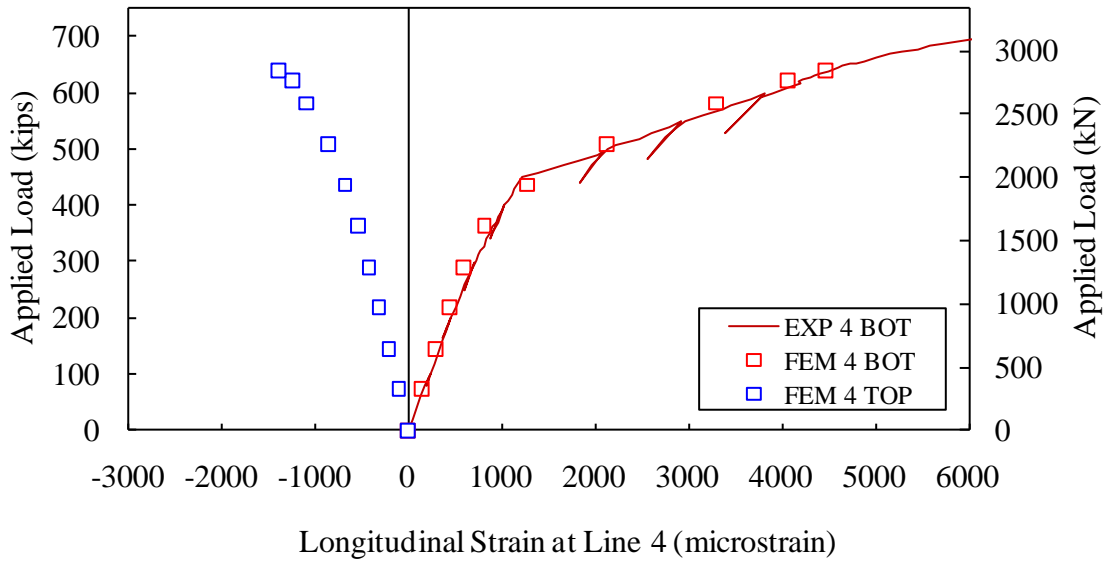


Figure 69. Graph. Predicted versus observed longitudinal strain on the top and bottom surfaces of the girder 24S along Instrumentation Line 4.

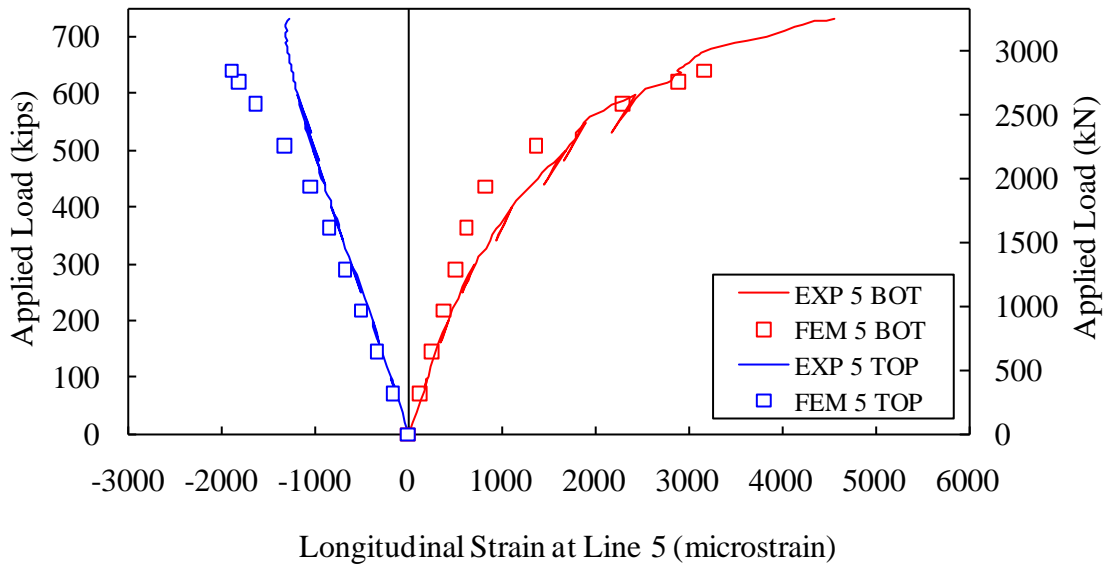


Figure 70. Graph. Predicted versus observed longitudinal strain on the top and bottom surfaces of the girder 24S along Instrumentation Line 5.

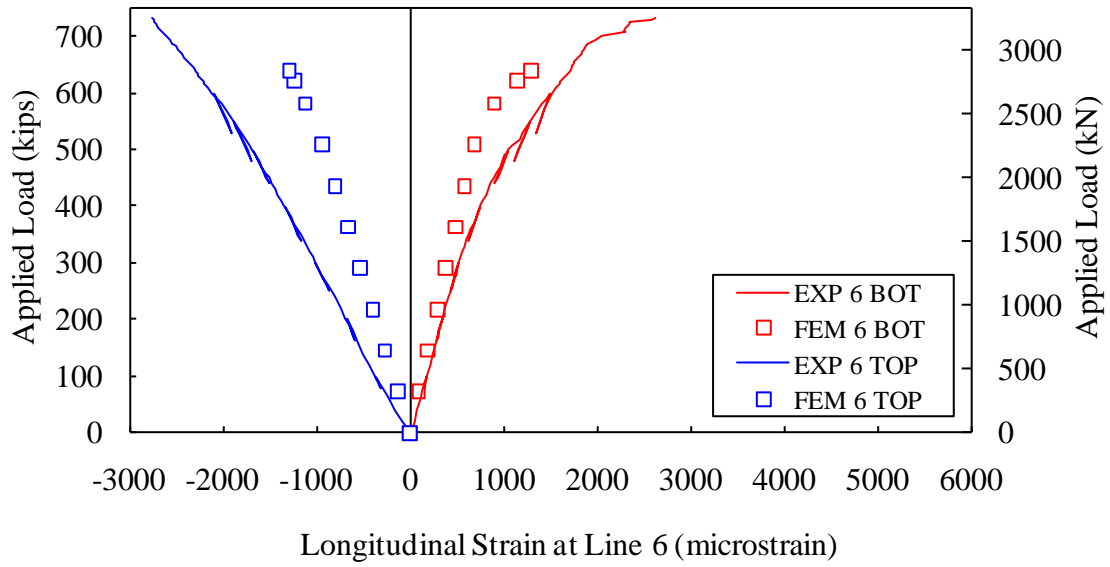


Figure 71. Graph. Predicted versus observed longitudinal strain on the top and bottom surfaces of the girder 24S along Instrumentation Line 6.

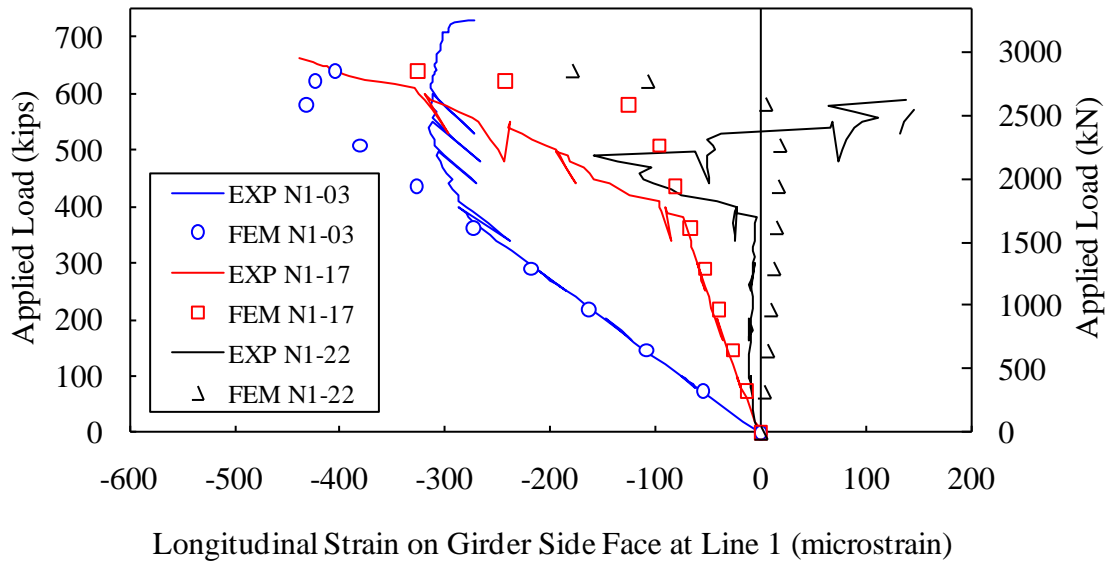


Figure 72. Graph. Predicted versus observed longitudinal strain on the side face of the girder 24S along Instrumentation Line 1.

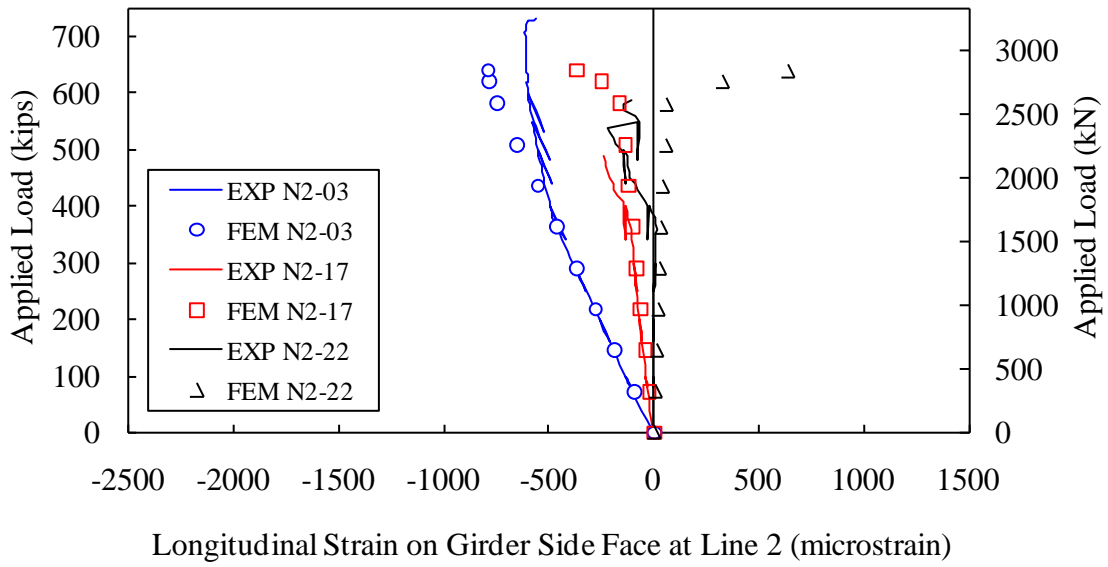


Figure 73. Graph. Predicted versus observed longitudinal strain on the side face of the girder 24S along Instrumentation Line 2.

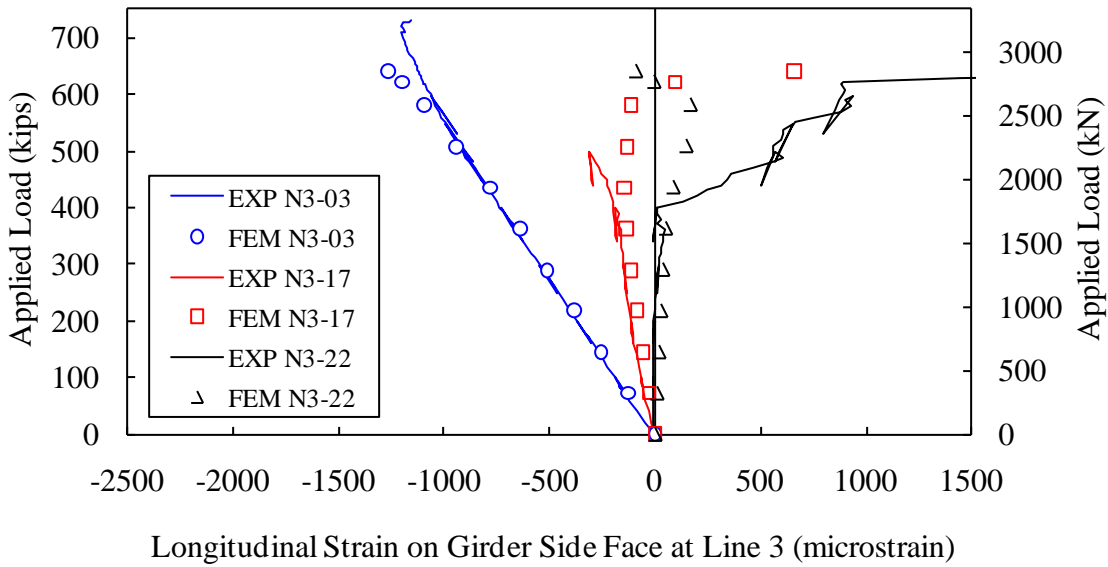


Figure 74. Graph. Predicted versus observed longitudinal strain on the side face of the girder 24S along Instrumentation Line 3.

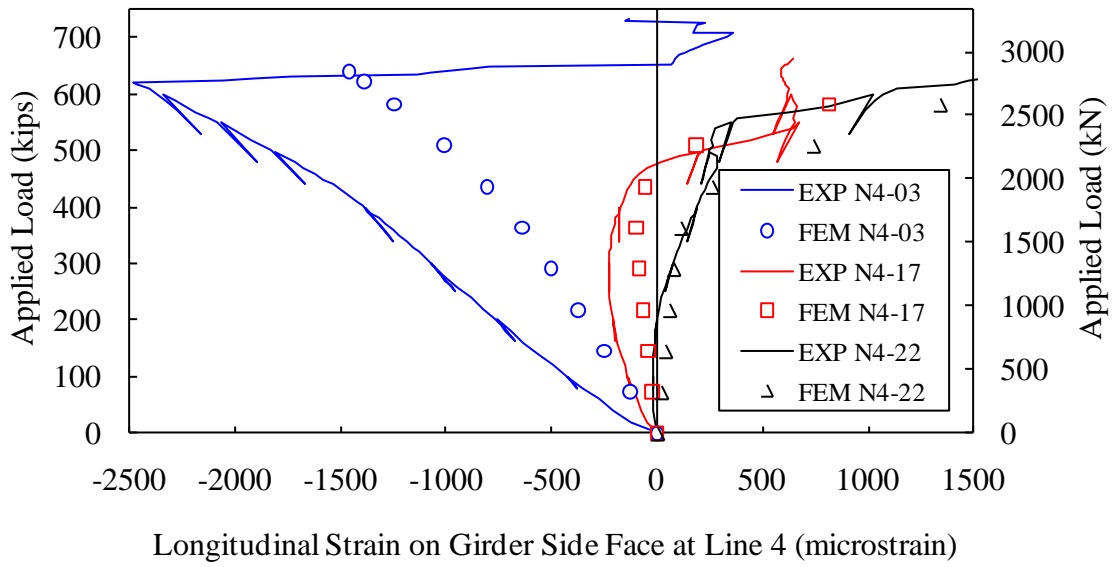


Figure 75. Graph. Predicted versus observed longitudinal strain on the side face of the girder 24S along Instrumentation Line 4.

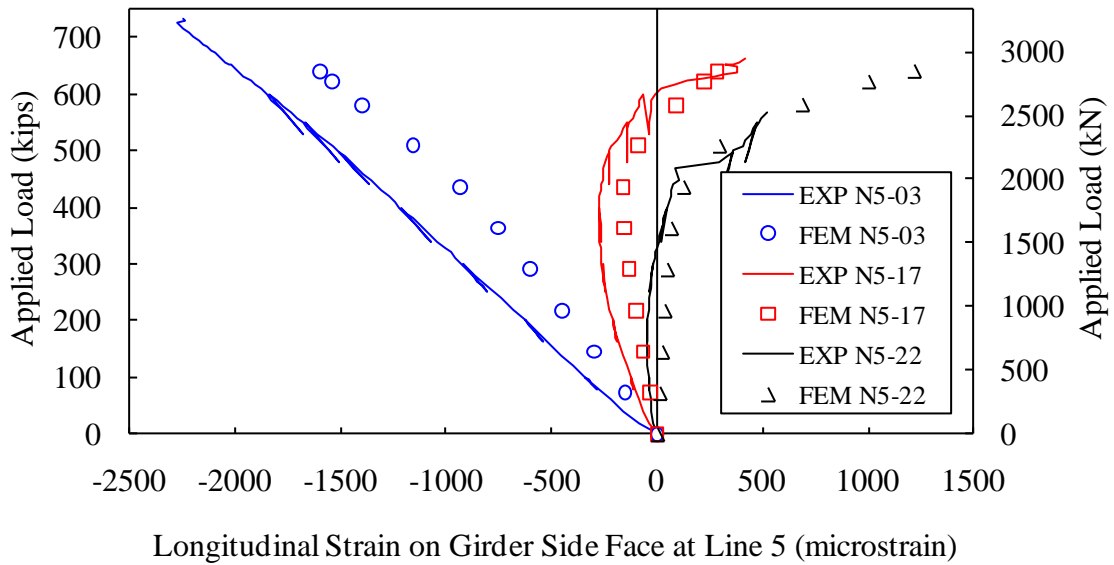


Figure 76. Graph. Predicted versus observed longitudinal strain on the side face of the girder 24S along Instrumentation Line 5.

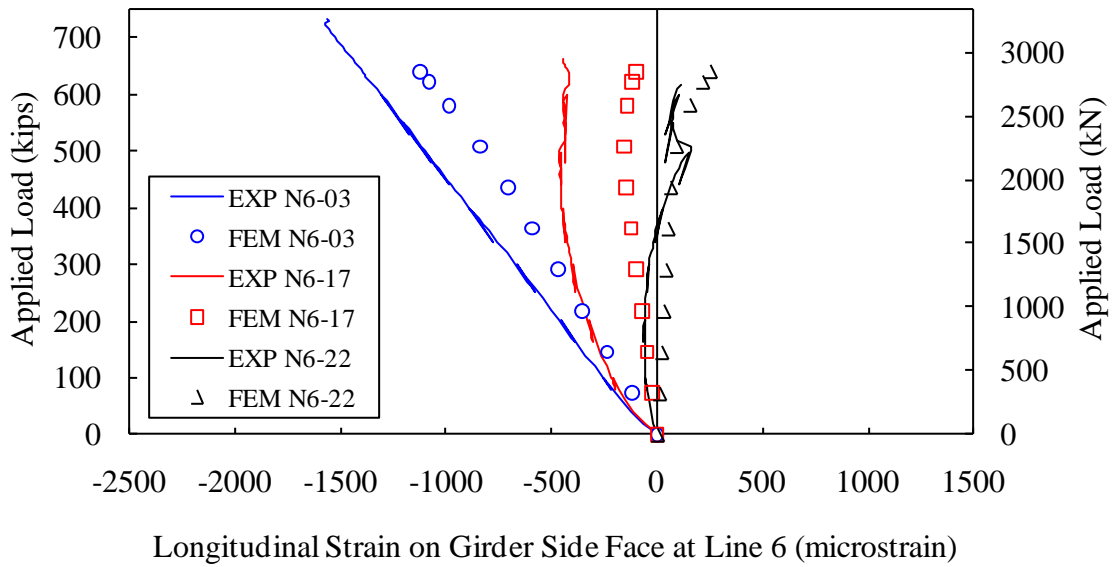


Figure 77. Graph. Predicted versus observed longitudinal strain on the side face of the girder 24S along Instrumentation Line 6.

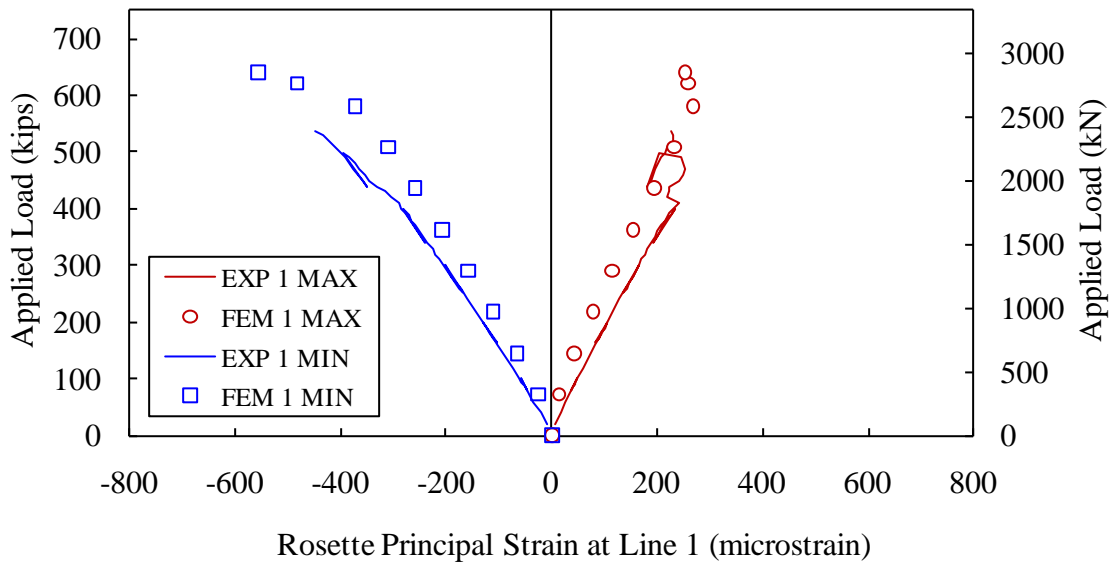


Figure 78. Graph. Predicted versus observed principal strains on the side face of the girder 24S along Instrumentation Line 1.

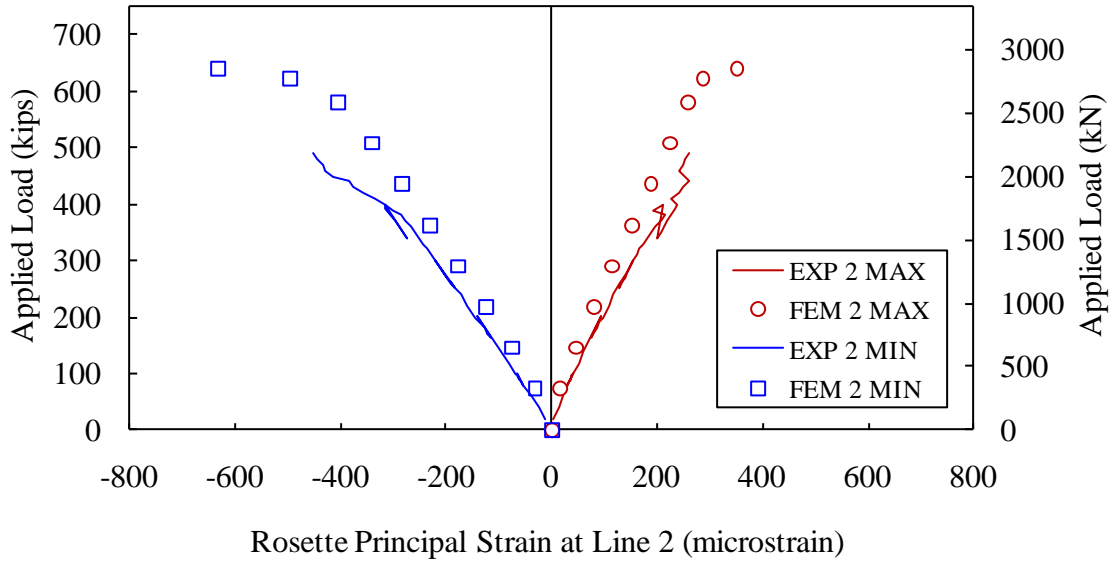


Figure 79. Graph. Predicted versus observed principal strains on the side face of the girder 24S along Instrumentation Line 2.

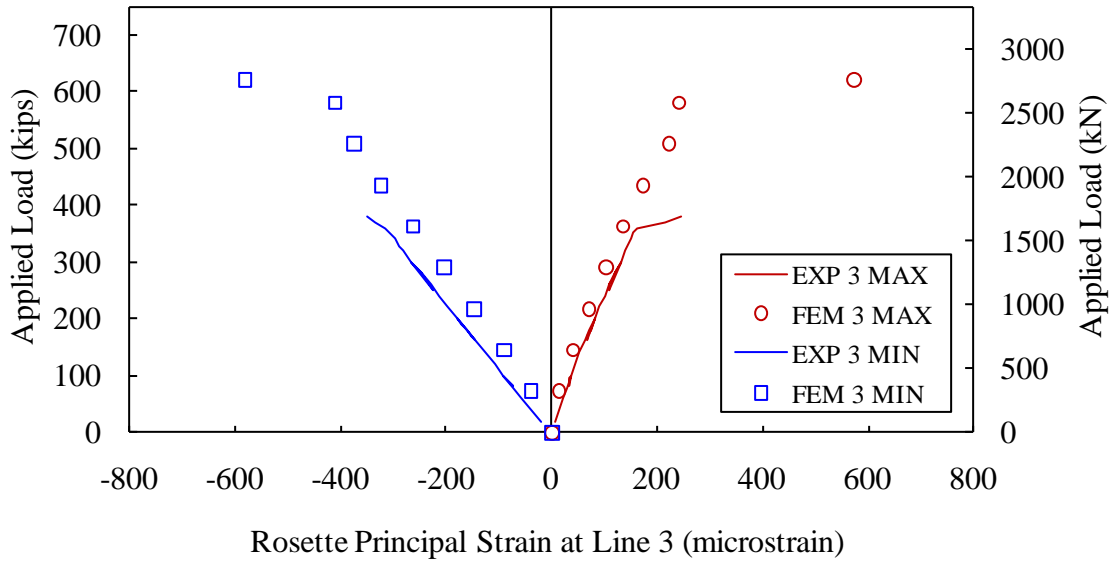


Figure 80. Graph. Predicted versus observed principal strains on the side face of the girder 24S along Instrumentation Line 3.

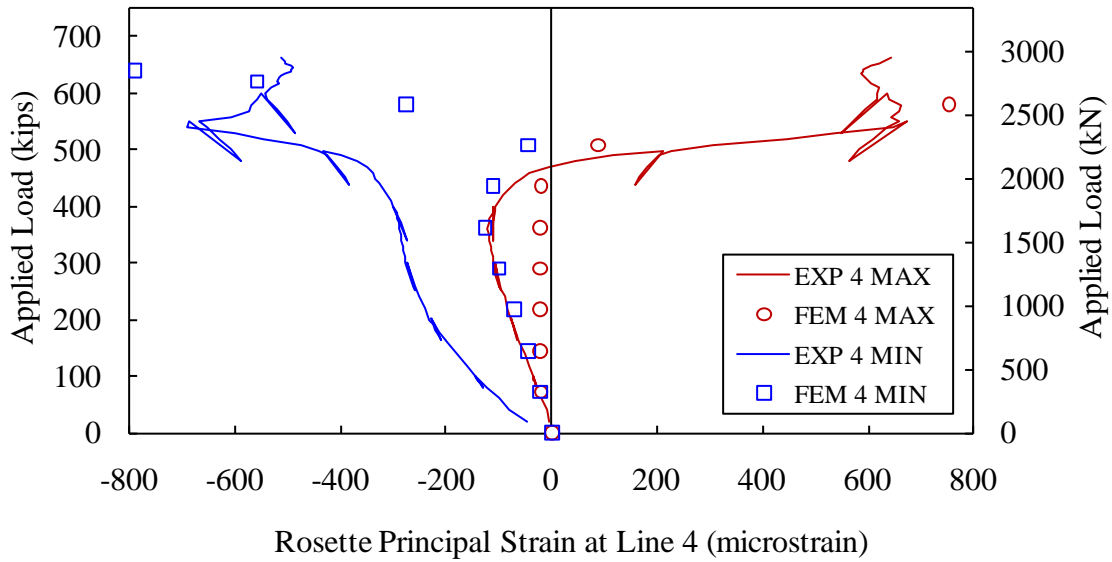


Figure 81. Graph. Predicted versus observed principal strains on the side face of the girder 24S along Instrumentation Line 4.

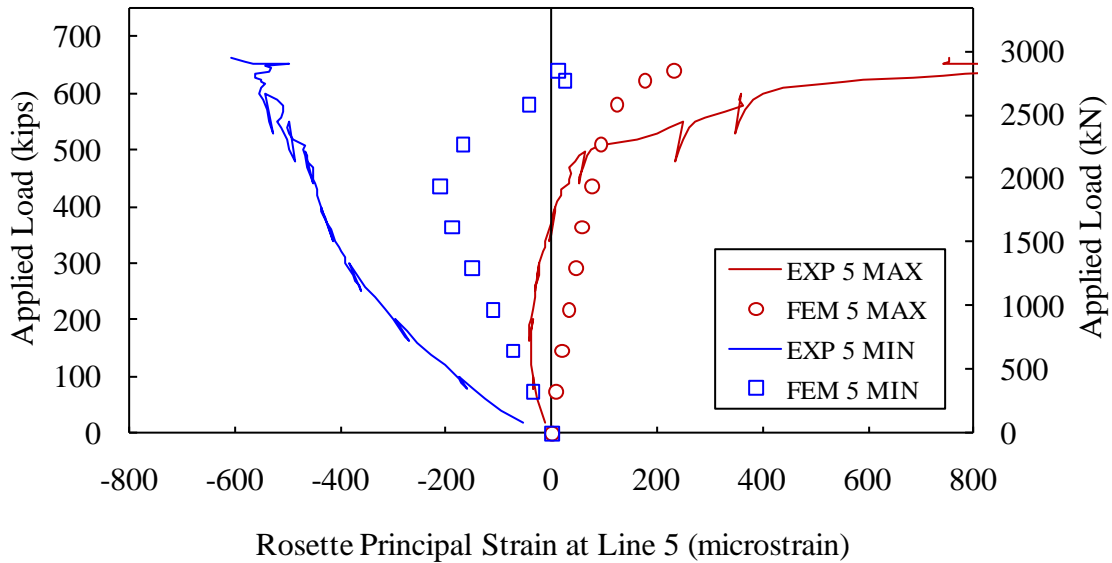


Figure 82. Graph. Predicted versus observed principal strains on the side face of the girder 24S along Instrumentation Line 5.

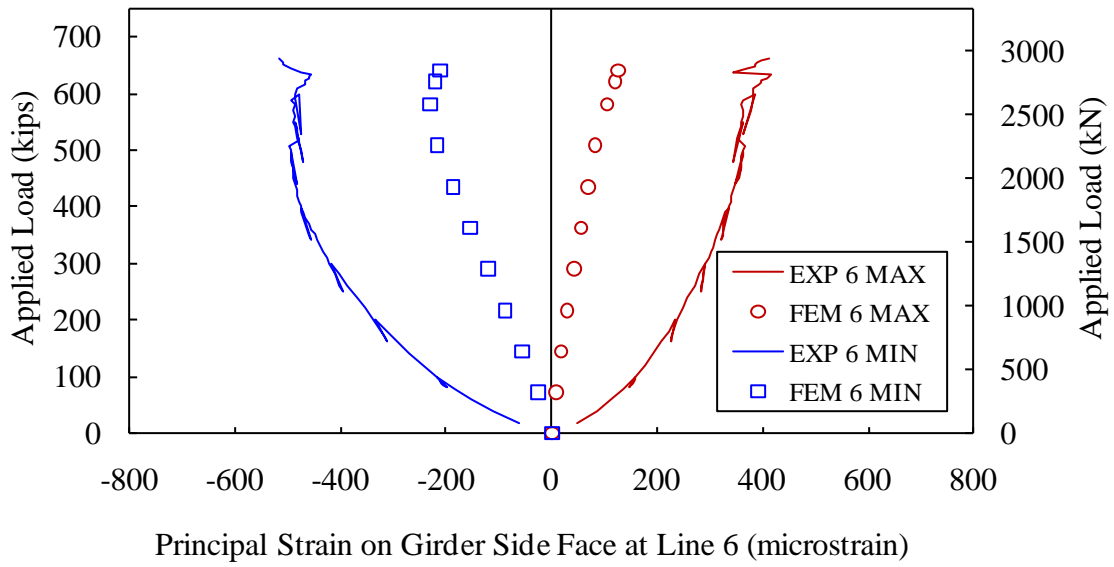


Figure 83. Graph. Predicted versus observed principal strains on the side face of the girder 24S along Instrumentation Line 6.

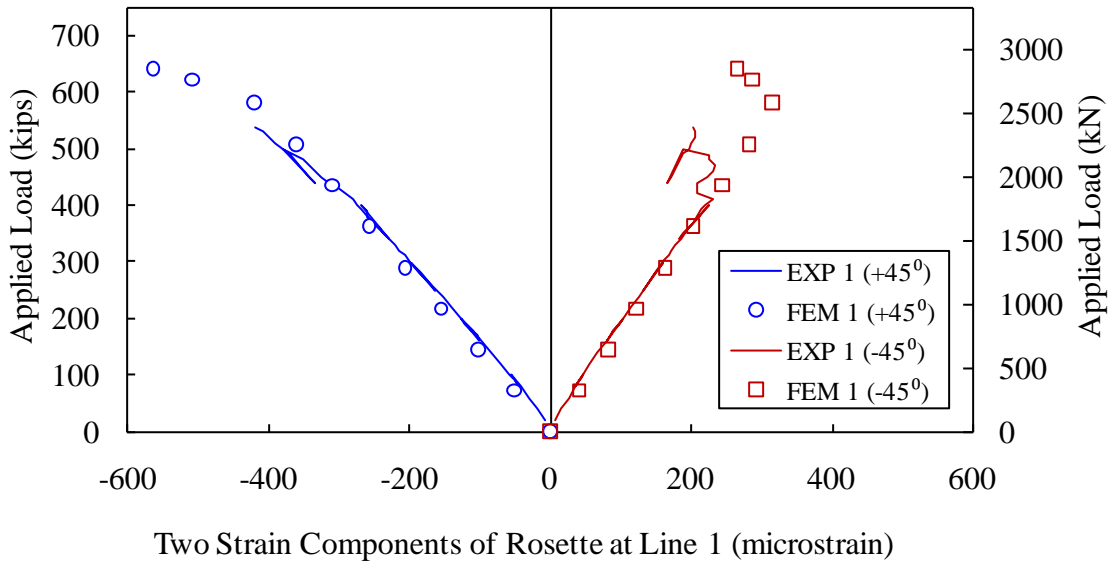


Figure 84. Graph. Predicted versus observed strain components from rosette strain gage at Instrumentation Line 1.

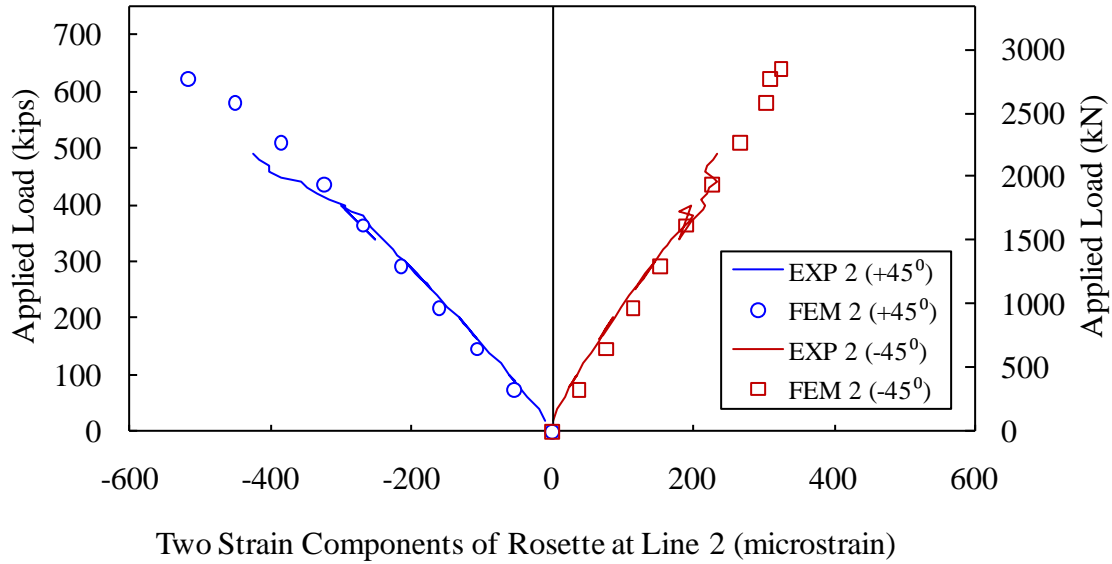


Figure 85. Graph. Predicted versus observed strain components from rosette strain gage at Instrumentation Line 2.

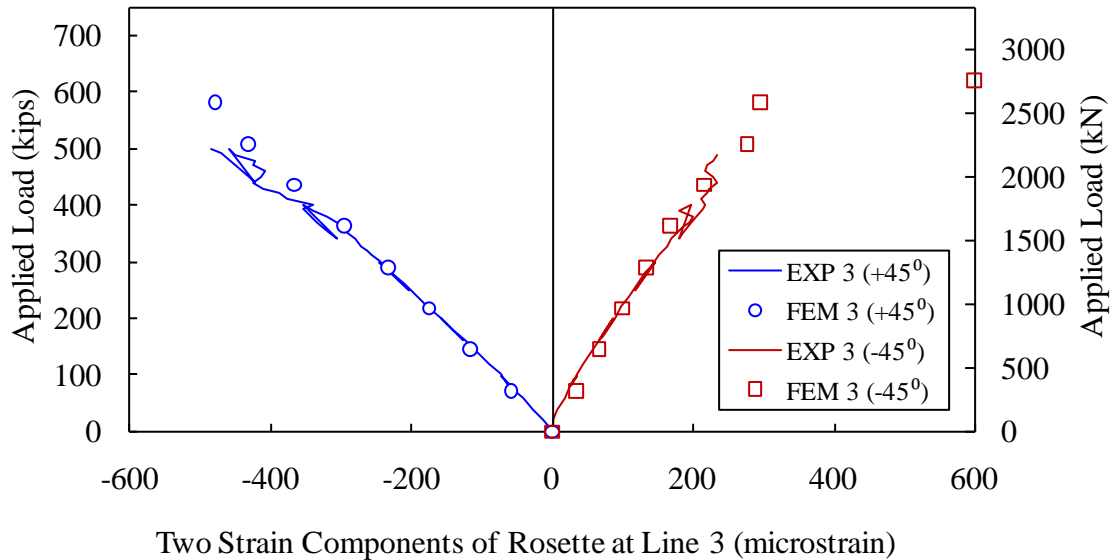


Figure 86. Graph. Predicted versus observed strain components from rosette strain gage at Instrumentation Line 3.

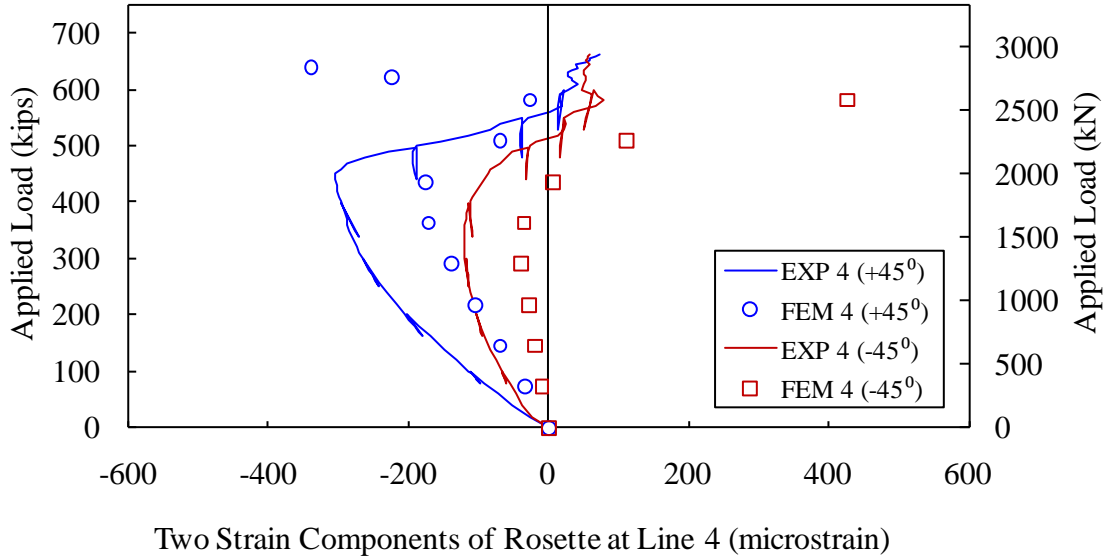


Figure 87. Graph. Predicted versus observed strain components from rosette strain gage at Instrumentation Line 4.

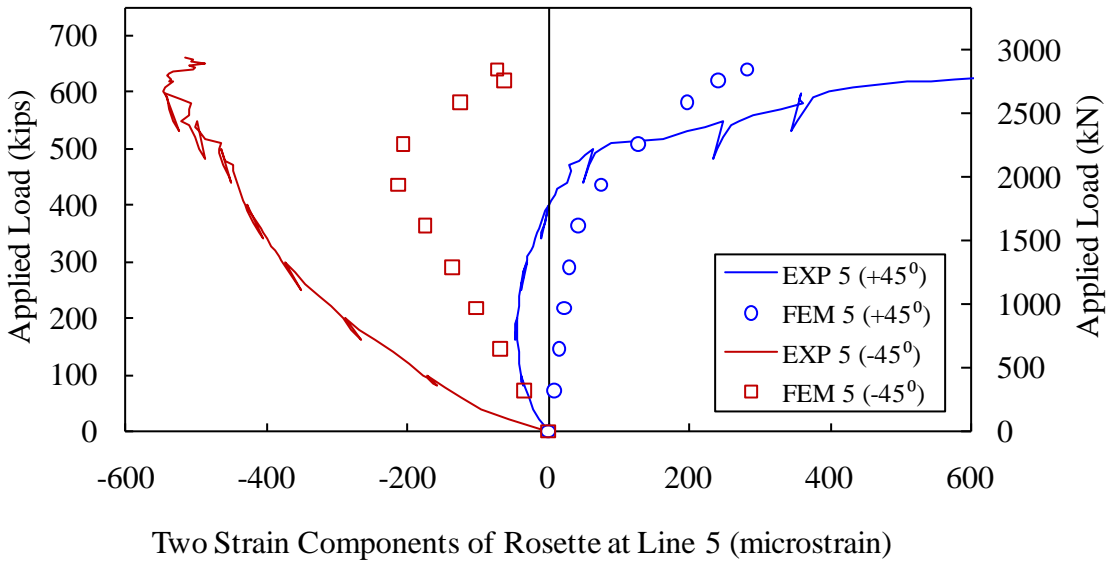


Figure 88. Graph. Predicted versus observed strain components from rosette strain gage at Instrumentation Line 5.

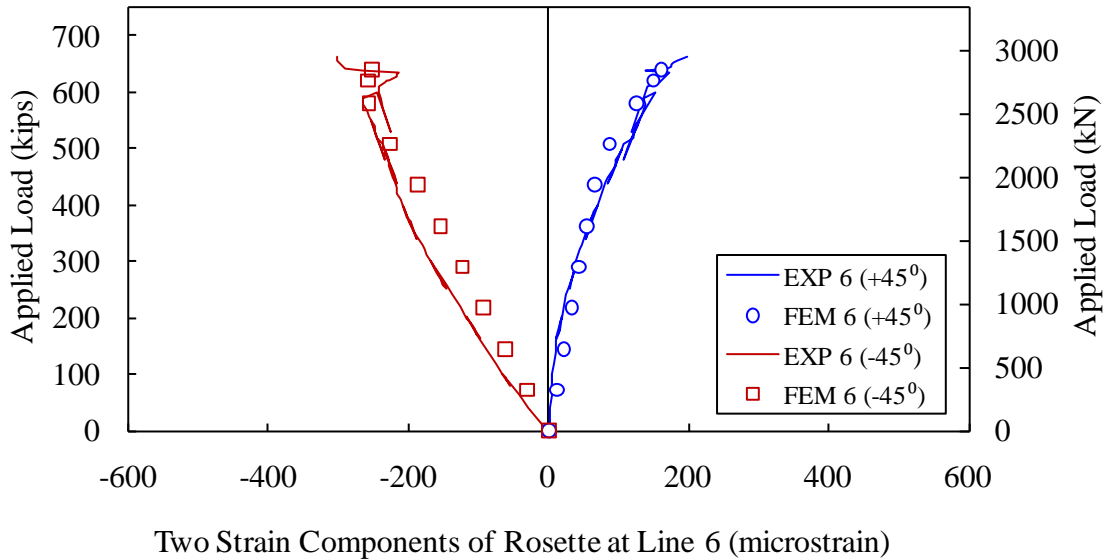


Figure 89. Graph. Predicted versus observed strain components from rosette strain gage at Instrumentation Line 6.

I-girder 14S

The analysis of the I-girder 14S follows the same scheme used in the previous section for the analysis of the I-girder 24S. The vertical displacement is examined first to investigate if a similar uniform vertical rigid body movement exists. Then the longitudinal strains on the top, bottom, and side faces of the girder are compared between the experiment and the finite element model. The comparison is also extended to three strain components of six rosette gages and their computed principal strains.

Figure 90 and Figure 91 presented the predicted and observed vertical deflection of the girder along the six instrumentation lines. Similarly, it appears that the finite element predictions are offset from the experimental measurements at all instrumentation lines in an almost uniform fashion. Figure 92 plots the deflection difference “Delta” between the finite element and experimental results at Instrumentation Line 4. The “Delta” appears almost linear with respect to the applied load when an applied load is less than 540 kips (2402 kN) and above the load the nonlinear difference becomes increasingly apparent. The linear difference is thought to be elastic response of the seats while the nonlinear difference is mainly because of significant slippage of prestressing strands in the bottom flange at the girder east end as was reported in reference (12). In order to keep consistent with the case of the I-girder 24S, the nonlinear difference is not included in the compensation and the proposed offset on the experimental vertical displacement is idealized exactly linear as shown in Figure 92. Figure 93 and Figure 94 show that the modified experimental results agree with the finite element results very well in the linear loading stage at almost all instrumentation lines. The reduced asymmetry of loading in Test 14S than Test 24S may have contributed to the reduction in perceived rigid body rotation.

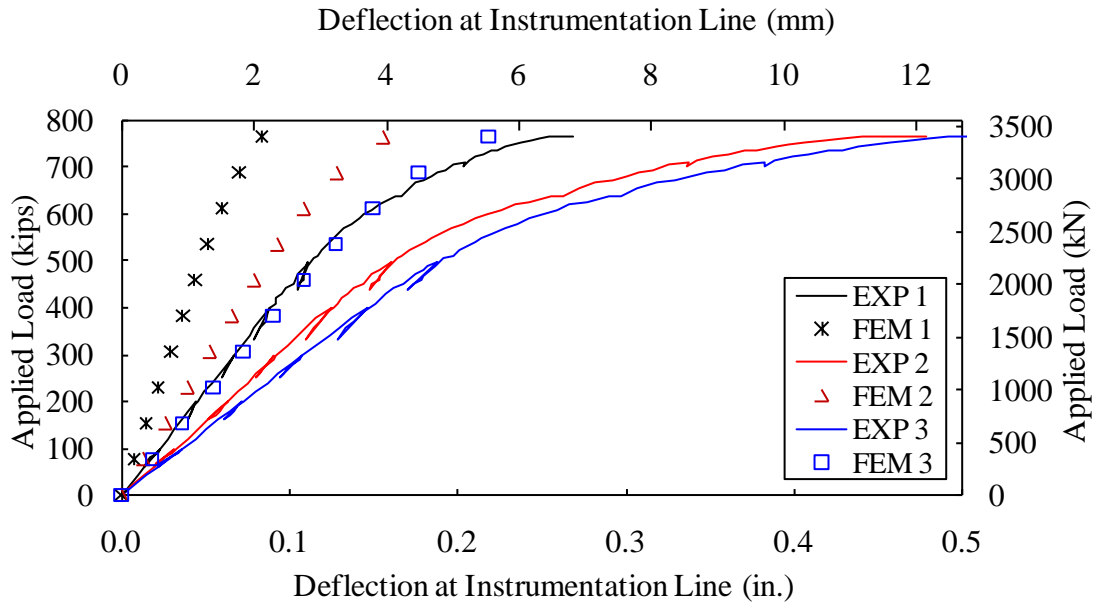


Figure 90. Graph. Predicted versus observed deflection of the girder 14S along Instrumentation Lines 1, 2, and 3.

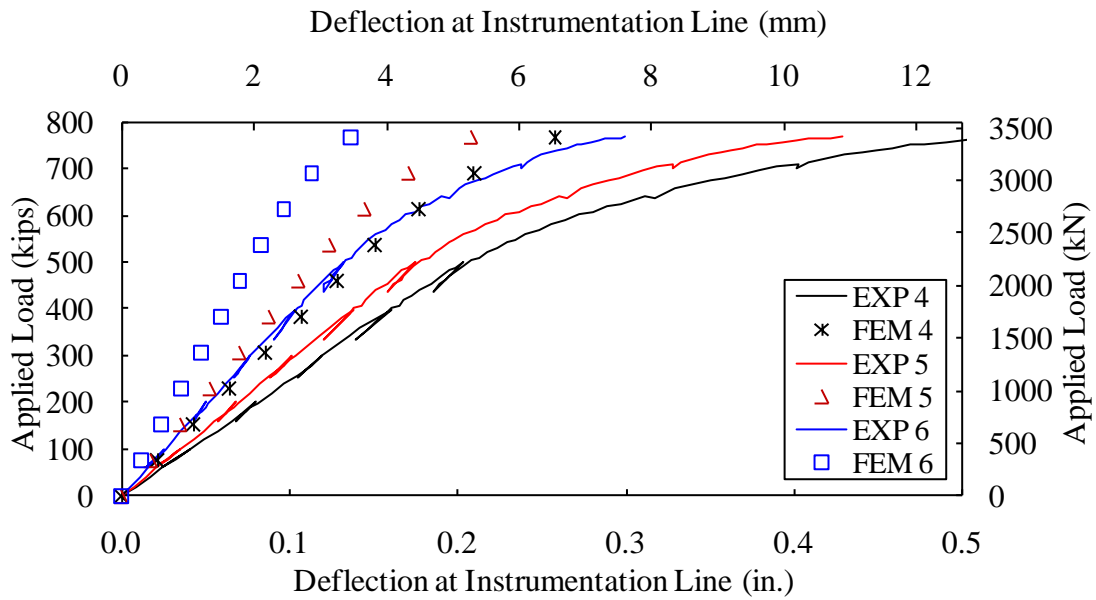


Figure 91. Graph. Predicted versus observed deflection of the girder 14S along Instrumentation Lines 4, 5, and 6.

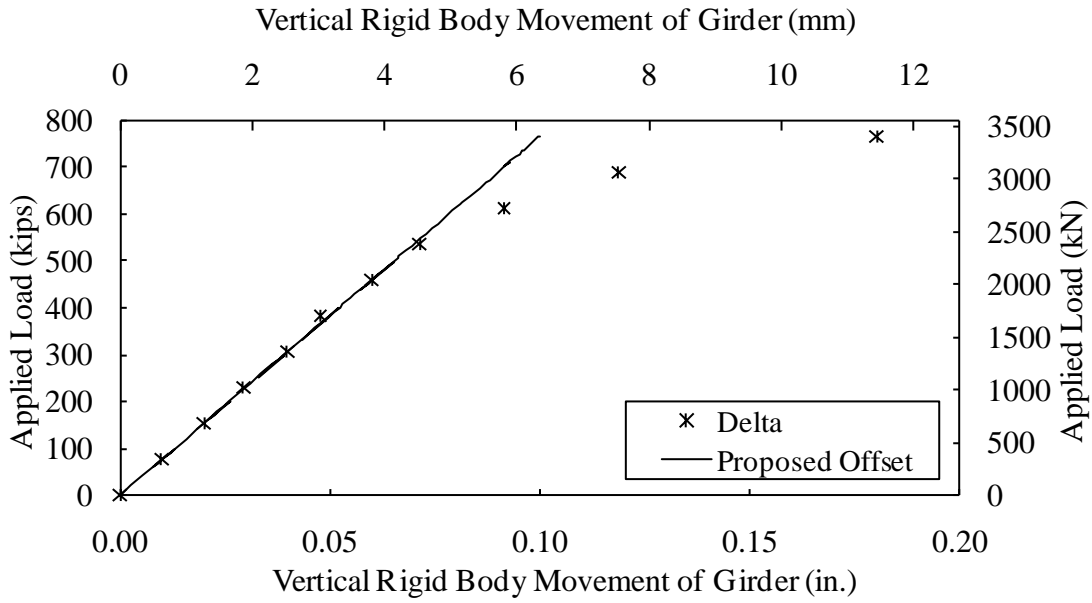


Figure 92. Graph. Assumed vertical rigid body movement of the girder 14S.

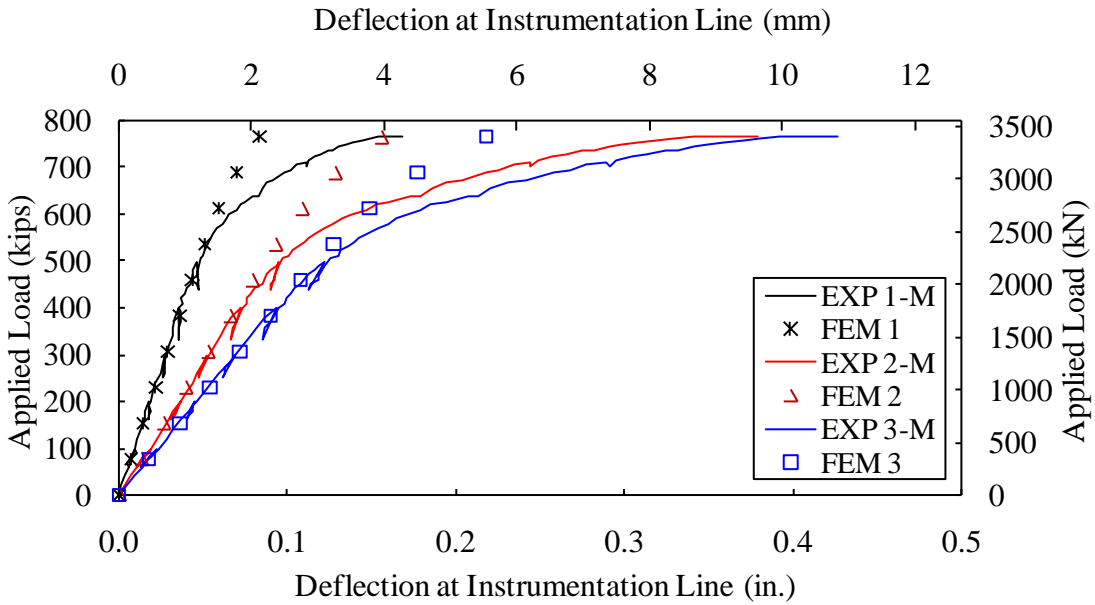


Figure 93. Graph. Predicted versus observed (modified) deflection of the girder 14S along Instrumentation Lines 1, 2, and 3.

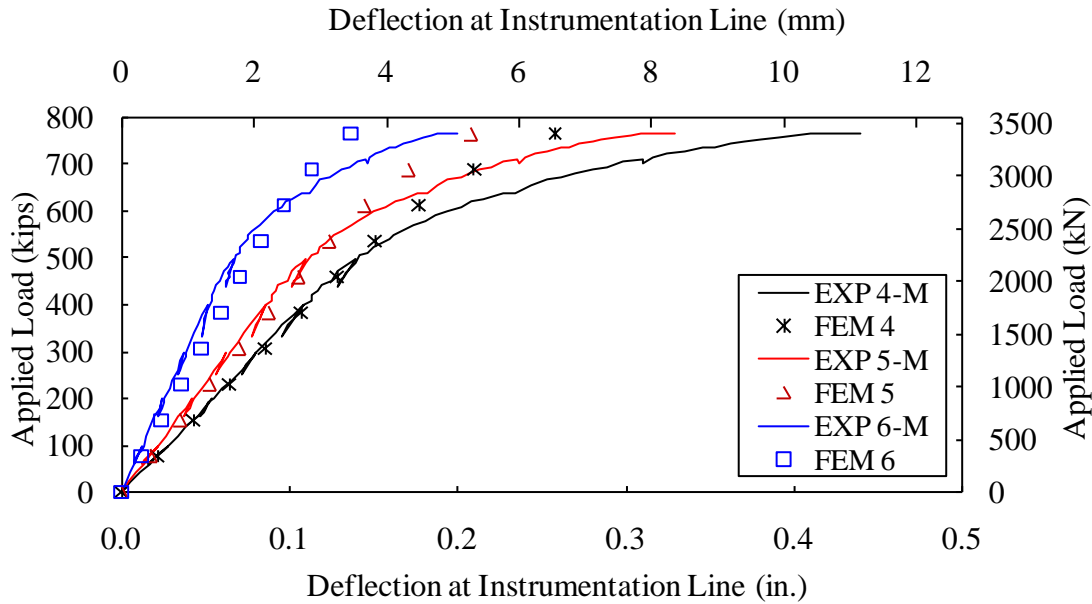


Figure 94. Graph. Predicted versus observed (modified) deflection of the girder 14S along Instrumentation Lines 4, 5, and 6.

Figure 95 through Figure 100 present the comparison on the longitudinal strain on the top and bottom surfaces of the girder along all the instrumentation lines. Both tensile and compressive strains have a decent agreement between the model and the experiment at all the instrumentation lines including Instrumentation 6. Figure 101 through Figure 106 present the longitudinal strain on the side face of the girder with 3 inch (76.2 mm), 17 inch (432 mm), and 22 inch (559 mm) below the girder top surface. Again, the agreement is fairly good at all instrumentation lines including Instrumentation Line 4 which is aligned with the loading point.

Figure 107 through Figure 112 present the maximum and minimum principal strains at the rosette strain locations as indicated in Figure 13. The rosette strain gages were installed 17 inch (432 mm) below the girder top surface along the six instrumentation lines and orientated with the 45° diagonal gage component in a horizontal direction and two other gage components in $\pm 45^\circ$ from the horizontal direction. The horizontal strain component has been presented as longitudinal strain on the girder side face, i.e. EXP NX-17, in Figure 101 through Figure 106. Maximum and minimum principal strains are computed from three independent measurements in three directions on a single rosette. Figure 111 and Figure 112 demonstrate an excellent agreement between the experiment and the finite element model at Instrumentation Lines 5 and 6. The agreement at Instrumentation Lines 1, 2, and 3 is reduced, with the majority of the difference occurring early in the response possibly due to seating effects. Figure 113 through Figure 118 present the direct measurements from two remaining rosette strain gage components which were oriented 45° upward and downward with respect to the horizontal direction. Figure 117 and Figure 118 demonstrate a decent agreement between the experiment and the model at

Instrumentation Lines 5 and 6. Figure 113 through Figure 115 show some difference but a decent agreement is also expected if the effect of seating in the experimental results is excluded. The stress state at Instrumentation Line 4 is complex and is prone to be affected by the local stress distribution from the loading and tie constraint between loading patch and concrete imposed on the model.

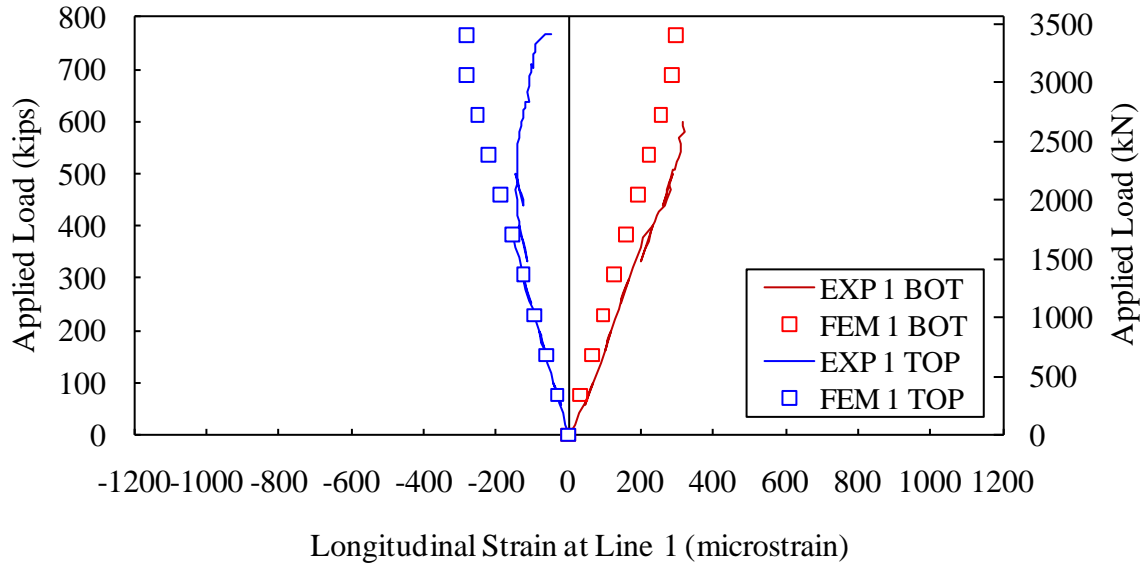


Figure 95. Graph. Predicted versus observed longitudinal strain on the top and bottom surfaces of the girder 14S along Instrumentation Line 1.

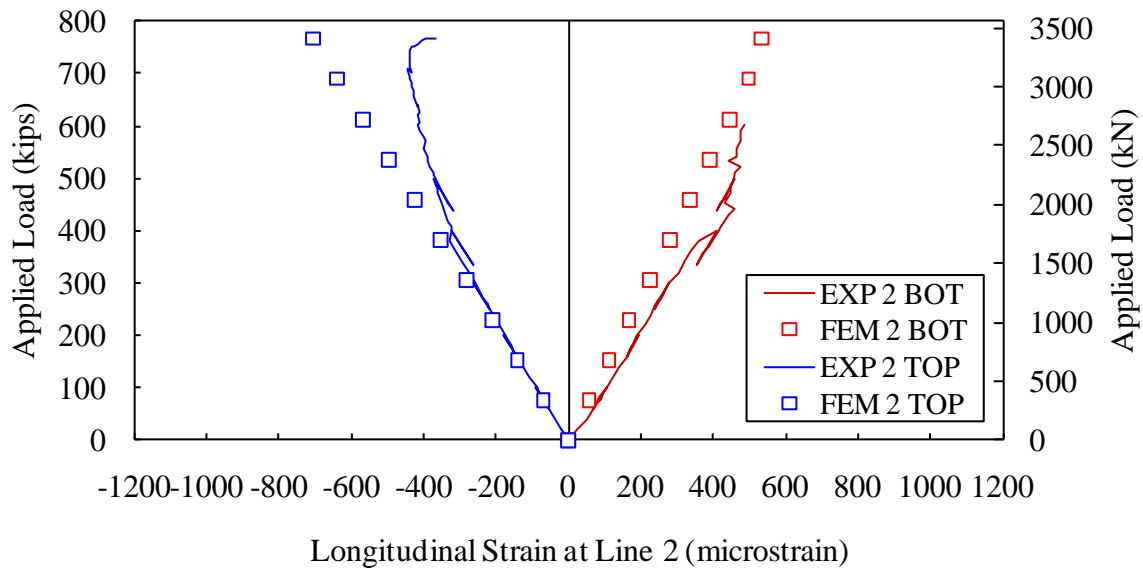


Figure 96. Graph. Predicted versus observed longitudinal strain on the top and bottom surfaces of the girder 14S along Instrumentation Line 2.

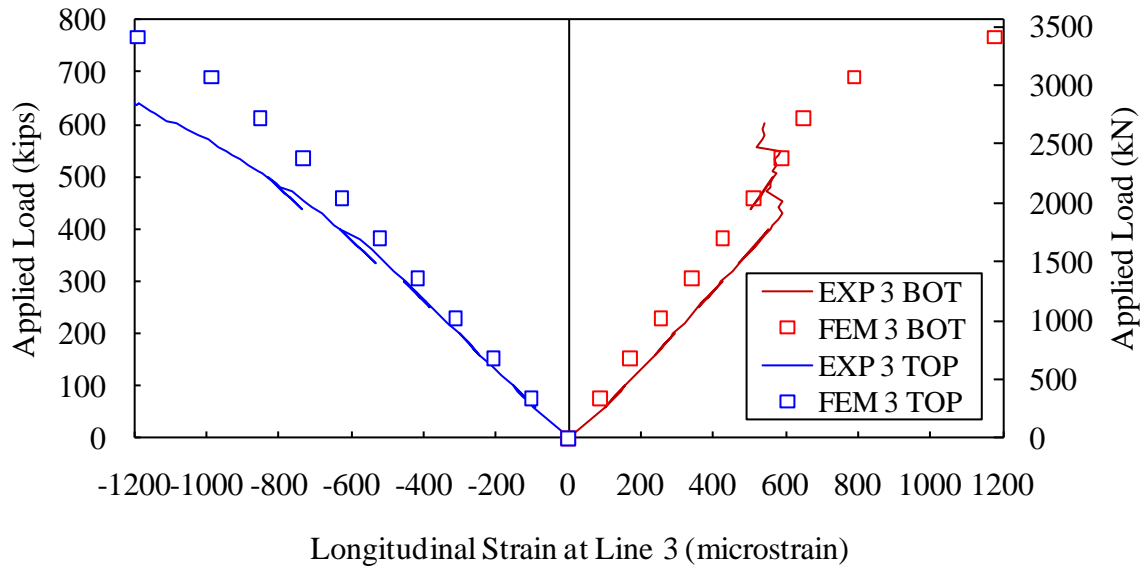


Figure 97. Graph. Predicted versus observed longitudinal strain on the top and bottom surfaces of the girder 14S along Instrumentation Line 3.

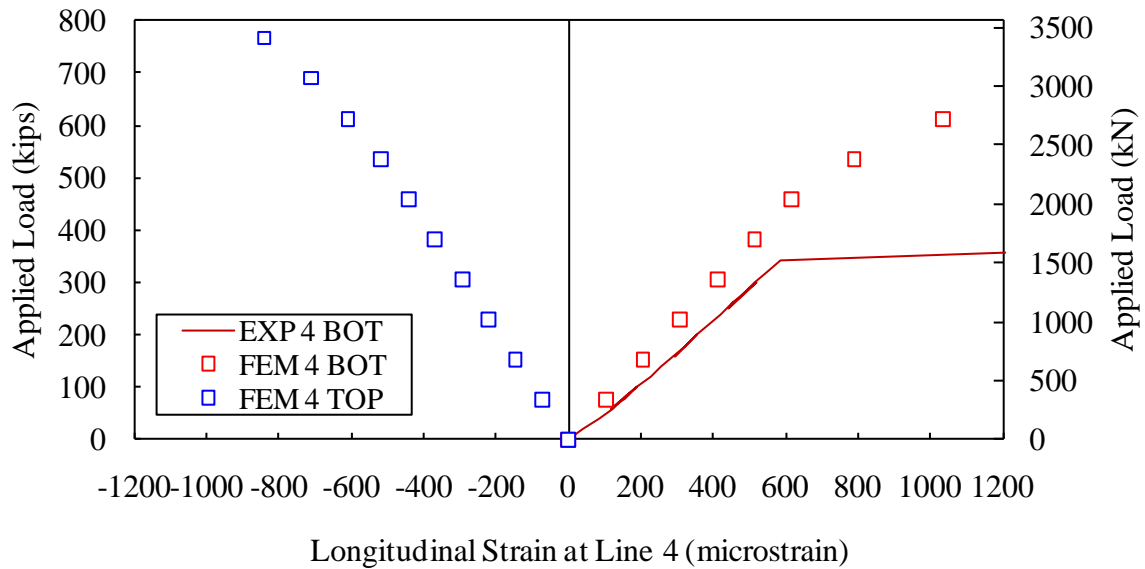


Figure 98. Graph. Predicted versus observed longitudinal strain on the top and bottom surfaces of the girder 14S along Instrumentation Line 4.

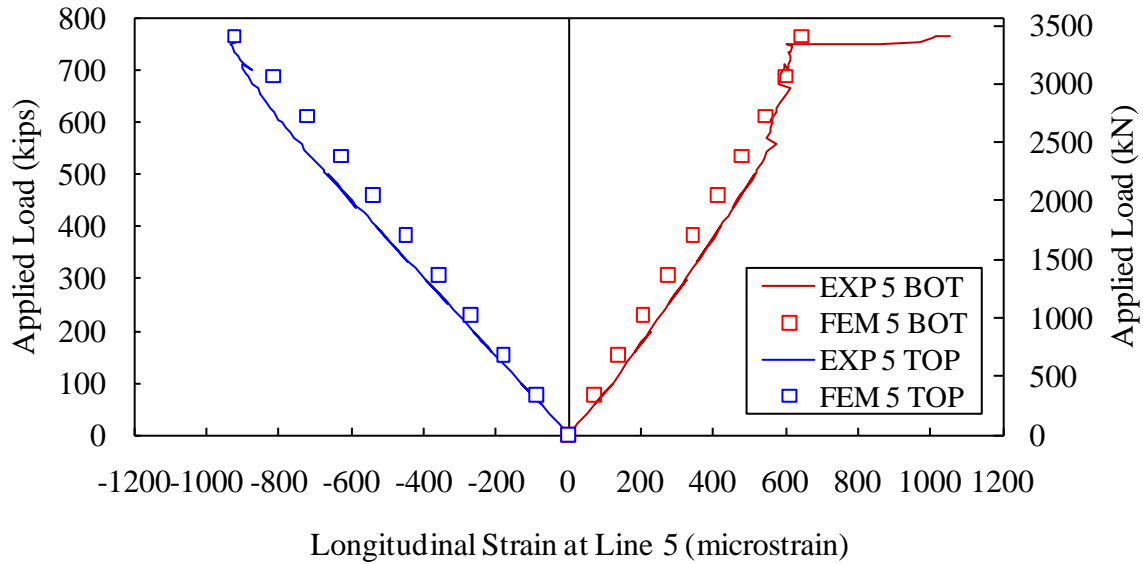


Figure 99. Graph. Predicted versus observed longitudinal strain on the top and bottom surfaces of the girder 14S along Instrumentation Line 5.

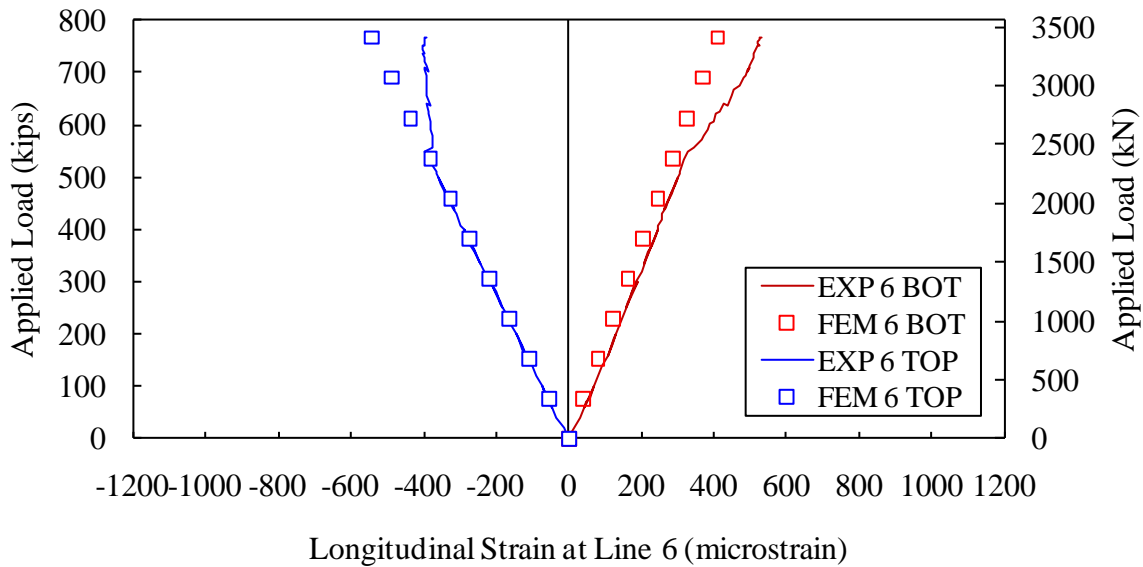


Figure 100. Graph. Predicted versus observed longitudinal strain on the top and bottom surfaces of the girder 14S along Instrumentation Line 6.

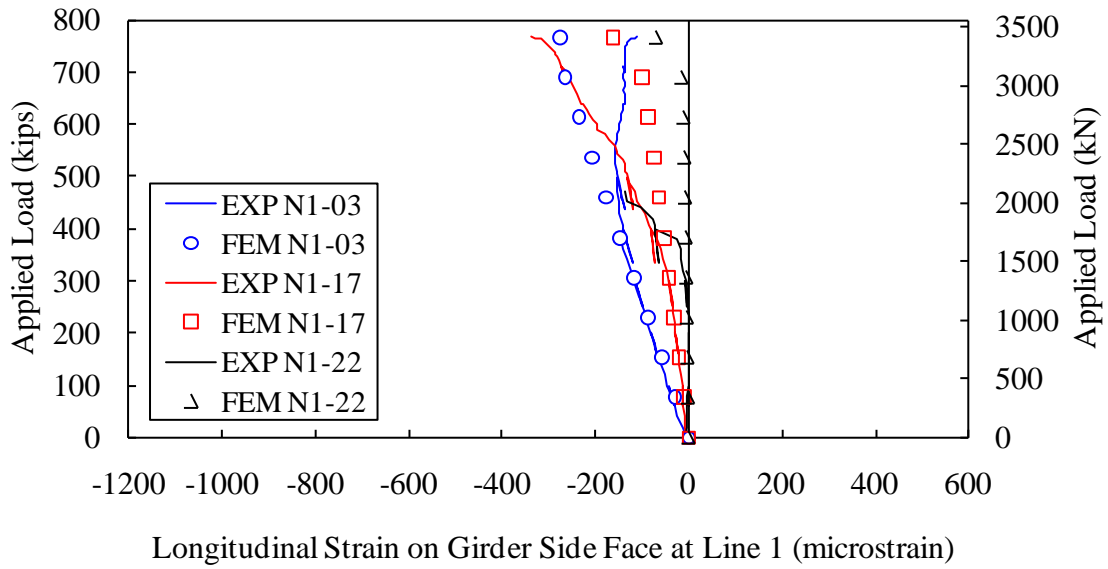


Figure 101. Graph. Predicted versus observed longitudinal strain on the side face of the girder 14S along Instrumentation Line 1.

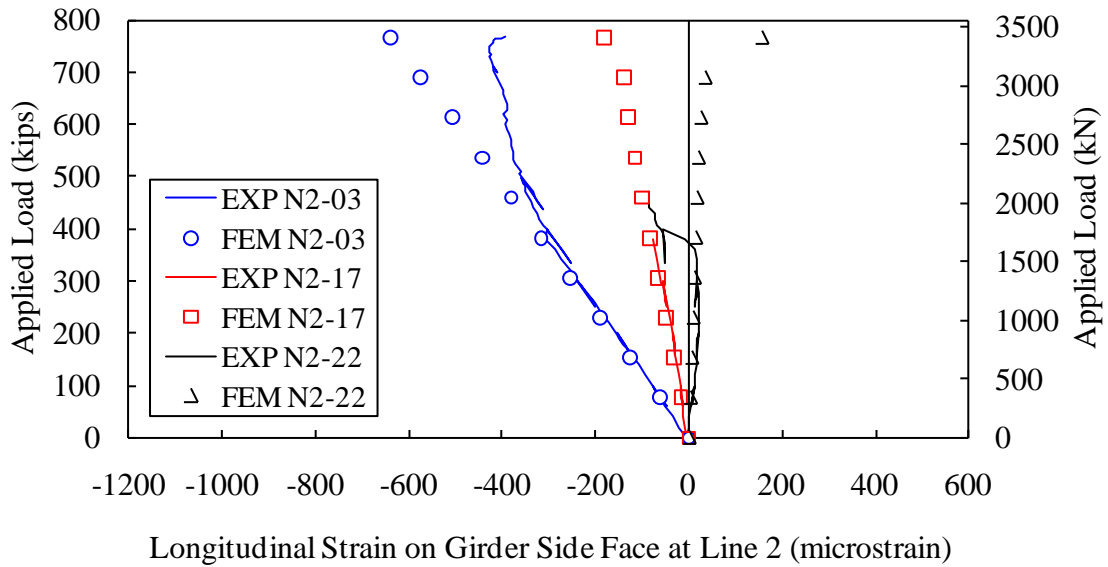


Figure 102. Graph. Predicted versus observed longitudinal strain on the side face of the girder 14S along Instrumentation Line 2.

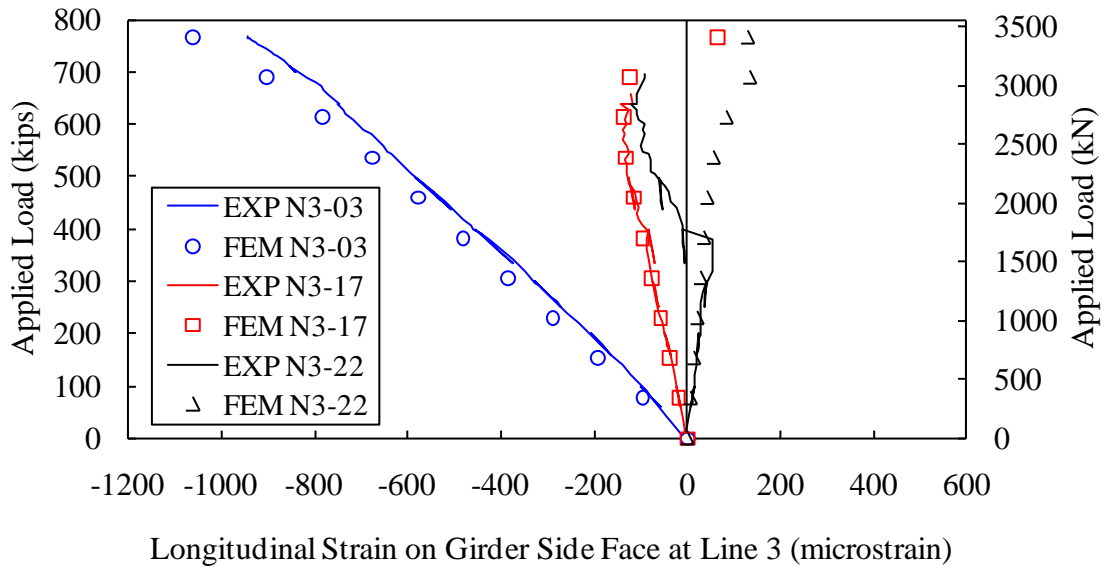


Figure 103. Graph. Predicted versus observed longitudinal strain on the side face of the girder 14S along Instrumentation Line 3.

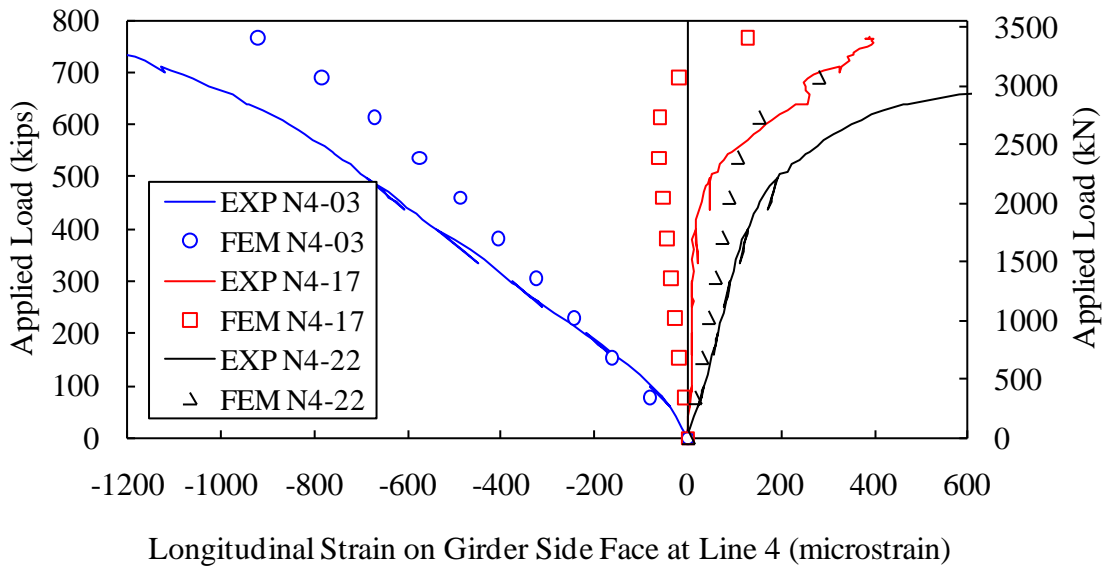


Figure 104. Graph. Predicted versus observed longitudinal strain on the side face of the girder 14S along Instrumentation Line 4.

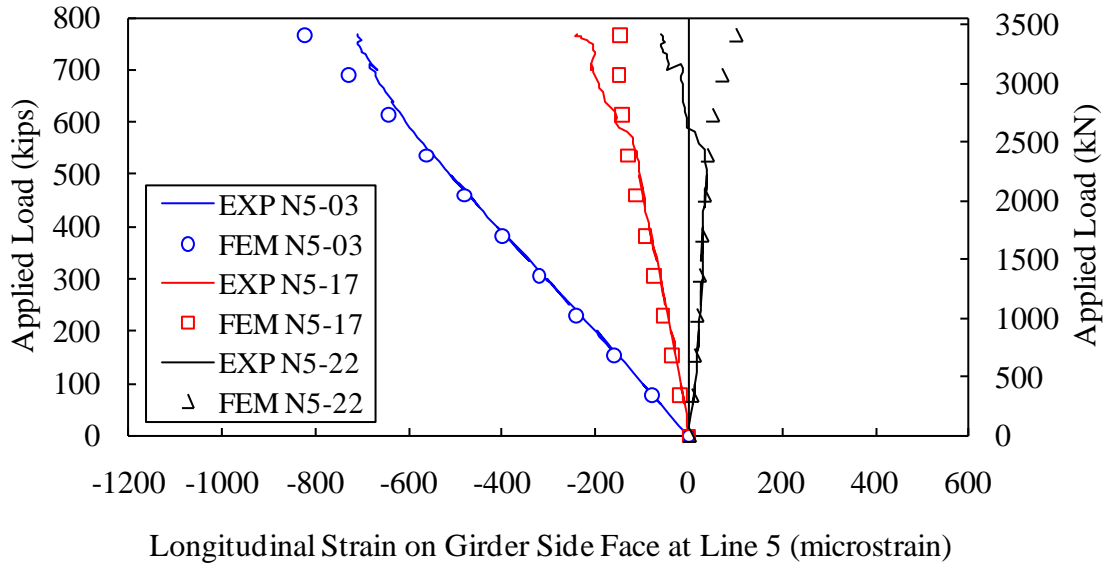


Figure 105. Graph. Predicted versus observed longitudinal strain on the side face of the girder 14S along Instrumentation Line 5.

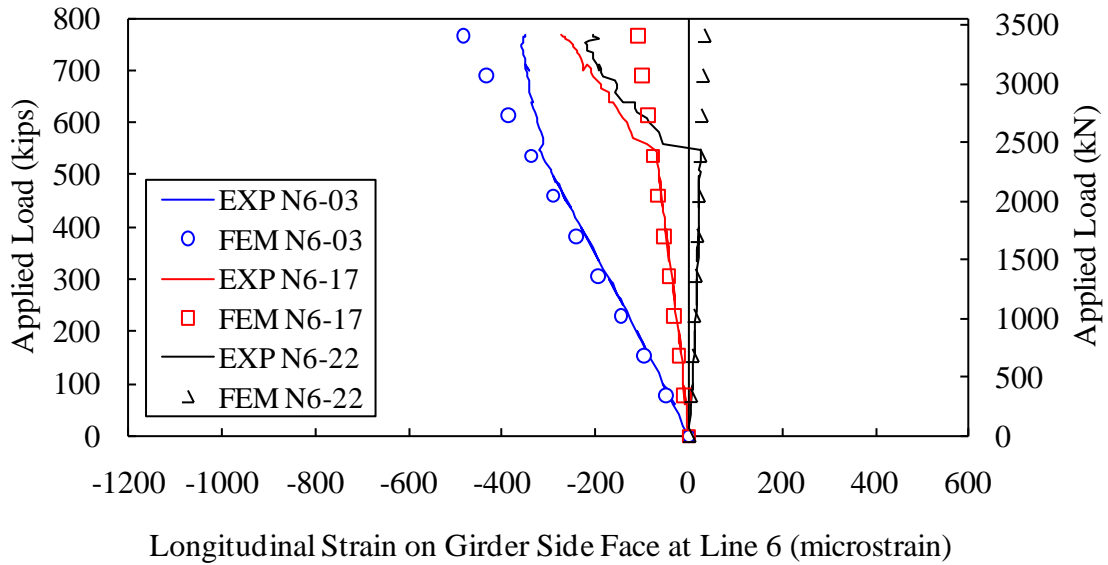


Figure 106. Graph. Predicted versus observed longitudinal strain on the side face of the girder 14S along Instrumentation Line 6.

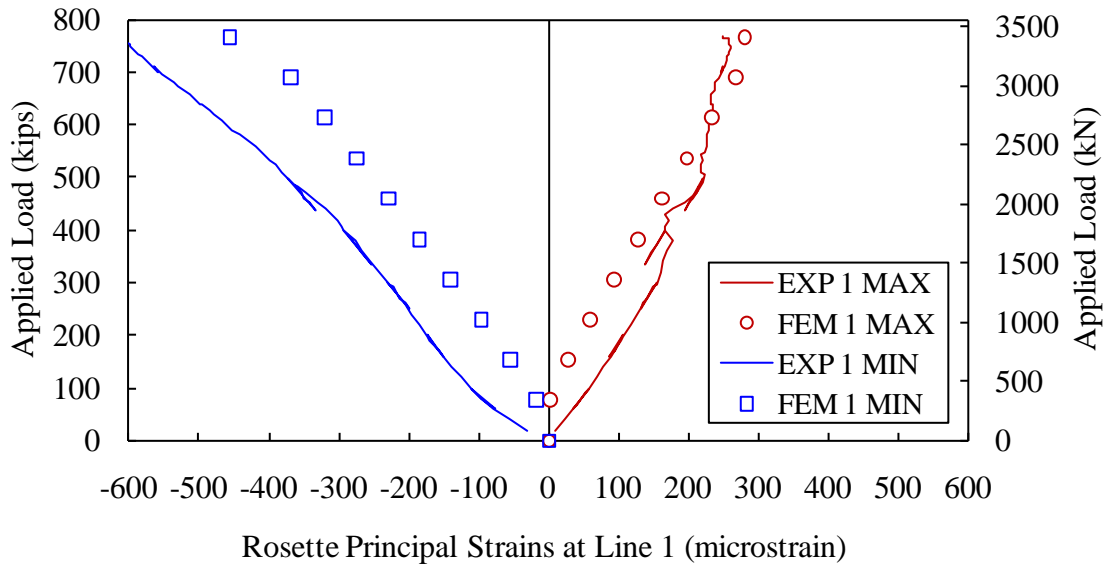


Figure 107. Graph. Predicted versus observed principal strains on the side face of the girder 14S along Instrumentation Line 1.

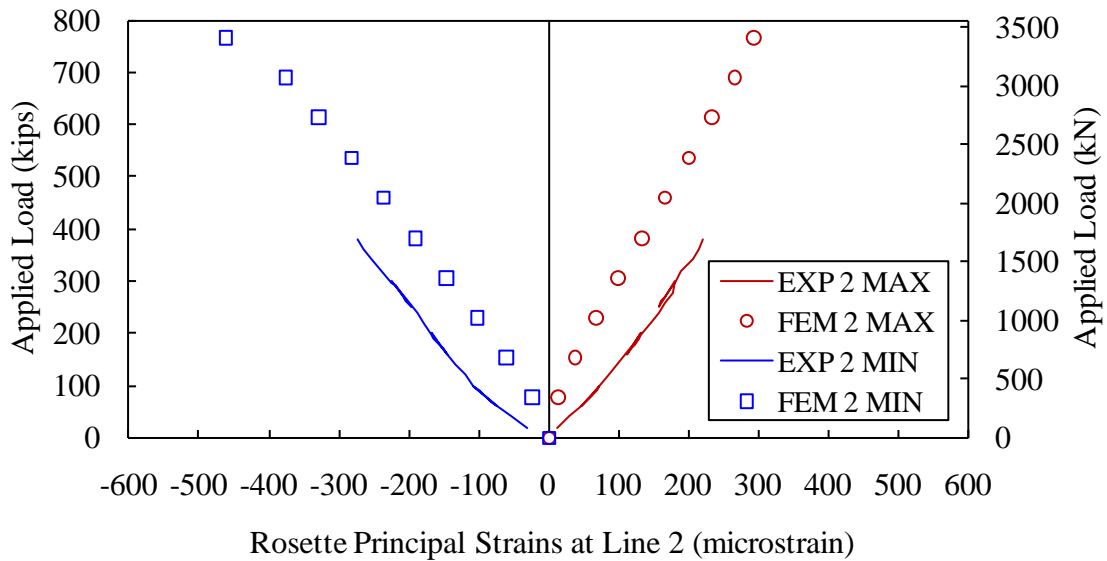


Figure 108. Graph. Predicted versus observed principal strains on the side face of the girder 14S along Instrumentation Line 2.

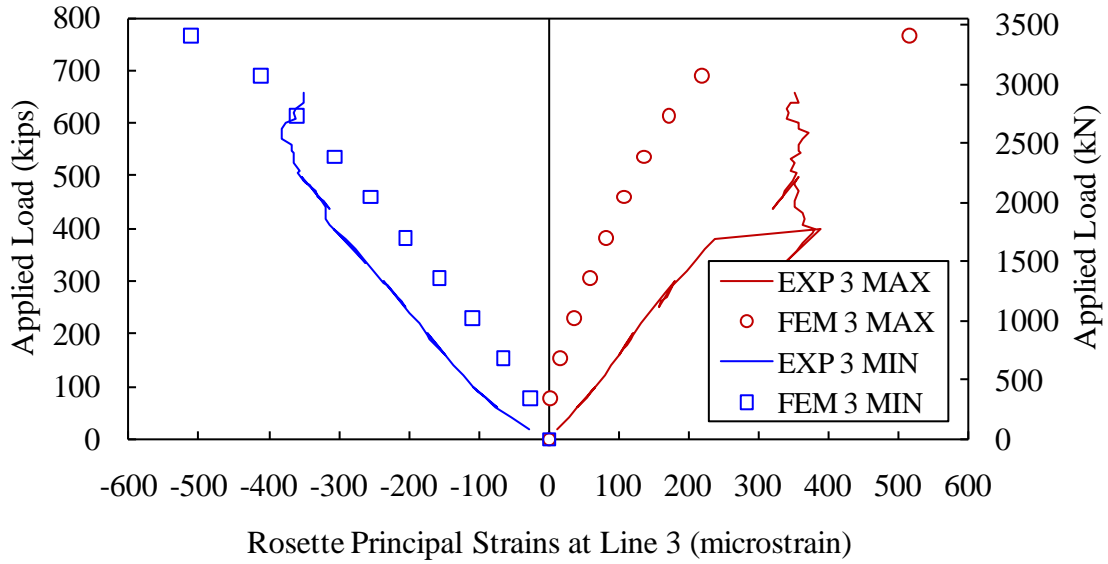


Figure 109. Graph. Predicted versus observed principal strains on the side face of the girder 14S along Instrumentation Line 3.

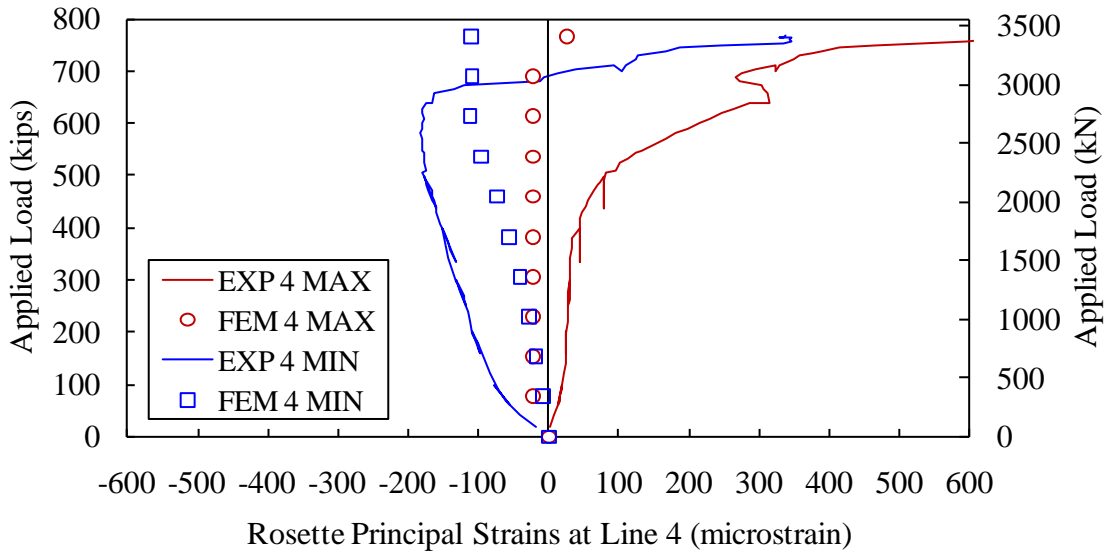


Figure 110. Graph. Predicted versus observed principal strains on the side face of the girder 14S along Instrumentation Line 4.

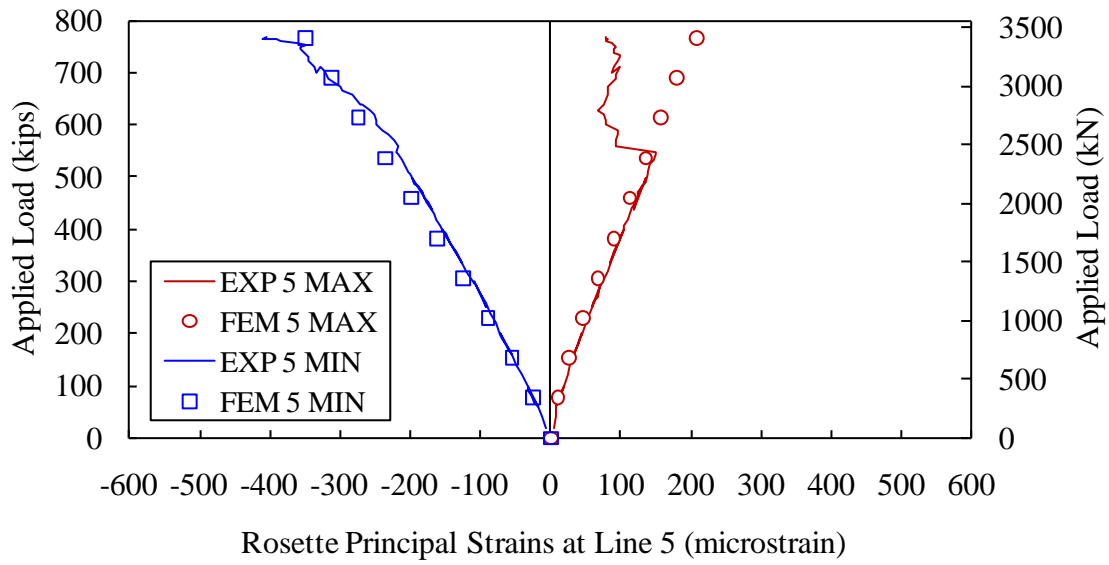


Figure 111. Graph Predicted versus observed principal strains on the side face of the girder 14S along Instrumentation Line 5.

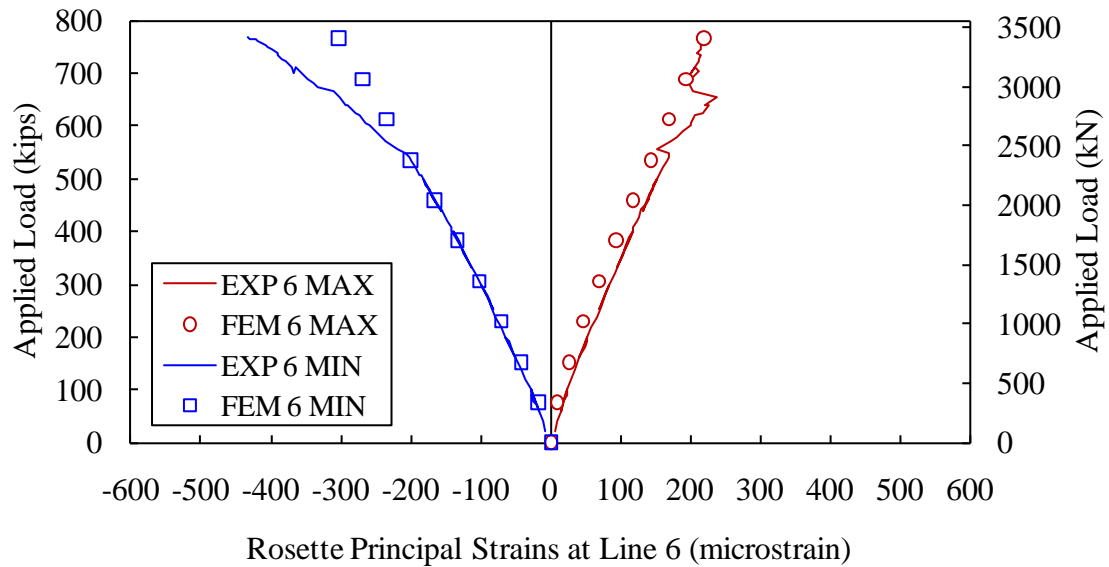


Figure 112. Graph. Predicted versus observed principal strains on the side face of the girder 14S along Instrumentation Line 6.

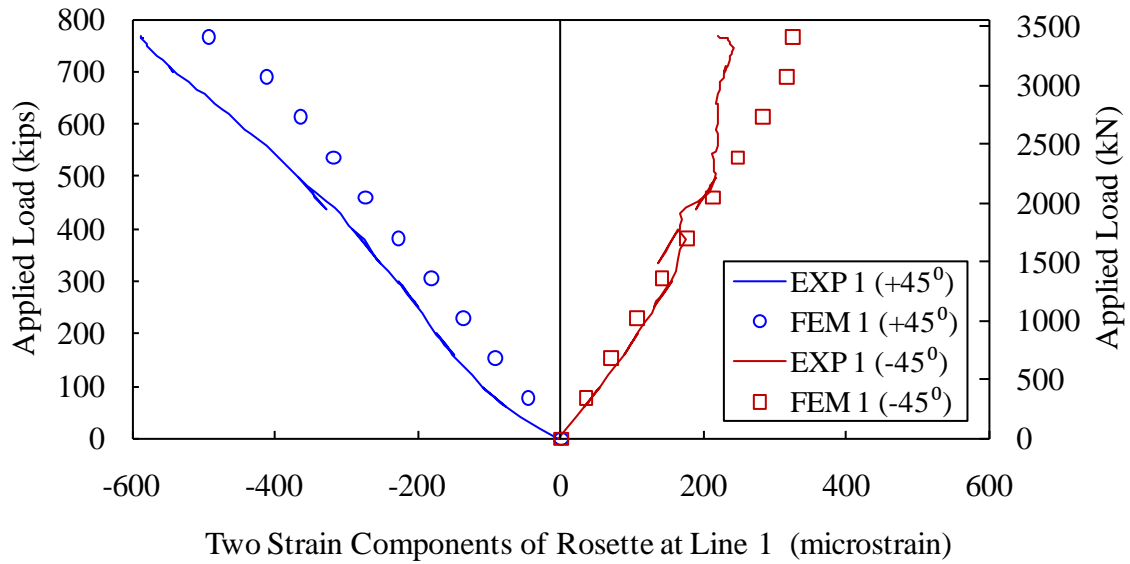


Figure 113. Graph. Predicted versus observed strain components from rosette strain gage at Instrumentation Line 1.

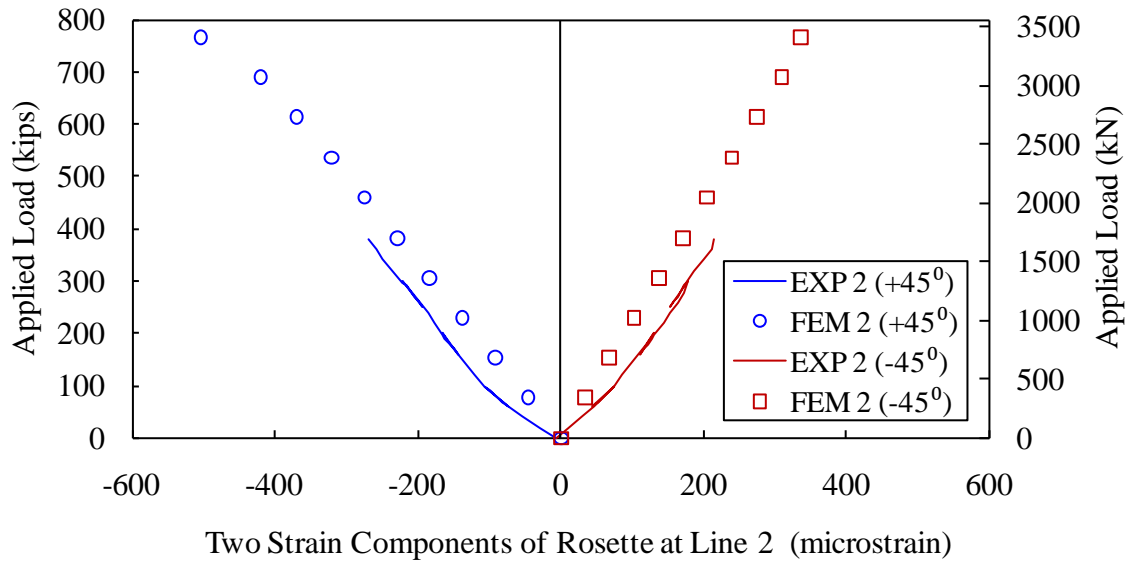


Figure 114. Graph. Predicted versus observed strain components from rosette strain gage at Instrumentation Line 2.

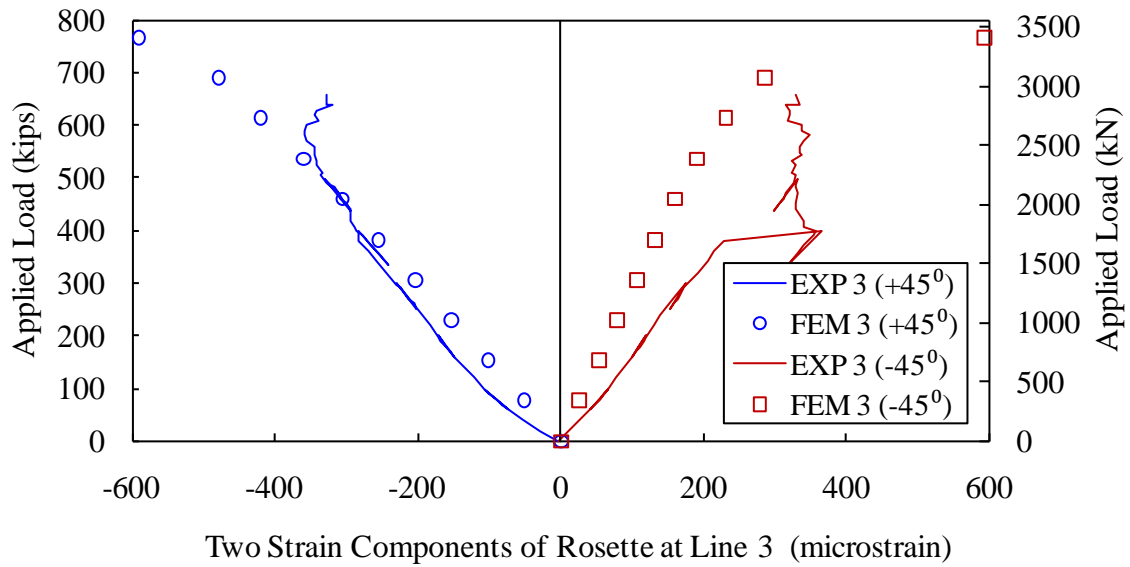


Figure 115. Graph. Predicted versus observed strain components from rosette strain gage at Instrumentation Line 3.

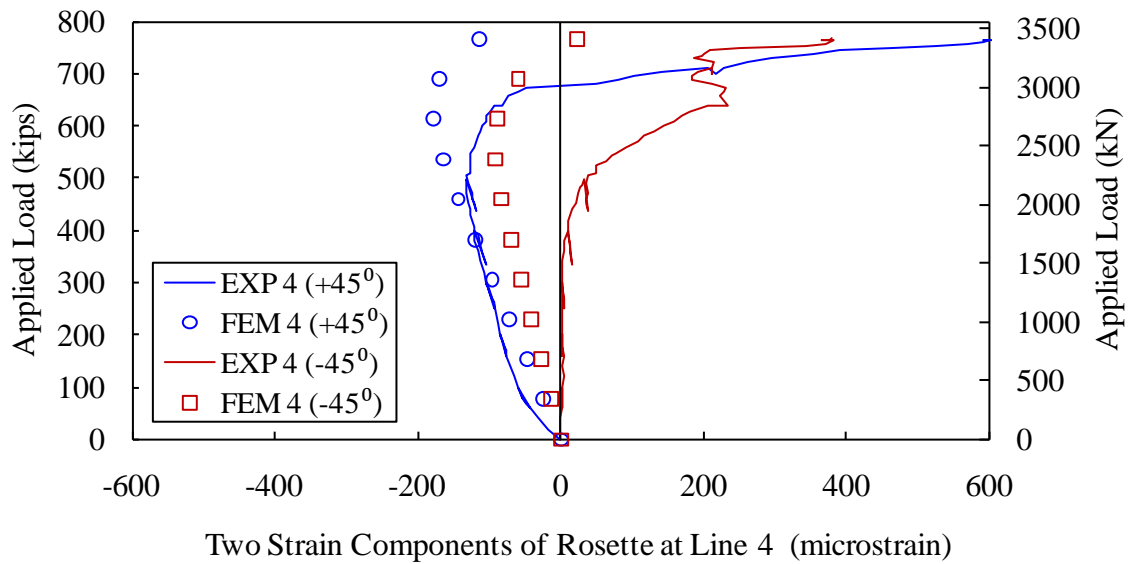


Figure 116. Graph. Predicted versus observed strain components from rosette strain gage at Instrumentation Line 4.

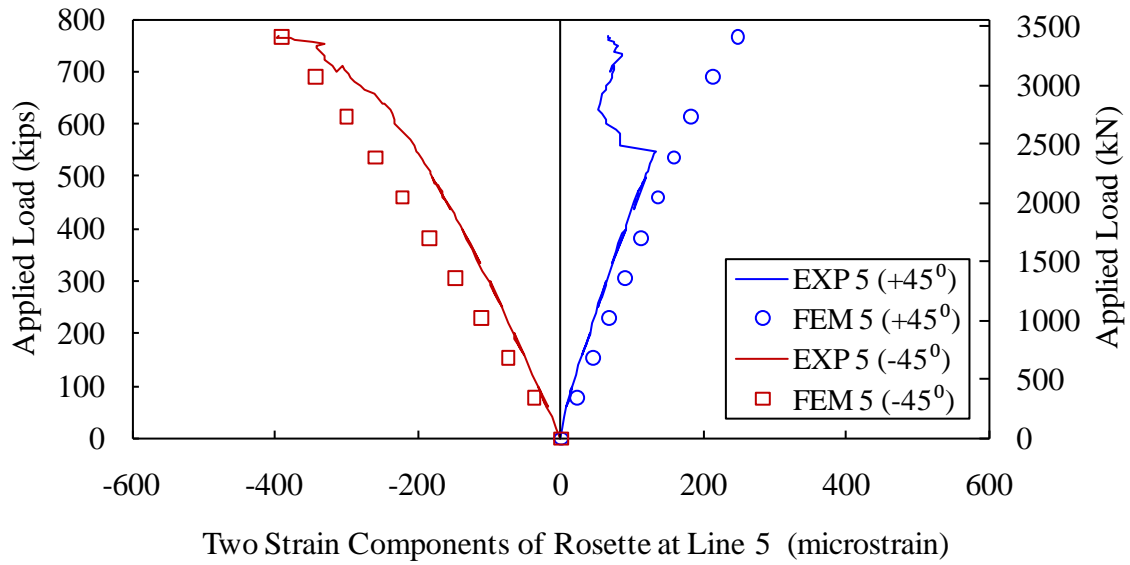


Figure 117. Graph. Predicted versus observed strain components from rosette strain gage at Instrumentation Line 5.

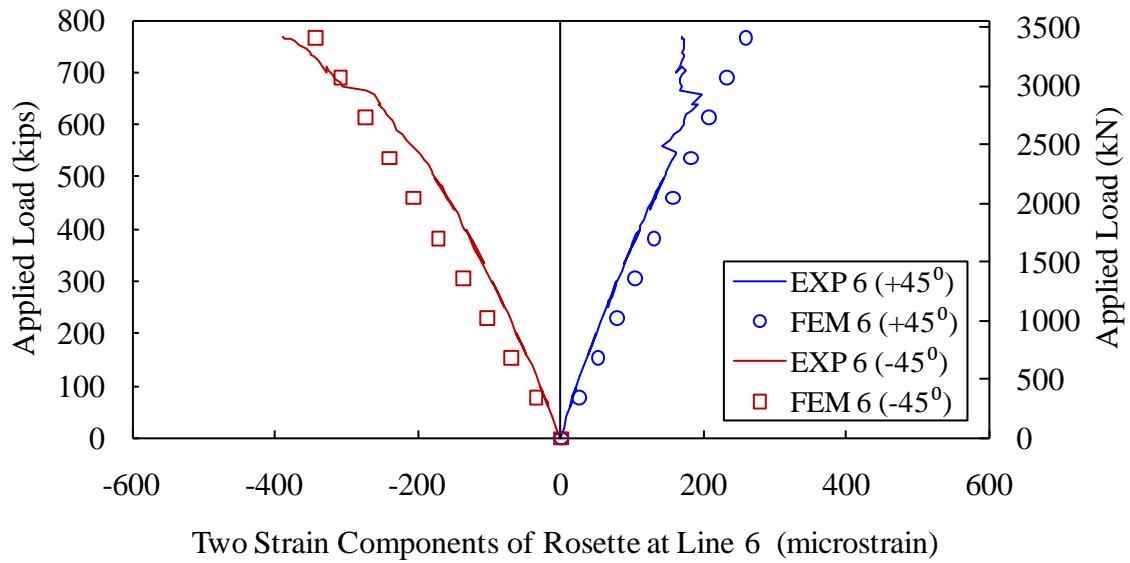


Figure 118. Graph. Predicted versus observed strain components from rosette strain gage at Instrumentation Line 6.

CONCLUSIONS

Based on the modeling results compared to the experimentally observed shear response of the UHPC I-girders 24S and 14S, the following conclusions are presented.

1. The damaged plasticity model with proposed material properties listed in Table 2 replicates the observed deflection and strain responses of both I-girders fairly well. The CDP material model is tested to be consistent for the same girder with different spans under both flexural and shear tests.
2. Both girders appeared to experience certain uniform vertical rigid body movement which increases linearly with respect to the applied load. The movement is possibly caused by elastic deformation of supporting systems. The good agreement on vertical displacements is achieved by subtracting the uniform vertical rigid body movement from the experimental vertical deflection results. The longitudinal strains and the three rosette strain components in various locations also have fairly good agreement between the experimental and finite element results if the effect of seating is considered.
3. The effect of prestressing strands' slippage in Test 14S was observed as a nonlinear difference between the experimental and finite element vertical deflection results when the applied load was above 540 kips (2402 kN).

CHAPTER 6. PI-GIRDER

FINITE ELEMENT MODEL

Unlike the I-girder previously discussed which primarily experienced simple beam-type responses, the 2nd generation pi-girder was subjected to loadings which induced a more complex response including transverse flexure in the deck and longitudinal flexure in the bulbs and webs. A three dimensional pi-girder model as seen in Figure 119 was developed in order to calibrate its UHPC properties and simulate both linear and nonlinear behaviors of the pi-girder.

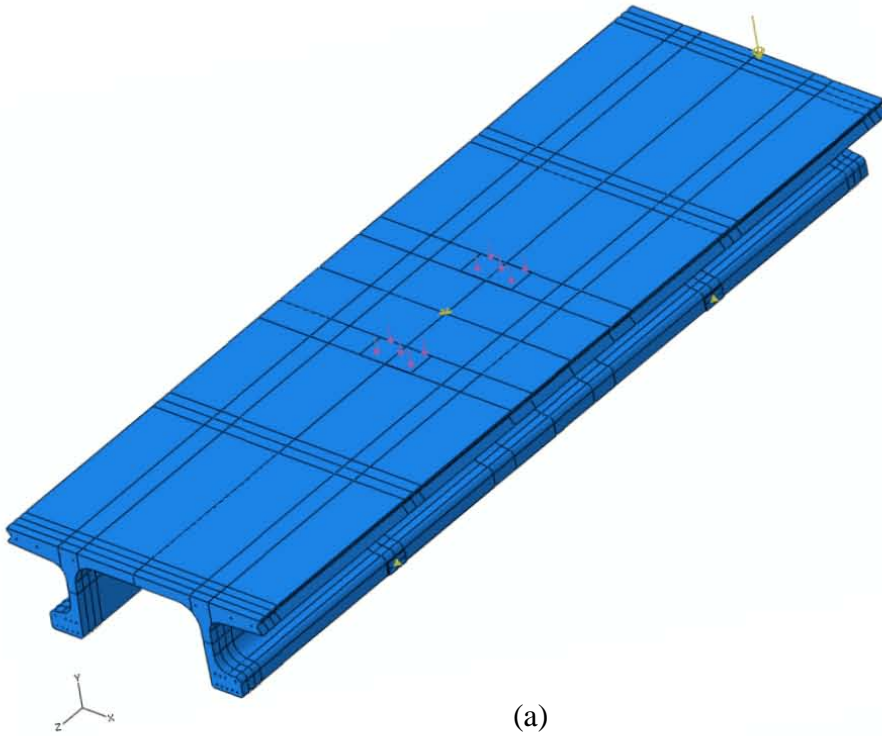
This modeling effort focused on Test T2D. Figure 119(a) covers the whole model. The girder was partitioned to facilitate the definitions of the loading surface, diaphragms, and supports. Loading surfaces which were tied to the adjacent concrete surface were provided to mimic the elastomeric pads used in the physical tests. To simulate the diaphragms, which included steel tubes, end plates, and threaded rods, four end plates were tied to the underlying concrete and linked via wire-style nonlinear springs. Figure 119(b) presents the strands and rebars embedded in the pi-girder which cannot be clearly identified in Figure 119(a). The pi-girder was supported vertically by linear springs located at the support points. Linear springs of negligible stiffness in transverse x-direction and longitudinal y-direction were provided only to eliminate large rigid body movement. The horizontal restraint provided by the supporting elastomeric pads on the girder bulbs was assumed to be trivial.

Loading surfaces were modeled in 4-node quadrilateral surface element and did not have any associated material property. The steel plates at the diaphragm locations were modeled in 3D continuum shell element SC8R. For strands and concrete, continuous solid element with reduced integration C3D8R was used. Figure 120 illustrates the mesh with 2-inch (50.8-mm) global seeds. The deck and webs were partitioned to have four layers through their thickness, as these portions of the pi-girder in this experimental setup were subjected to significant bending forces.

The stress-strain curve for 270 ksi (1862 MPa) strand is already shown in Figure 31. In the pi-girder, eighteen strands in the bulbs and four strands in the deck were prestressed to magnitudes of 175.8 ksi (1212 MPa) and 20.7 ksi (143 MPa), respectively in the longitudinal z-direction. In order to reduce mesh density in the modeled strands, a square of equivalent steel area 0.22 in^2 (142 mm^2) replaces the original circle bundle as depicted in Figure 33.

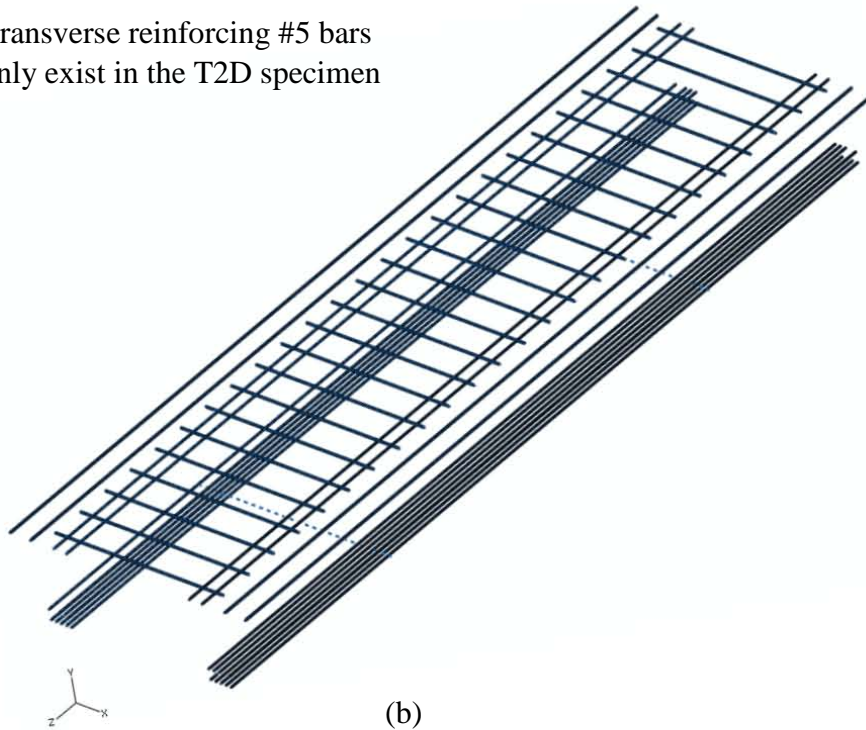
CONSTITUTIVE MODELS FOR UHPC

UHPC material assumptions regarding the density, elasticity, compression hardening, tension stiffening, and other CDP and CSC parameters are listed in Table 4. The boldfaced values have been revised from the values previously used in the I-girder model. Young's modulus is assumed to 7650 ksi (53 GPa) in accordance with the tests on steam-treated cylinders from reference (21). The maximum tensile stress in the concrete tension stiffening is assumed to be 1.4 ksi (9.7 MPa). Failure ratio 2 in the CSC model is correspondingly revised to 0.0509. Other parameters stay the same as those for the I-girder. The changes in the constitutive model for UHPC may reflect, among other things, that the I-girder and pi-girders were fabricated 8 years apart and would thus have included slightly different constituent materials along with different overall curing conditions.



(a)

Transverse reinforcing #5 bars
only exist in the T2D specimen



(b)

Figure 119. Illustration. (a) Full pi-girder model, and (b) hidden rebar and strands embedded in UHPC.

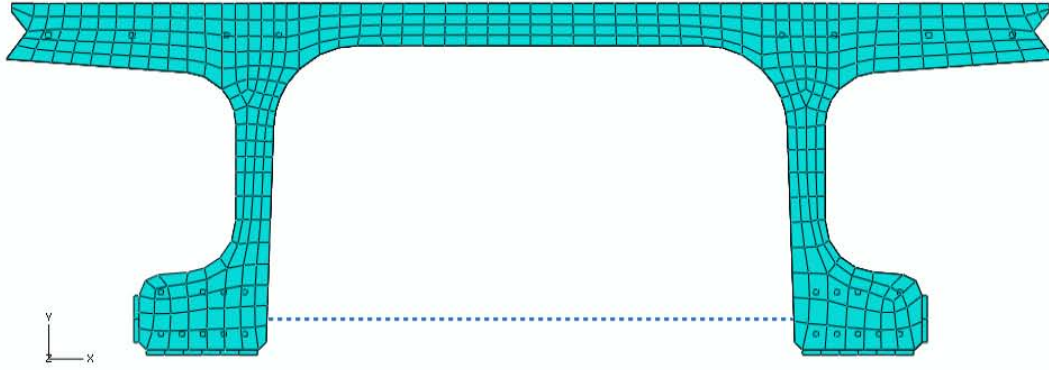


Figure 120. Illustration. Pi-girder model with a 2-inch (51-mm) seeded mesh.

Table 4. Material parameters for the CSC & CDP models of the UHPC used in the pi-girder tests.

Density, lb/ft ³ (kg/m ³)	160 (2565)	
Concrete elasticity		
E, ksi (GPa)	7650 (53)	
ν	0.18	
Concrete compression hardening		
Compressive stress, ksi (MPa)	Plastic strain (-)	
14.0 (96.5)	0.0000000	
16.0 (110.3)	0.0000284	
20.0 (137.9)	0.0000720	
24.0 (165.5)	0.0001410	
27.5 (189.6)	0.0004140	
Concrete tension stiffening		
Maximum tensile stress ksi (MPa)	Plastic strain (+)	
1.4 (9.7)	0.000	
1.4 (9.7)	0.010	
0.0 (0.0)	0.011	
The parameters of CDP model		
Dilation angle	15°	
Eccentricity	0.1	
fb0/fc0	1.16	
K	2/3	
Viscosity parameter	0	
The parameters of CSC model		
	Ratio 1	1.16
Failure ratio	Ratio 2	0.0509
	Ratio 3	1.28
	Ratio 4	1/3
	Rho_close	1
Shear retention	Eps_max	0.1

DIAPHRAGMS

The diaphragms were modeled as nonlinear springs. The properties of these springs were estimated from the combination of two experimentally observed parameters, namely, the spreading between the bulbs at midspan and the tensile force in the diaphragms. It is assumed that the nonlinear response of the springs located 6.33 ft (1.93 m) from midspan should have similar profile to the observed midspan spreading, but should differ slightly in magnitude. The tension tie provided by the diaphragms was modeled in this way as the full modeling of diaphragm components not only would require significant additional computational resource but also may not be able to capture the actual experienced mechanical behavior of the diaphragms during the whole loading process. In Test T2D, the diaphragm end plates contributed to the majority of the diaphragm elongation through prying of end plates and cracking of welds between the tube and the end plates. Figure 121 shows the discussed diaphragm behavior as was observed during peak load application in Test T2D. Table 5 lists the properties of the assumed nonlinear spring which was used to approximate the diaphragms in the pi-girder. It is also plotted in Figure 122. In the same figure, both separate and combined contributions from the HSS5×5×1/4 tube and the two 7/8-inch diameter high strength threaded rods at each end are plotted. The prying of the end plates begins at low load levels and plays an increasingly significant role in diaphragm elongation. The finite element model which was used to replicate the pi-girder response engaged this nonlinear spring up through a tensile force of 32 kips (142 kN).

The nonlinear springs were connected to the steel plates which were situated outside of the pi-girder's bulbs, as illustrated in Figure 120.



Figure 121. Photo. Prying of end plates at peak applied load in Test T2D.

Table 5. Properties of the nonlinear springs which replicate the diaphragms in the pi-girder tests.

Axial Force, kip (kN)	Axial Elongation, inch (mm)
-9 (-40)	-0.035 (-0.89)
0 (0)	0.000 (0.00)
9 (40)	0.035 (0.89)
16 (71)	0.072 (1.83)
20 (89)	0.110 (2.79)
23 (102)	0.150 (3.81)
26 (116)	0.200 (5.08)
29 (129)	0.280 (7.11)
32 (142)	0.380 (9.65)
35 (156)	0.550 (13.97)

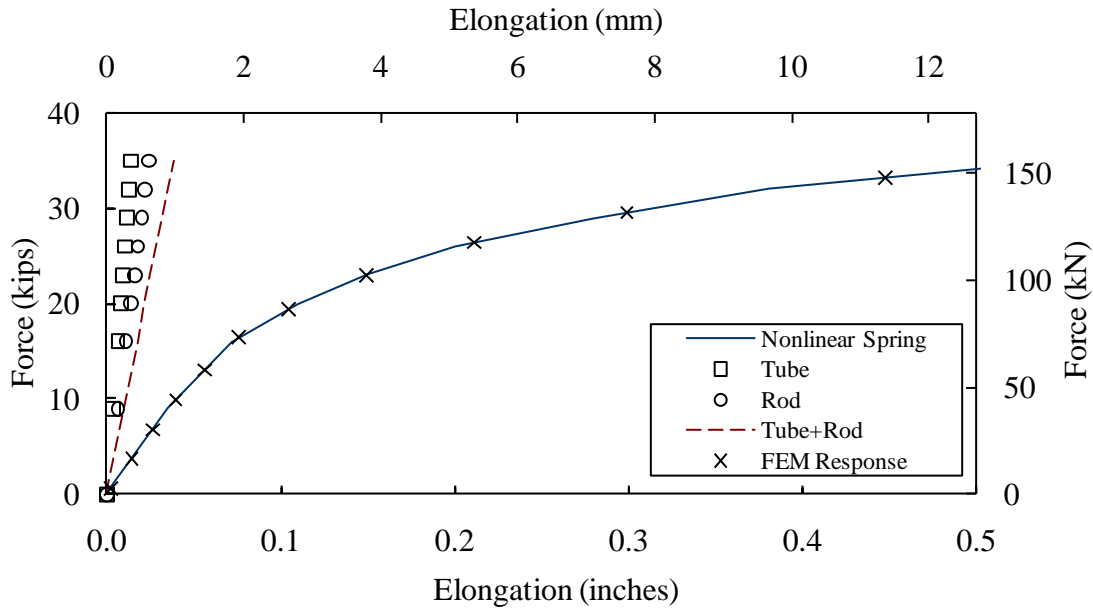


Figure 122. Graph. Behaviors of diaphragm subcomponents and assumed nonlinear spring for the diaphragms in the pi-girder T2D.

ELASTOMERIC PADS

The pi-girder T2D was supported on 6-inch by 12-inch (0.15-m by 0.3-m) elastomeric pads placed under the girder bulbs at the four support locations. These elastomeric pads were 1-inch (25-mm) thick. In order to avoid the complex hyperelastic modeling of these pads, a linear spring whose properties were estimated from the experimental measurements was used to simulate the support in the vertical direction. In Figure 123, an applied force of 338.7 kips (1507 kN) deformed the pad 0.115 inch (2.9 mm) vertically, which means that the linear spring stiffness K

= $338.7/4/0.115 = 736$ kip/inch (129 kN/mm). When the stiffness K is used in a finite element model, the response of the linear spring follows the dashed line shown in Figure 123. This assumption of the linear spring behavior results in a FEM model which replicates the experimental data at the start and the end. However, a difference between the FEM model with $K = 736$ kip/inch (129 kN/mm) and the experimental measurement during the loading is observed. This difference was addressed by adding the difference into vertical displacement component based on the assumption that four pads deformed in the same magnitude and this difference only affected the rigid body movement of the pi-girder. Therefore, the modified FEM result for the vertical deformation of the pad which supports the girder can be always fitted to the experiment as shown in Figure 123.

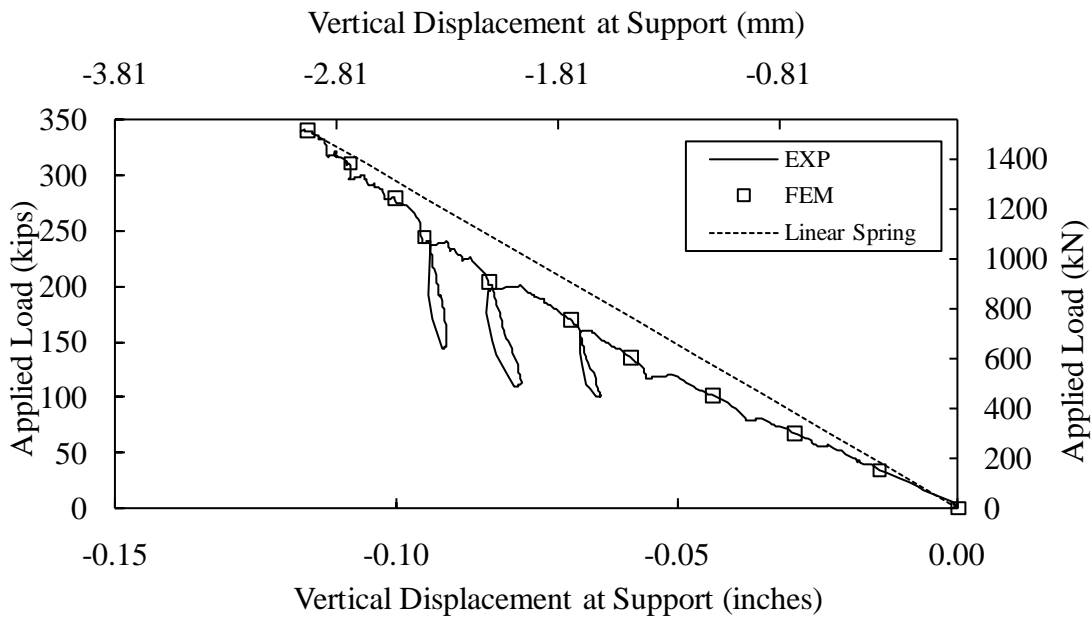


Figure 123. Graph. Vertical deformation of an elastomeric pad support in the experiment and its approximation using a linear spring.

ABAQUS RESULTS

The following results are based on the CDP model using the UHPC material parameters in Table 4. Its mesh is illustrated in Figure 120.

Figure 124 and Figure 125 provide the comparison between the FEM and experimentally observed vertical deflections of the bulbs at midspan and of the deck at midspan middeck position, respectively. As opposed to the midspan middeck vertical deflection which represents deformation due to both global longitudinal bending of the girder and local transverse bending of the deck, the midspan vertical deflection of the bulbs is primarily representative of the global longitudinal flexure of the girder. The vertical deflection response of the bulbs is fairly linear. The apparent stiffening of the vertical deflection of the bulbs in the experiment and difference

between the FEM and experimental results may be related to the following potential causes. First, it is likely that the nonlinear deformation of elastomeric pads has not been entirely compensated through the method previously described. Second, an experimentally observed difference between the deflection of the north and south bulbs exists and exceeds the difference between the FEM and experimental results for the south bulb. As such, the FEM assumption of perfect symmetry along the girder centerline may not accurately reflect the actual behavior observed in the progress of the test. Third, the lateral spreading of the bulbs at increasing loads can be perceived through the vertical deflections measured via linear string potentiometers as an apparent stiffening of the girder response.

The vertical deflection response at the middeck midspan location in Figure 125 displays an increasing difference between the FEM and experimental results. Similar causes as mentioned above could relate again here to this deflection results. Additionally, the difference in response may be attributed to potentially different tensile responses being exhibited by the UHPC in the deck and in the bulbs. The tensile response of the deck may be different from the bulbs due to the casting process. Preferential fiber alignment toward the direction of casting flow may show benefits in beam components and detriments in transversely loaded plate components (reference (22)). Stiffness reduction in the middeck may be one of the factors too.

Vertical deflections were also measured at the quarterspan location in the deck and bulbs. As with the midspan results, the FEM result again predicts the increased stiffness as compared to the experimentally observed result.

Figure 126 and Figure 127 illustrate the diaphragm force and the bulb lateral spreading at midspan, respectively. The properties of the nonlinear springs listed in Table 5 were calibrated through the use of the experimental measurements contained within these two figures. As would be expected, agreement between FEM and experimental results are observed during nearly all of the loading process. The abrupt reduction in diaphragm load carrying capacity at an applied load of approximately 300 kips (1334 kN) was likely the result of the initiation of a local diaphragm subcomponent failure. The proposed spring model for the diaphragms was not intended to capture this kind of the behavior.

Figure 128 depicts the lateral spreading of the bulbs at the support location. Experimentally, this value was captured by measuring the outward movement of one bulb at one support location. A similar method was used to capture the FEM result. Given that the FEM model predicts symmetrical behavior of the girder while the experiment setup may not have ensured perfectly symmetrical behavior, the difference between the FEM and experimental results are not considered to be significant.

Figure 129 and Figure 130 show the longitudinal strains at midspan on the bottom of the north bulb and on the deck immediately above the north web, respectively. These portions of girder concrete primarily experienced longitudinal flexural deformation and as such excellent agreement was obtained between the FEM and experimental results. It should be noted that the

strain is fairly linear in both tensile and compressive regions. Additionally, the concurrence of results lends support to the chosen Young's modulus of 7650 ksi (53 GPa) for the UHPC.

Figure 131 illustrates the transverse strains on the top and bottom surfaces of the deck at the midspan middeck location. When an applied load is below 60 kips (267 kN), the FEM and experimental results are consistent. The abrupt change in the response observed experimentally below the deck combined with other observations during the test, indicate that local longitudinal cracking of the deck disrupted the ability of the gage to accurately measure the response in this location. This cracking likely also affected the compressive strain observed immediately above this location on top of the deck.

Figure 132 provides contour plots of the predicted maximum principal stress on the surface of the girder as viewed from above, below, and beside the girder. The gray areas indicate locations where maximum principal stress approaches or exceeds the defined maximum uniaxial tensile strength of 1.4 ksi (9.7 MPa) for the concrete. The limit of the color bar is deliberately set at 1.35 ksi (9.3 MPa) to highlight areas experiencing tensile stress states approaching or exceeding the uniaxial tensile strength. Figure 132(a) primarily illustrates the areas on top of the deck expressing the tensile response equal or close to the uniaxial tensile strength due to negative moments induced as a result of the diaphragm resistance to lateral leg spreading. This response is consistent with the experimentally observed cracking as presented in reference (14). Figure 132(b) shows that the maximum principal stress reaches the maximum tensile stress on most of the underside deck, a result which is consistent with the underside deck cracking map which seems consistent with underside deck cracking map reproduced from reference (14) in Figure 133. From the side view in Figure 132(c), some portions of the web and outside bulb surface near midspan also express inelastic tensile behavior, again consistent with the experimental observation.

Figure 134 shows the contour plots of predicted minimum principal stress as viewed from above, below, and beside the girder. The maximum compressive stress of approximately 14.3 ksi (99 MPa) is observed to occur immediately under the loading pads and is significantly below the ultimate compressive stress. Outside of the loading and support application areas, the maximum compressive stress of approximately 8 ksi (55 MPa) was induced due to the negative moment on the loading cross section at the junctions of the underside of the deck and the interior surfaces of the webs.

Figure 135 shows the contour plots of the model predicted maximum principal plastic strain from above, below, and beside the girder. The elastic strain response is shown as light gray in the contour plots. The tensile plastic strain response from low to high values is scaled in a color bar from blue to red. Although the exact contour boundaries may be affected by mesh dependence and a random trivial graphic plastic threshold (0.000001 as specified here), the general inelastic areas are well predicted. The yield surface separates the inelastic response from elastic one under various stress states. A material can yield with a principal stress in biaxial or triaxial stress states less than the uniaxial tensile strength limit, i.e., 1.4 ksi (9.7 ksi) for the UHPC in the girder.

Therefore, a maximum principal plastic strain contour can predict the inelastic response areas more accurately than a maximum principal stress one, as here Figure 135 shows slightly larger and more inelastic response areas than the maximum principal stress predictions in Figure 132. Figure 135 also illustrates the degree of inelastic response. The underside of the deck under the loading patches experienced the highest inelastic response with a value of approximately 0.01. The top of the deck near the loading pads, most of underside of the deck, and some exterior portions of bulbs and webs near midspan shown in blue exhibited inelastic deformation under the ultimate load of 340 kips (1512 kN). Additional inelastic response can be observed from the bulb ends where the strands anchored and the bulb sections where the two diaphragms were installed.

Additional figures were provided to present the FEM prediction of maximum principal stress and plastic strain contour plots at two girder cross sections, namely, at midspan and at the center of a loading patch. The maximum principal stress is shown in Figure 136 while the maximum principal plastic strain is shown in Figure 137. Undeformed sectional profiles are illustrated with a dashed line, while deformed shapes are amplified by a scale of five. The deformed shape at the center of the loading patch is similar to the one at midspan, including legs spreading and deck bending. The maximum principal stress reaches the maximum tensile stress in a small area near the bottom face of the bulbs at midspan, consistent with longitudinal bending, as shown in both Figure 136(a) and Figure 137(a). Most portions of bulbs remain elastic under the ultimate applied load, and given the tensile strain capacity of the UHPC, there is still additional potential to resist additional longitudinal bending moment. The deck between two legs experiences widespread inelastic behavior consistent with the cracking observed. The underside of the deck directly under loading pads reach the assumed ultimate plastic strain 0.01 as shown in Figure 137(b). The inelastic response is consistent with the crack pattern observed in the experiment and presented in Figure 133. Negative moment generated by the transverse bending on the deck also caused normal stress to reach the maximum tensile stress on the top surface of the deck above girder webs as is seen in Figure 136(b) and Figure 137(b), and again consistent with the experimental result detailed in reference (14). Figure 137 also demonstrates that the exterior face of the webs experience inelastic deformation as a result of negative moments generated by the applied load.

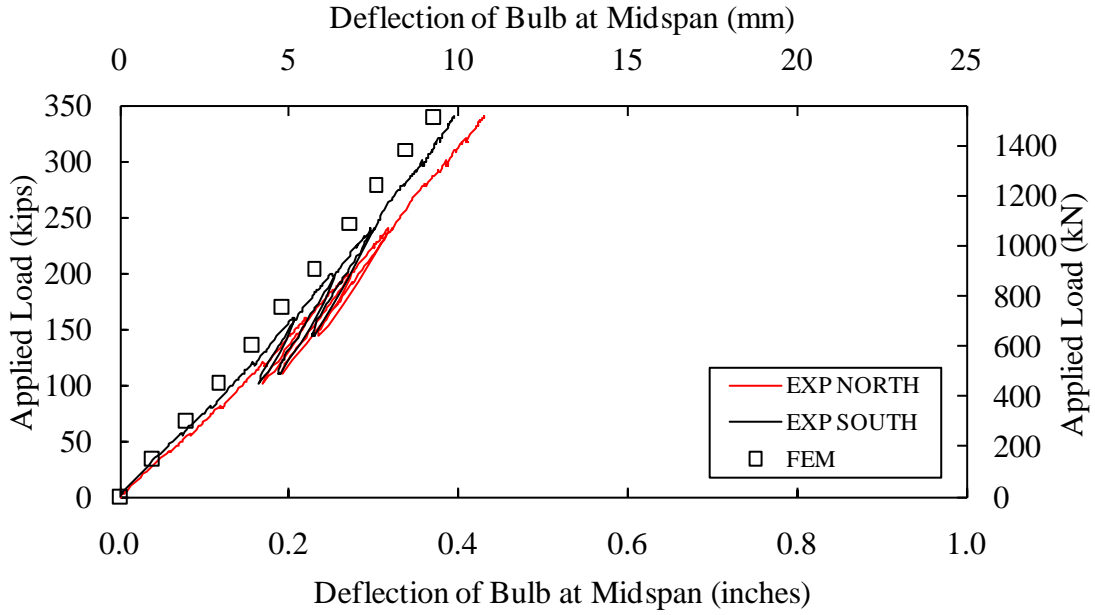


Figure 124. Graph. FEM vs. experimentally observed vertical deflection of the bulbs at midspan.

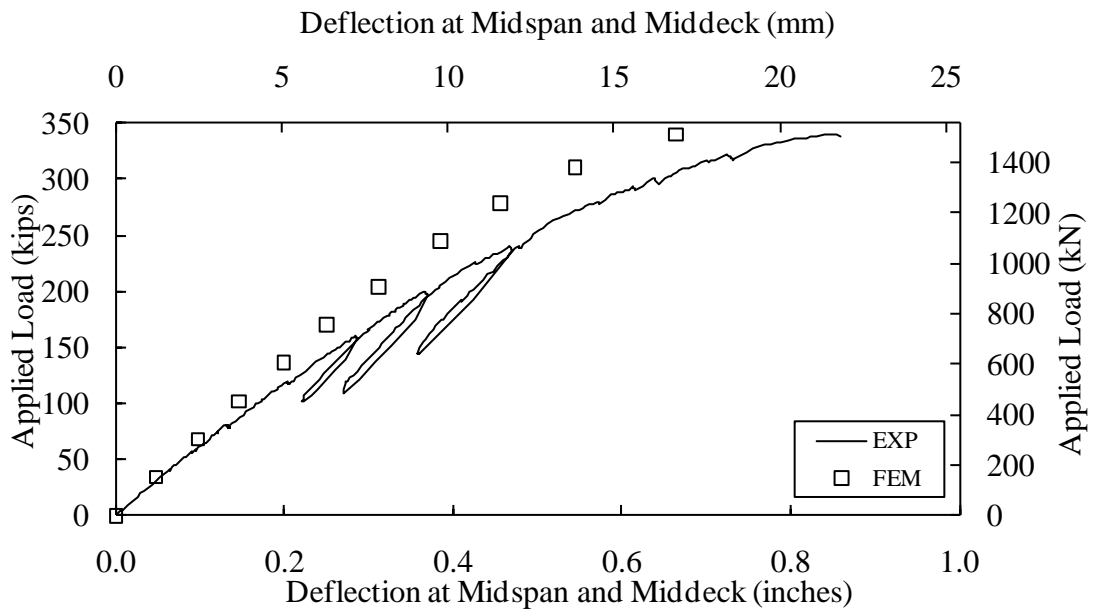


Figure 125. Graph. FEM vs. experimentally observed vertical deflection at the midspan middeck position.

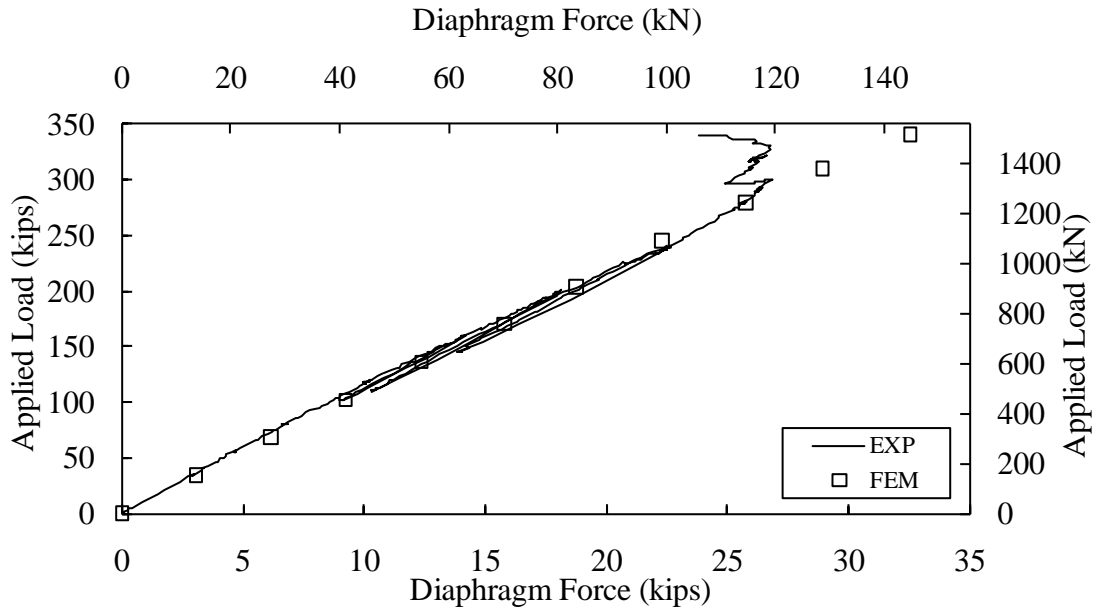


Figure 126. Graph. FEM vs. experimentally observed diaphragm force.

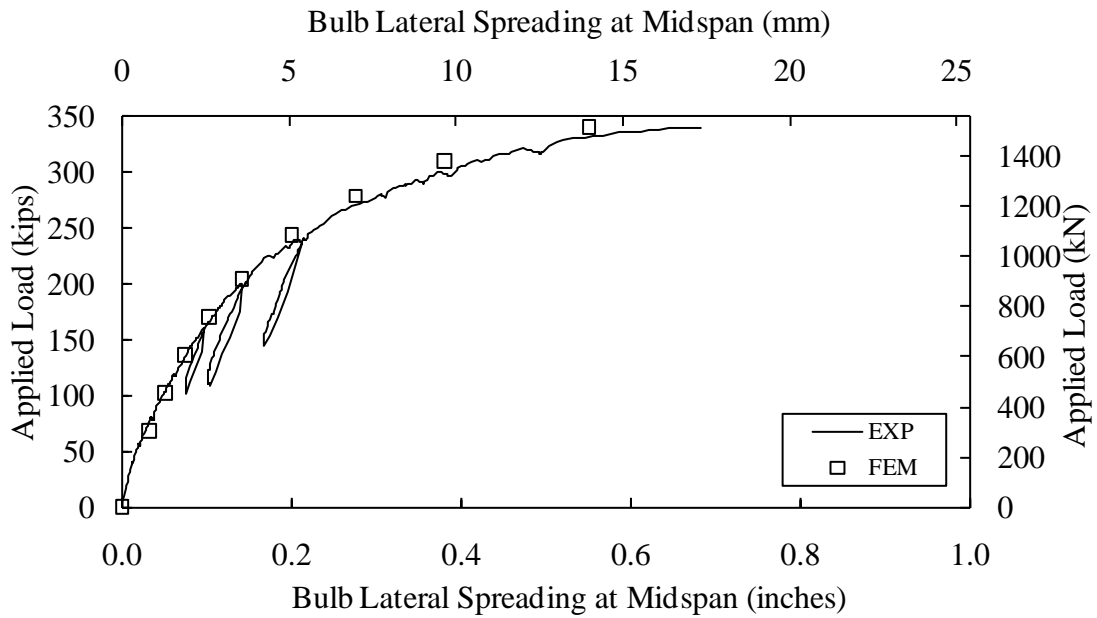


Figure 127. FEM vs. experimentally observed bulb lateral spreading at midspan.

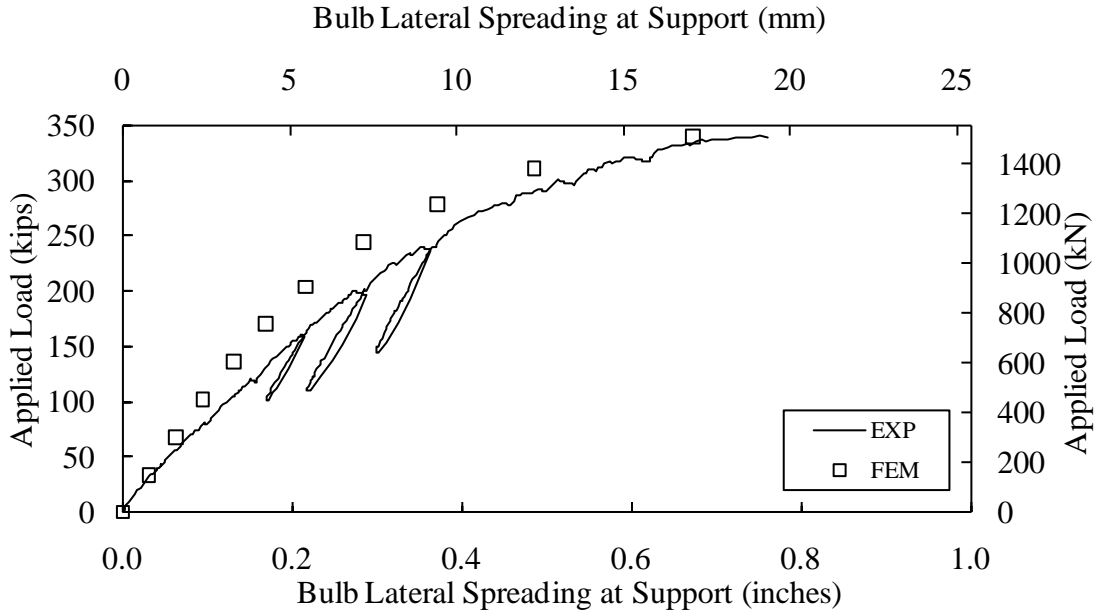


Figure 128. FEM vs. experimentally observed bulb lateral spreading at support.

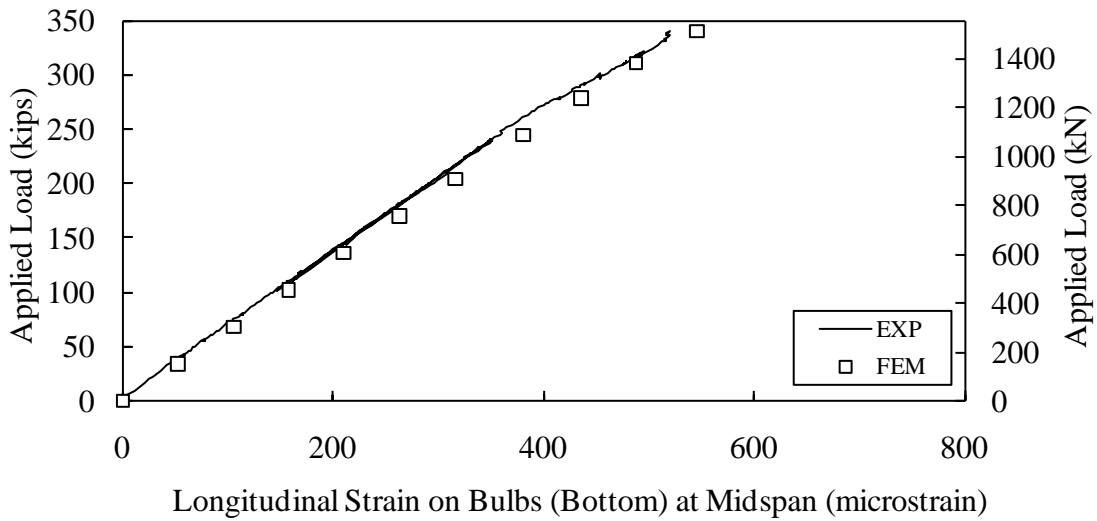


Figure 129. FEM vs. experimentally observed longitudinal strain on the bottom surface of the north bulb at midspan.

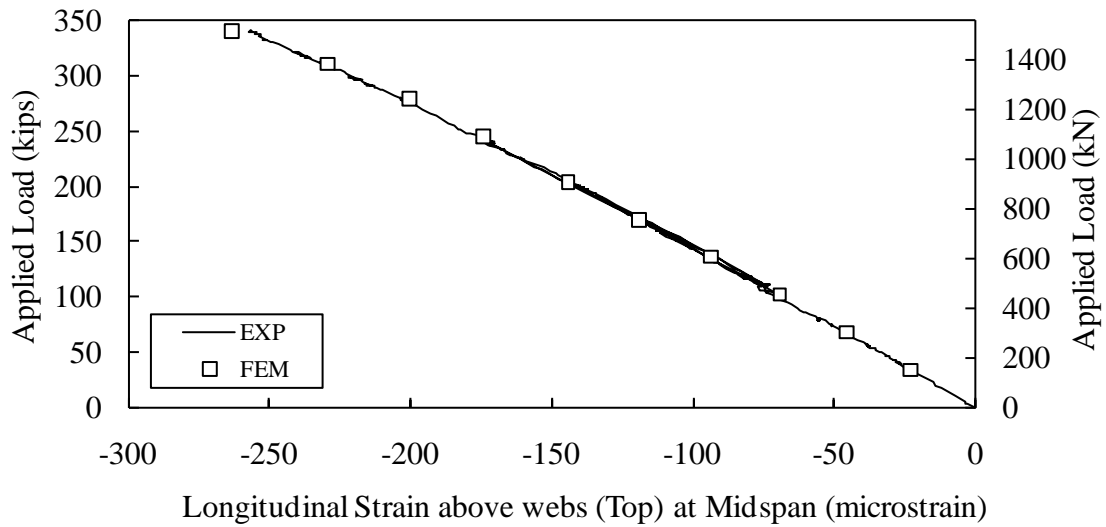


Figure 130. Graph. FEM vs. experimentally observed longitudinal strain on the deck immediately above the north web at midspan.

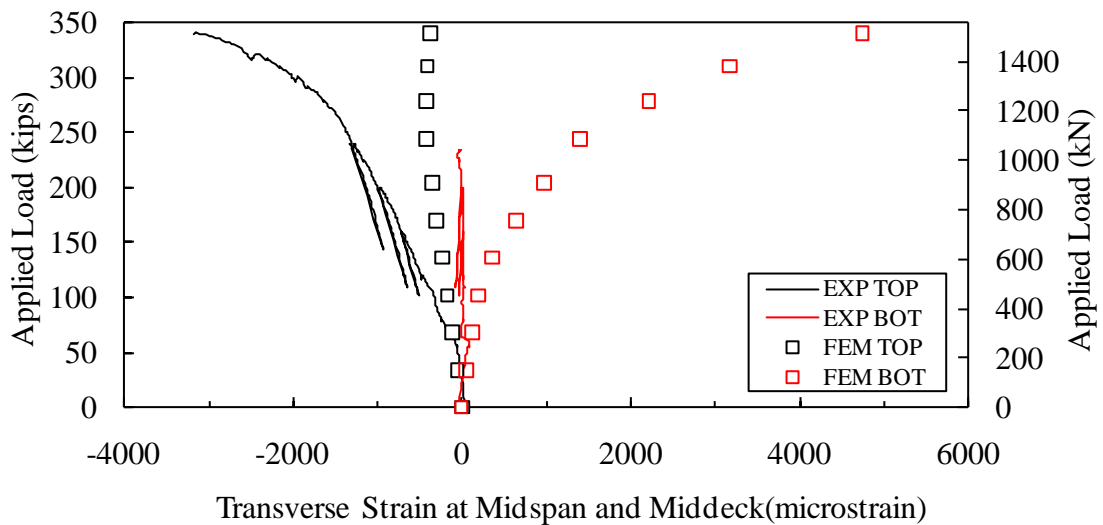
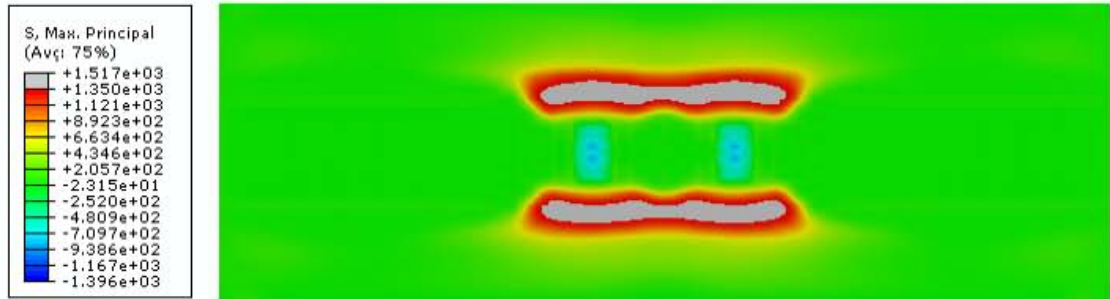
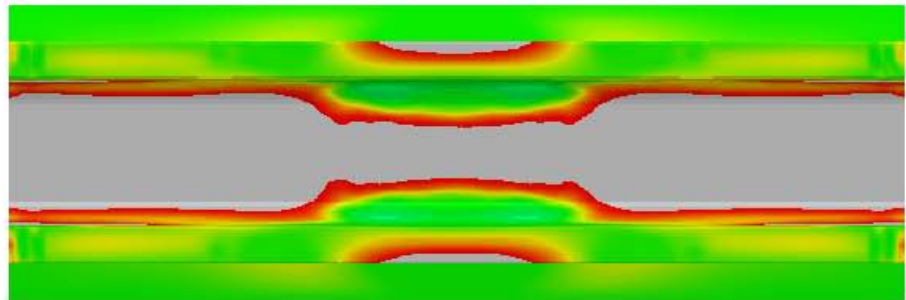


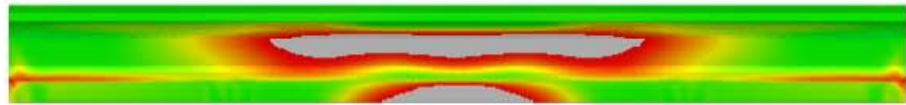
Figure 131. Graph. FEM vs. experimentally observed transverse strains on the top and bottom surfaces of the deck at the midspan middeck location.



(a)



(b)



(c)

Figure 132. Graph. FEM predicted maximum principal stress on the surface of the girder as viewed from (a) above, (b) below, and (c) beside the girder.

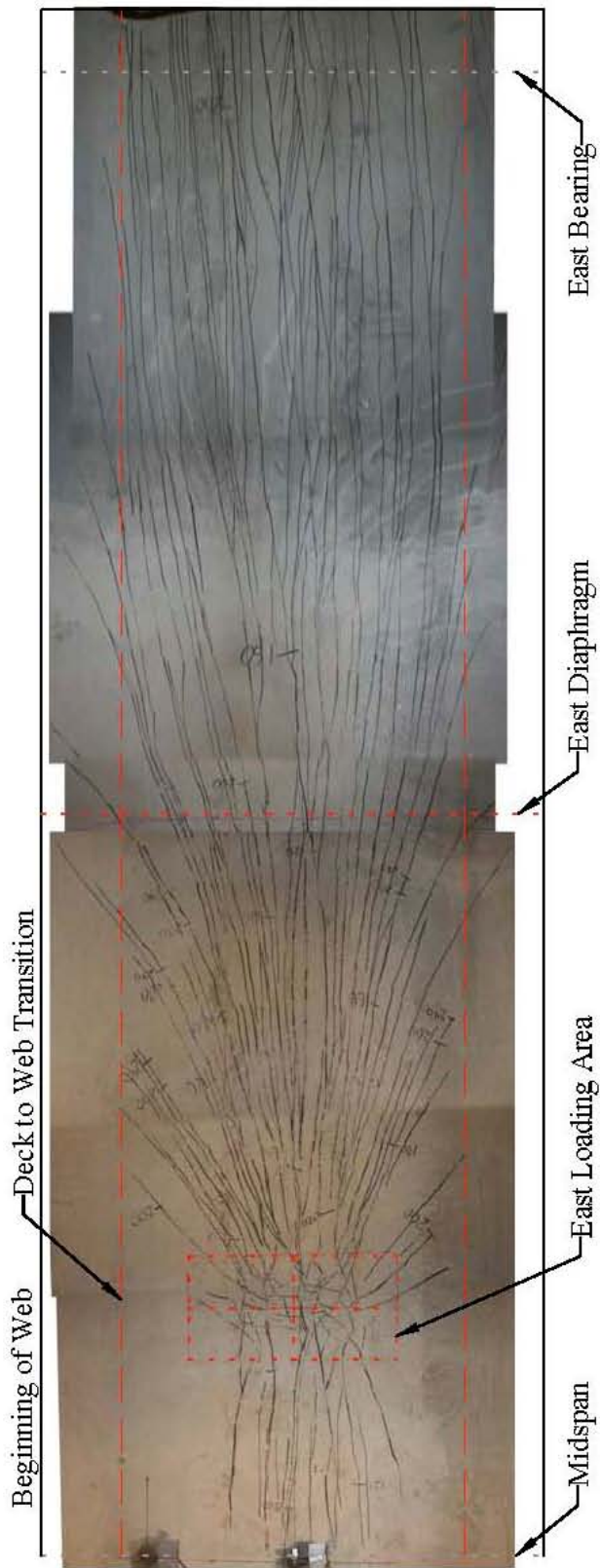
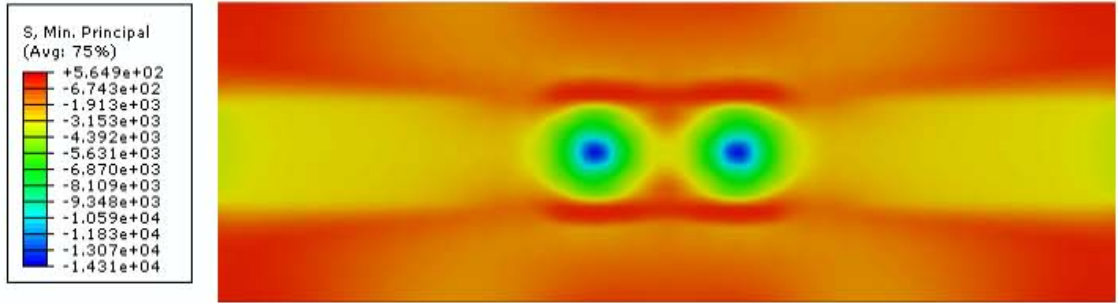
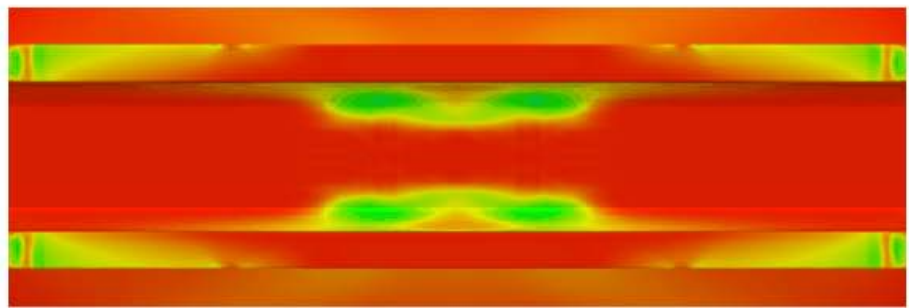


Figure 133. Photo. Underside deck cracking map of T2D after conclusion of test (reproduced from reference (14)).



(a)

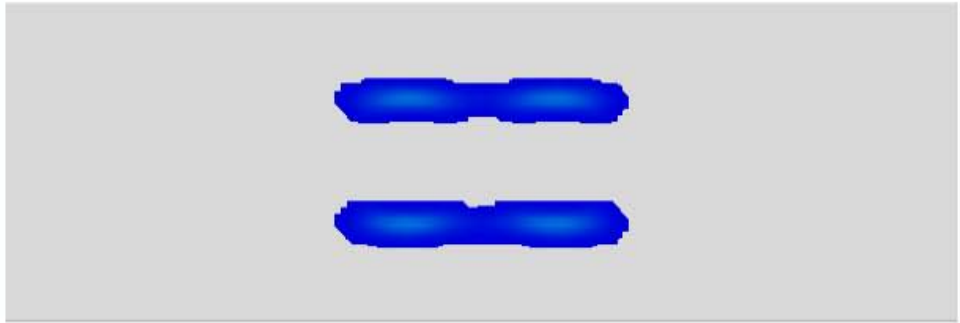
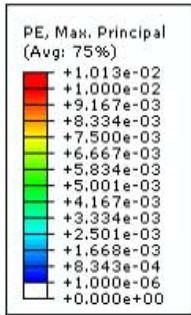


(b)

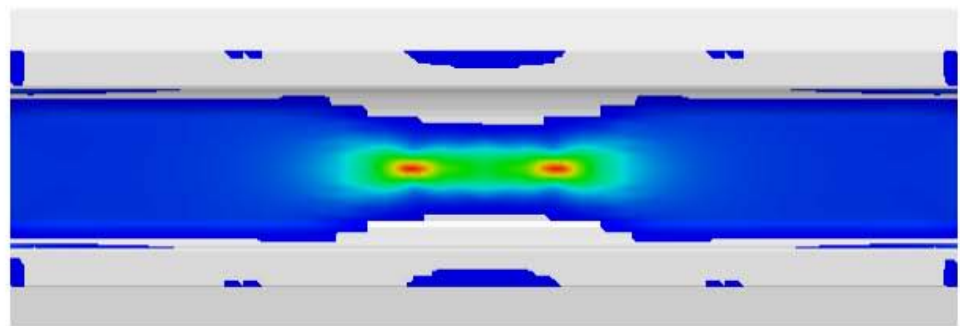


(c)

Figure 134. Graph. FEM predicted minimum principal stress on the surface of the girder as viewed from (a) above, (b) below, and (c) beside the girder.



(a)

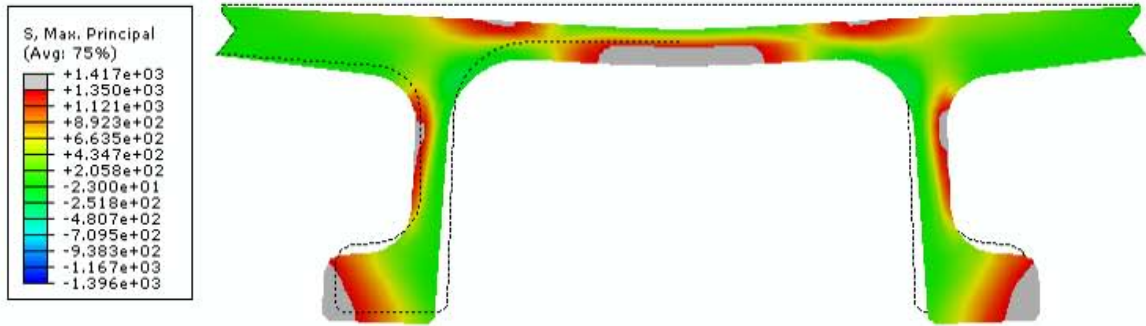


(b)

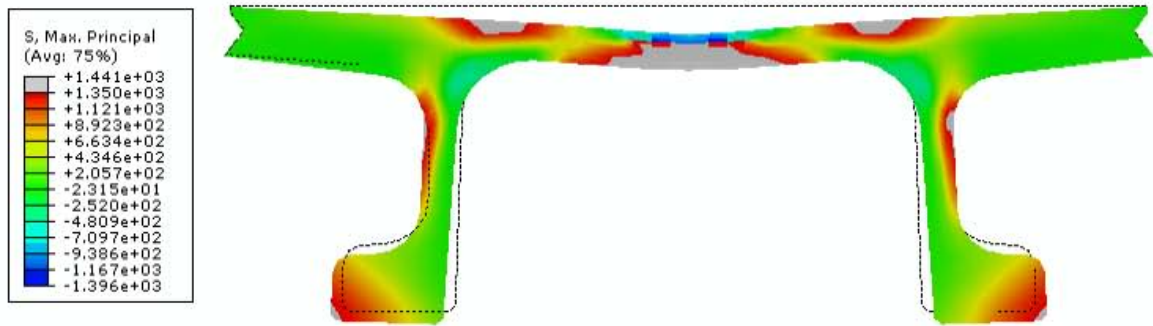


(c)

Figure 135. Graph. FEM predicted maximum principal plastic strain on the surface of the girder as viewed from (a) above, (b) below, and (c) beside the girder.

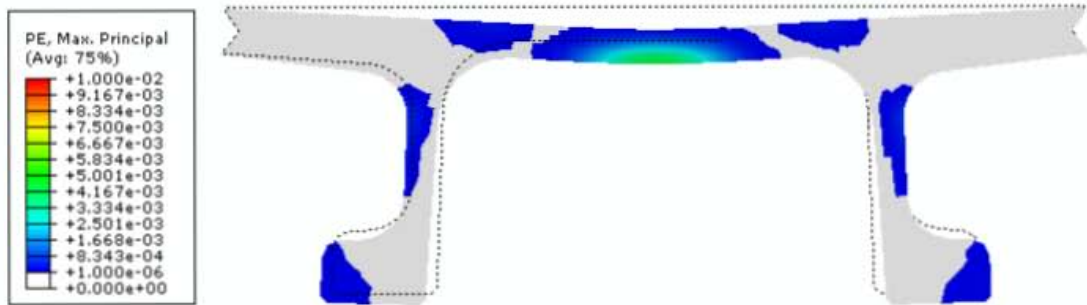


(a)

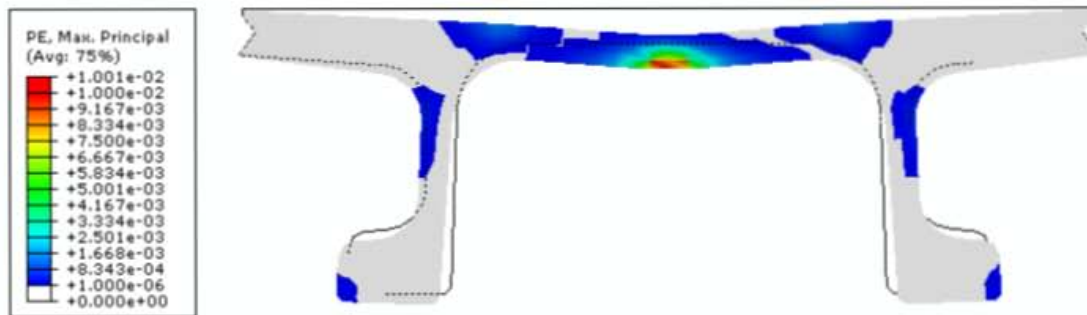


(b)

Figure 136. Graph. FEM predicted maximum principal stress at the (a) midspan, and (b) center of loading patch cross sections (Note: deformation scale factor = 5).



(a)



(b)

Figure 137. Graph. FEM predicted maximum principal plastic strain at the (a) midspan, and (b) center of loading patch cross sections (Note: deformation scale factor = 5).

PARAMETRIC STUDIES

The above model was calibrated through a series of parametric studies. The model sensitivity has been analyzed and is to be discussed below. The above model with a 2-inch (51-mm) seeded mesh and the CDP material parameters as specified in Table 4 serves as a benchmark in the following comparisons.

Mesh sensitivity

In the previous calibrated case presented in the results above, 2-inch (51-mm) global seeds were used to mesh UHPC, strands, rebar, plates, and loading surfaces. Another case for 3-inch (76-mm) global seeds applied to UHPC only was completed for comparison. Figure 138 through Figure 144 present these results. There is slight effect of mesh density on the bulb lateral spreading at the support as shown in Figure 142 and on the longitudinal strain on the bulb bottom surface at midspan as shown in Figure 143. Where any differences exist, the finer mesh predicts results closer to the experimental observed results.

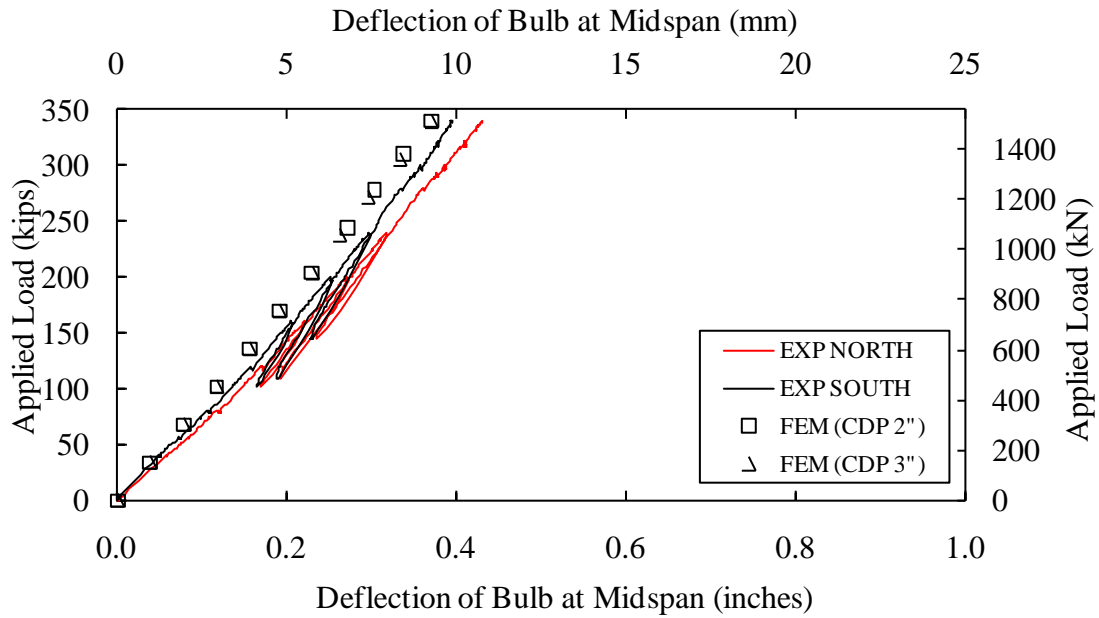


Figure 138. Graph. Effect of mesh density on the vertical deflection of the bulbs at midspan.

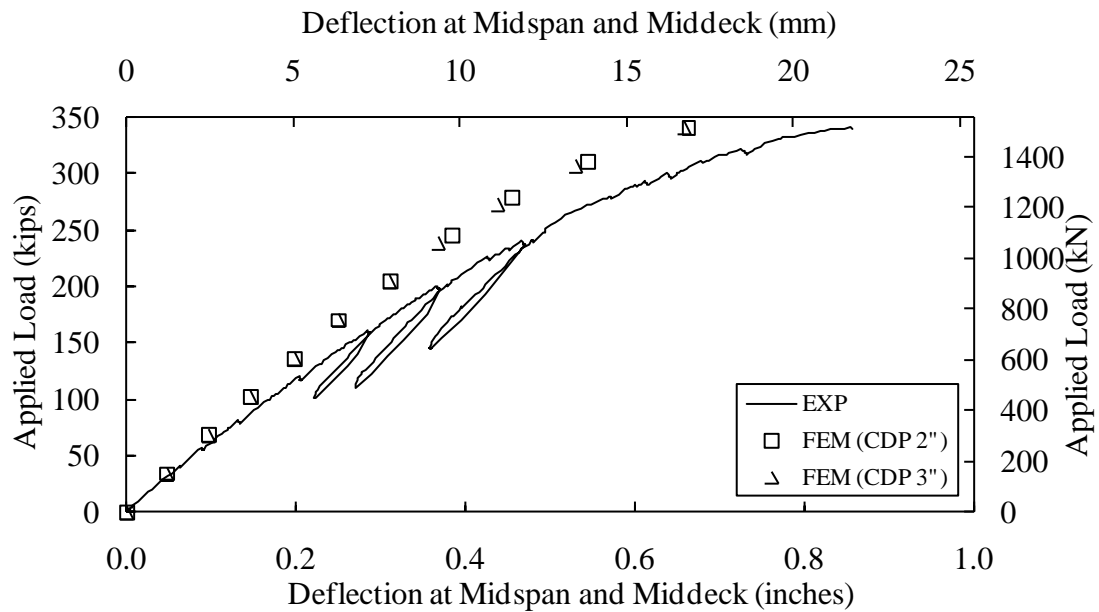


Figure 139. Graph. Effect of mesh density on the vertical deflection at the midspan middeck location.

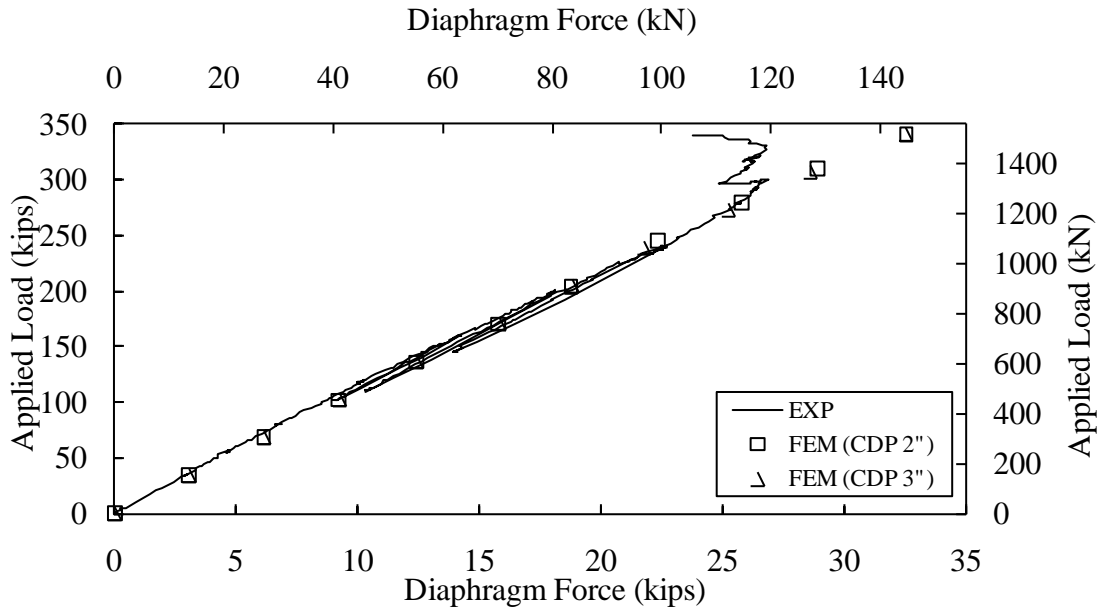


Figure 140. Graph. Effect of mesh density on the diaphragm force.

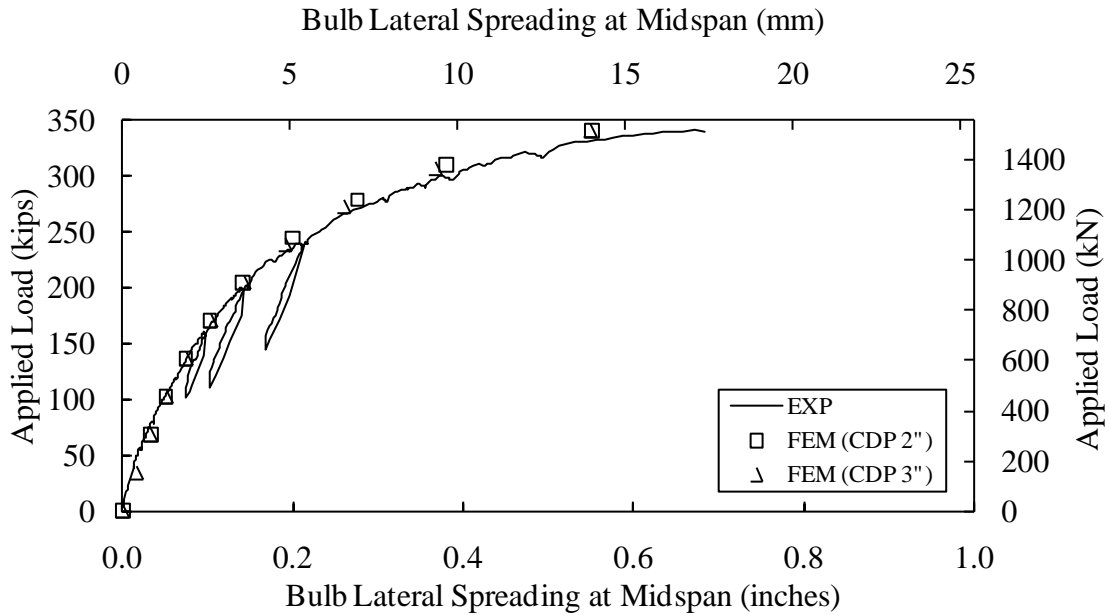


Figure 141. Graph. Effect of mesh density on the bulb lateral spreading at midspan.

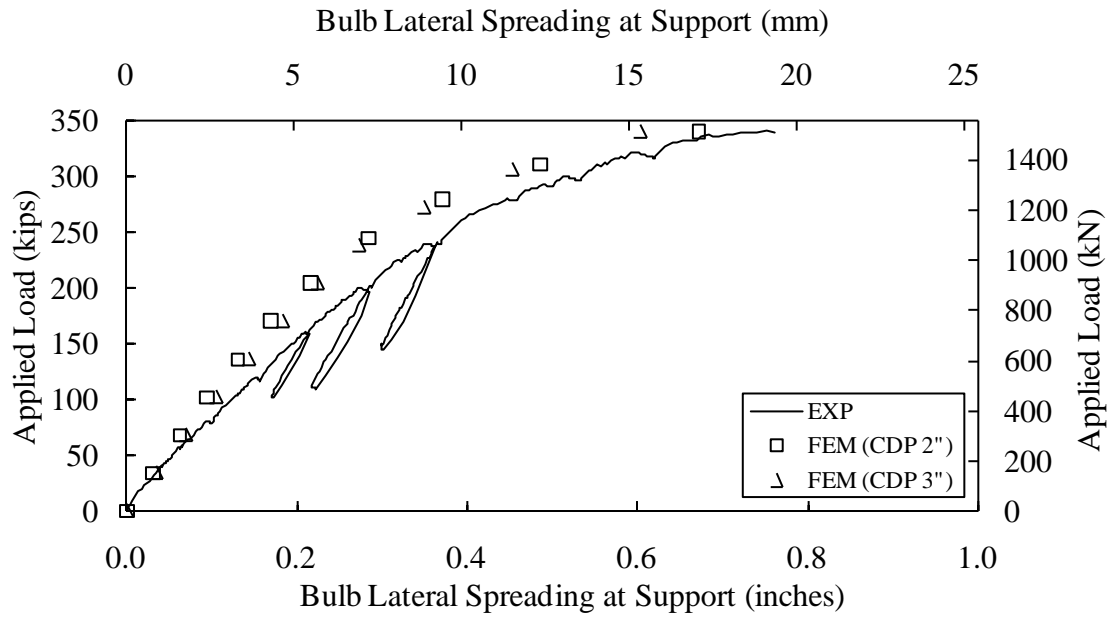


Figure 142. Graph. Effect of mesh density on the bulb lateral spreading at support.

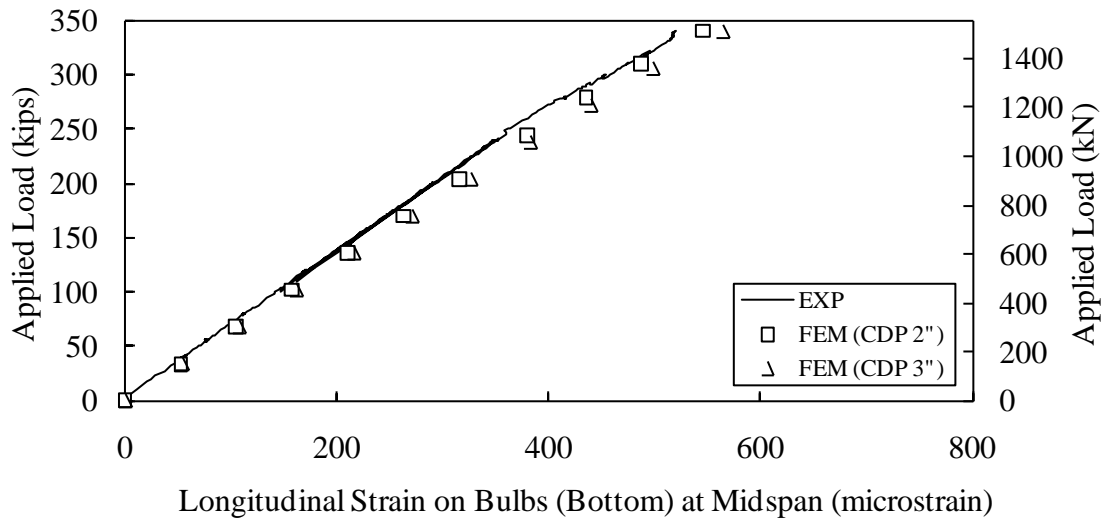


Figure 143. Graph. Effect of mesh density on the longitudinal strain on the bottom surface of the north bulb at midspan.

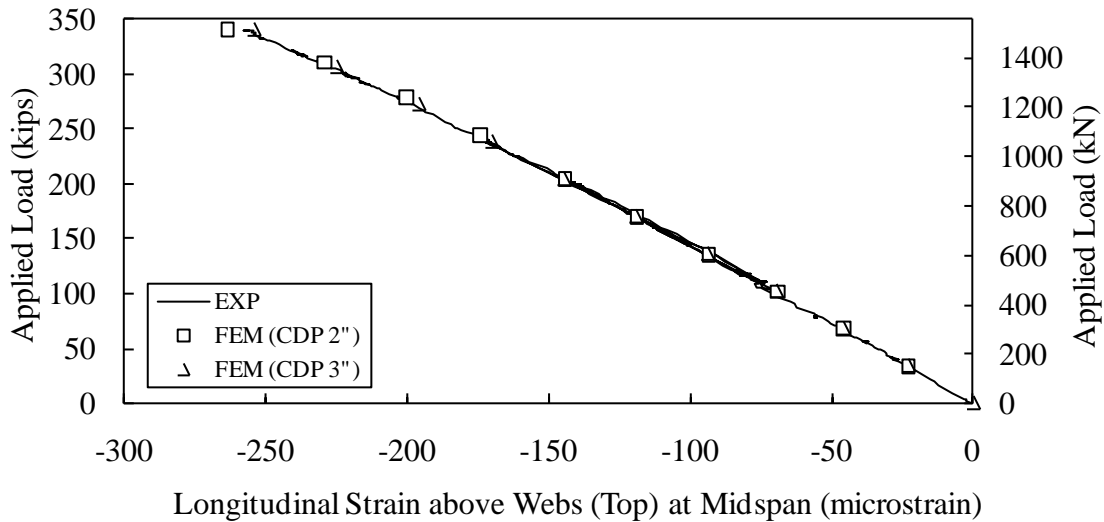


Figure 144. Graph. Effect of mesh density on the longitudinal strain on the deck immediately above the north web at midspan.

CDP vs. CSC

In a similar manner to that implemented with the I-girder model, the CSC model for UHPC is applied here using the properties given in Table 4. However, the CSC model failed to converge at applied loads greater than 125 kips (556 kN). Since the CDP and CSC models share the same elastic properties of UHPC, it is not surprising to see that these models agreed well in the early loading stage as illustrated in Figure 145 through Figure 151.

Young's modulus

Young's modulus of UHPC can be estimated from the experimental data for longitudinal strains on the bottom surfaces of the bulbs and the top surfaces of the deck immediately above the webs. A larger (i.e., 8000 ksi (55 GPa)) and a smaller (i.e., 7000 ksi (48 GPa)) Young's modulus were tested in the CDP model to determine their effect on the results. These model results bracketed the experimental results as shown in Figure 152 and Figure 153. This verified that the value of 7650 ksi (53 GPa) is a reasonable estimate for Young's modulus of the UHPC in this pi-girder.

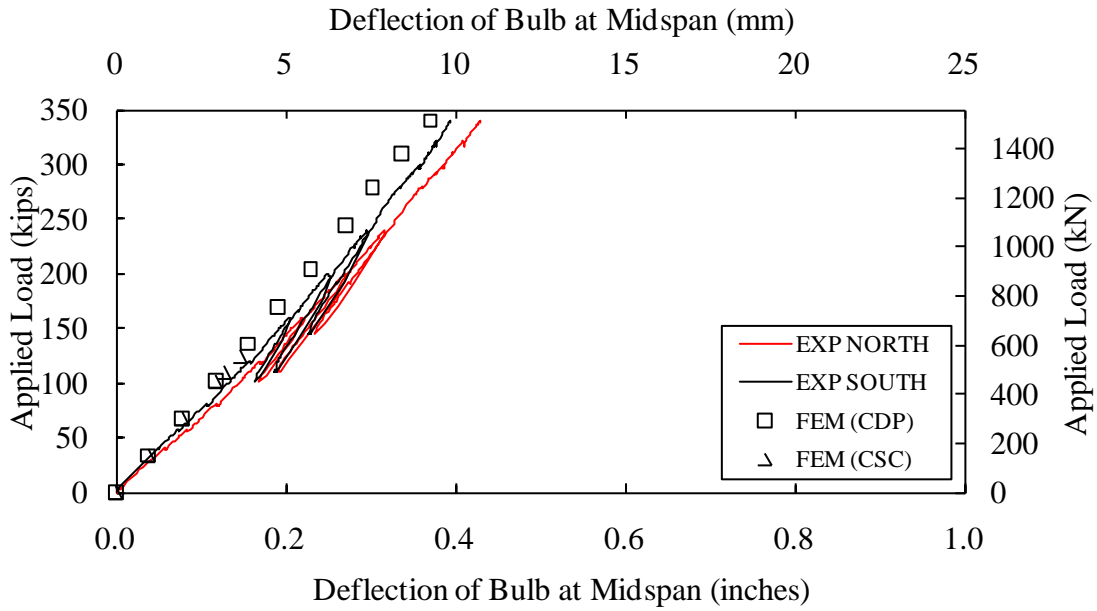


Figure 145. Graph. CDP vs. CSC in the vertical deflection of the bulbs at midspan.

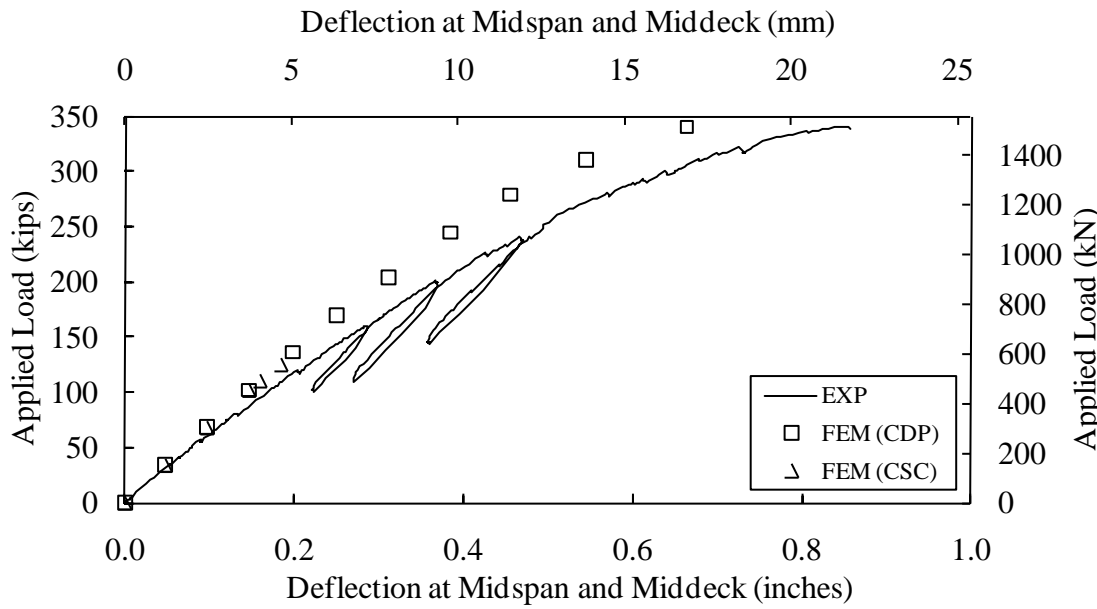


Figure 146. Graph. CDP vs. CSC in the vertical deflection at the midspan middeck position.

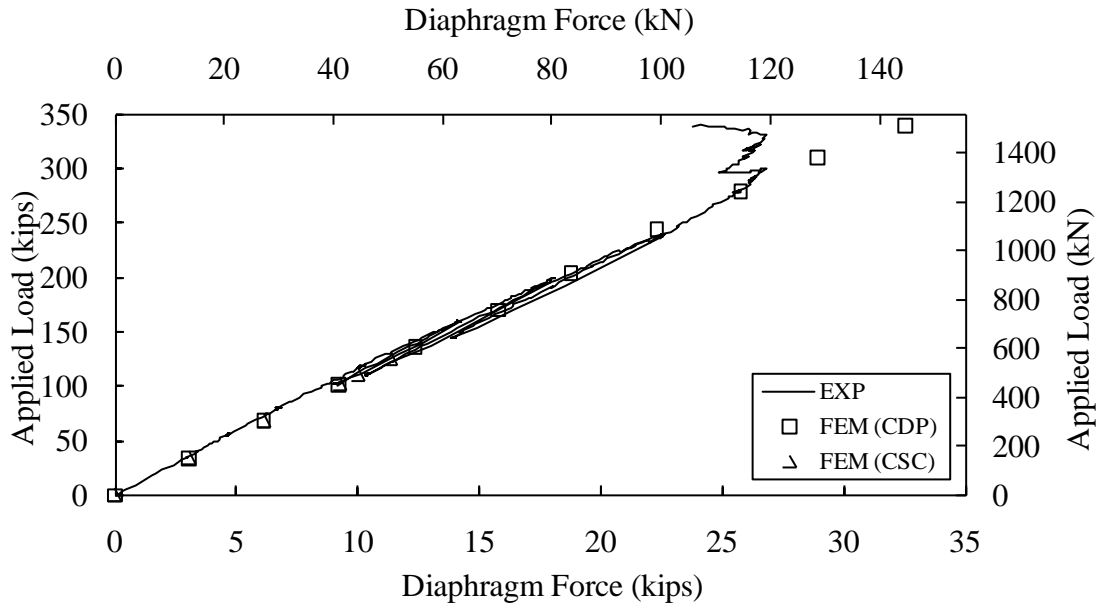


Figure 147. Graph. CDP vs. CSC in the diaphragm force.

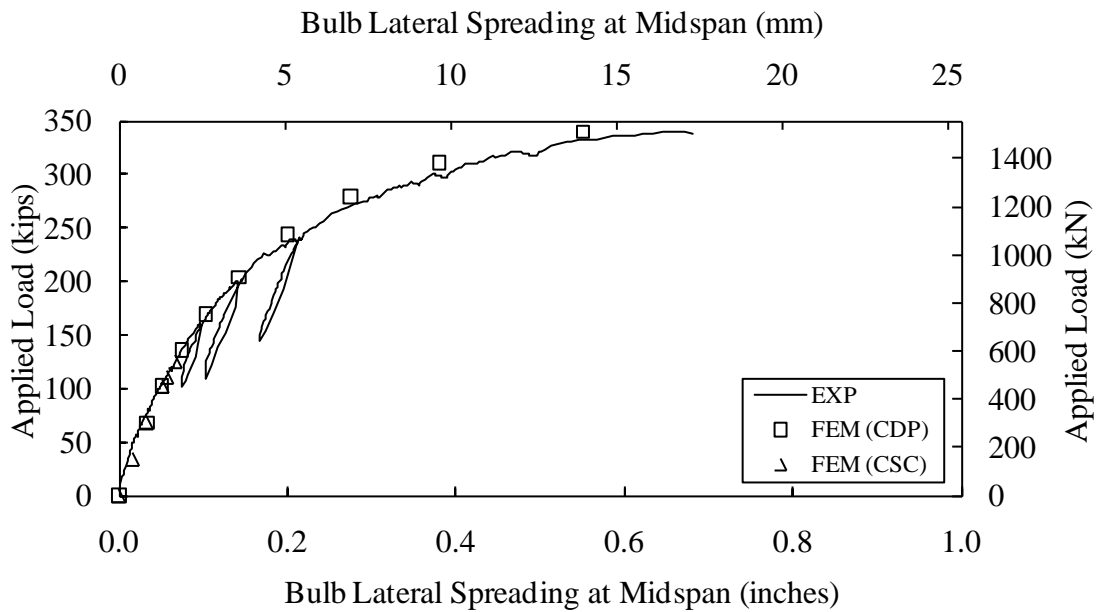


Figure 148. Graph. CDP vs. CSC in the bulb lateral spreading at midspan.

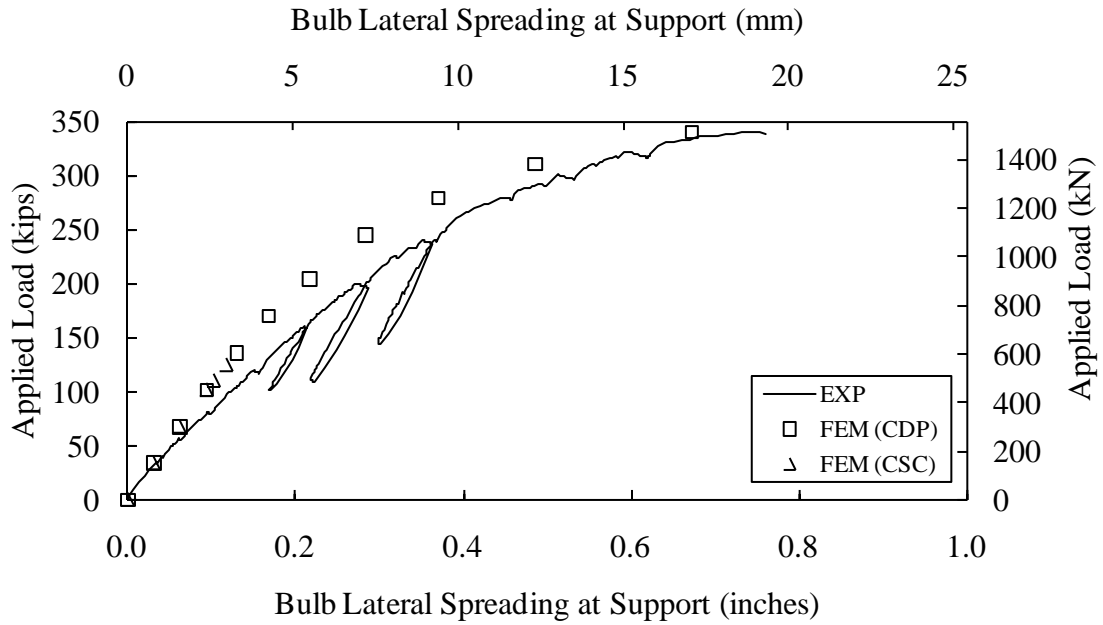


Figure 149. Graph. CDP vs. CSC in the bulb lateral spreading at support.

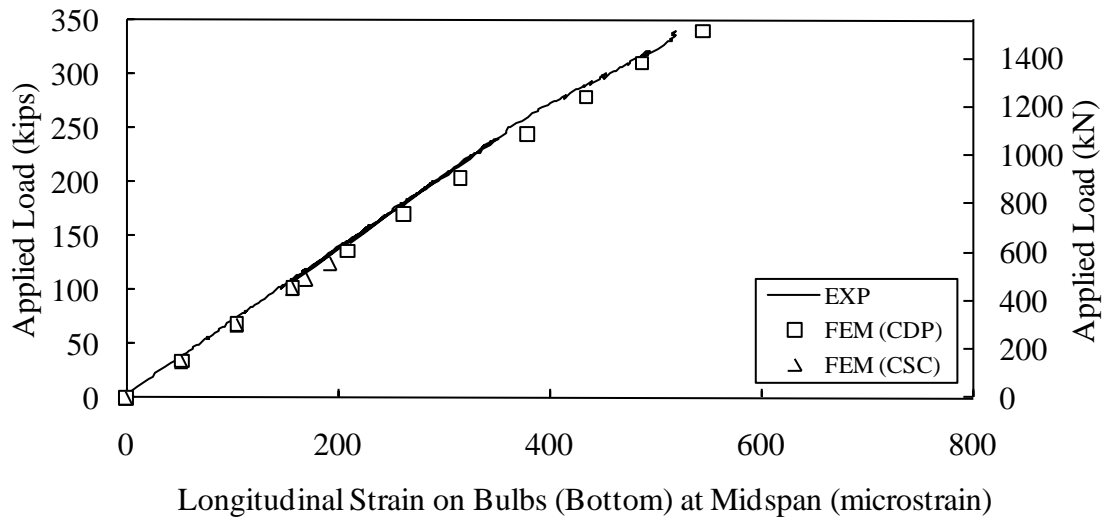


Figure 150. Graph. CDP vs. CSC in the longitudinal strain on the bottom surface of the north bulb at midspan.

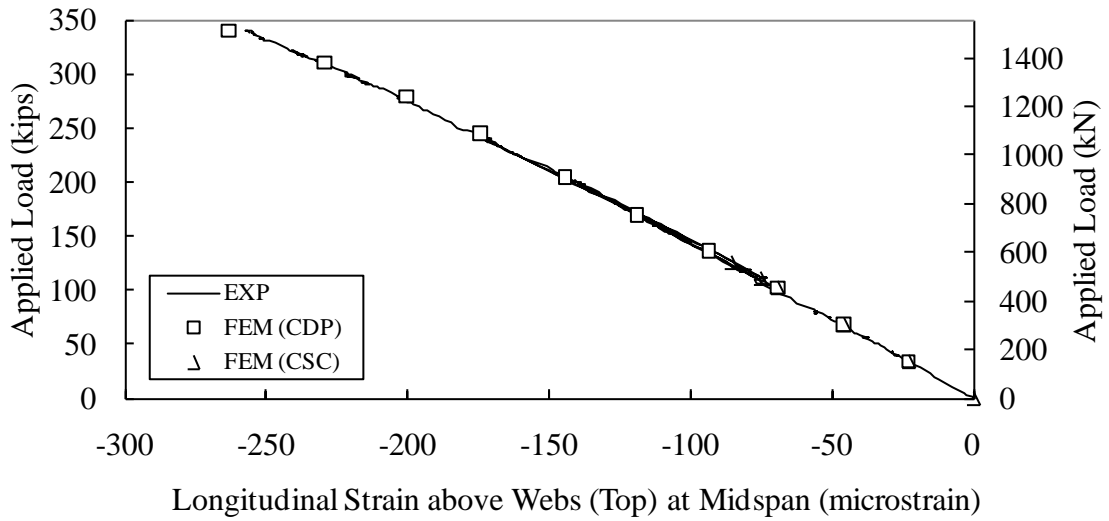


Figure 151. Graph. CDP vs. CSC in the longitudinal strain on the deck immediately above the web at midspan.

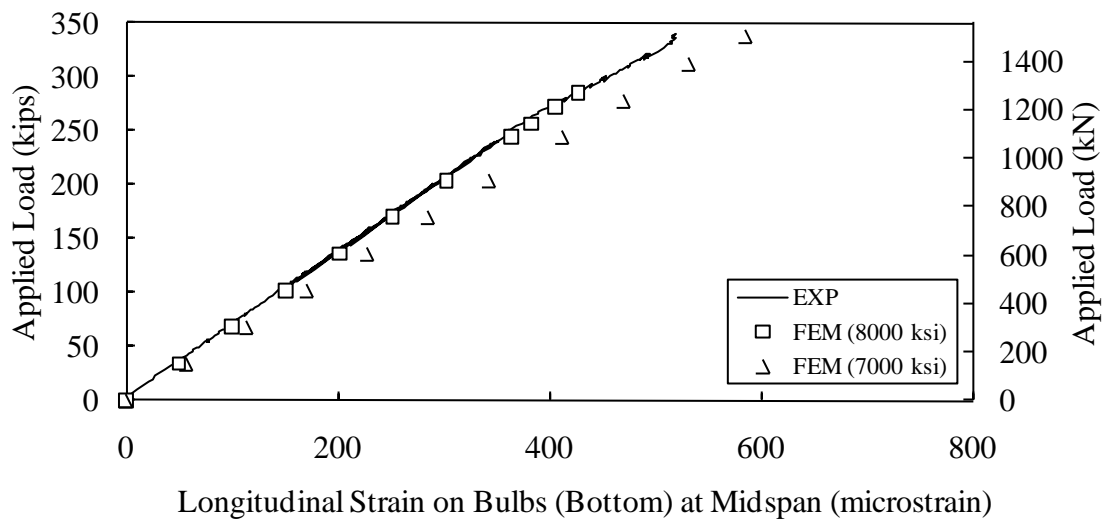


Figure 152. Graph. Effect of Young's modulus on the longitudinal strain on the bottom surface of the north bulb at midspan.

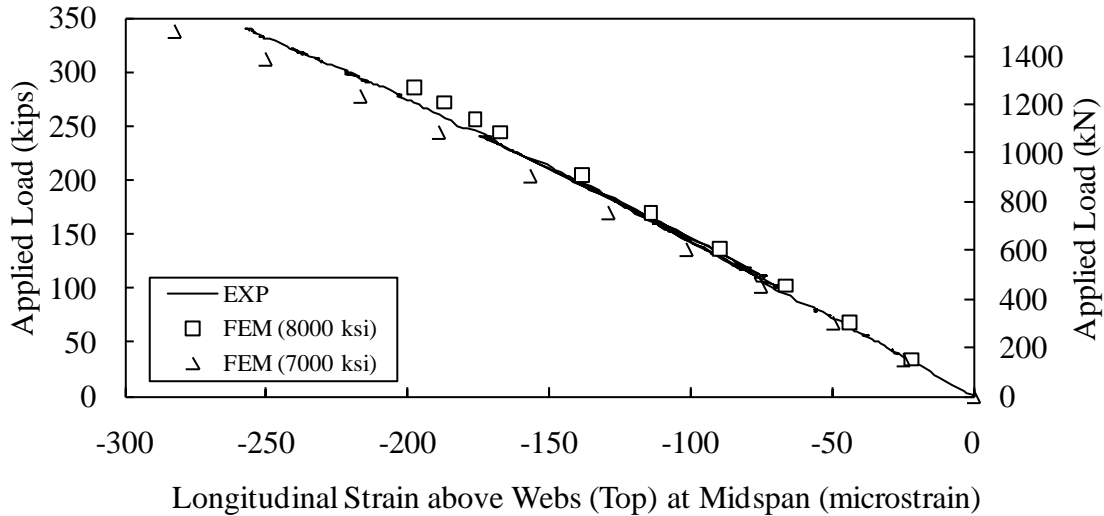


Figure 153. Graph. Effect of Young’s modulus on the longitudinal strain on the surface of the deck immediately above the web at midspan.

Concrete tension stiffening of CDP

Concrete tension stiffening can be defined in three ways, i.e., post-failure stress-strain relationship, post-failure stress-displacement relationship, and post-failure stress-fracture energy relationship. Details of these definitions have been discussed in the previous presentation of the I-girder model results. The latter two definitions belong to fracture energy criterion and may be more suitable to plain or scarcely reinforced concrete. Table 6 lists the calibrated parameters for these three definitions of concrete tension stiffening.

Table 6. Concrete tension stiffening in the CDP models of the UHPC in the pi-girder.

Post-failure stress-strain relationship	
Maximum tensile stress, ksi (MPa)	Plastic strain (+)
1.4 (9.7)	0.000
1.4 (9.7)	0.010
0.0 (0.0)	0.011
Post-failure stress-displacement relationship (constant)	
Maximum tensile stress ksi, (MPa)	Cracking displacement, inch (mm)
1.4 (9.7)	0.00 (0.00)
1.4 (9.7)	0.10 (2.54)
0.0 (0.0)	0.11 (2.79)
Post-failure stress-fracture energy relationship	
Maximum tensile stress, ksi (MPa)	Fracture energy, lb/inch (N/m)
1.4 (9.7)	500 (87560)

The post-failure stress-strain relationship includes two parameters: maximum tensile stress and ultimate tensile plastic strain. The effect of maximum tensile stress is presented in Figure 154 through Figure 160. As would be expected, this parameter has little impact on the behaviors governed by longitudinal bending which was primarily resisted by the portions of the girder which did not experience high tensile strains. However, a noticeable difference can be observed in responses pertaining to transverse flexural behavior of the cross section. Figure 155 through Figure 158 focus on these behaviors. The experimental data appears to fall between the given upper and lower cases in terms of stiffness of response, indicating that the selected maximum tensile stress of 1.4 ksi (9.7 MPa) is reasonable for locations governed by these types of behaviors. Meanwhile Figure 161 through Figure 167 demonstrate that a specific value of ultimate tensile plastic strain has very little effect on the trends. The only notable difference is that a smaller ultimate tensile plastic strain may reduce the ability of the model to converge under the proposed ultimate testing load, a result consistent with that observed in the I-girder modeling. As was observed with the results presented in Figure 135, the ultimate tensile plastic strain is approximately 0.01 and therefore any larger value than 0.01 would not be activated in this model and thus should provide identical results.

Fracture energy criteria with the parameters listed in Table 6 were also implemented and the results were plotted in Figure 168 through Figure 174. All three definitions in Table 6 agree with each other and fit well with the experimental results in this pi-girder model. The post-failure stress-fracture energy relationship displays a more rapid convergence than the other two definitions.

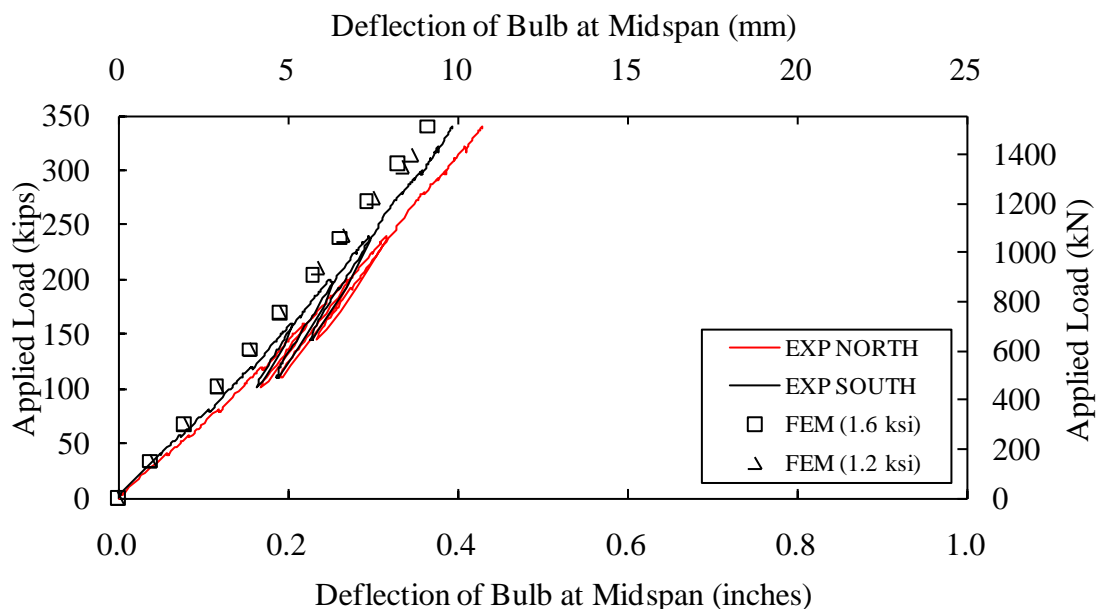


Figure 154. Graph. Effect of maximum tensile stress on the vertical deflection of the bulbs at midspan.

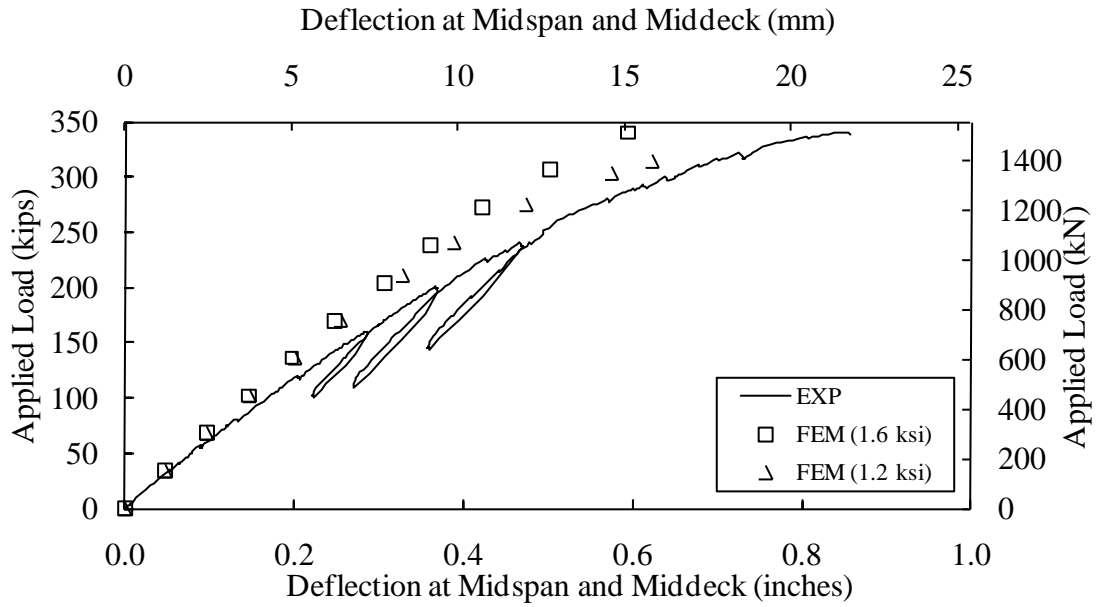


Figure 155. Graph. Effect of maximum tensile stress on the vertical deflection at the midspan middeck location.

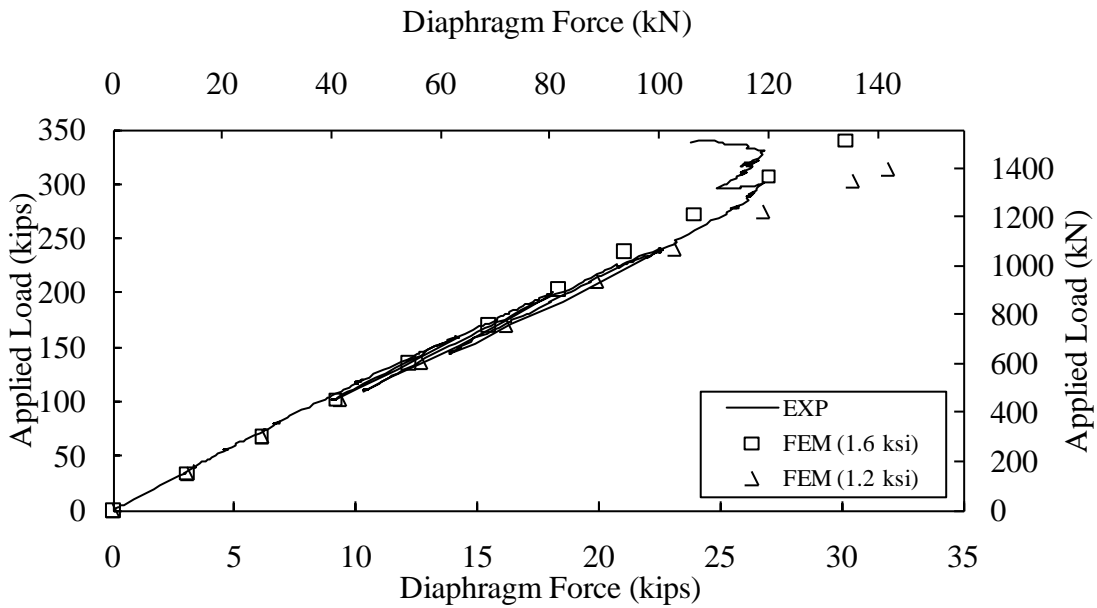


Figure 156. Graph. Effect of maximum tensile stress on the diaphragm force.

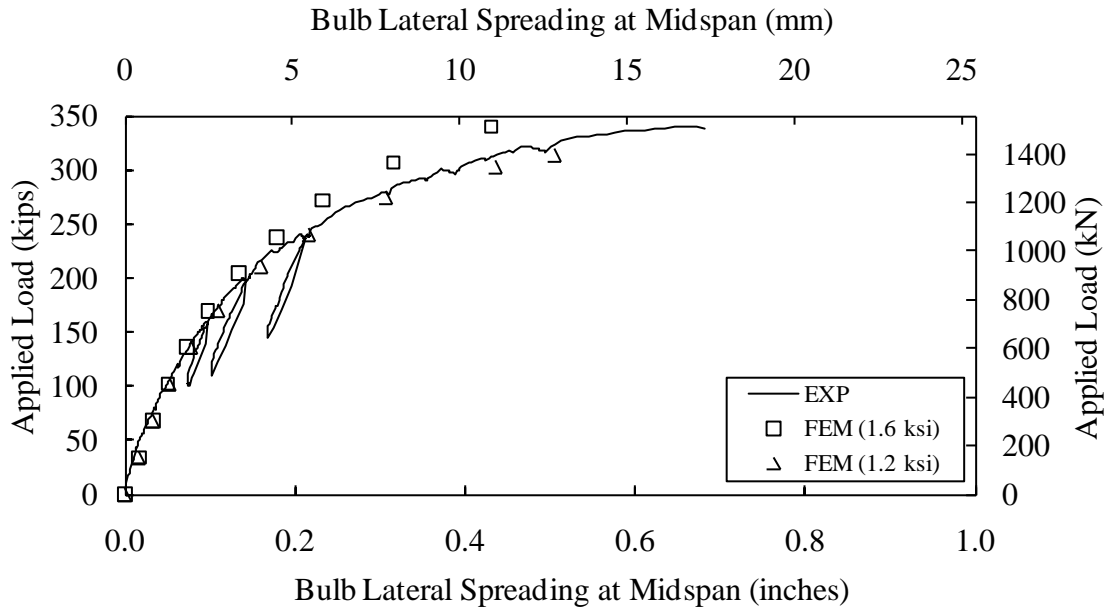


Figure 157. Graph. Effect of maximum tensile stress on the bulb lateral spreading at midspan.

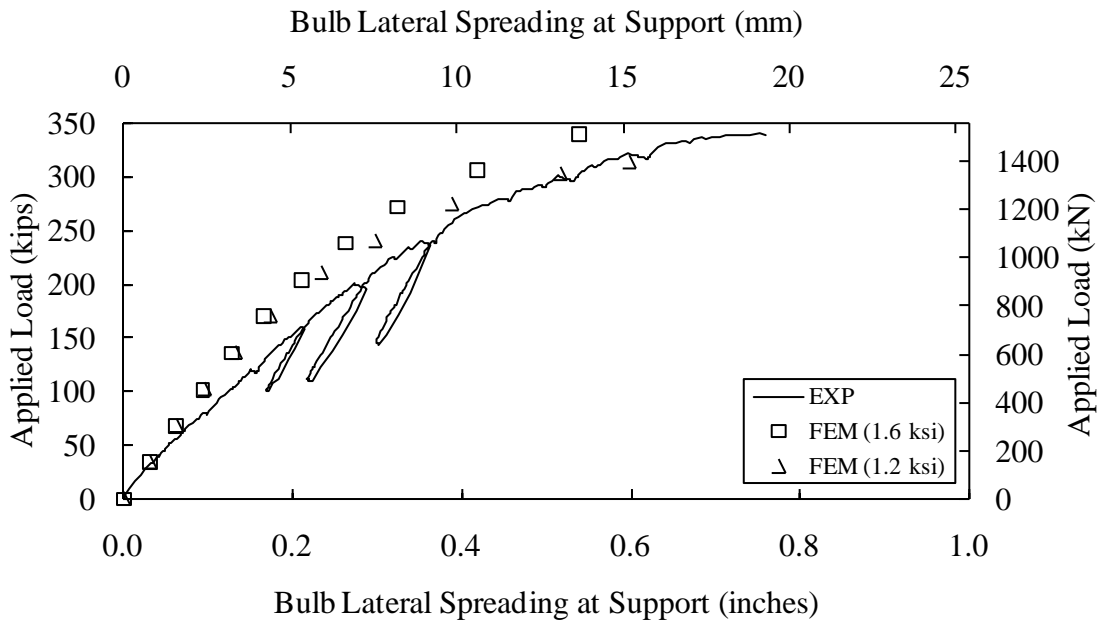


Figure 158. Graph. Effect of maximum tensile stress on the bulb lateral spreading at the support.

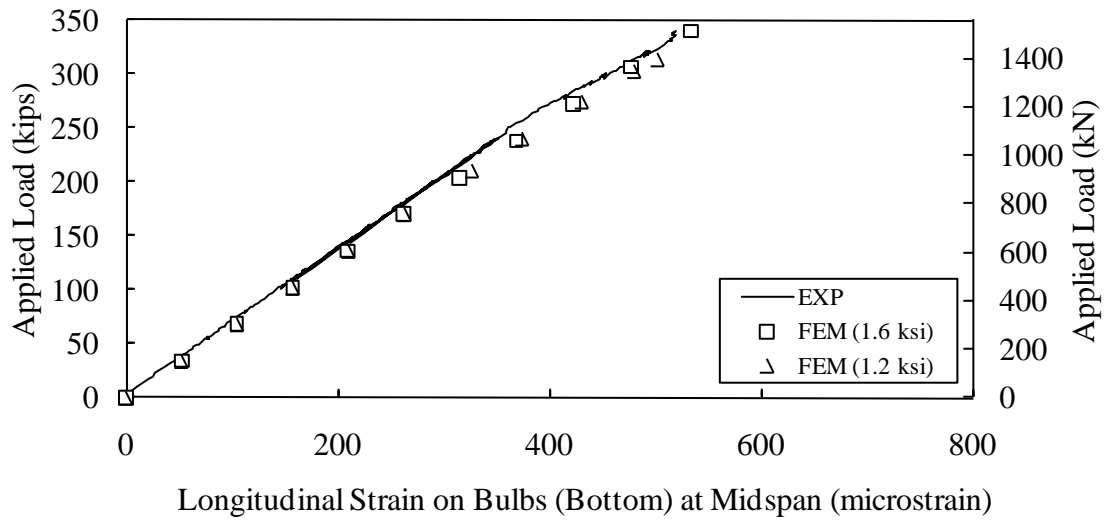


Figure 159. Graph. Effect of maximum tensile stress on the longitudinal strain on the bottom surface of the bulb at midspan.

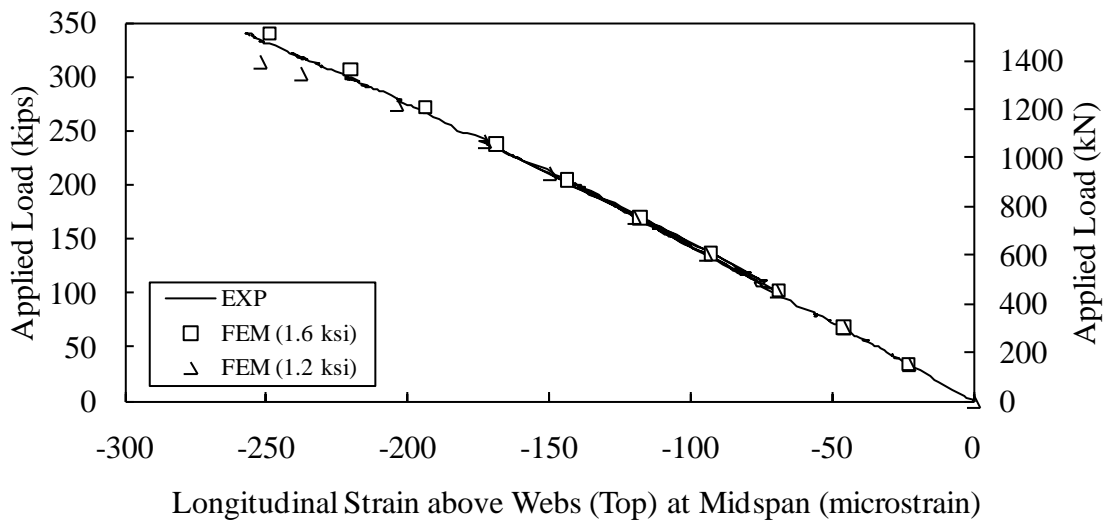


Figure 160. Graph. Effect of maximum tensile stress on the longitudinal strain on the deck immediately above the web at midspan.

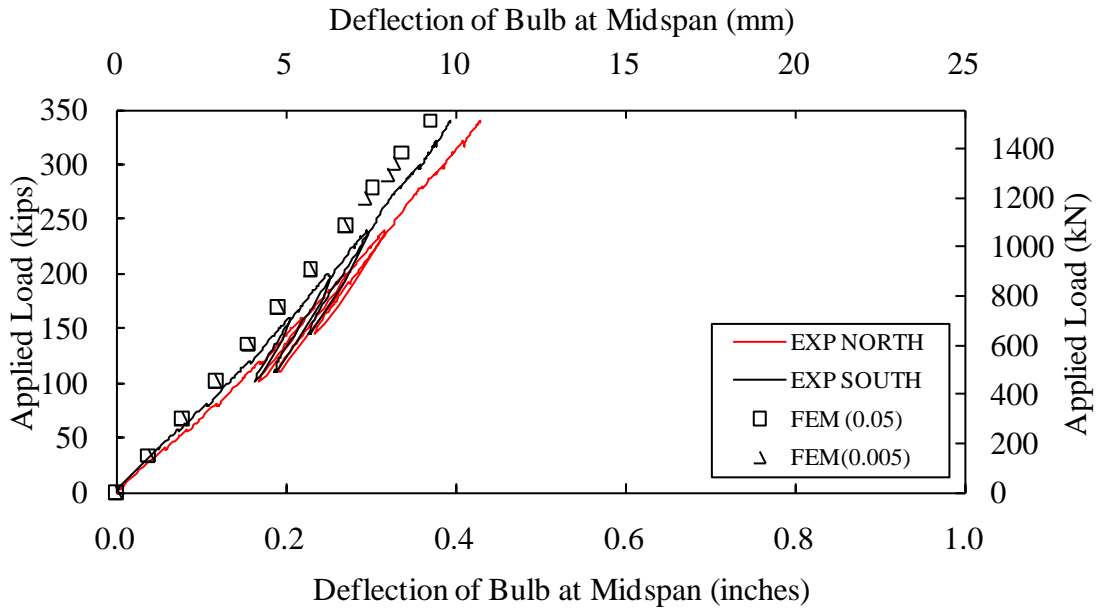


Figure 161. Graph. Effect of ultimate tensile plastic strain on the vertical deflection of the bulbs at midspan.

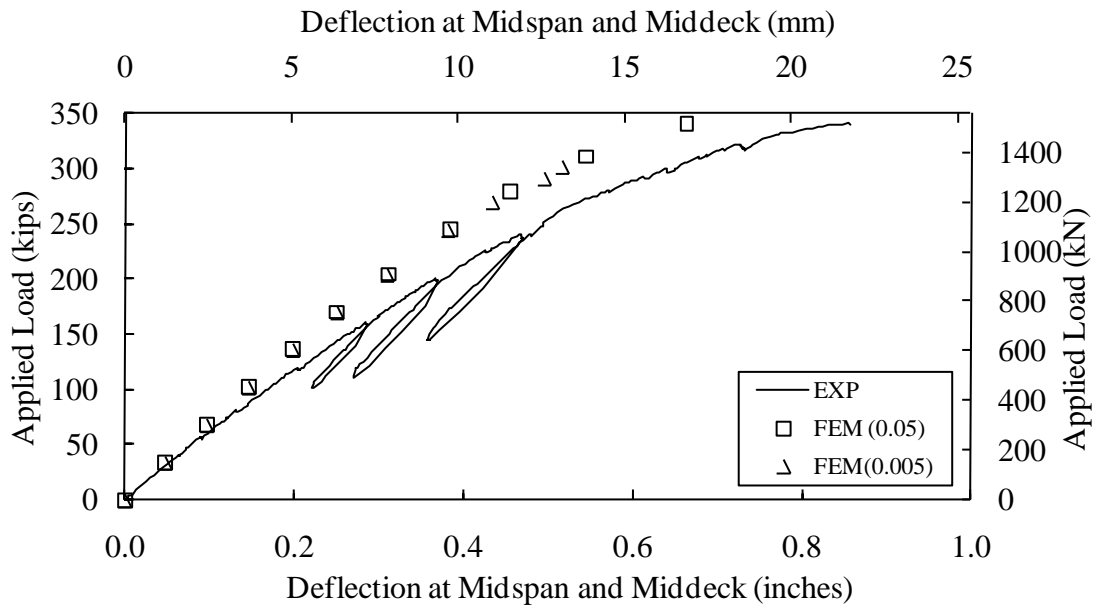


Figure 162. Graph. Effect of ultimate tensile plastic strain on the vertical deflection at the midspan middeck location.

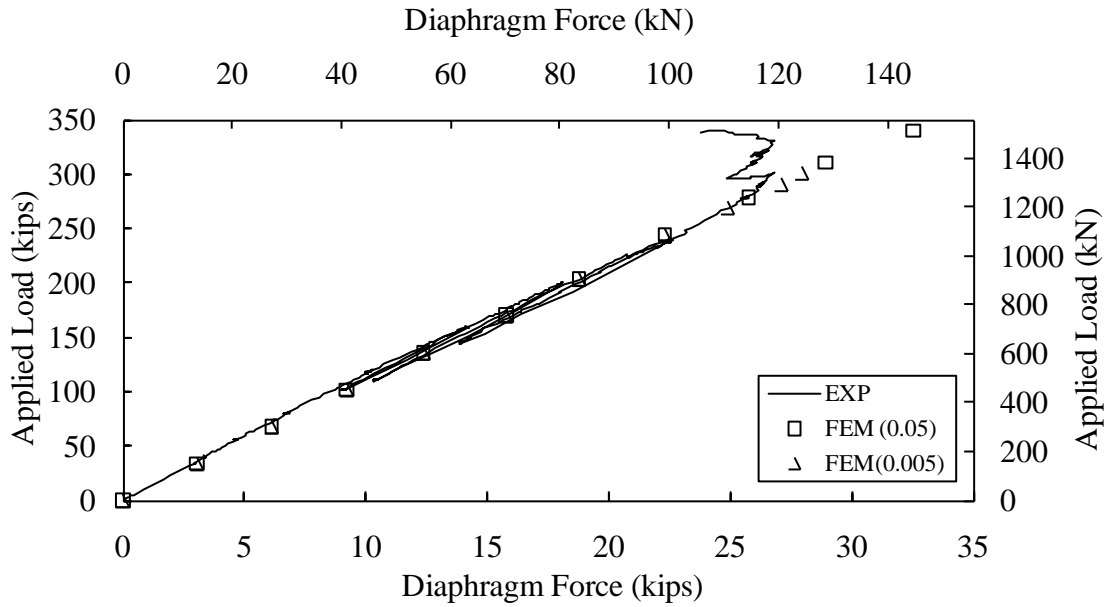


Figure 163. Graph. Effect of the ultimate tensile plastic strain on the diaphragm force.

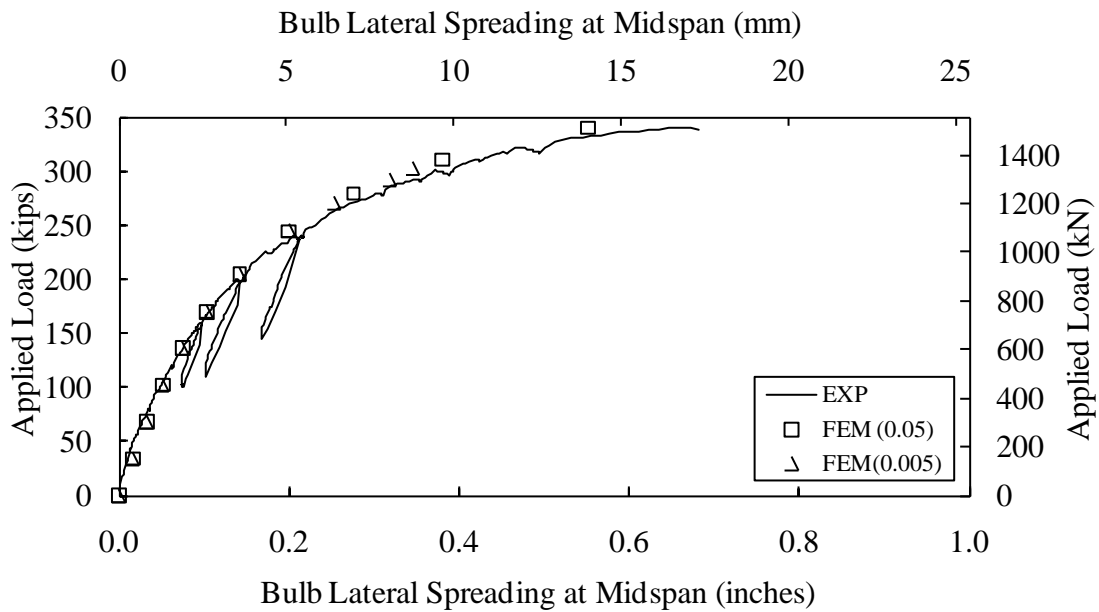


Figure 164. Graph. Effect of the ultimate tensile plastic strain on the bulb lateral spreading at midspan.

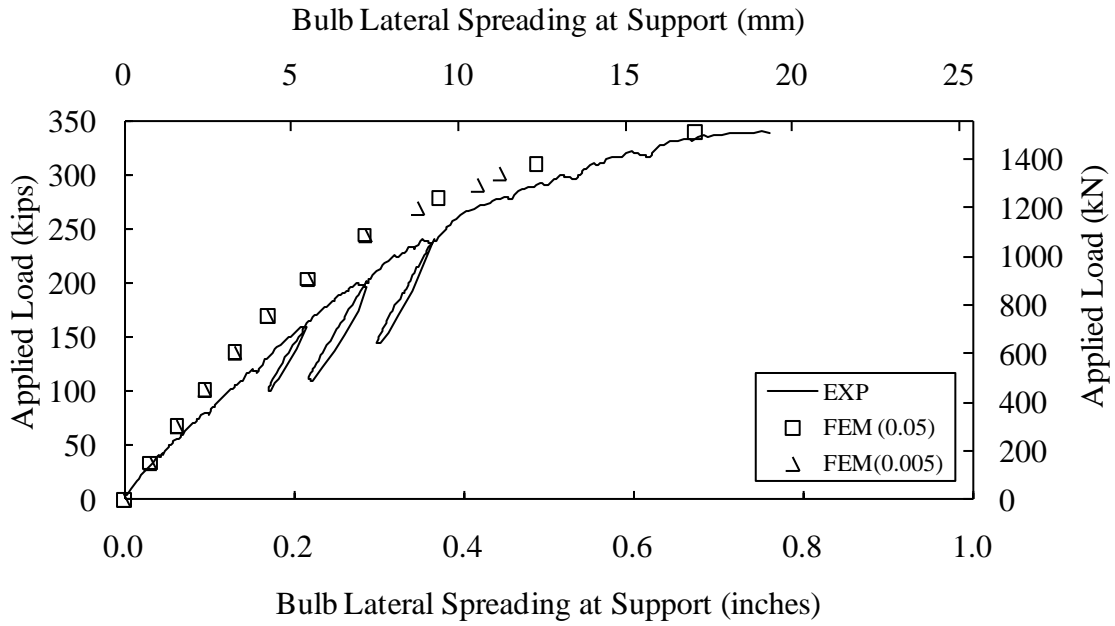


Figure 165. Graph. Effect of the ultimate tensile plastic strain on the bulb lateral spreading at support.

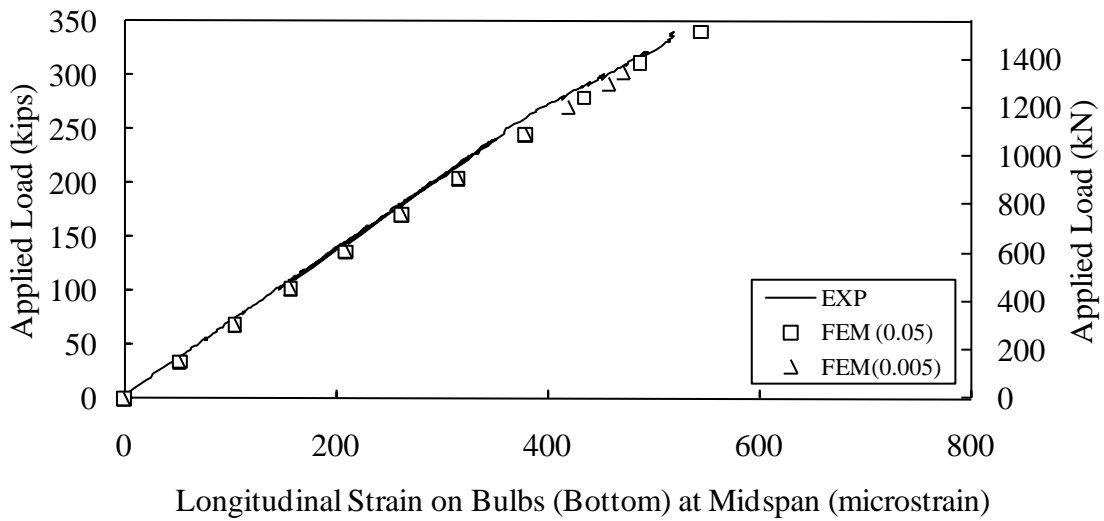


Figure 166. Graph. Effect of the ultimate tensile plastic strain on the longitudinal strain on the bottom surface of the north bulb at midspan.

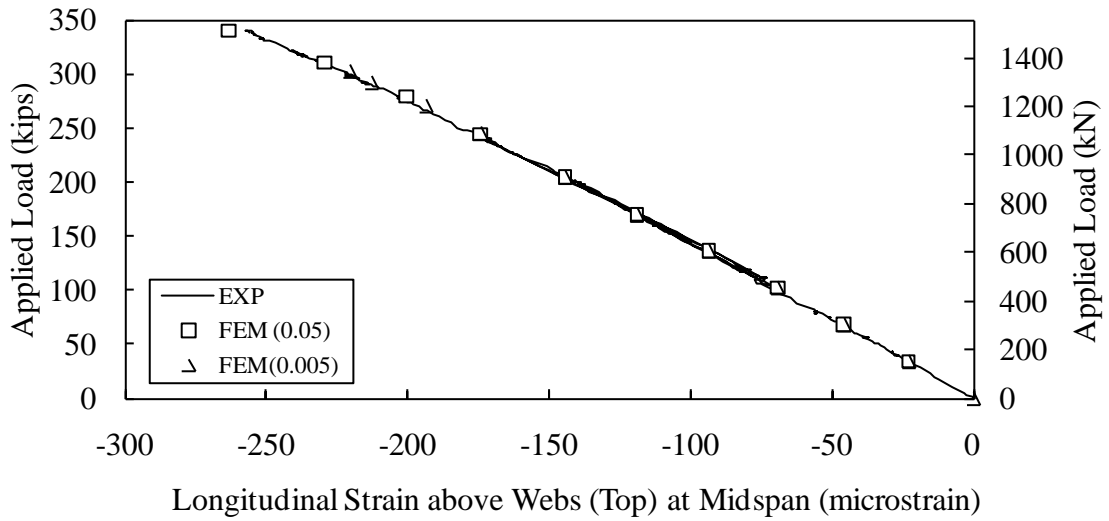


Figure 167. Graph. Effect of the ultimate tensile plastic strain on the longitudinal strain on the deck immediately above the web at midspan.

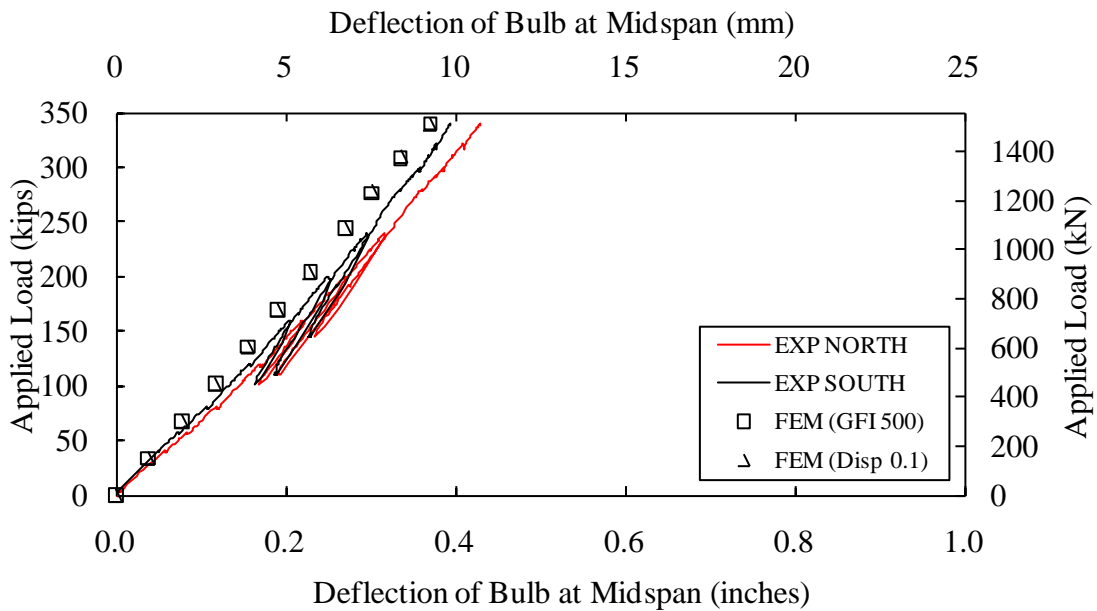


Figure 168. Graph. Effect of fracture energy criterion on the vertical deflection of the bulbs at midspan.

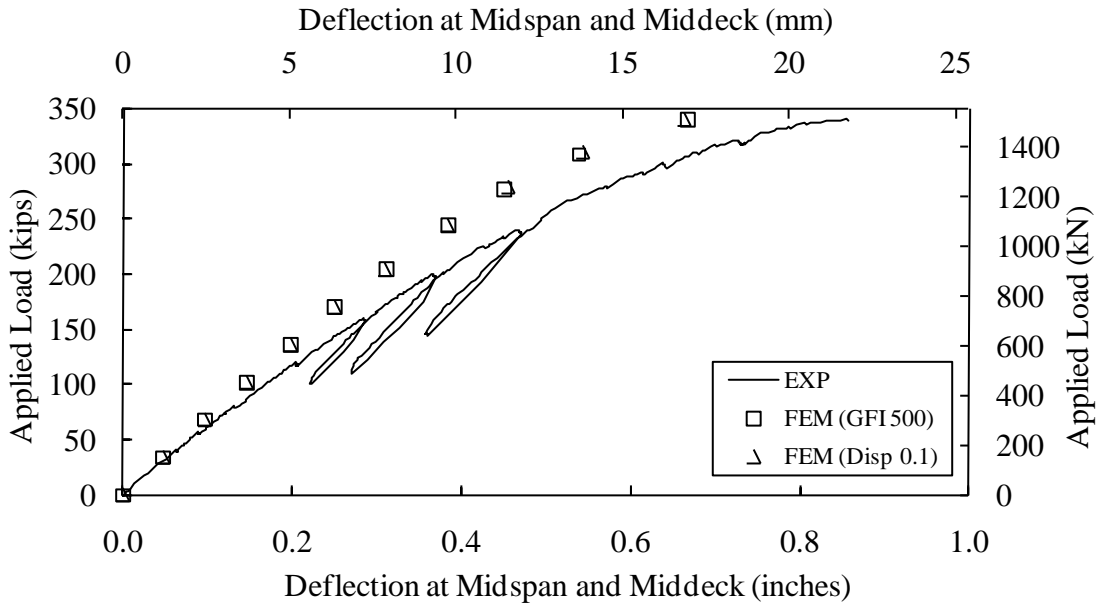


Figure 169. Graph. Effect of fracture energy criterion on the vertical deflection at the midspan middeck location.

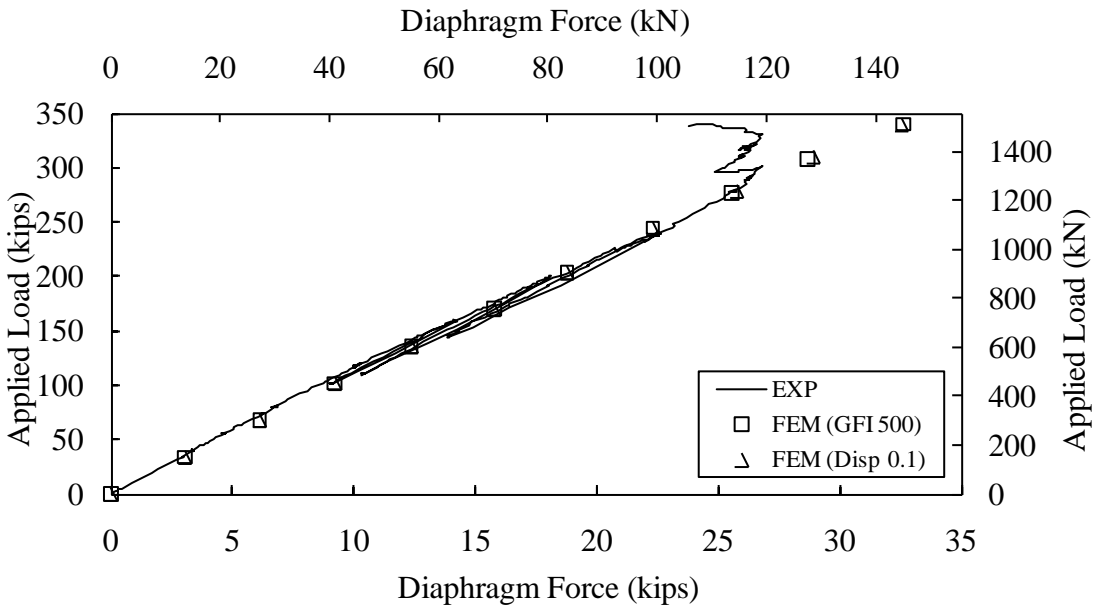


Figure 170. Graph. Effect of fracture energy criterion on the diaphragm force.

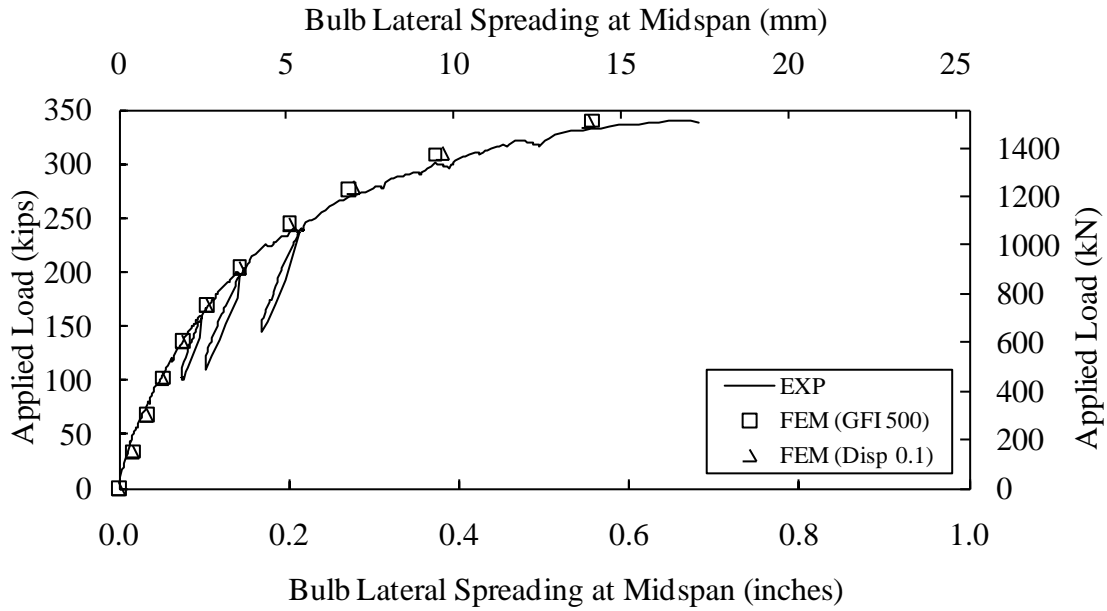


Figure 171. Graph. Effect of fracture energy criterion on the bulb lateral spreading at midspan.

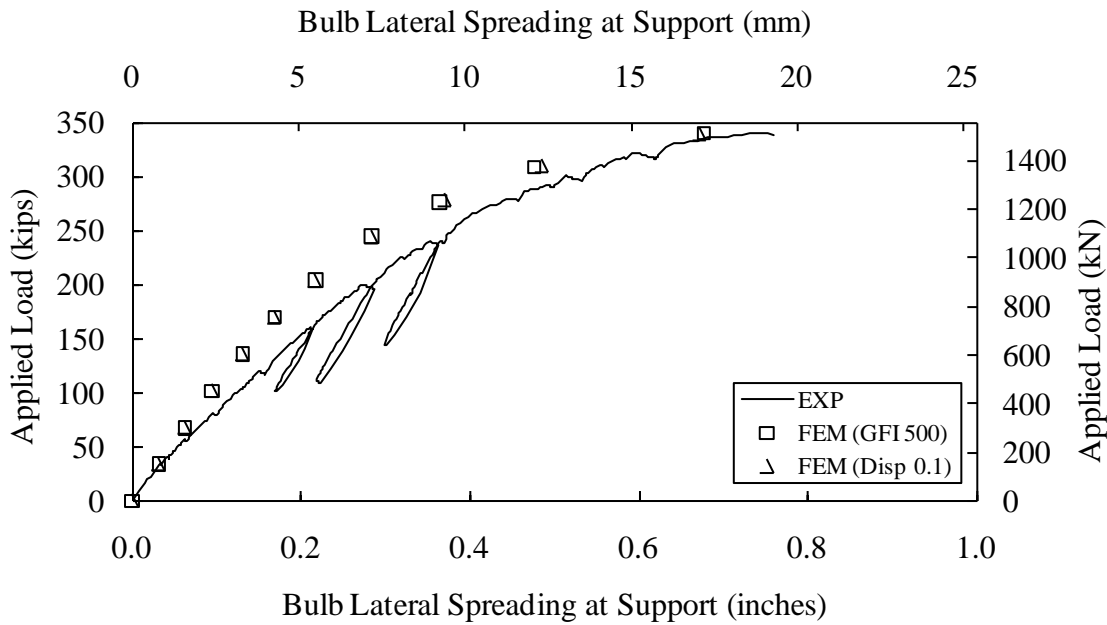


Figure 172. Graph. Effect of fracture energy criterion on the bulb lateral spreading at support.

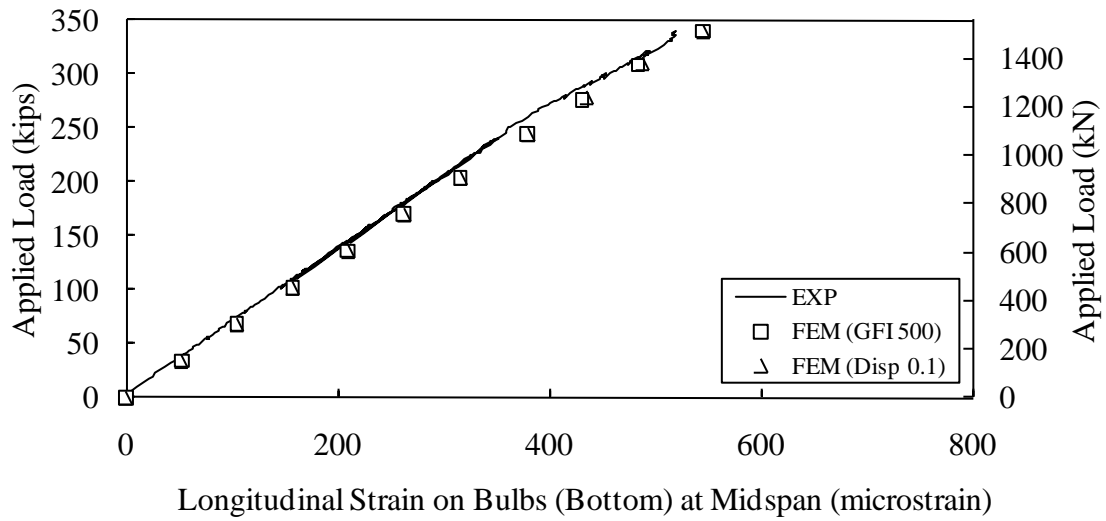


Figure 173. Graph. Effect of fracture energy criterion on the longitudinal strain on the bottom surface of the north bulb at midspan.

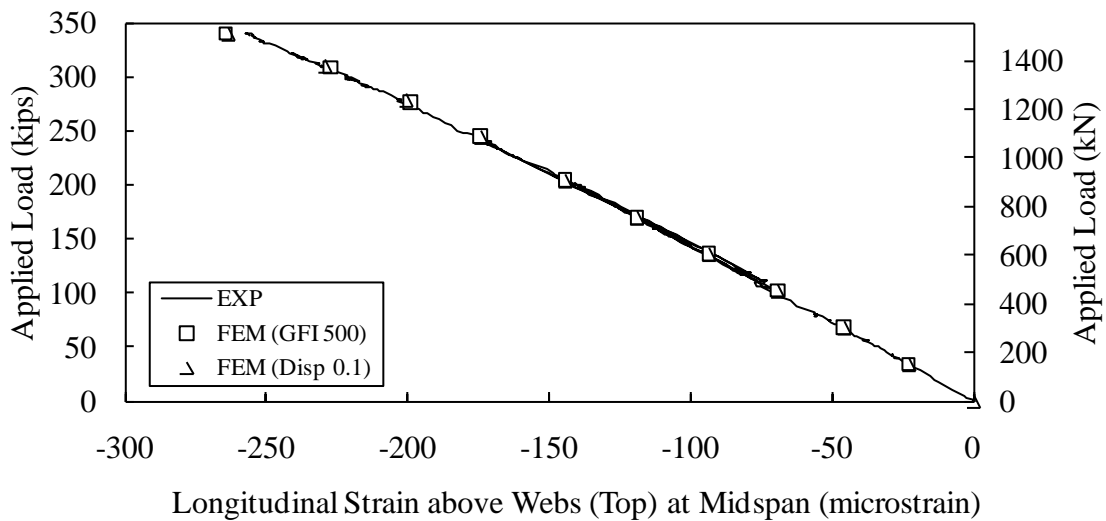


Figure 174. Graph. Effect of fracture energy criterion on the longitudinal strain on the deck immediately above the web at midspan.

Diaphragms

The diaphragms played a significant role in girder structural response. Failure of the diaphragm end steel plates and the welded connection between steel tube and plate led to lateral spreading of the legs and eventual failure of the deck via transverse bending and crack localization. For the load case investigated in this portion of the study, the design of diaphragms must satisfy both strength and stiffness demands. Figure 175 through Figure 181 present an upper bound case that the diaphragms have almost infinite stiffness and a lower bound case that no diaphragms are provided at all. The obvious difference between the two cases is that the no-diaphragm case failed to reach convergence at total applied loads greater than of 214 kips (952 kN), roughly 63% of the targeted 340 kips (1512 kN). The bulbs and webs predominantly resist the longitudinal bending of the girder, so little effect of diaphragm stiffness is observed in the vertical deflection of the bulbs at midspan in Figure 175 and the longitudinal strain on the top and bottom surfaces of that portion of the girder in Figure 180 and Figure 181. In the rigid-diaphragm case, the midspan middeck deflection decreases and becomes almost linear as shown in Figure 176 while, as expected, the leg spreading is significantly reduced at both midspan and support as illustrated in Figure 178 and Figure 179. Figure 182 provides contour plots of maximum principal stress for the rigid-diaphragm case. Compared to Figure 132, the inelastic region experiencing tensile cracking on the deck underside is significantly reduced. The applied load is more efficiently carried to the adjacent girder legs and then to the supports. Without the spreading resistance provided by the diaphragms, the deck experiences very large deformation and spreading of the legs is not sufficiently restrained. Figure 183(b) shows that the underside of the deck exhibits significant tensile inelasticity even at the much smaller ultimate load of 214 kips (952 kN) in the no-diaphragm case.

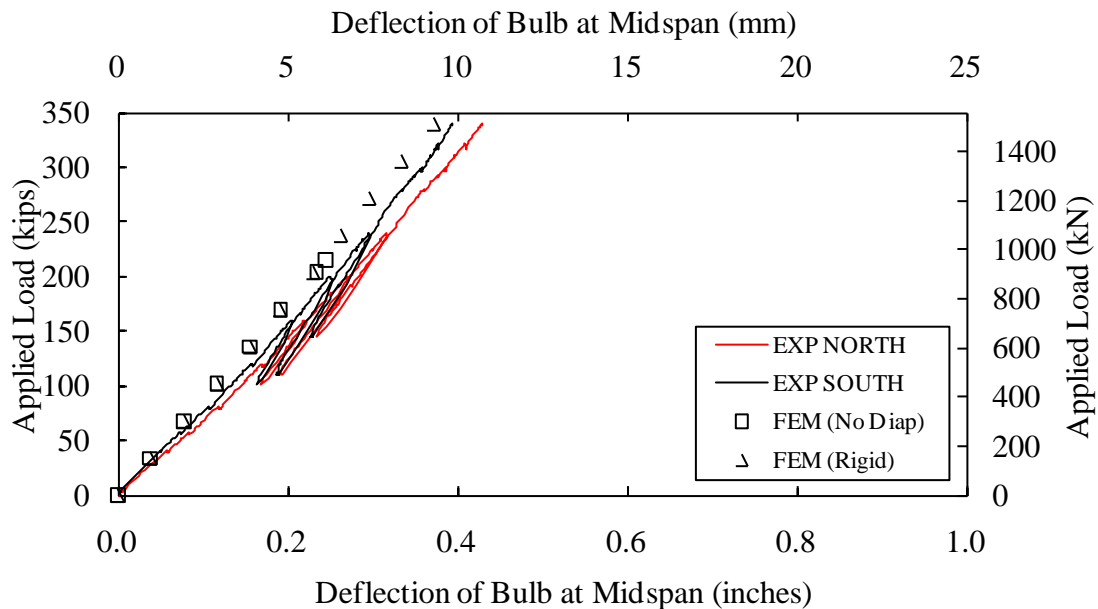


Figure 175. Graph. Effect of rigid and no diaphragms on the vertical deflection of the bulbs at midspan.

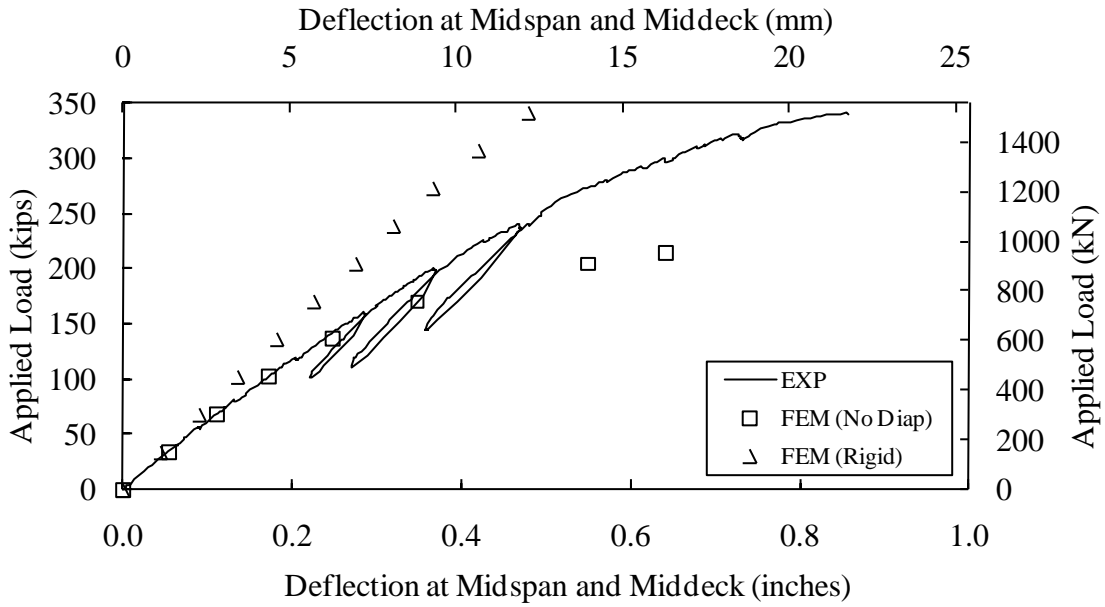


Figure 176. Graph. Effect of rigid and no diaphragms on the vertical deflection at the midspan middeck location.

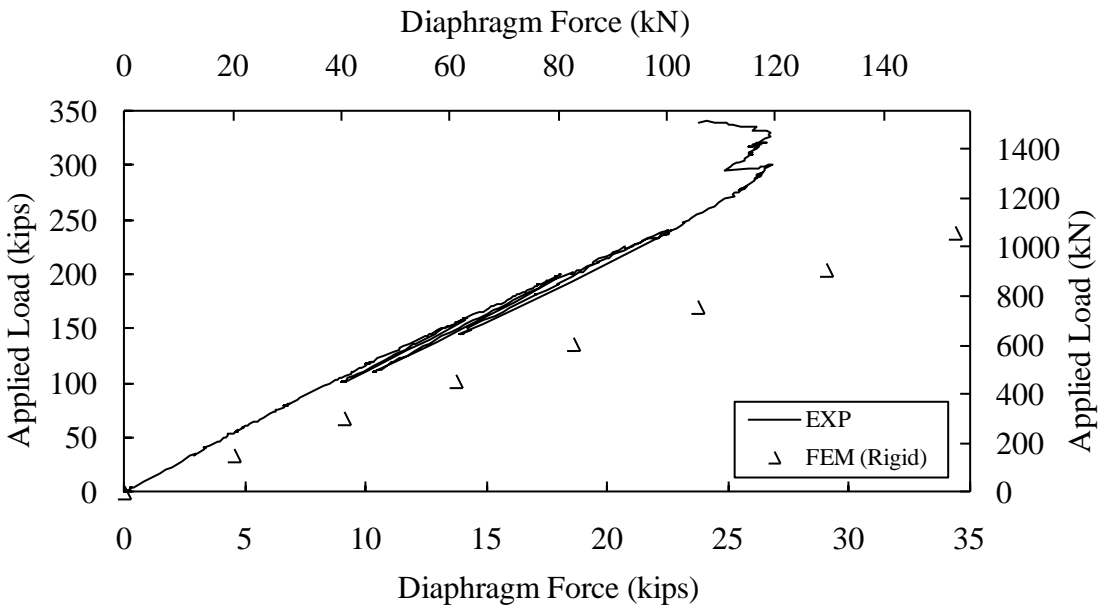


Figure 177. Graph. Effect of rigid diaphragms on the diaphragm force.

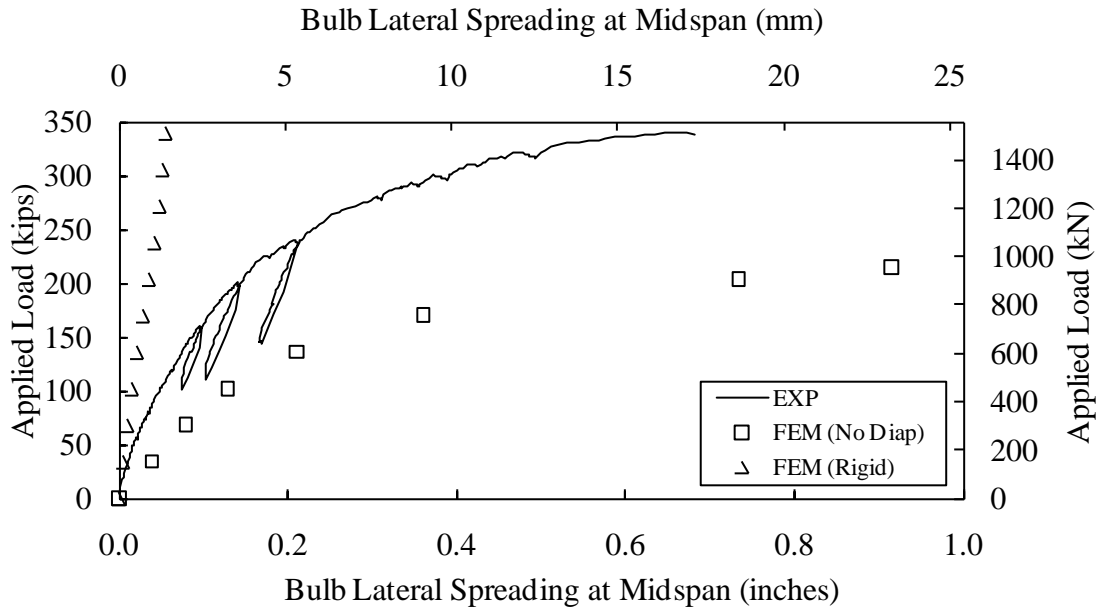


Figure 178. Graph. Effect of rigid and no diaphragms on the bulb lateral spreading at midspan.

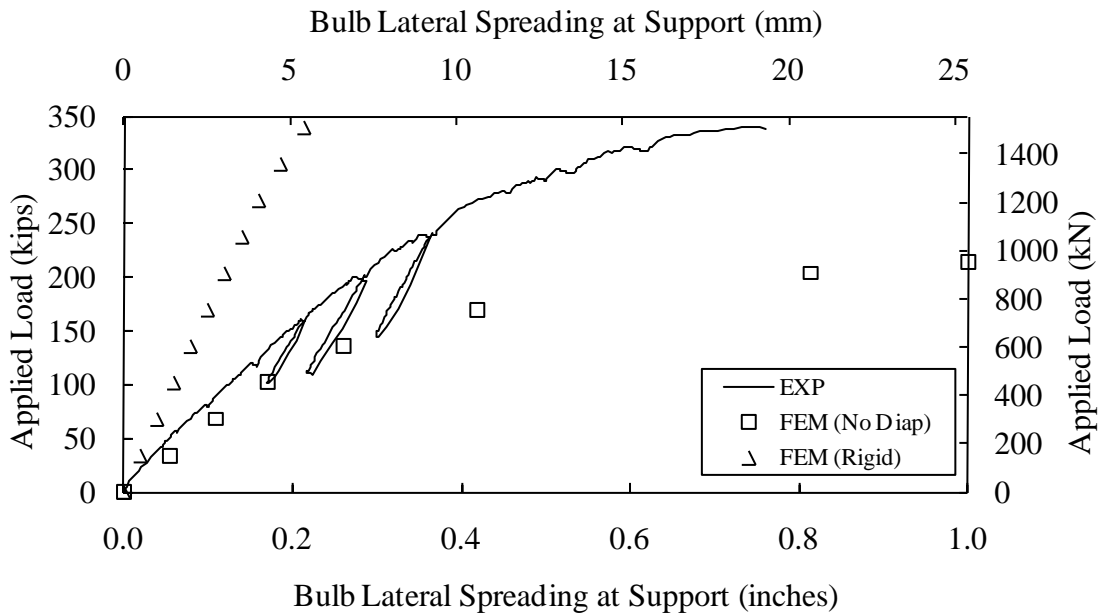


Figure 179. Graph. Effect of rigid and no diaphragms on the bulb lateral spreading at support.

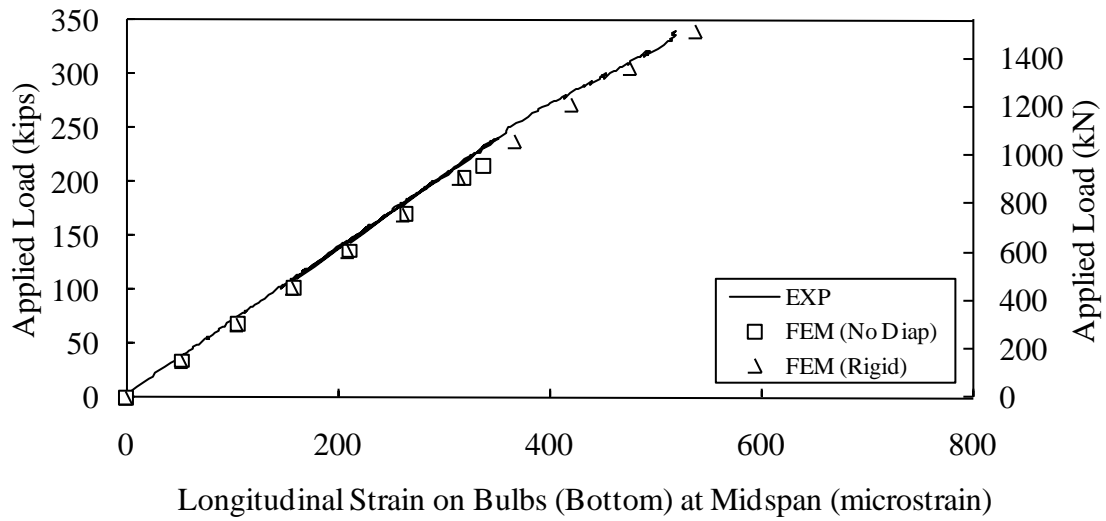


Figure 180. Graph. Effect of rigid and no diaphragms on the longitudinal strain on the bottom surface of the north bulb at midspan.

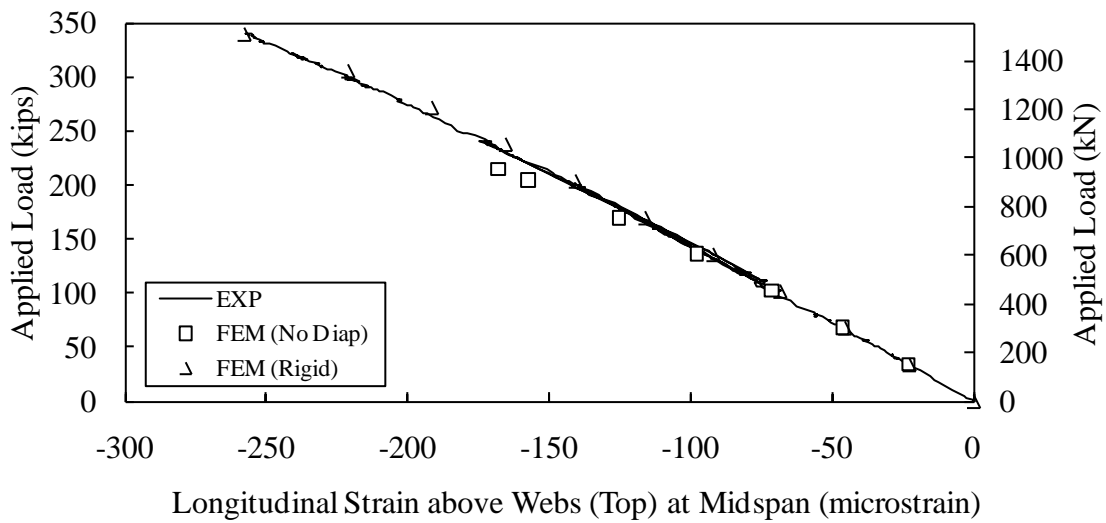
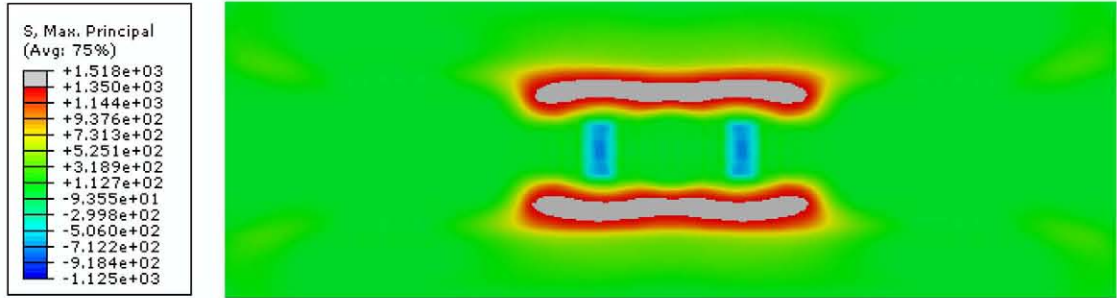
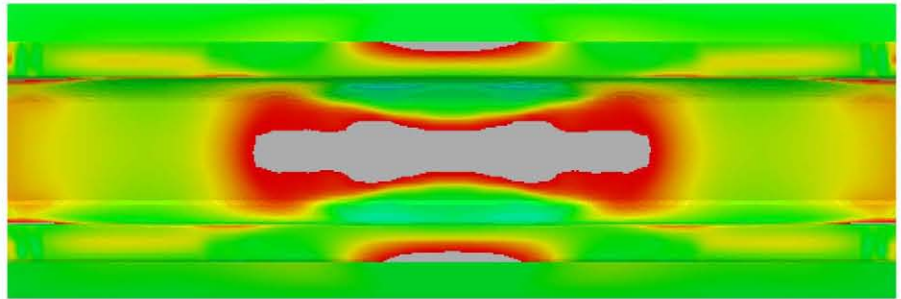


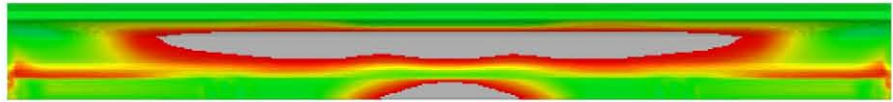
Figure 181. Graph. Effect of rigid and no diaphragms on the longitudinal strain on the deck immediately above the web at midspan.



(a)



(b)



(c)

Figure 182. Graph. FEM predicted maximum principal stress as viewed from (a) above, (b) below and (c) beside the girder for the rigid-diaphragm case.

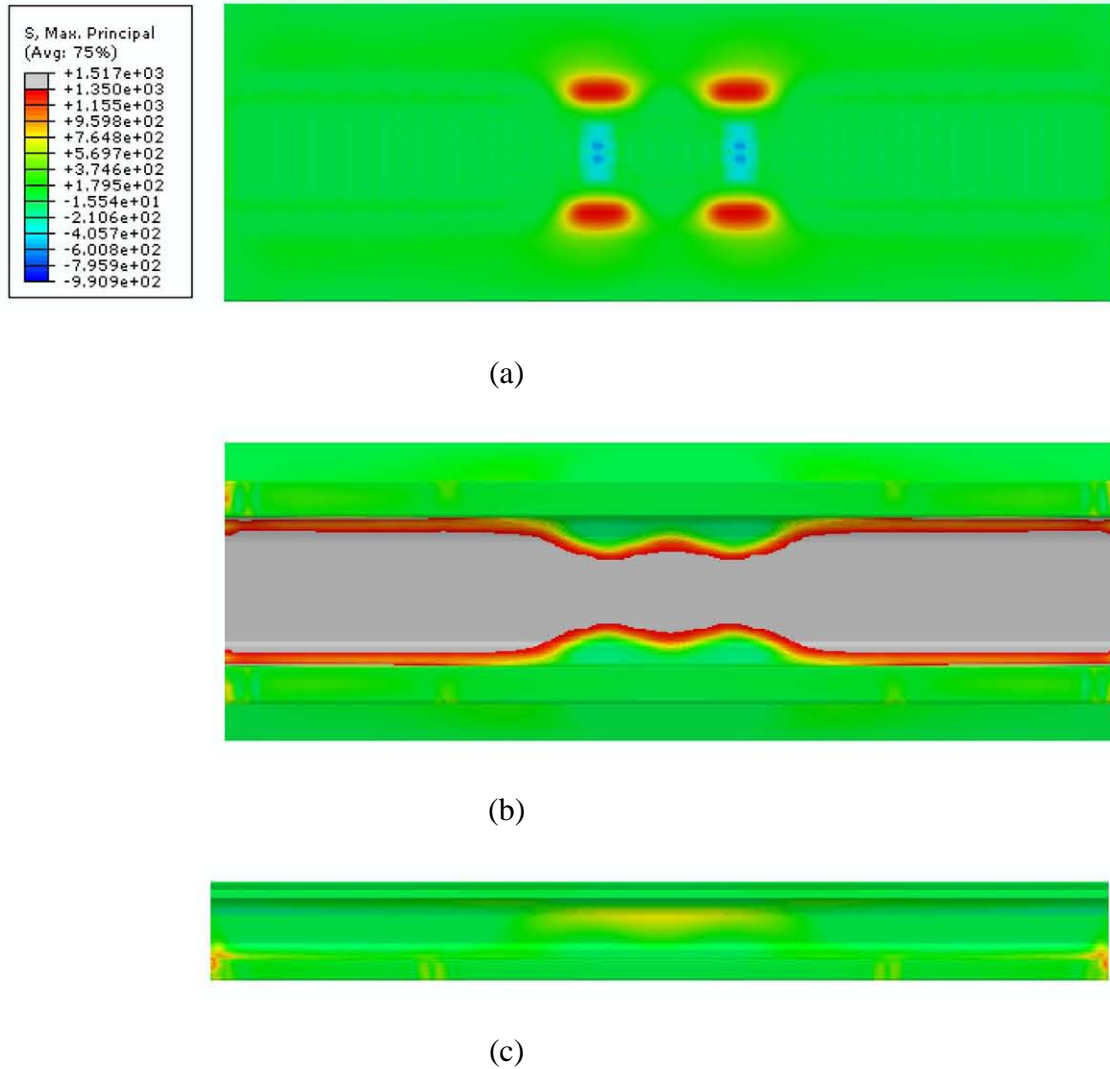


Figure 183. FEM predicted maximum principal stress as viewed from (a) above, (b) below, and (c) beside the girder for the no-diaphragm case at an ultimate load of 215 kips (954 kN).

Transverse #5 reinforcement in the deck

As discussed in reference (14), there were two similar tests conducted on as-fabricated pi-girders, namely, Test T1D and Test T2D. The only difference between the specimens is that the pi-girder for Test T1D did not contain transverse #5 reinforcement in the deck. Test T1D was halted at a peak applied load 221 kips (983 kN) due to concern with tensile force being carried by diaphragms and the need for their reuse in the following test, Test T2D. However, a FEM model for Test T1D can simulate the remainder of this test and examine the effect of transverse reinforcement when compared to the original model for Test T2D. The T1D model failed to reach convergence at applied loads greater than 308 kips (1370 kN). Figure 184 through Figure 190 compare the results generated by the models for T1D and T2D. Absence of transverse

reinforcement results in somewhat larger deck deflection and increase of diaphragm force when the applied load exceeded approximately 200 kips (890 kN). From Figure 191 at the Test T2D ultimate load of 340 kips (1512 kN), the rebar in the deck are still elastic with highest stresses occurring due to stress concentration near the loading areas.

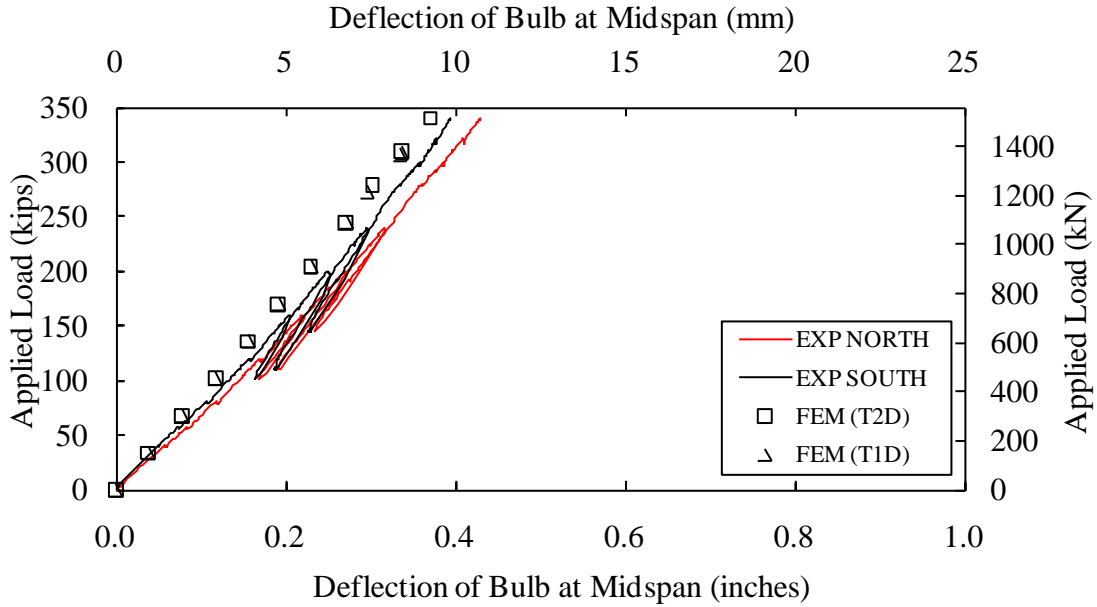


Figure 184. Graph. Effect of deck transverse reinforcement on the vertical deflection of the bulbs at midspan.

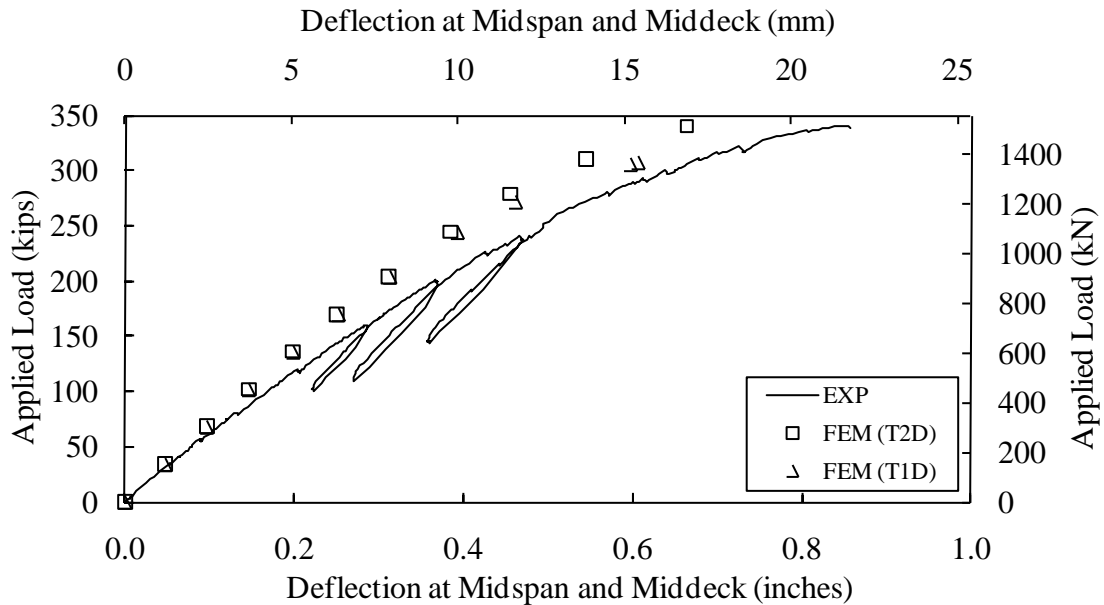


Figure 185. Graph. Effect of deck transverse reinforcement on the vertical deflection at the midspan middeck location.

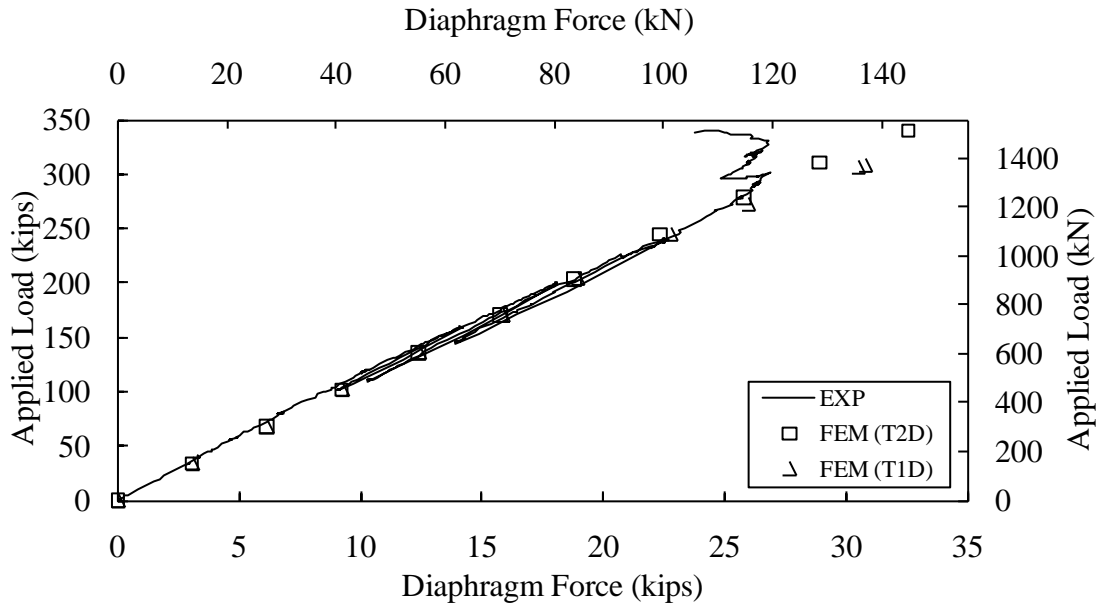


Figure 186. Graph. Effect of deck transverse reinforcement on the diaphragm force.

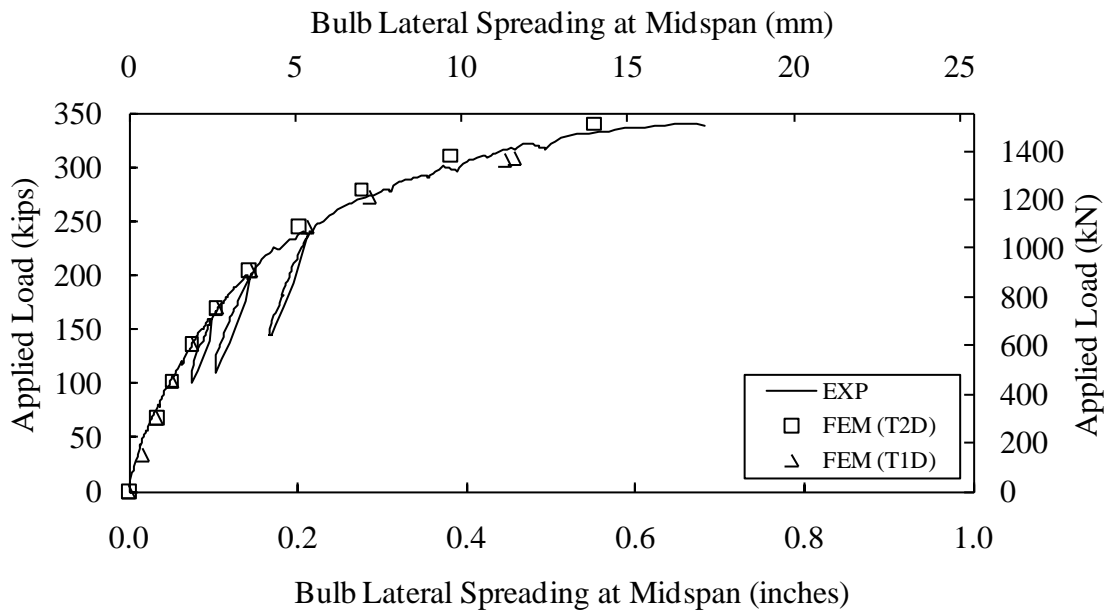


Figure 187. Graph. Effect of deck transverse reinforcement on the bulb lateral spreading at midspan.

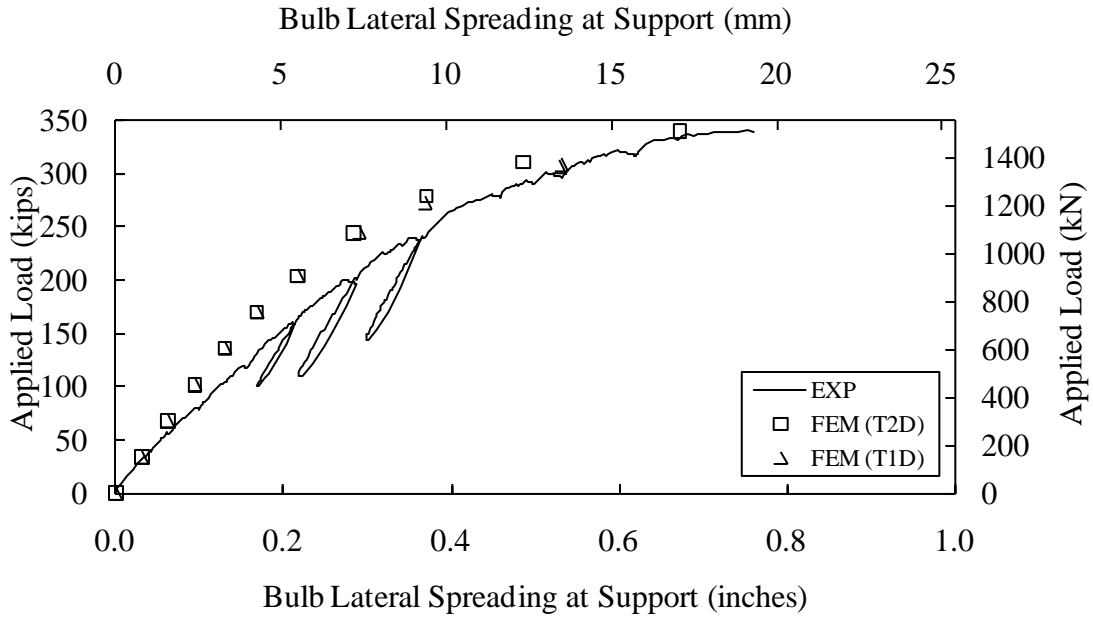


Figure 188. Graph. Effect of deck transverse reinforcement on the bulb lateral spreading at support.

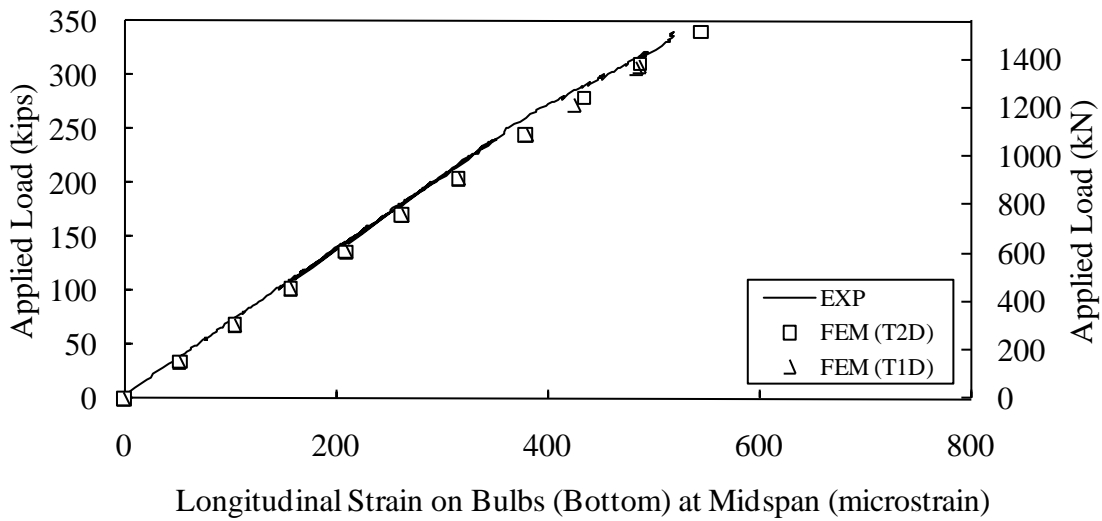


Figure 189. Graph. Effect of deck transverse reinforcement on the longitudinal strain on the bottom surface of the north bulb at midspan.

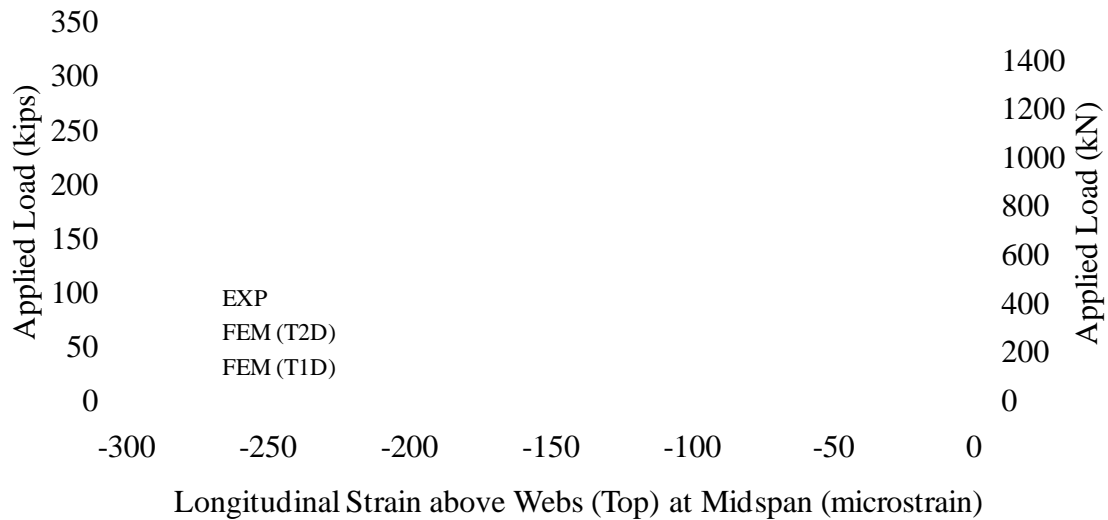


Figure 190. Graph. Effect of deck transverse reinforcement on the longitudinal strain on the deck immediately above the web at midspan.

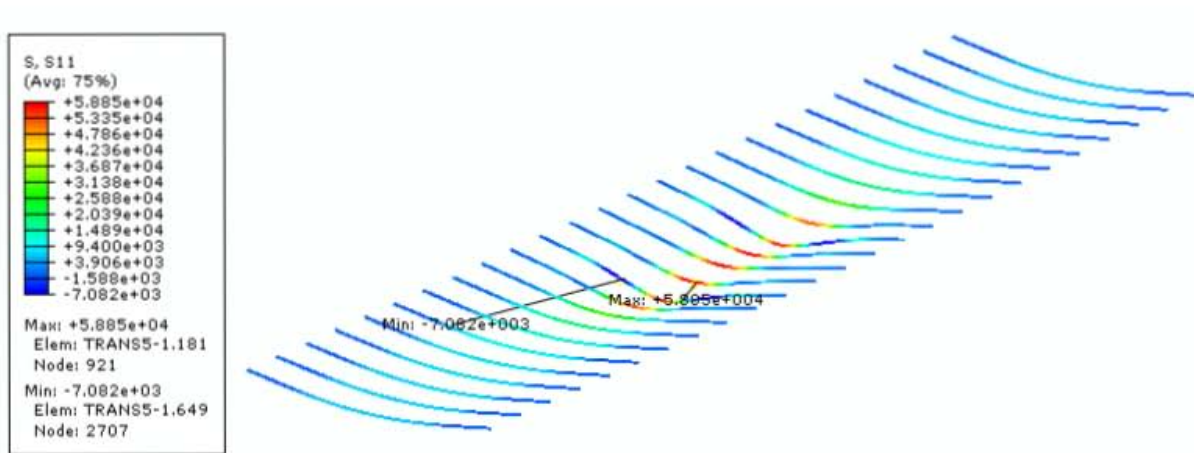


Figure 191. Graph. FEM predicted stress and deformation in the transverse deck reinforcement (Note: deformation scale factor = 20).

CONCLUSIONS

Based on the results of the above parametric studies compared to the experimentally observed flexural response of a UHPC pi-girder in Test T2D, the following conclusions are presented.

1. The mesh sensitivity of this model is quite low. A 2-inch (51-mm) seeded mesh can capture pi-girder behavior reasonably well. There is minimal difference between the

results of 2-inch (51-mm) seeded mesh and 3-inch (76-mm) seeded mesh. Note that deck and webs were partitioned to have four layers through their thickness, as these portions of the pi-girder in this experimental setup were subjected to significant bending forces.

2. The concrete damaged plasticity model implemented herein replicates the observed strain and deflection responses using three definitions of concrete tension stiffening moderately well, while the concrete smeared cracking model fails to converge at reduced load levels.
3. The maximum tensile stress of UHPC plays a significant role in the predicted finite element model response. A value of 1.4 ksi (9.7 MPa) produces reasonable results. Also, a Young's modulus of 7650 ksi (53 GPa) is a reasonable estimate for the UHPC modeled herein.
4. The maximum tensile plastic strain is a limiting value beyond which the model will not converge. Similarly, the girder loses capacity at strain localization caused by fiber pullout. Models may be defined to include a larger value of ultimate tensile plastic strain than that was normally observed in experiments to ensure the models capable of converging to the observed ultimate loads. However, in this case the predicted maximum tensile plastic strain is approximately 0.01, which is near a typical observed limiting value.
5. Diaphragms play a significant role in maintaining structural integrity and allowing the cross section to carry the applied loads. Stronger and stiffer diaphragms would have allowed for enhanced performance in the modeled tests. Reducing diaphragm stiffness significantly impacts the transverse flexural response and thus reduces the overall capacity of the pi-girder.
6. Transverse reinforcement in pi-girder deck can reduce tensile strains and deflections in the middeck region at loads which would have caused damaging inelastic response in this region. This could potentially result in an increase the structural capacity, although it has little effect on the elastic response of the girder.

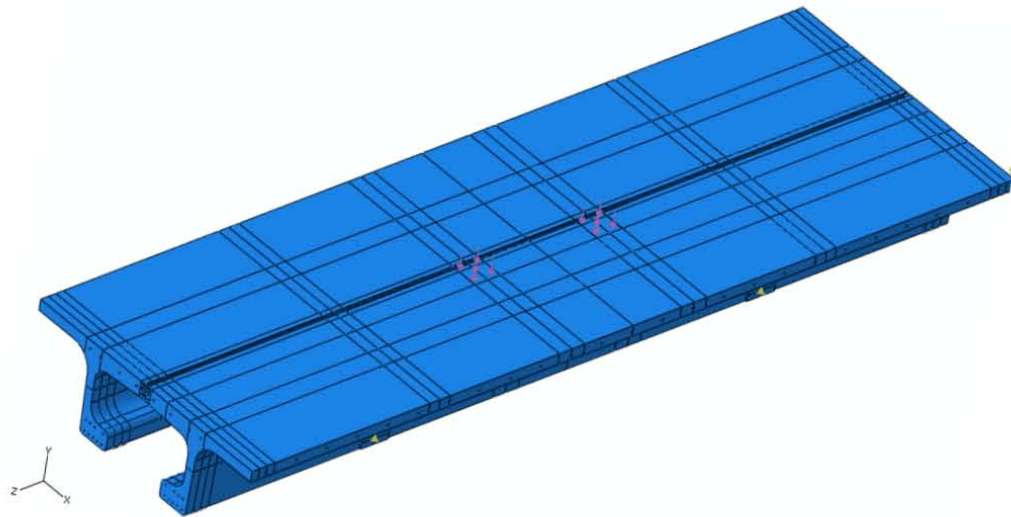
CHAPTER 7. PI-GIRDER WITH JOINT

FINITE ELEMENT MODEL

Tests T1J and T2J were in many ways similar to Tests T1D and T2D. From a finite element modeling standpoint, the significant addition is the modeling of the behavior of the grouted connection. A three dimensional pi-girder model as shown in Figure 192 was developed to simulate both linear and nonlinear behaviors of the pi-girder with joint in Tests T1J and T2J. Figure 192(a) covers the whole model while Figure 192(b) shows the embedded rebar and strands including #8 bars in the joint. Since the specimen tested in Test T2J was created from the specimen previously used in Test T2D, the UHPC kept the same properties on the assumption that Test T2D did not alter the material significantly in the areas subjected to high stresses in Test T2J. The girder used partitions for convenience of defining loading areas, diaphragms, and supports. The girder with joint was supported vertically by linear springs and constrained by linear springs of 1 lb/inch (0.175 N/mm) stiffness in transverse x-direction to eliminate large rigid body movement. Element types and prestressing of strands are kept the same as was used in the pi-girder model presented in Chapter 6.

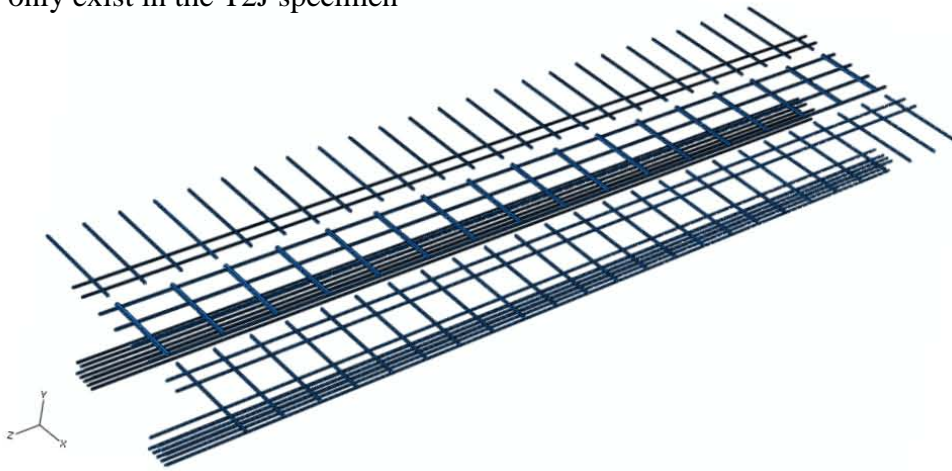
In Test T2J, the diamond-shaped shear key is grouted by a magnesium phosphate grout, called Eucospeed MP. The mechanical properties of this grout, tested according to ASTM C39⁽²³⁾ and C496⁽²⁴⁾, included an average modulus of elasticity of 5880 ksi (41 GPa) and an average compressive strength of 6.5 ksi (44.7 MPa) as reported in reference (14). The tensile behavior of the grout is assumed to follow a linear elastic relationship until the tensile stress reaches a tensile strength of 0.65 ksi (4.5 MPa), followed by a linear loss of strength after cracking defined through a fracture energy of 0.67 lb/in (120 N/m) similar to a typical response of a high-strength concrete. Table 7 gives the assumed properties for the CDP model of the grout. The key is partitioned to match the mesh of the surrounding deck with a global seed size of 2-inch (51-mm) as illustrated in Figure 193. Matching of the mesh geometry is necessary in order to reduce the convergent difficulty of the contact interaction between the key and deck.

In addition to the modeling of Test T2J, an alternative model was created to simulate the performance of Test T1J. The T1J specimen does not have transverse reinforcing #5 bars in the flanges projecting out from the webs as noted in Figure 192(b). Lack of the transverse reinforcement in the outside flanges is expected to have minimal impact on the girder's structural behavior. The only significant difference between Tests T1J and T2J was that Test T1J used field-cast UHPC as the grout in the joint. As such, the performance of these grouting materials was the focus of comparison between Tests T2J and T1J. The average compressive strength of the field-cast UHPC in the T1J joint was 29 ksi (200 MPa). The modulus of elasticity for the field-cast UHPC was assumed to be 7860 ksi (54 GPa) based on the relationship presented in reference (16). The tensile behavior of the UHPC assumes linear elastic perfectly plastic stress-strain relationship with a tensile strength of 1.4 ksi (9.7 MPa), as was illustrated schematically in Figure 35. Table 8 provides the assumed properties for the CDP model of the field-cast UHPC.



(a)

Reinforcing bars in each flange
only exist in the T2J specimen



(b)

Figure 192. Illustration. (a) Full pi-girder with joint model, and (b) hidden rebar and strands embedded in UHPC.

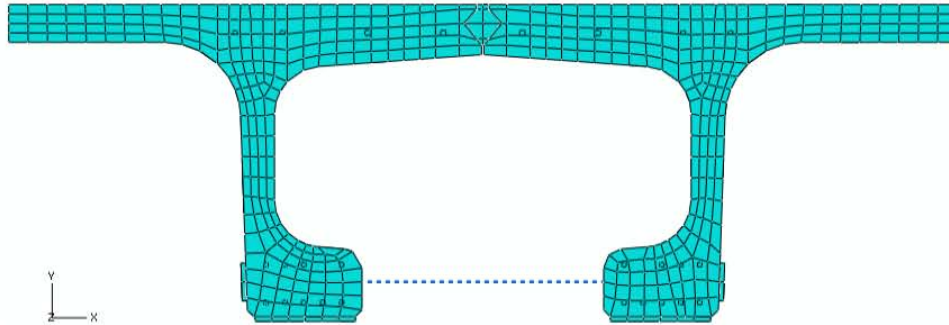


Figure 193. Illustration. Pi-girder with joint model with a 2-inch (51-mm) seeded mesh.

Table 7. Material parameters for the CDP model of the magnesium phosphate grout used in Test T2J.

Density, lb/ft ³ (kg/m ³)	155 (2485)
Concrete elasticity	
E, ksi (GPa)	5880 (41)
ν	0.15
Concrete compression hardening	
Compressive stress, ksi (MPa)	Plastic strain (-)
2.0 (13.8)	0.000000
2.6 (17.9)	0.000020
4.0 (27.6)	0.000060
5.2 (35.9)	0.000154
6.5 (44.8)	0.000760
5.2 (35.9)	0.002600
2.6 (17.9)	0.005700
0.7 (4.80)	0.012000
Concrete tension stiffening	
Maximum tensile stress, ksi (MPa)	Fracture energy lb/inch (N/m)
0.65 (4.5)	0.67 (120)
The parameter of CDP model	
Dilation angle	15°
Eccentricity	0.1
fb0/fc0	1.16
K	2/3
Viscosity parameter	0

Table 8. Material parameters for the CDP model of the field-cast UHPC used in Test T1J.

Density, lb/ft ³ (kg/m ³)	160 (2565)
Concrete elasticity	
E, ksi (GPa)	7860 (54)
ν	0.18
Concrete compression hardening	
Compressive stress, ksi (MPa)	Plastic strain (-)
14.8 (102.0)	0.0000000
16.9 (116.5)	0.0000284
21.4 (147.6)	0.0000720
25.3 (174.4)	0.0001410
29.0 (200.0)	0.0004140
Concrete tension stiffening	
Maximum tensile stress, ksi (MPa)	Plastic strain (+)
1.4 (9.7)	0.000
1.4 (9.7)	0.010
0.0 (0.0)	0.011
The parameter of CDP model	
Dilation angle	15°
Eccentricity	0.1
f_{b0}/f_{c0}	1.16
K	2/3
Viscosity parameter	0

The ultimate tensile plastic strain used to defining the concrete tension stiffening in Table 4 is revised from 0.01 to 0.025, at least twice larger than what was normally observed for a typical UHPC material, in the following pi-girder with joint models. These finite element models assume that the center of the supporting reaction is always aligned with the longitudinal centerline of the bulb. However, in the physical test, the elastomeric pads allowed the center of the supporting reaction to migrate outward as the bulbs rotated inward with respect to an increasing applied load. Even though the model greatly simplifies the supporting mechanism, it also generates artificially larger plastic tensile strain on the exterior surface of the girder webs. Other than the webs at the reaction points, the whole girder has a maximum plastic strain less than 0.008 under an applied load of 428 kips (1904 kN). The assumption of larger ultimate plastic tensile strain is done intentionally in order to project the predicted response longer and more clearly demonstrate nonlinear or global trends as compared to experimental results.

DIAPHRAGMS

Similar to the previous pi-girder model, the diaphragms were modeled as nonlinear springs. Table 9 lists the key parameters in the load-displacement response of the spring. Figure 194 plots the assumed response. In the same figure, both separate and combined contributions from the HSS5×5×1/4 tube and the two 7/8 Φ H.S. rods at each end are plotted. In Test T2J, the end plates

retained their as-fabricated thickness of 0.5 inch (12.7 mm). The diaphragm elongation is dominated by the tube and rods when the force is less than 10 kips (44 kN), after which the deformation of end plates begins to play an increasingly important role. The elongations of the tube and rods were computed analytically from axial loads based on their lengths and cross section areas. Because of the shorter length and thicker end plates, the diaphragm in Test T2J is stiffer than the one used in Test T2D. The nonlinear springs were connected to steel plates adjacent to the outside face of the bulbs as illustrated in Figure 193.

Table 9. Properties of the nonlinear springs which replicate the diaphragms in the pi-girder with joint tests.

Axial Force, kip (kN)	Axial Elongation, inch (mm)
-10 (-44)	-0.0095 (-0.241)
0 (0)	0.0000 (0.000)
5 (22)	0.0046 (0.117)
10 (44)	0.0095 (0.241)
15 (67)	0.0154 (0.391)
20 (89)	0.0252 (0.640)
25 (111)	0.0441 (1.120)
30 (133)	0.0800 (2.032)
35 (156)	0.1300 (3.302)
40 (178)	0.2000 (5.080)
50 (222)	0.4000 (10.160)

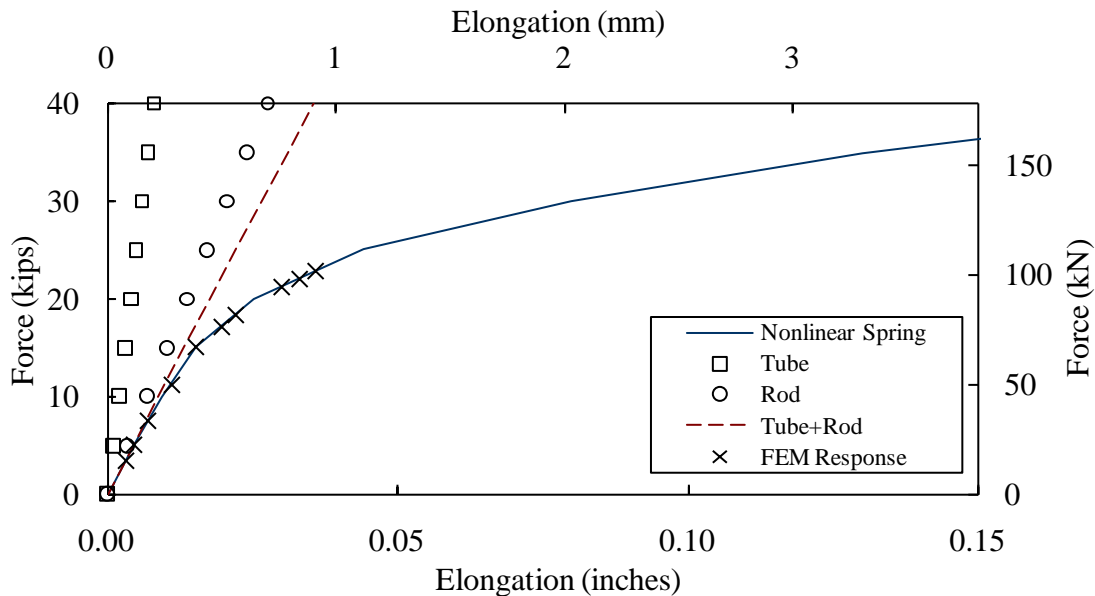


Figure 194. Graph. Behaviors of diaphragm subcomponents and assumed nonlinear spring for the diaphragms in the pi-girder with joint tests.

ELASTOMERIC PADS

Similar to the pi-girder in Test T2D, T2J was also situated on 6-inch by 12-inch (0.15-m by 0.3-m) elastomeric pads placed under the girder bulbs at the four support locations. Again, a linear spring whose properties were estimated from the experimental measurements was used to simulate the support in the vertical direction. The linear spring included a stiffness of $K = 100.7/4/0.0508 = 496$ kip/inch (87 kN/mm). Nonlinear deformation of pads was neglected due to the limited deformation information available from the experiment.

The linear springs link the centers of the bearing areas of the bulbs to the ground. It should be noted that the actual support center, especially on the north side, increasingly migrated from the centerline of the bulb outward as the bulb rotated inward with the increasing applied load. It may reduce the eccentricity of the support and result in less longitudinal bending on the web. However, this support migration was not modeled due to limited quantitative information on its specific location during the experiment.

ABAQUS RESULTS

The following results are based on the CDP models of the joint using the material parameters of the magnesium phosphate grout in Table 7 (MP-Joint case) and the material parameters of the field-cast UHPC in Table 8 (UHPC-Joint case). Both cases employ a stabilization function with default parameters ($stabilize = 0.0002$ and $allsdtol = 0.05$). The interaction between deck and joint is modeled as friction contact with a coefficient of friction equal to 0.1.

In the experiment, Test T1J used field-cast UHPC as the joint fill material and Test T2J used magnesium phosphate grout. From Figure 94 through Figure 97 in reference (14), it can be observed that T1J and T2J follow similar trends with T1J being slightly stiffer.

Figure 195 through Figure 202 present the results of these finite element analyses as compared to the experimental results for Test T2J. The modeled UHPC-Joint case reaches a total applied load of 428 kips (1904 kN), which is larger than the MP-Joint case which was unable to converge above an applied load of 302 kips (1343 kN). There is minimal difference observed between the two cases in the linear stage. Due to the inability to converge at higher loads, the MP-Joint case did not exhibit significant nonlinear effect. The UHPC-Joint case can capture the nonlinearity of the vertical displacement at middeck midspan locations quite well as illustrated in Figure 196. Figure 195 shows that the FEM predicted vertical displacements of the bulbs at midspan are slightly stiffer when compared to experimentally observed data. The difference between the UHPC-Joint case prediction and the experimental response is almost constant until the response becomes nonlinear.

Figure 197 and Figure 198 demonstrate that the diaphragm force and bulb lateral spreading are approximated reasonably well by the nonlinear spring diaphragm until the applied load exceeds 340 kips (1512 kN). The increasing difference after the applied load of approximately 270 kips (1201 kN) observed in Figure 197 and Figure 198 cannot be reconciled by adjusting the

proposed nonlinear spring properties for the diaphragms alone. Specifically, less stiff nonlinear springs for diaphragms could be proposed for an axial load exceeding 21 kips (93 kN) in order to allow larger bulb lateral spreading at midspan. However, the less stiff springs would attract less diaphragm force, which would thus result in larger difference observed in Figure 197. Simplification of joint connection detail from that shown in Figure 23 may contribute to a portion of the difference between the FEM and experimental results.

Figure 199 illustrates the longitudinal strain on the bottom surfaces of the bulbs at midspan. FEM predicts the strains of both the north and south bulbs fairly well when an applied load is less than 250 kips (1112 kN). With a higher applied load, the experimental strain data captured by surface-mounted resistance gages in these tensile areas became either highly nonlinear or no longer reliable while both modeled cases only show slightly nonlinear behavior.

Figure 200 illustrates the longitudinal strain on the deck immediately above the webs at midspan. The longitudinal strain in the experiment becomes increasingly nonlinear on both the north and south sides after the applied load reaches 160 kips (712 kN) while the FEM results are generally more linear during the whole process.

Figure 201 plots the transverse deformation of the joint at midspan, with reference to the measurement setup shown in Figure 28. The separation under the joint predicted in both finite element models is significantly smaller. The UHPC-Joint case is slightly stiffer than the MP-Joint case, reflecting that UHPC grouting material is stiffer than the magnesium phosphate grout. On the top of the joint, the experiment also has larger compressive deformation than the finite element models. Embedment of the #8 dowel bars in the UHPC deck in the finite element models rather than in the pockets filled with either of the grouting materials in the real structures may also have artificially stiffened the model reported joint connection performance.

Figure 202 presents the axial strains in the dowel bars embedded in the midspan and quarterspan points compared with the experimental measurements obtained from Test T2J. The experimental strain measurements are initially similar to the model predictions, but become increasingly larger than the predictions, at both midspan and quarterspan points as inelastic behaviors are encountered. This is consistent with the observation in Figure 201 because the larger separation under the joint would induce larger axial strain in the bars across the joint.

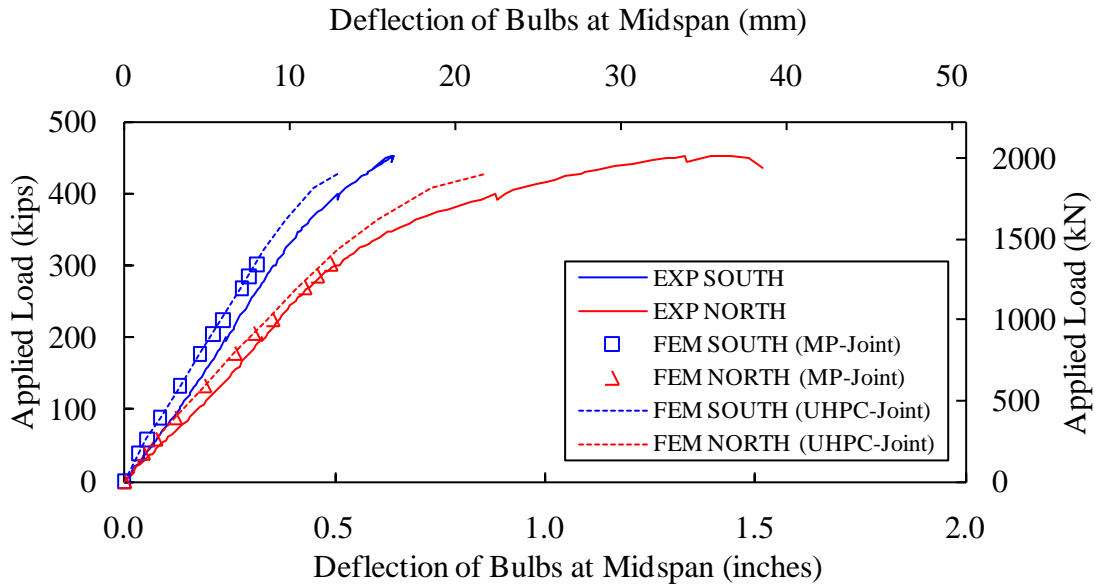


Figure 195. Graph. FEM vs. experimentally observed vertical deflection of the bulbs at midspan in Test T2J.

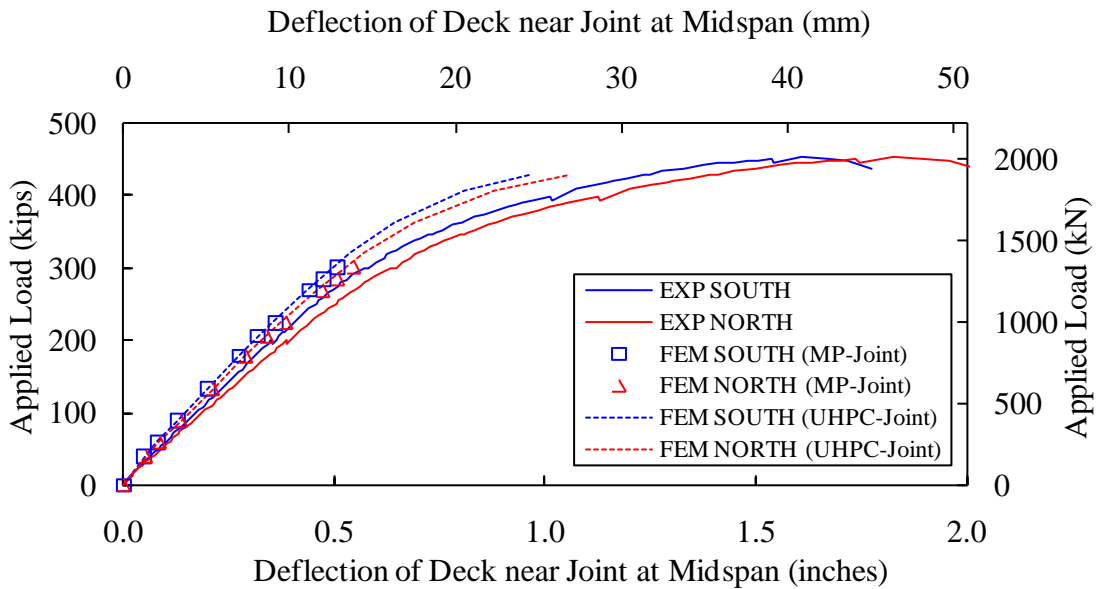


Figure 196. Graph. FEM vs. experimentally observed vertical deflection of the deck near the joint at midspan in Test T2J.

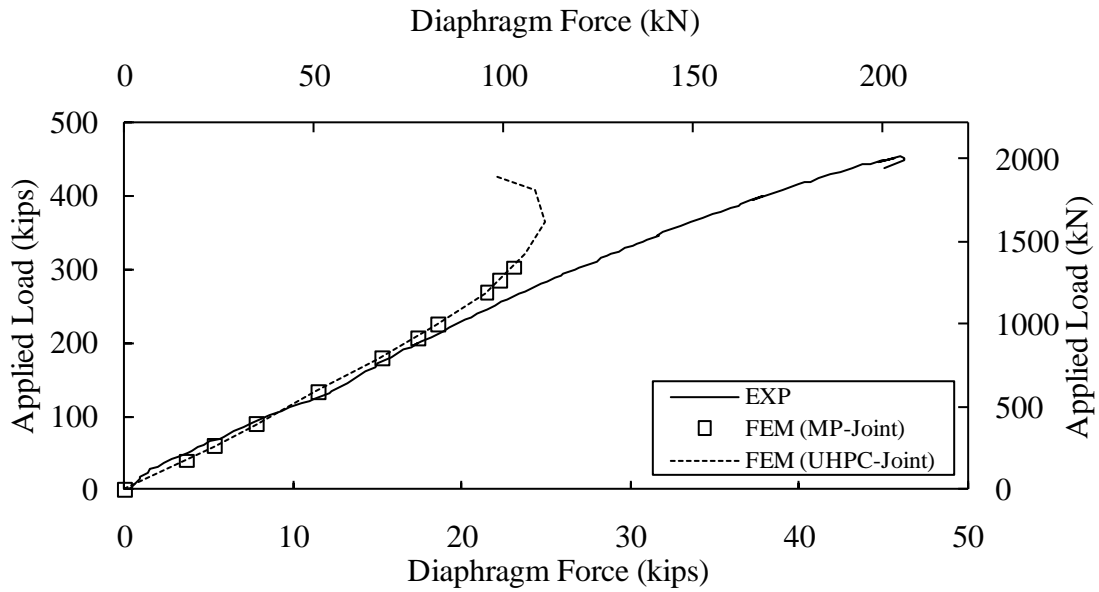


Figure 197. Graph. FEM vs. experimentally observed diaphragm force in Test T2J.

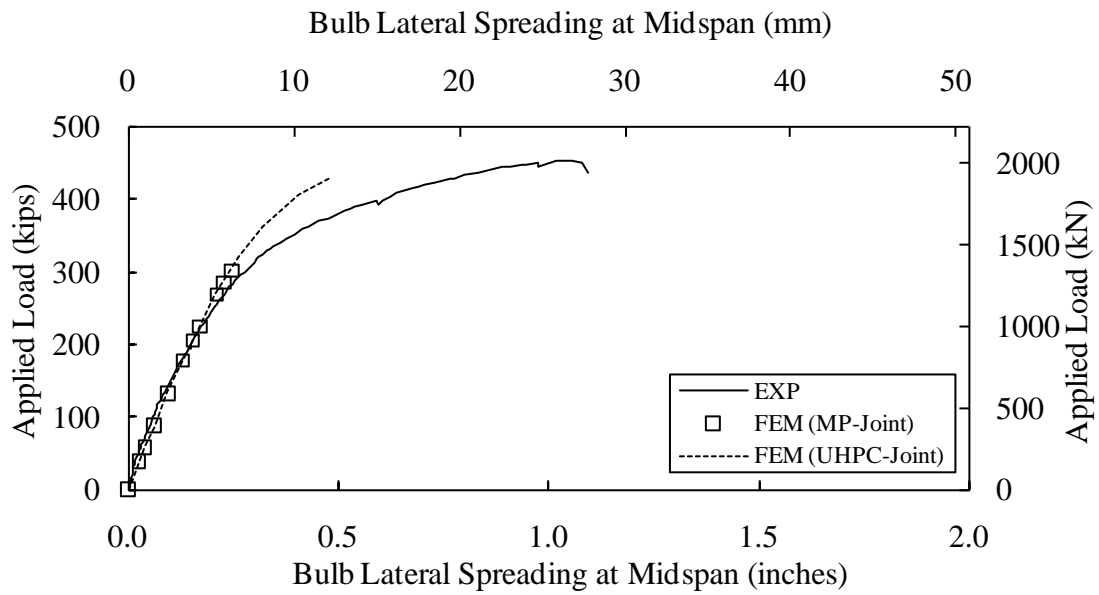


Figure 198. Graph. FEM vs. experimentally observed bulb lateral spreading at midspan in Test T2J.

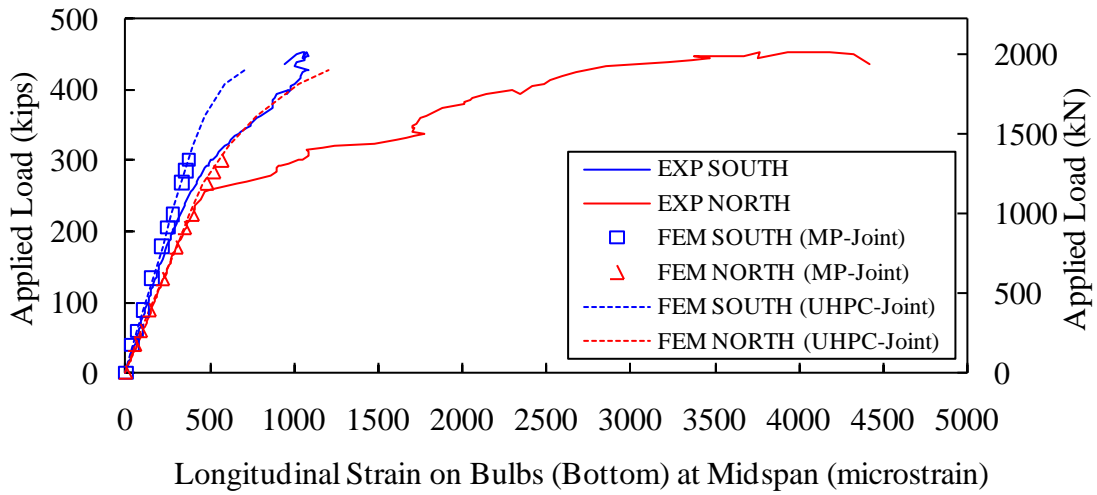


Figure 199. Graph. FEM vs. experimentally observed longitudinal strain on the bottom surfaces of the bulbs at midspan in Test T2J.

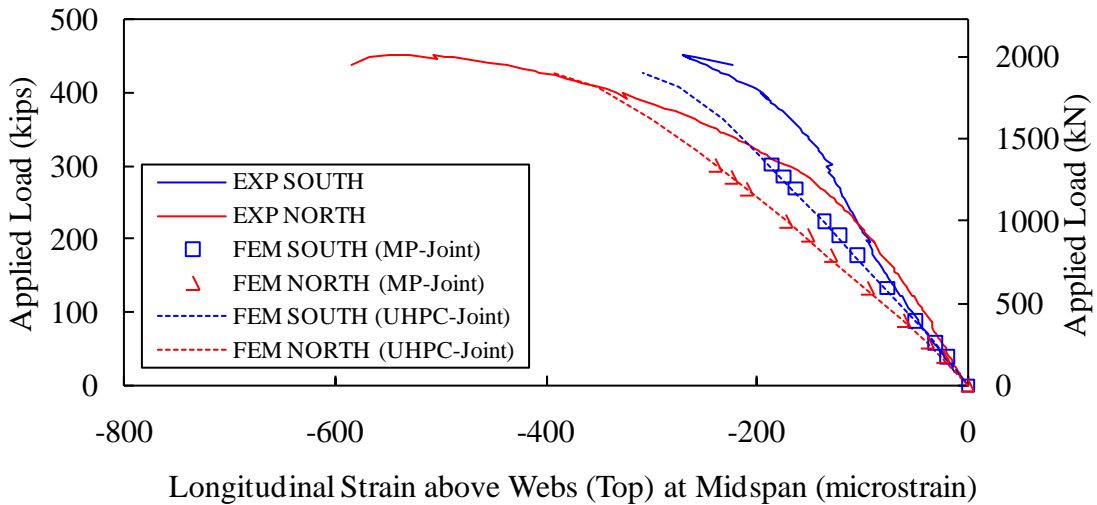


Figure 200. Graph. FEM vs. experimentally observed longitudinal strain on the deck immediately above the webs at midspan in Test T2J.

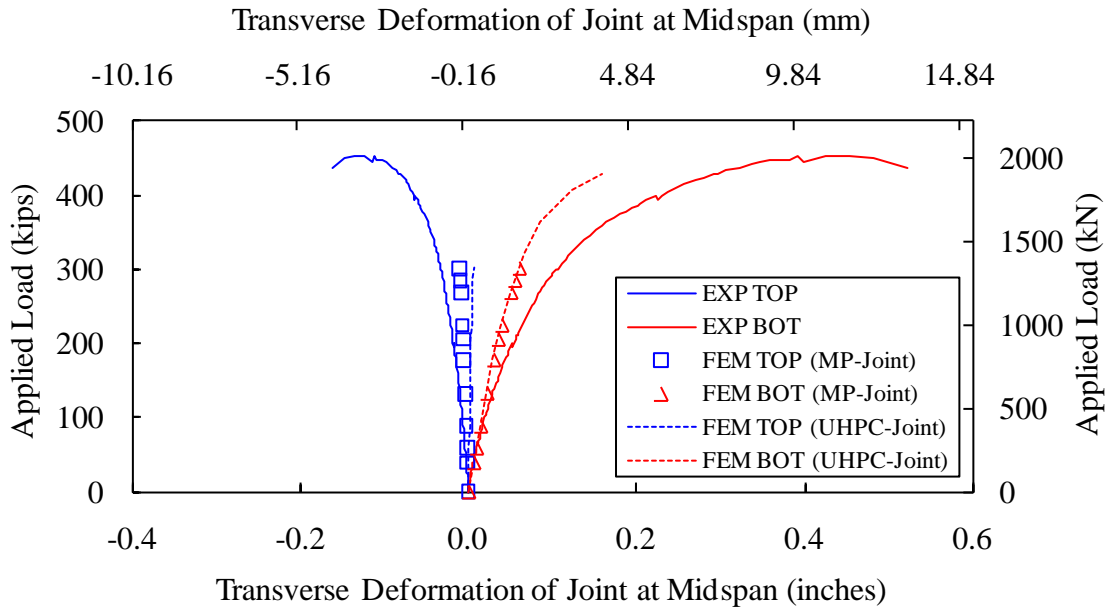


Figure 201. Graph. FEM vs. experimentally observed transverse deformation of the joint at midspan in Test T2J.

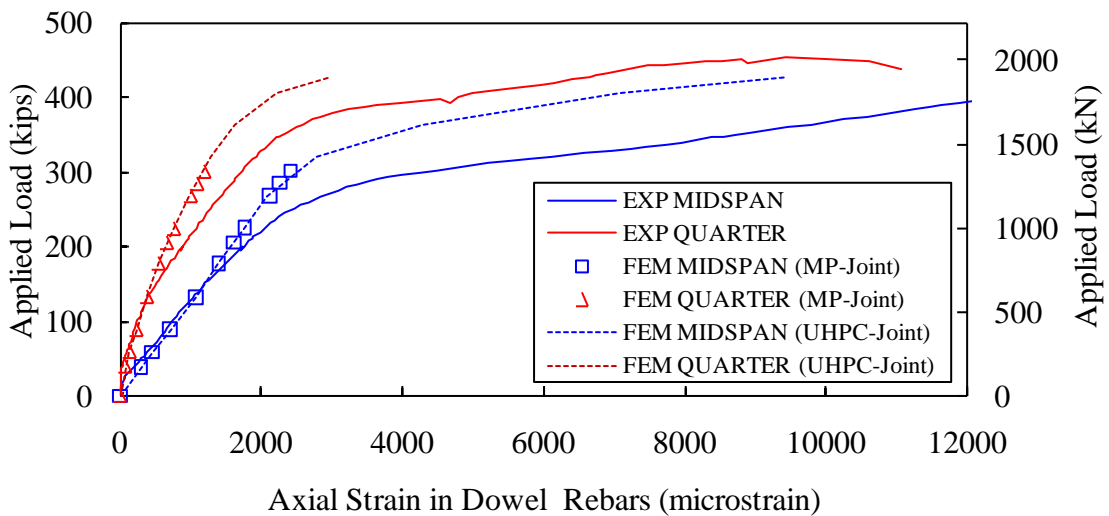


Figure 202. Graph. FEM vs. experimentally observed axial strains in the dowel bars at the midspan and quarterspan in Test T2J.

As mentioned above, the MP-Joint case was unable to converge above an applied load of 302 kips (1343 kN). The numerical convergence difficulty reflects the local failure of the

diamond-shaped shear key under compressive crushing, which was also observed experimentally toward the conclusion of Test T2J. Figure 203 illustrates the contour plots of the minimum principal stress of the whole concrete girder (as viewed from above) and zoomed-in shear key (as viewed through a midline cross-sectional slice) under the ultimate applied load in the MP-Joint case. It is apparent that the top portions of the shear key under the loading patches experienced compressive stress status far exceeding the assumed uniaxial compressive strength of 6.5 ksi (44.7 MPa). It has been verified that a higher assumed compressive strength of the grout would result in a higher ultimate applied load. This local behavior does not present a convergence problem for the UHPC-Joint case since the field-cast UHPC has a much higher compressive strength of 29 ksi (200 MPa).

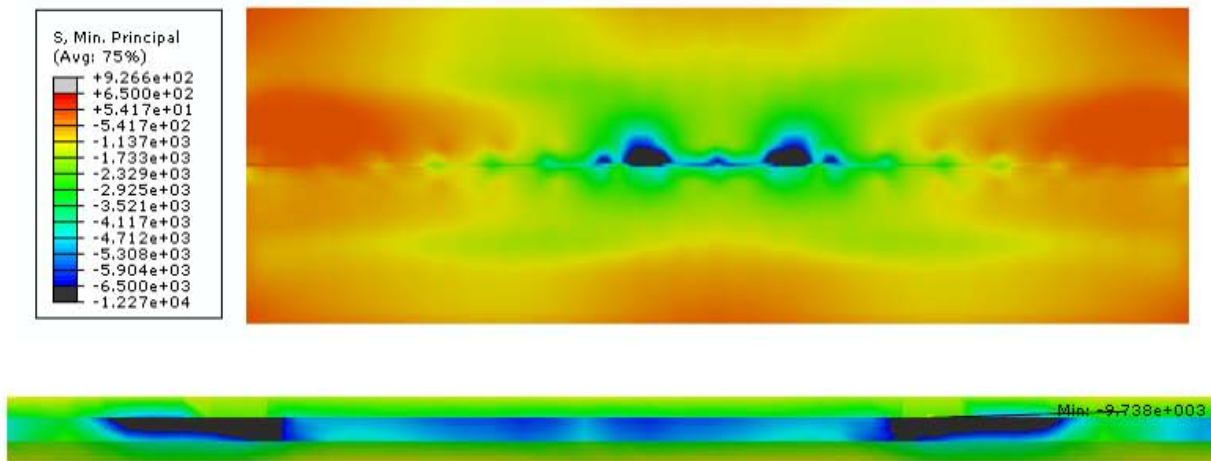


Figure 203. Graph. FEM predicted minimum principal stress in the UHPC girder and MP-Joint in Test T2J (ultimate load = 302 kips).

Figure 204 through Figure 211 present the model results from the UHPC-Joint case in comparison to the experimental results from the corresponding test, namely Test T1J. Figure 204 demonstrates that the results of the UHPC-Joint model case agree well with the experimental results on both bulbs in terms of midspan deflection. Similarly, the midspan middeck deflections compare favorably as shown in Figure 205. The diaphragm behavior also corresponds reasonably well until the modeled girder appears to collapse after an applied load of 363 kips (1614 kN) as depicted in Figure 206 and Figure 207. Adjustment on the nonlinear spring properties listed in Table 9 may not resolve the slight discrepancy. The discrepancy may be caused by the simplified modeling of the pocket details which otherwise could provide non-negligible tensile bonding force in the tensile arm of this primarily flexural section, instead of the assumed contact interaction of little friction.

Figure 208 and Figure 209 show that the finite element model replicates the longitudinal strain on the bottom surfaces of the bulbs and on the deck immediately above webs at midspan quite well; however, it should also be noted that the experimental measurement on the bottom surface of the north leg was discontinued above applied loads of 292 kips (1299 kN) due to the tensile cracking near the sensors. The longitudinal strain on the deck immediately above the webs is represented better by the models in Figure 209 than in Figure 200.

Figure 210 illustrates that the transverse deformation of the joint represented by the model initially agrees well with the experimentally observed response, and then gradually demonstrates stiffer response after an applied load of approximately 180 kips (801 kN). The experimental result of Test T1J is stiffer than Test T2J as can be seen by comparing the transverse deformation of the joint in Figure 210 to that in Figure 201.

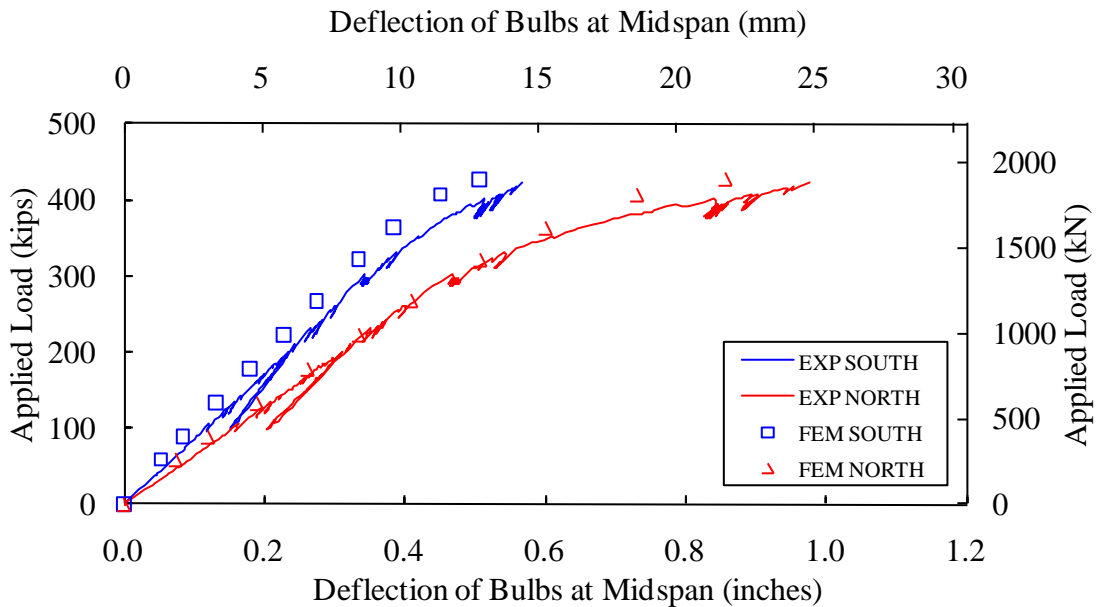


Figure 204. Graph. FEM vs. experimentally observed vertical deflection of the bulbs at midspan in Test T1J.

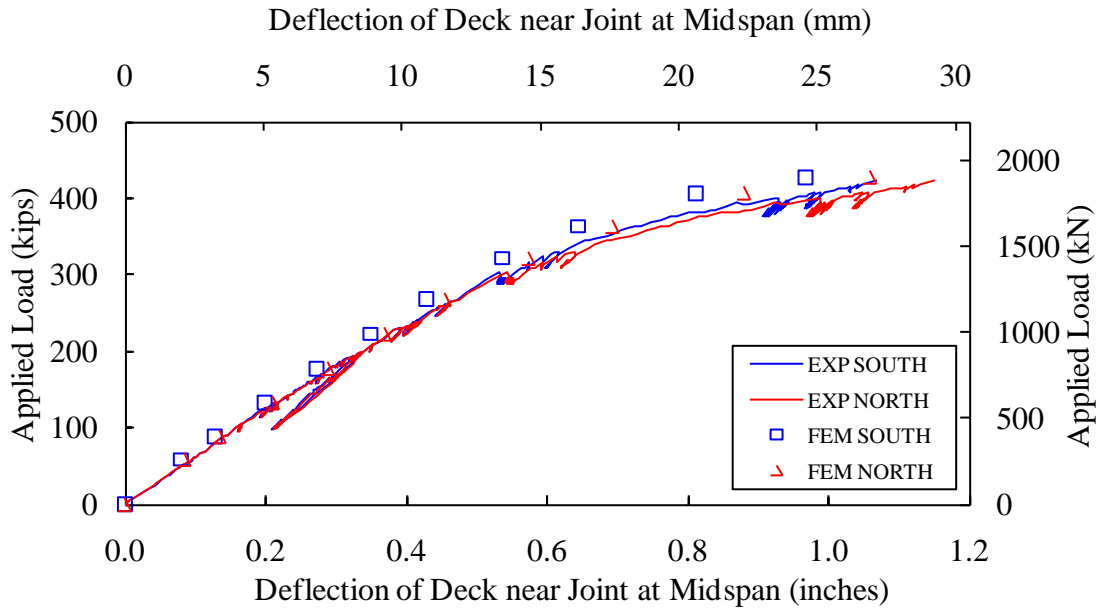


Figure 205. Graph. FEM vs. experimentally observed vertical deflection of the deck near the joint at midspan in Test T1J.

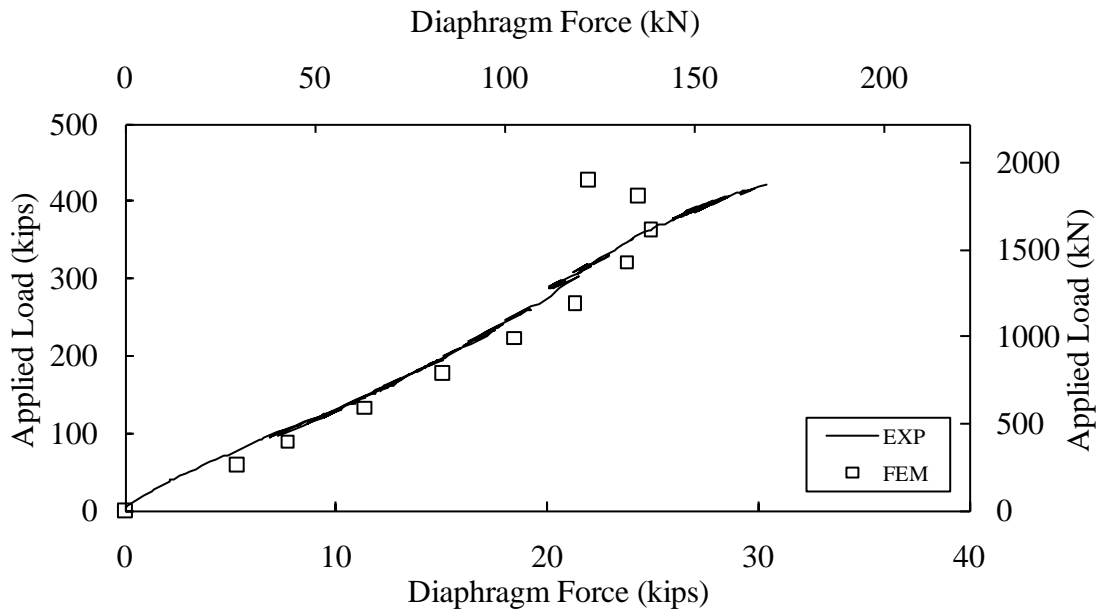


Figure 206. Graph. FEM vs. experimentally observed diaphragm force in Test T1J.

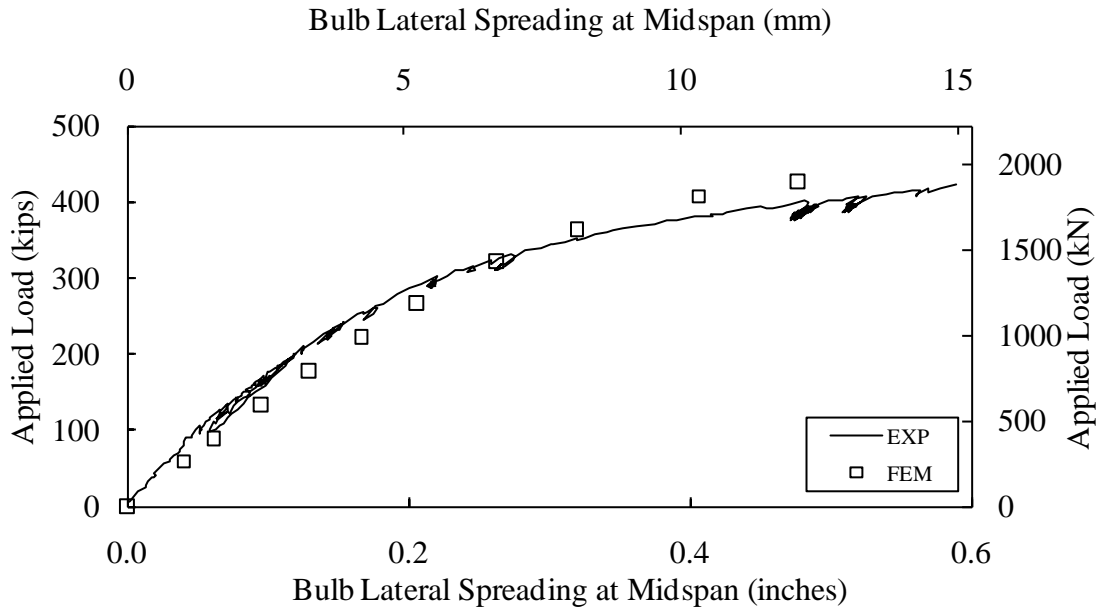


Figure 207. Graph. FEM vs. experimentally observed bulb lateral spreading at midspan in Test T1J.

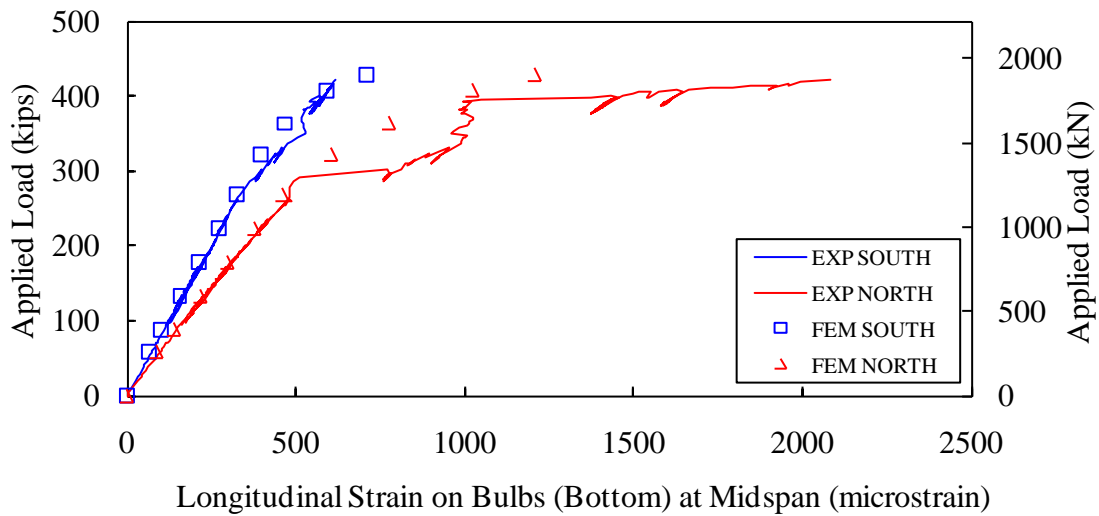


Figure 208. Graph. FEM vs. experimentally observed longitudinal strain on the bottom surfaces of the bulbs at midspan in Test T1J.

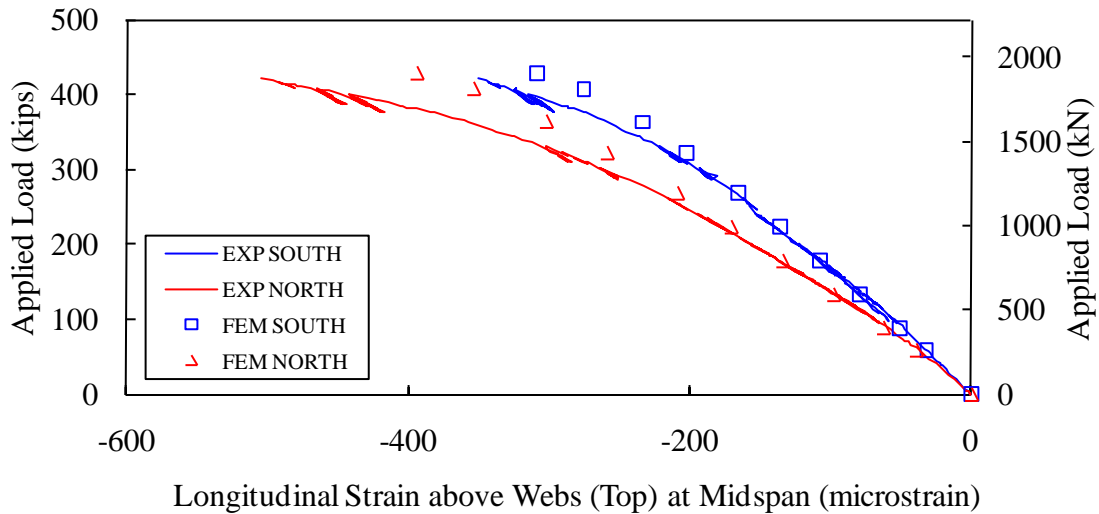


Figure 209. Graph. FEM vs. experimentally observed longitudinal strain on the deck immediately above the webs at midspan in Test T1J.

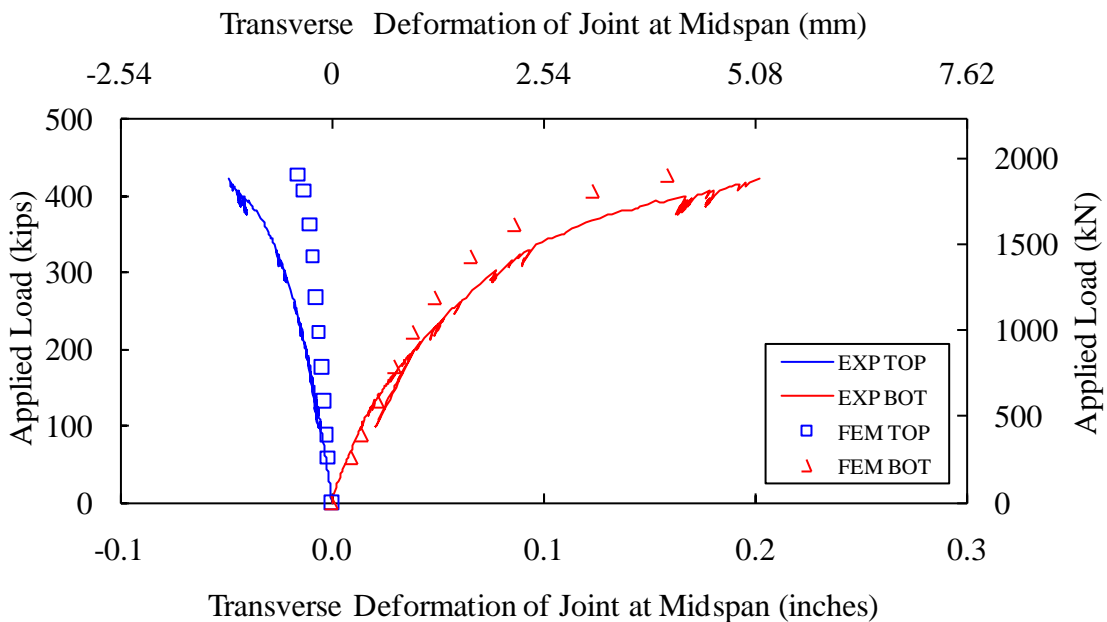


Figure 210. Graph. FEM vs. experimentally observed transverse deformation of the joint at midspan in Test T1J.

Figure 211 demonstrates that the predicted axial strains in the dowel bars embedded at the midspan and quarterspan points agree quite well with the experimental measurements obtained

from Test T1J. Both the bars' initial responses and later large plastic deformations including the yielding points are moderately well predicted.

Figure 212 and Figure 213 provide the contour plots of the predicted maximum principal stress and plastic strain on the surface of the girder as viewed from above, below, the north side of, and the south side of the girder in the UHPC-Joint case with the ultimate applied load of 428 kips (1904 kN). It should be noted that a maximum principal plastic strain contour can predict the inelastic response areas more accurately than a maximum principal stress one because the initiation of inelastic response in biaxial or triaxial stress states may not need the principal stress exceeding the maximum uniaxial tensile strength of the UHPC, as depicted in the yield surface in plane stress in Figure 6 and in the yield surface in three-dimensional stress space on page 41 of reference (7). As a stress state deviates from uniaxial tension, the stress contours based on tensile strength limit may underestimate the areas experiencing inelastic response. In Figure 212, the limit of the color bar is deliberately set at 1.35 ksi (9.3 GPa) to highlight the areas in a stress state equal or close to the uniaxial tensile strength. In Figure 213, the areas under plastic deformation are plotted in a color scale of blue to red if maximum principal plastic strain exceeds a small value of 0.000001 as an artificial threshold while the areas of elastic response are kept in light gray otherwise.

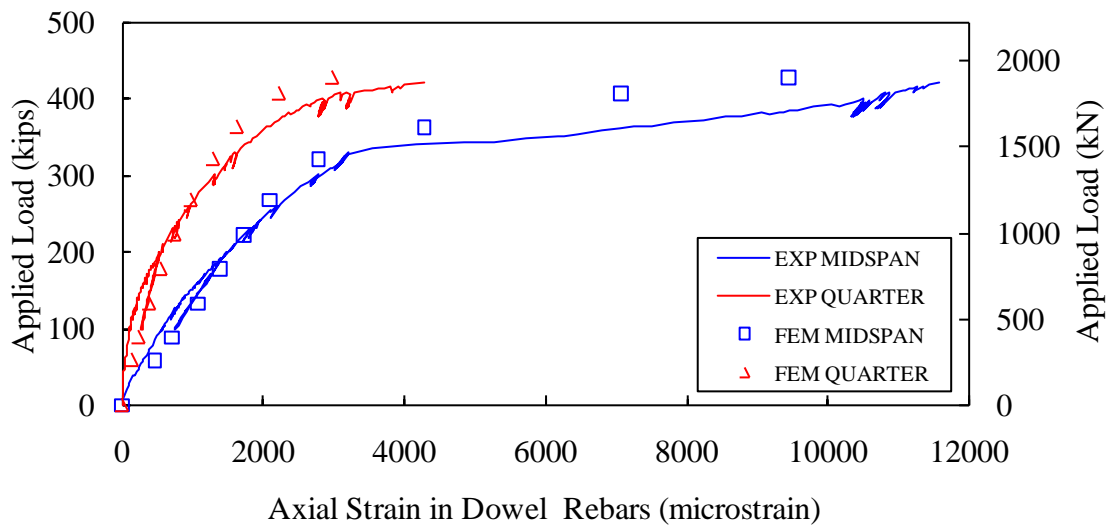
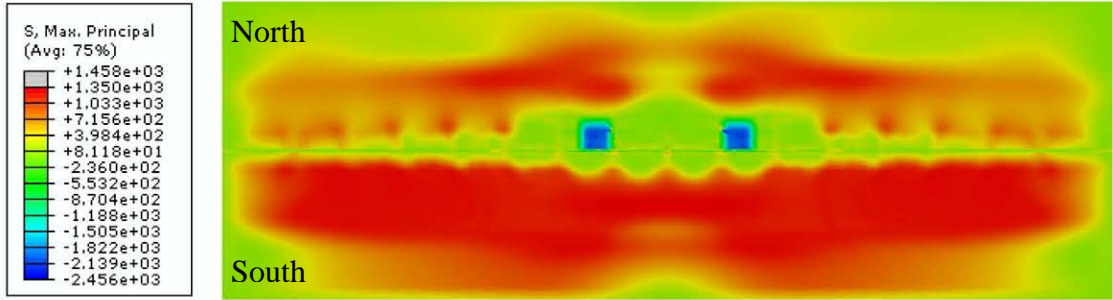


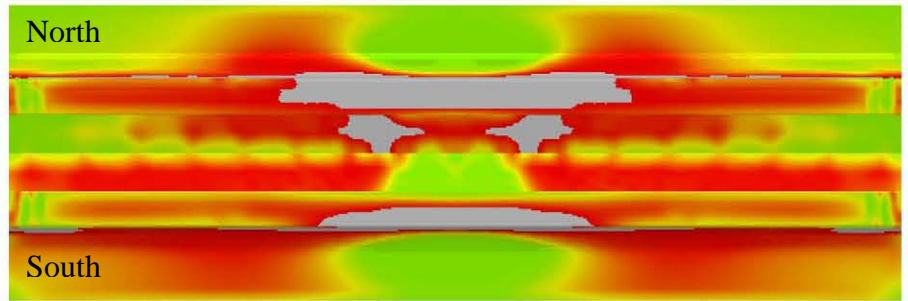
Figure 211. Graph. FEM vs. experimentally observed axial strains in the dowel bars at midspan and quarterspan in Test T1J.

Figure 212(a) illustrates the extensive areas of the top of the deck on the south half-girder experiencing high tensile stress approaching the uniaxial tensile strength due to negative moment induced as a result of the diaphragm resistance to lateral leg spreading. Figure 212(b) shows that

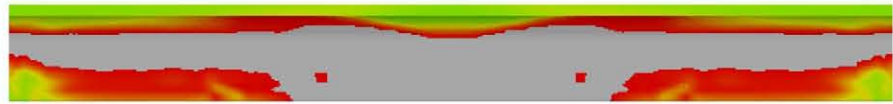
maximum principal stress reaches the uniaxial tensile strength on the bottom and exterior portions of both north and south bulbs near midspan as well as on the underside of the deck directly under the loading pads. Figure 213(a) and (b) predict more extensive areas of inelastic response on both top and underside of the deck than Figure 212(a) and (b) because of the relatively complex stress states in the deck in presence of the longitudinal joint. In Figure 213(b), the model reported inelastic response pattern on the underside of the deck is consistent with the Test T1J experimentally observed underside deck cracking map captured at the ultimate applied load of 422 kips (1877 kN) as shown in Figure 214 (reproduced from reference (14)). Compared to Figure 132(b), the gray areas on the underside of the deck are more localized to the proximity of the loading areas while the bulbs have significantly larger inelastic response areas because of the higher ultimate applied load. It is easy to understand that the north half-girder carries a greater proportion of the applied load due to eccentricity of loading and therefore has larger inelastic area on the bulb and web. Extensive inelastic response has also been observed on the exterior surfaces of both webs, as illustrated in Figure 212(c) and (d), and also Figure 213(c) and (d). This is also consistent with the experimental observations illustrated in Figure 215 (reproduced from reference (14)). According to the FEM prediction, the maximum tensile plastic strain did not happen on the underside deck directly under the loading patch as did the case in the pi-girder in Chapter 6, but instead was, on the exterior surface of the north web. It is also demonstrated through the density of cracks on the exterior surface of the north web near the ends of the girder in Figure 215(a). In addition, the migrated center of the north supports may induce less longitudinal bending on the north web. Additional inelastic response can be observed from the bulb ends where the strands anchored, the bulb sections where the two diaphragms were installed, and some grouted connections where the dowels were embedded.



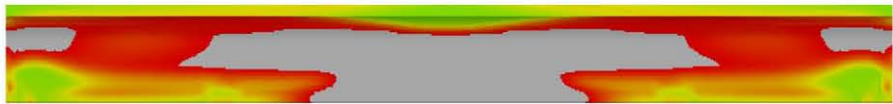
(a)



(b)

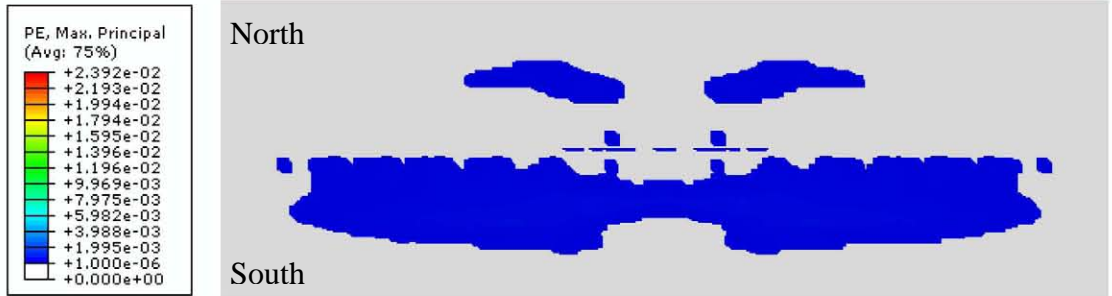


(c)

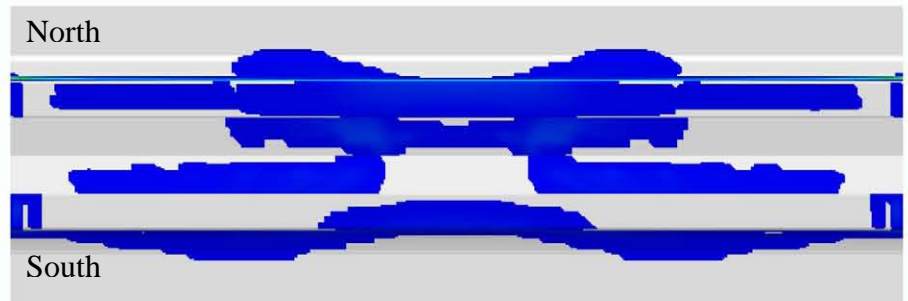


(d)

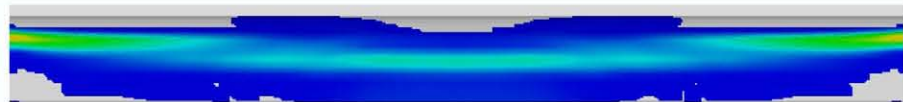
Figure 212. Graph. FEM predicted maximum principal stress on the surface of the girder as reviewed from (a) above, (b) below, (c) the north side of, and (d) the south side of the girder in Test T1J (ultimate load = 428 kips or 1904 kN).



(a)



(b)



(c)



(d)

Figure 213. Graph. FEM predicted maximum principal plastic strain on the surface of the girder as reviewed from (a) above, (b) below, (c) the north side of, and (d) the south side of the girder in Test T1J (ultimate load = 428 kips or 1904 kN).

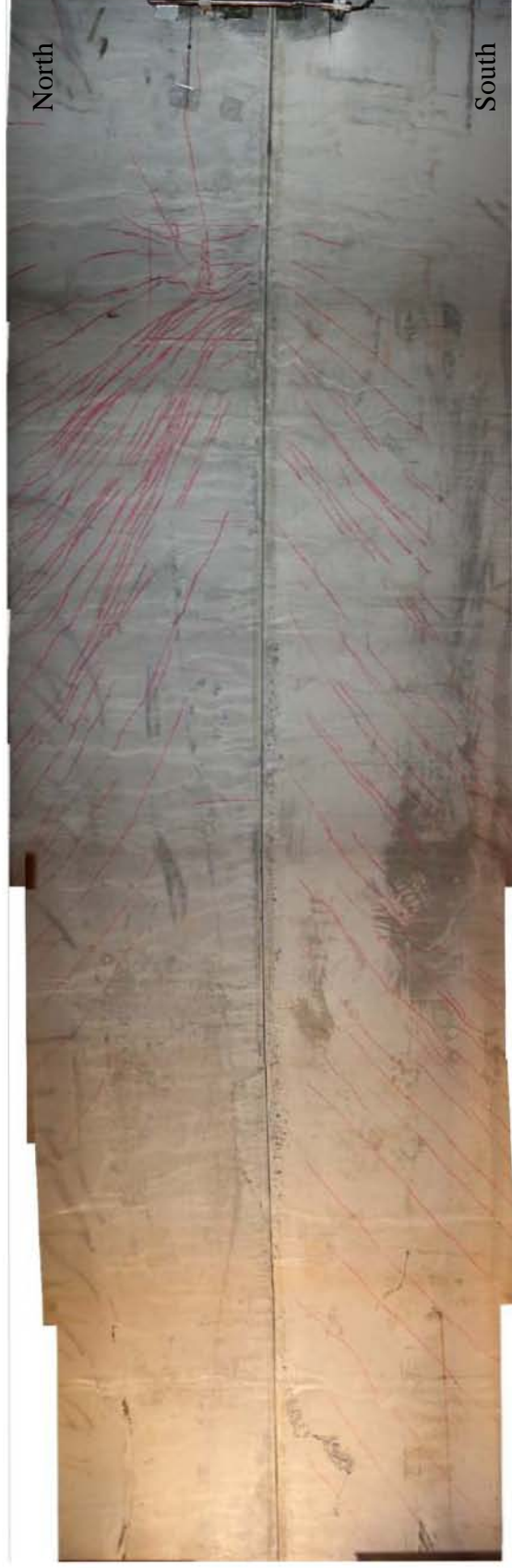
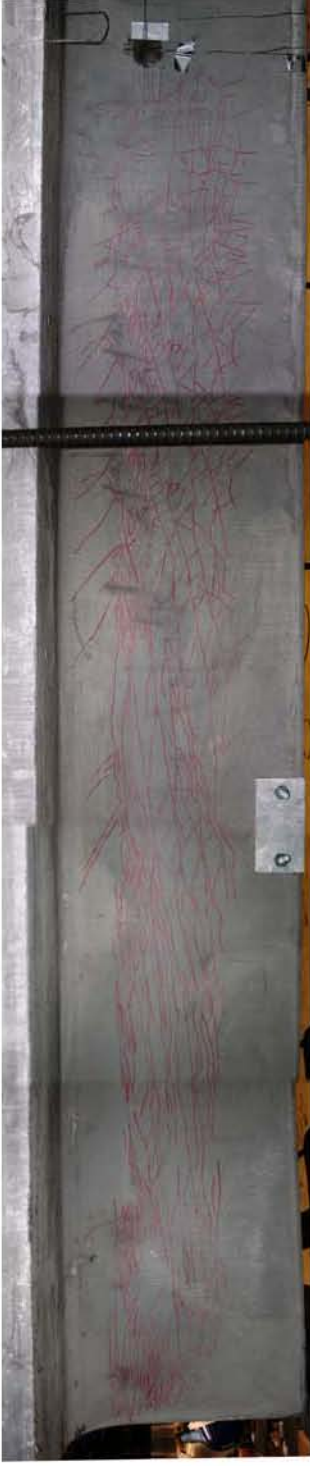


Figure 214. Photo. Underside of deck from midspan to east end after the conclusion of Test T1J with an ultimate applied load of 422 kips (1877 kN), (reproduced from reference (14)).



(a)



(b)

Figure 215. Photo. (a) North face of north web, and (b) south face of south web after the conclusion of Test T1J with an ultimate applied load of 422 kips (1877 kN), (reproduced from reference (14)).

The FEM prediction of maximum principal stress and plastic strain is also presented at two girder cross sections, namely at midspan and at the center of one of the load patches. The maximum principal stress illustrations are shown in Figure 216 while the maximum principal plastic strain illustrations are shown in Figure 217. Undeformed sectional profiles are illustrated with a dashed line while deformed shapes are amplified by a scale of five. The deformed shape at the center of the loading patch is similar to the one at midspan, including the deck rotating around the joint and significant inward bending at the north leg. In Figure 216, the maximum principal stress reaches the maximum tensile strength in a significant portion of the bulbs and webs. As a complement to Figure 213, Figure 217 demonstrates that the inelastic response area in the north leg is significantly larger than in the south one. Figure 217 illustrates that the deck of the south half-girder resists larger negative moment at loading patch center than at midspan sections while the effect of both positive and negative moments on the deck of the north half-girder seems localized to the loading areas, which was also illustrated in Figure 213(a).

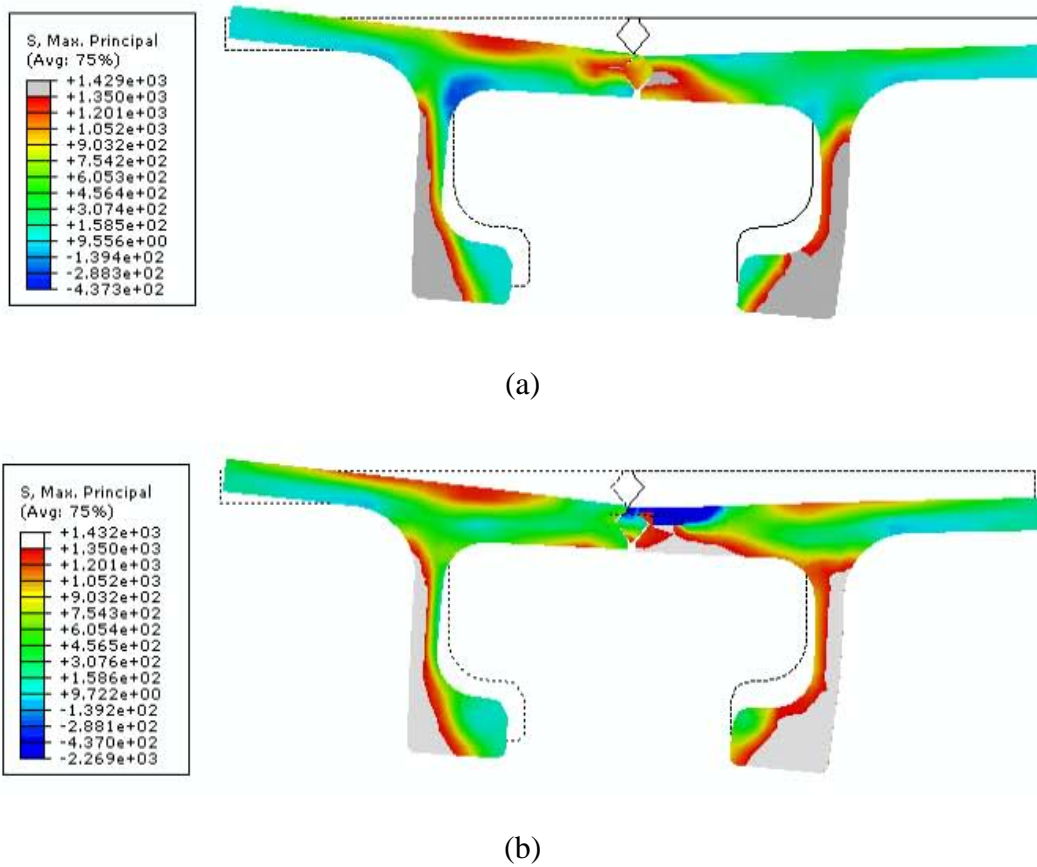
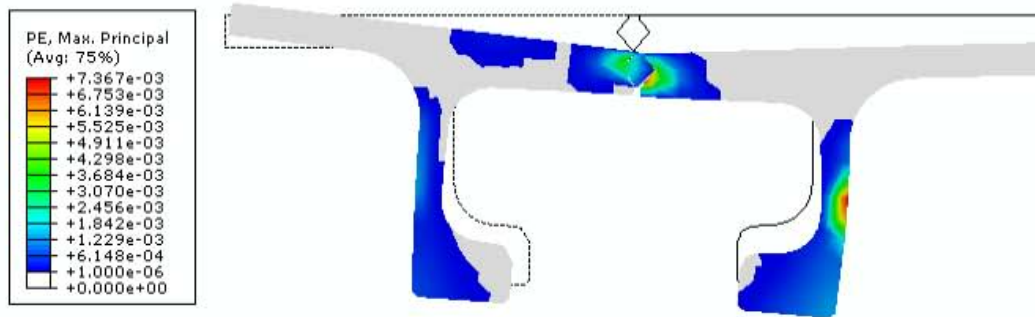
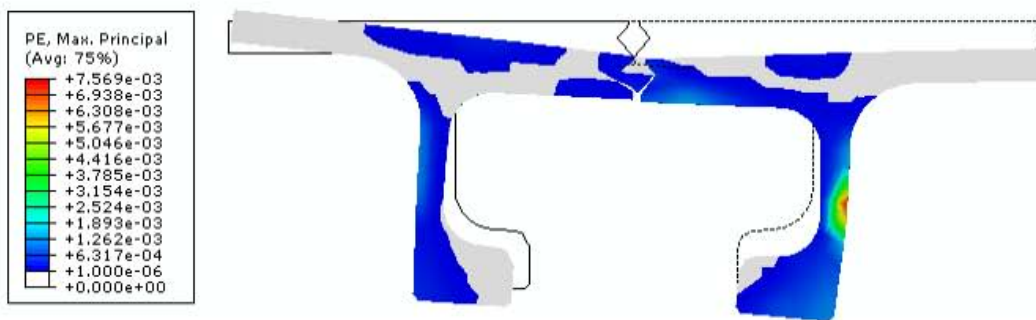


Figure 216. Illustration. FEM predicted maximum principal stress at the (a) midspan, and (b) center of loading patch cross sections in Test T1J (Note: deformation scale factor = 5 and ultimate load = 428 kips (1904 kN)).



(a)



(b)

Figure 217. Illustration. FEM predicted maximum principal plastic strain at the (a) midspan, and (b) center of loading patch cross sections in Test T1J (Note: deformation scale factor = 5 and ultimate load = 428 kips (1904 kN)).

PARAMETRIC STUDIES

The above models were calibrated through a series of parametric studies. Because of higher ultimate applied load resulting in longer projection of its nonlinear behavior, the model of test specimen T1J is more suitable to the sensitivity study and, therefore, it has been analyzed and is discussed below. The above model with a 2-inch (51-mm) seeded mesh, the girder UHPC CDP material parameters as specified in Table 4, the field-cast UHPC CDP material parameters as listed in Table 8, automatic stabilization, friction contact (coefficient of friction = 0.1) between diamond-shaped shear key and surrounding deck, and diaphragms of nonlinear spring properties listed in Table 9, serves as a benchmark in the following comparisons.

Stabilization

Automatic stabilization with default parameters, i.e., dissipated energy fraction = 0.0002 and maximum ratio of stabilization to strain energy = 0.05, was employed to stabilize the girder during the final loading stage. Figure 218 through Figure 224 illustrate that without stabilization

the model becomes unstable when the applied load exceeds approximately 320 kips (1423 kN) while automatic stabilization can significantly improve the model's stability by raising an ultimate applied load from 365 kips (1624 kN) to 428 kips (1904 kN).

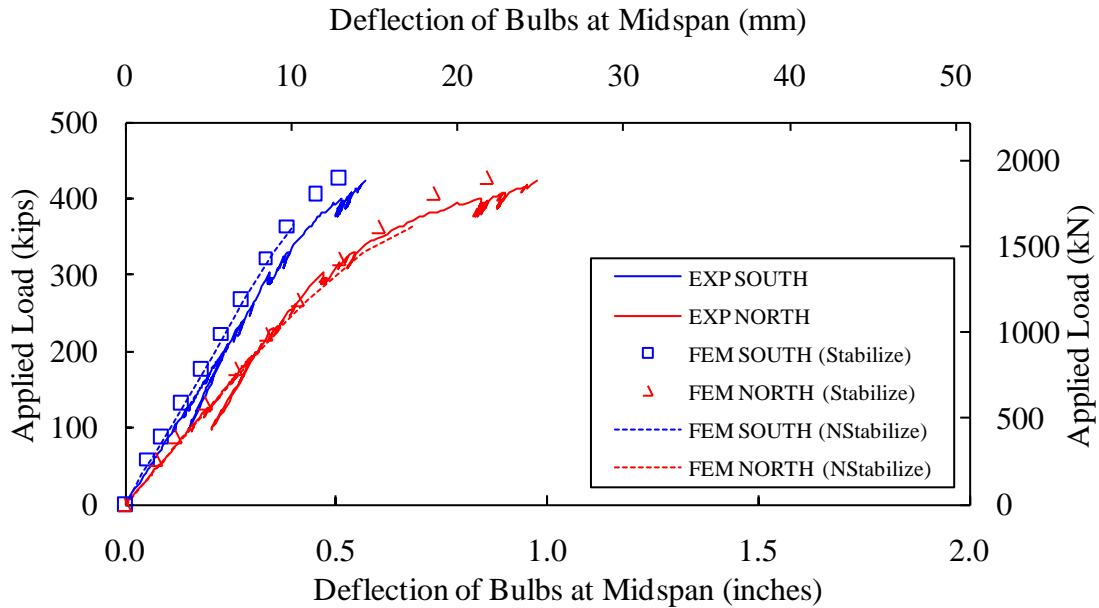


Figure 218. Graph. Effect of stabilization on the vertical deflection of the bulbs at midspan.

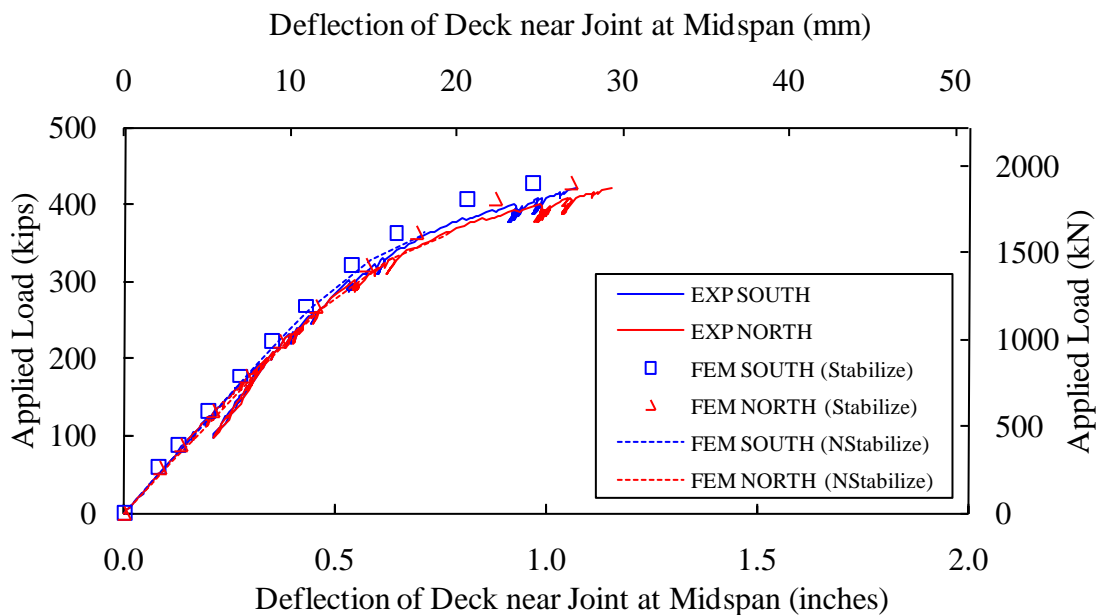


Figure 219. Graph. Effect of stabilization on the vertical deflection of the deck near the joint at midspan.

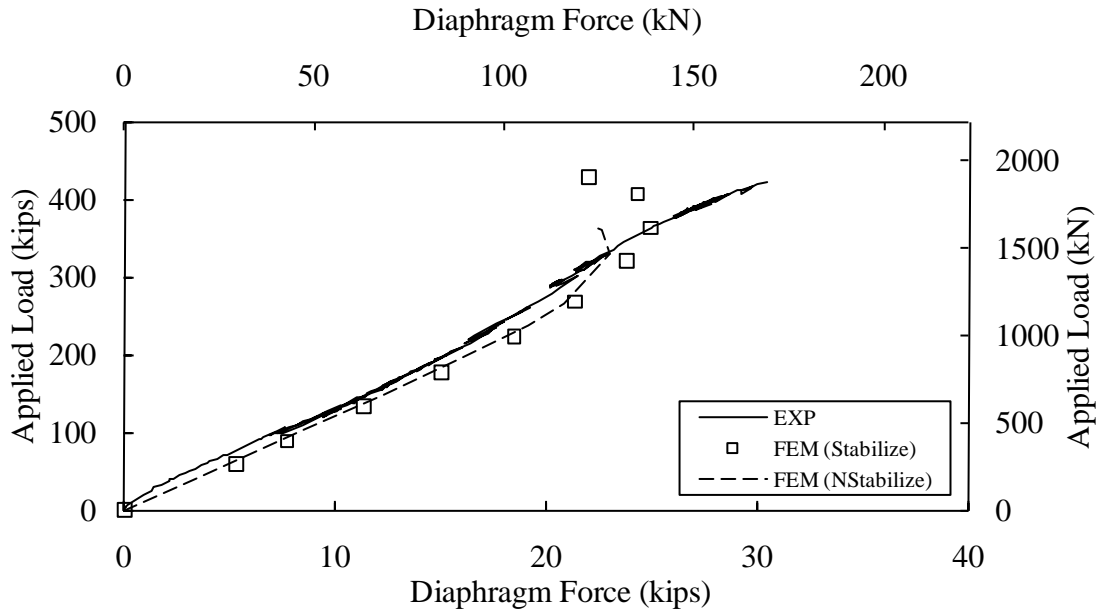


Figure 220. Graph. Effect of stabilization on the diaphragm force.

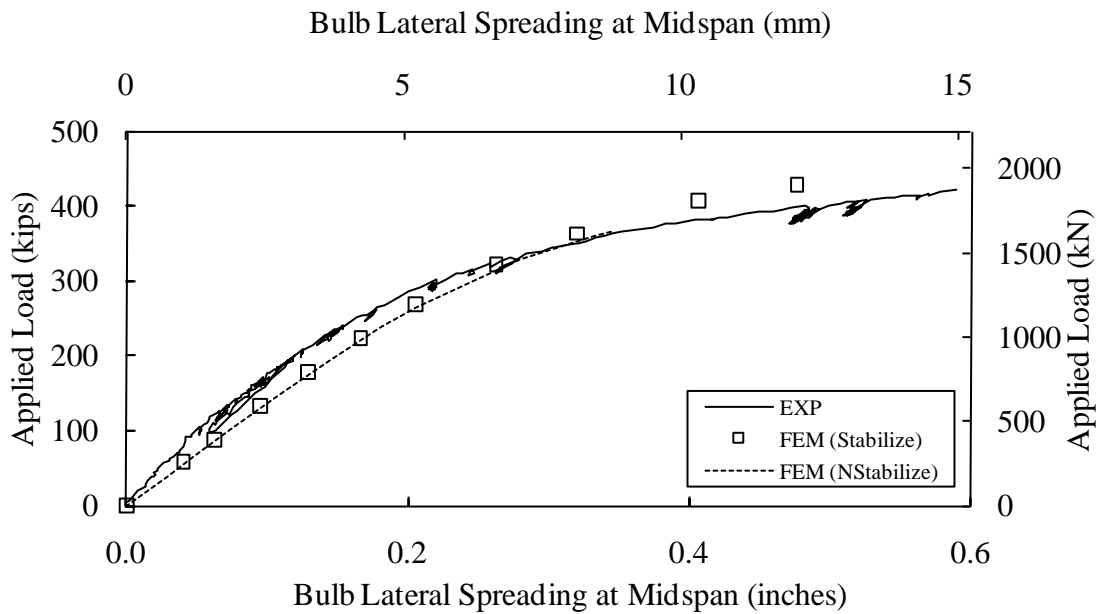


Figure 221. Graph. Effect of stabilization on the bulb lateral spreading at midspan.

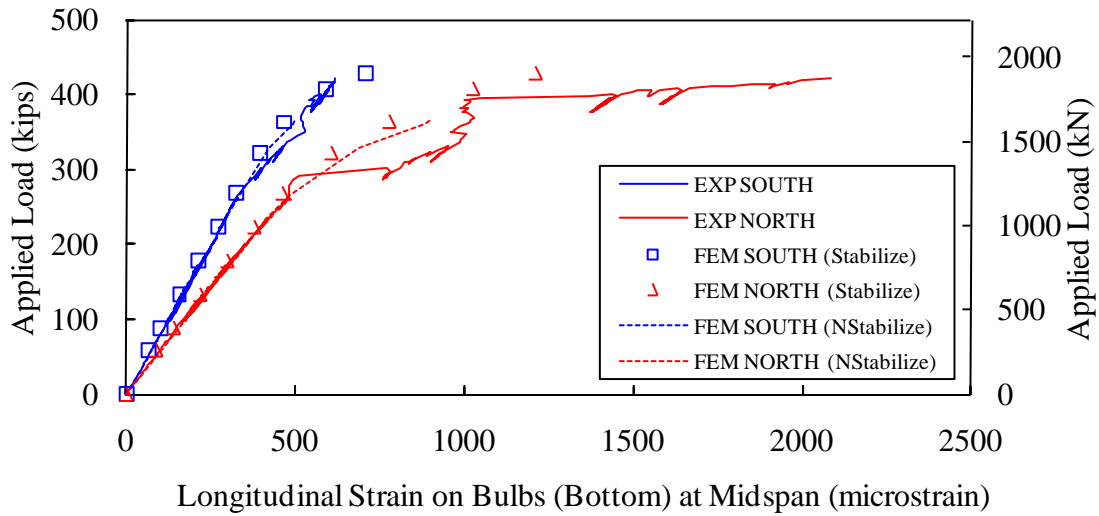


Figure 222. Graph. Effect of stabilization on the longitudinal strain on the bottom surfaces of the bulbs at midspan.

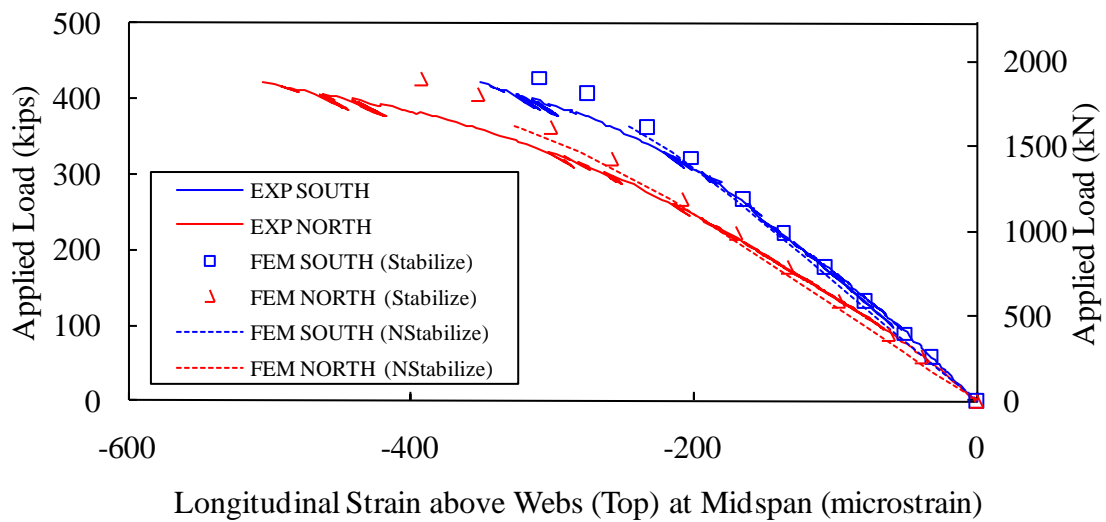


Figure 223. Graph. Effect of stabilization on the longitudinal strain on the deck immediately above the webs at midspan.

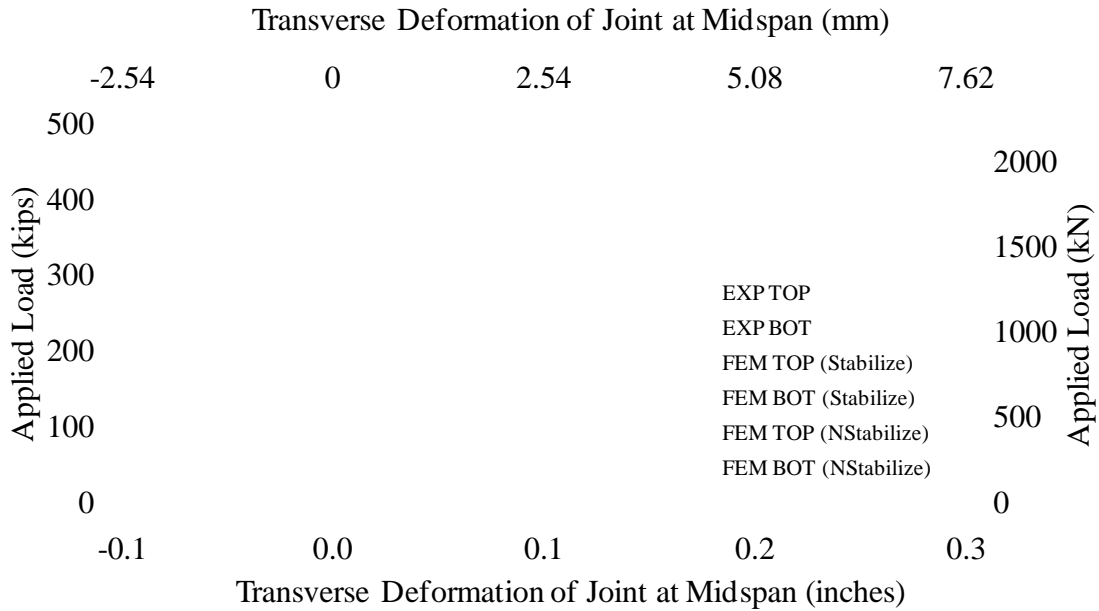


Figure 224. Graph. Effect of stabilization on the transverse deformation of the joint at midspan.

Joint

The grouted joint is the major subject of the pi-girder under investigation. Two questions relevant to the joint may arise and need to be addressed. First, is there any dramatic difference between using the magnesium phosphate grout and using field-cast UHPC as the grouting material in terms of the girder structural performance? This has been discussed in the previous results section. Second, how does the grouted joint behave as compared to a continuous deck case representing perfectly bonded girder flange tips without the presence of the joint? The model geometry related to the second question is shown in Figure 225.

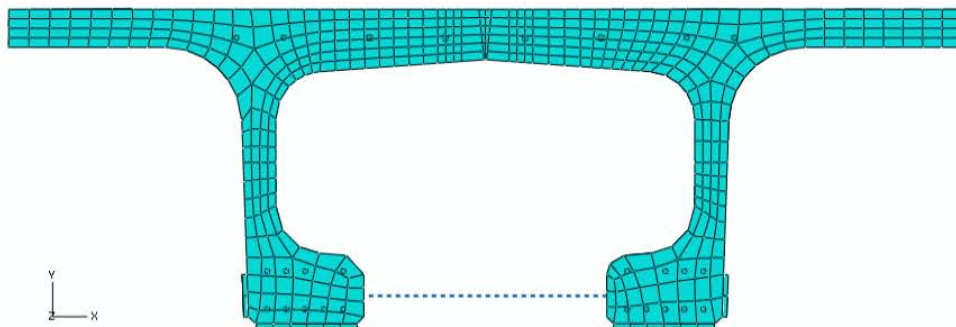


Figure 225. Illustration. Pi-girder model with continuous deck and a 2-inch (51-mm) seeded mesh.

The fully bonded pi-girder model is as an upper bound case of pi-girder with joint. Figure 227, Figure 228, Figure 229, Figure 232 and Figure 233 illustrate that the fully bonded connection between the half-girders significantly reduces the vertical displacement on the deck near the joint, the diaphragm force, the bulb lateral spreading at midspan, the transverse deformation of the joint, and the axial strain in the dowel bars. However, the difference between the fully bonded model and the UHPC-joint model is barely observed in terms of the vertical displacement of the bulbs, the longitudinal strains on the bottom surfaces of the bulbs and on the deck immediately above the webs as illustrated in Figure 226, Figure 230 and Figure 231.

In the full-bond case, the predicted maximum tensile plastic strain occurred in the middeck near the loading patches is approximately 0.01 at an applied load of 338 kips (1503 kN) and 0.02 at the ultimate applied load of 438 kips (1948 kN). In its physical test, the underside of the deck near the loading patches would be significantly cracked before reaching the ultimate load.

Figure 228 and Figure 229 show that, in contrast to the UHPC-Joint case, the fully bonded model exhibits significantly smaller diaphragm force and less bulb lateral spreading under the same applied load. The T1J model with friction contact between the joint and surrounding deck predicts a much closer result than the fully bonded model. The slight difference between the experimental and the finite element T1J results suggests that the real joint detail has stronger bonding effect than what the hard contact with friction can provide and, therefore, it results in smaller diaphragm force and less bulb lateral spreading at midspan.

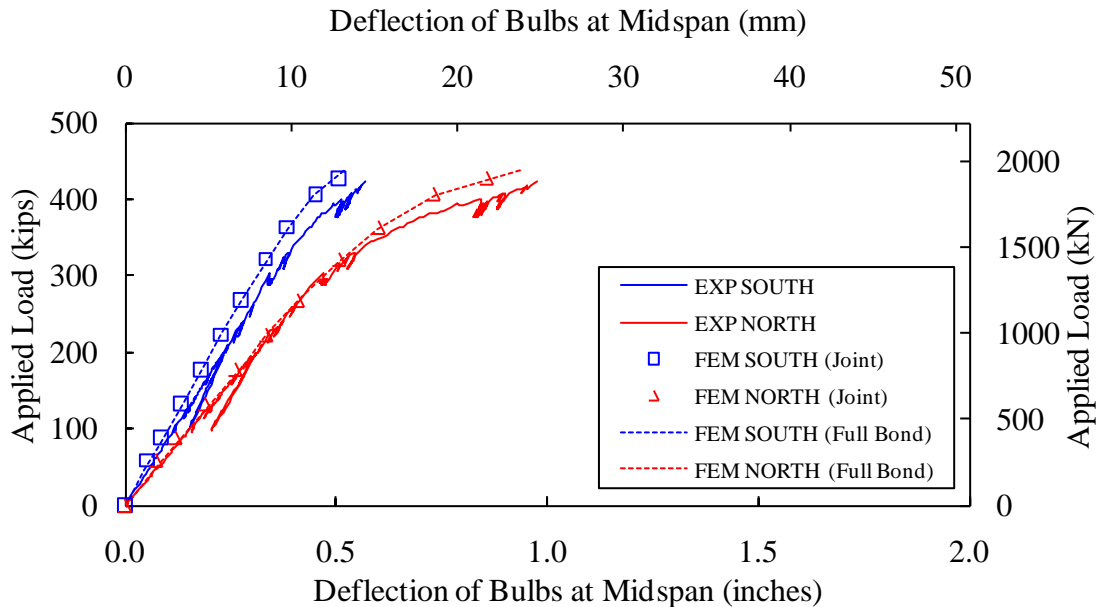


Figure 226. Graph. Joint vs. full bond in the vertical deflection of the bulbs at midspan.

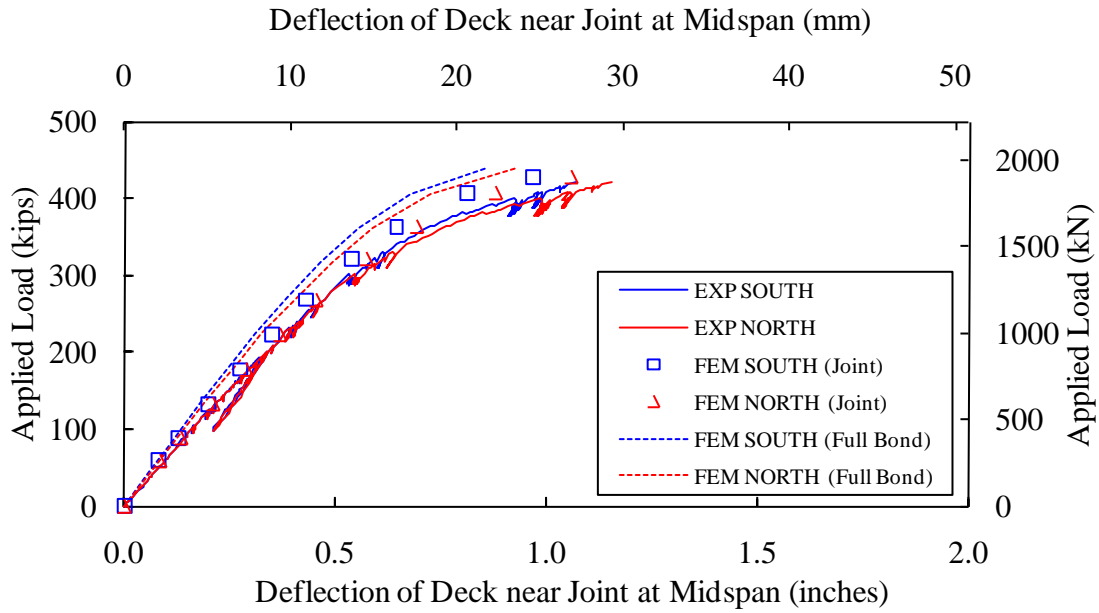


Figure 227. Graph. Joint vs. full bond in the vertical deflection of the deck near the joint at midspan.

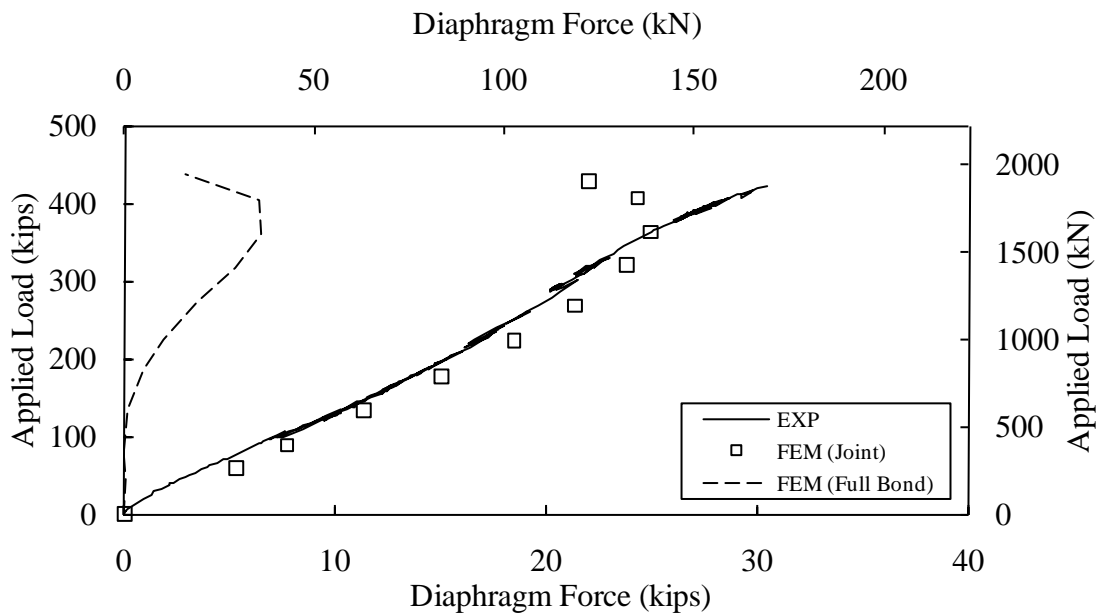


Figure 228. Graph. Joint vs. full bond in the diaphragm force.

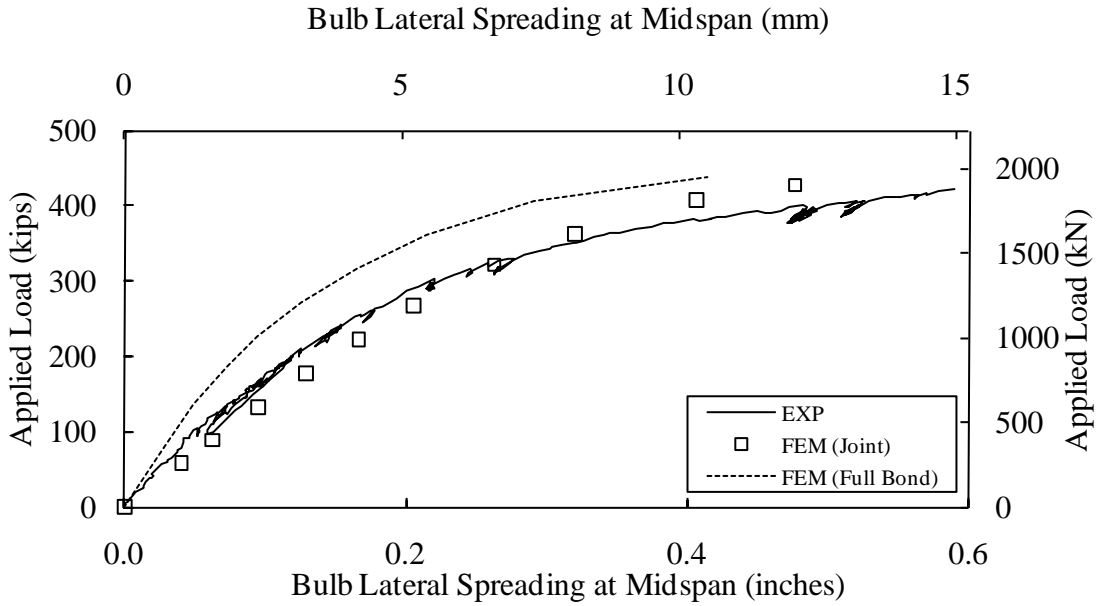


Figure 229. Graph. Joint vs. full bond in the bulb lateral spreading at midspan.

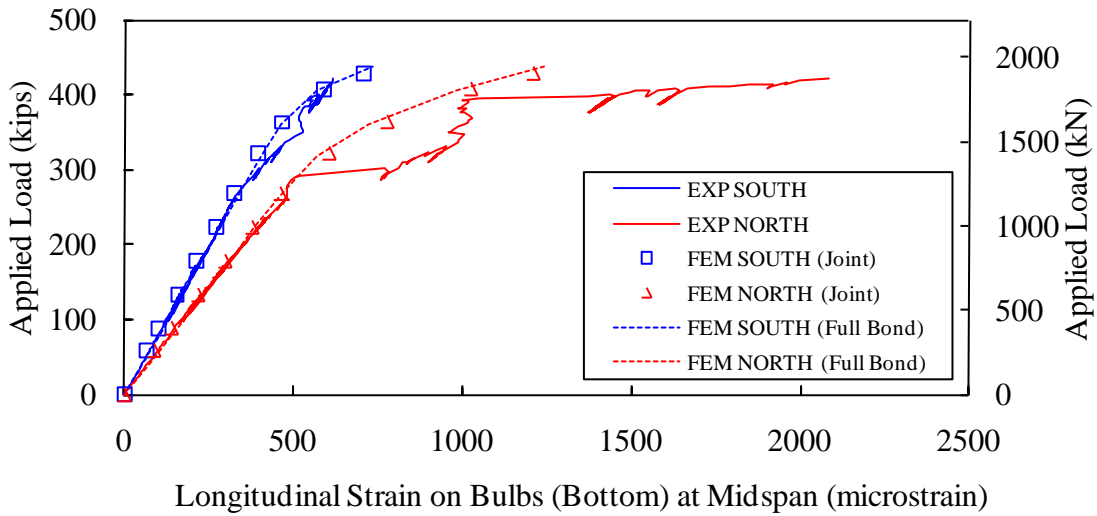


Figure 230. Graph. Joint vs. full bond in the longitudinal strain on the bottom surfaces of the bulbs at midspan.

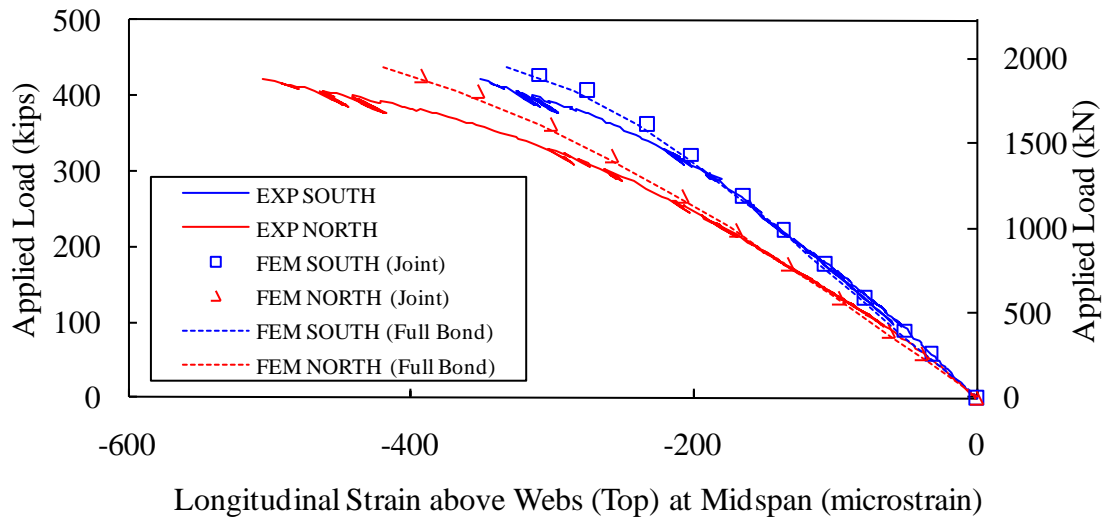


Figure 231. Graph. Joint vs. full bond in the longitudinal strain on the deck immediately above the webs at midspan.

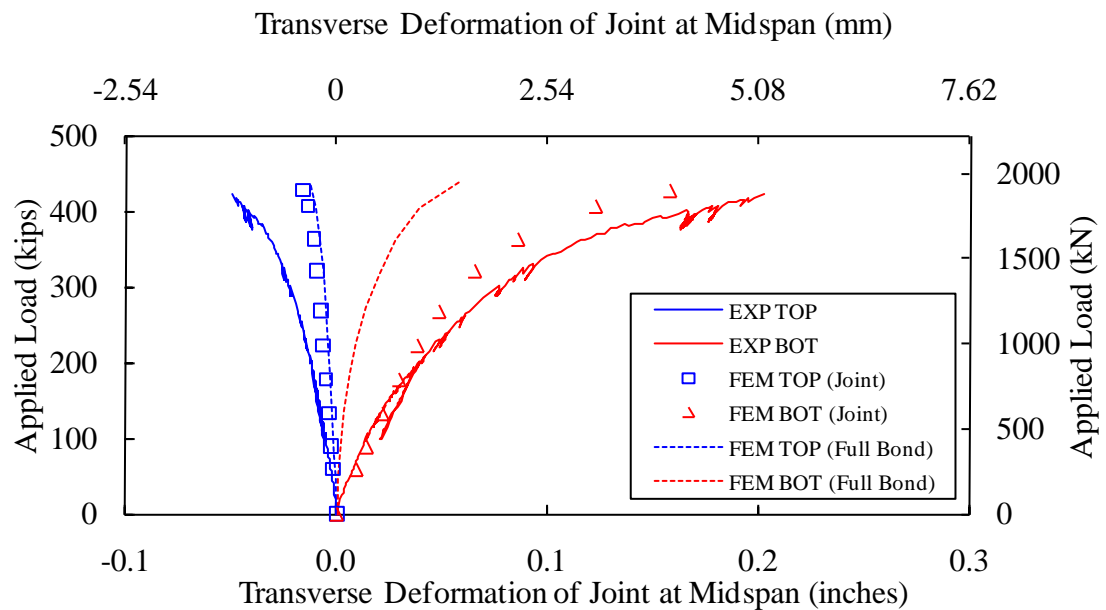


Figure 232. Graph. Joint vs. full bond in the transverse deformation of the joint at midspan.

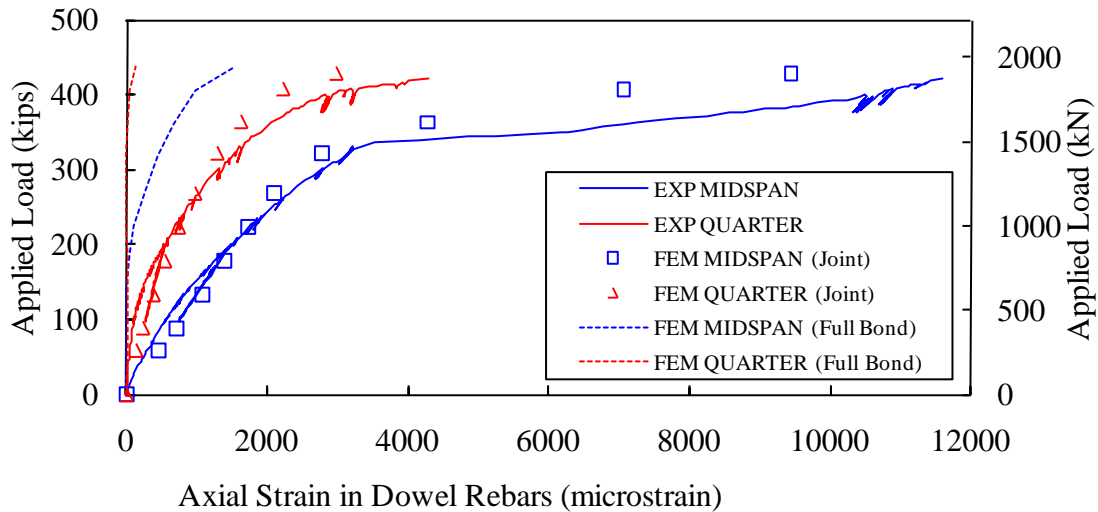


Figure 233. Graph. Joint vs. full bond in the axial strains in the dowel bars at the midspan and quarterspan.

Contact

As demonstrated in the previous study of the joint, the bond between joint and deck cannot be assumed as fully bonded. This also can be observed from the transverse deformations immediately above and below the joints as shown in Figure 78 in reference (14). Instead, it is reasonable to model the connection as surface-to-surface contact with allowable separation and adjustable coefficient of friction. The finite sliding formulation is preferred over the small sliding formulation because both contact area and contact pressure change throughout the analysis.

Contact is implemented with normal behavior using “hard” contact and tangential behavior using a customized coefficient of friction. The joint and deck have matching meshes resulting in node-to-node contact and eliminating any potential penetration problems. The contact side on the deck is modeled as the master surface while the contact side on the joint is considered the slave surface. The coefficient of friction in a contact interaction can affect the convergence of the model. The “rough” contact, which has such a large coefficient of friction that no sliding is allowed, initially met the convergence problem. Figure 234 through Figure 240 present the results for two cases: frictionless contact and contact with a coefficient of friction equal to 0.3. The two cases have ultimate applied loads of approximately 424 kips (1886 kN) and 416 kips (1850 kN), which are slightly smaller than 428 kips (1904 kN) in the calibrated case with a coefficient of friction equal to 0.1. Aside from convergence, the coefficient of friction seems to have minimal effect on the observed structural behavior.

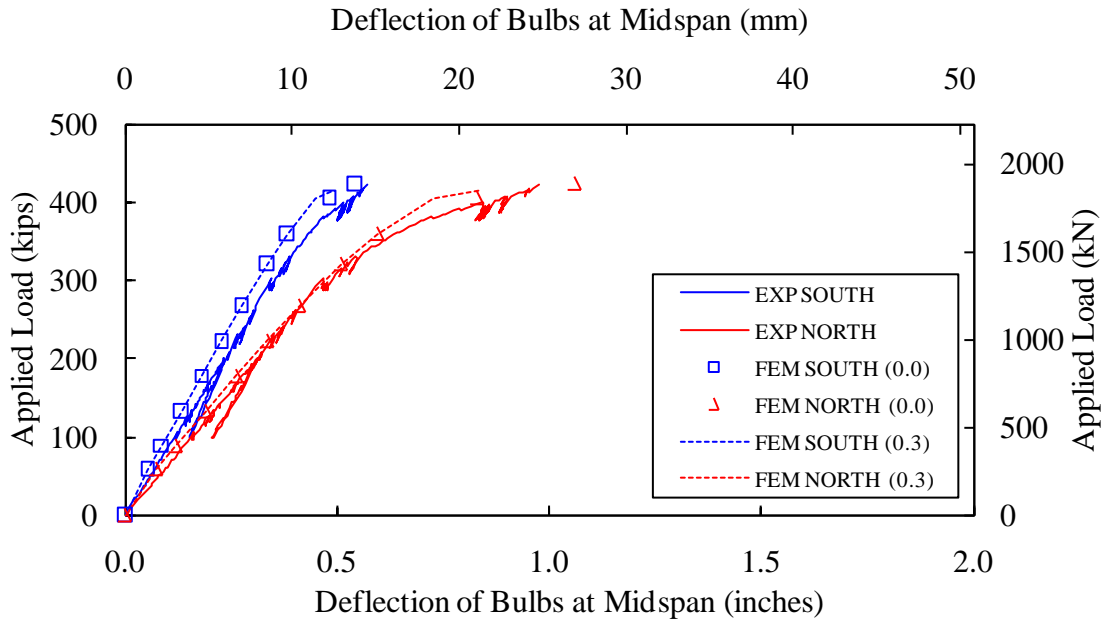


Figure 234. Graph. Effect of coefficient of friction on the vertical deflection of the bulbs at midspan.

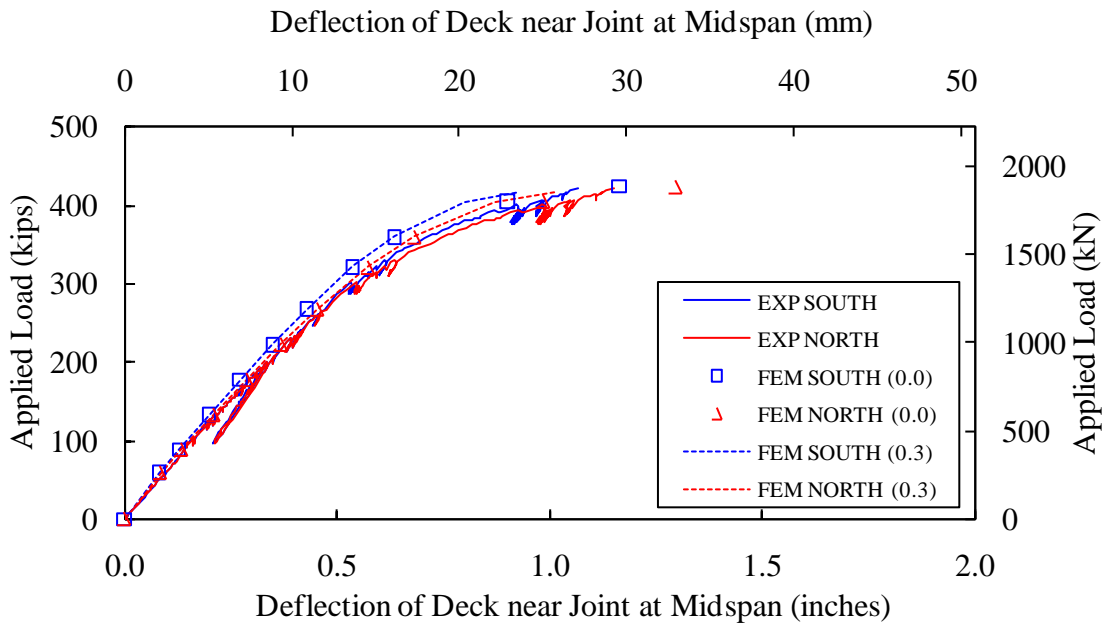


Figure 235. Graph. Effect of coefficient of friction on the vertical deflection of the deck near the joint at midspan.

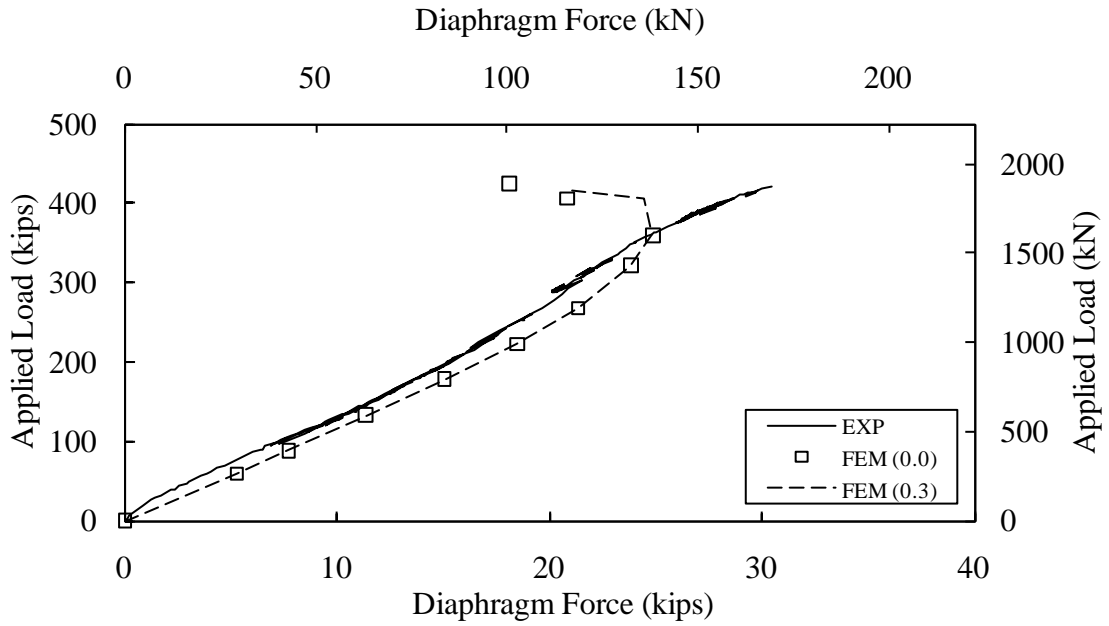


Figure 236. Graph. Effect of coefficient of friction on the diaphragm force.

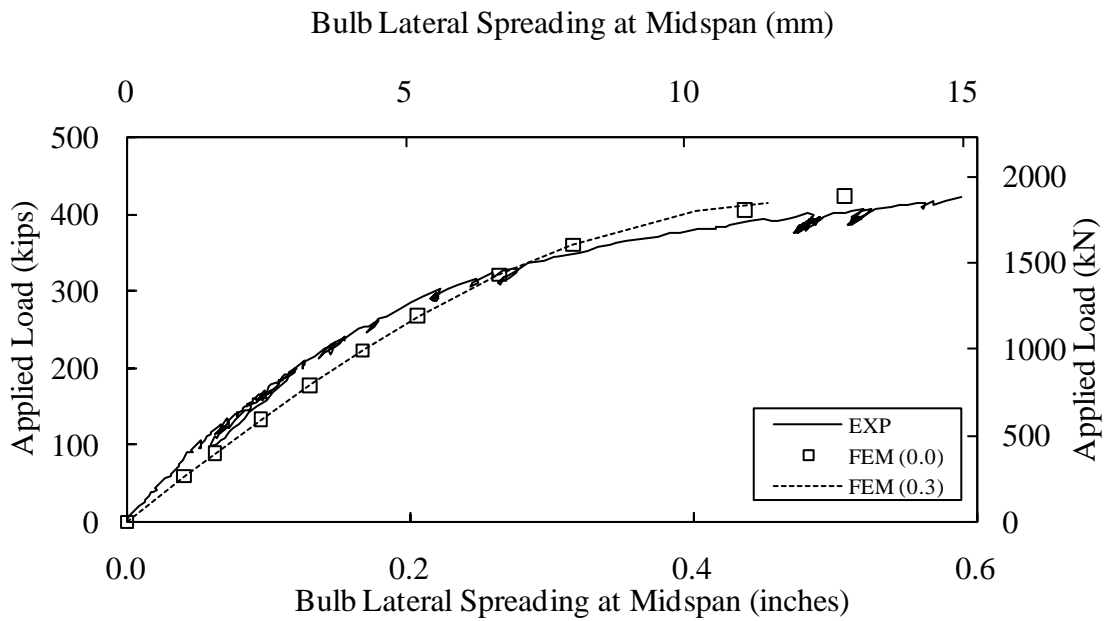


Figure 237. Graph. Effect of coefficient of friction on the bulb lateral spreading at midspan.

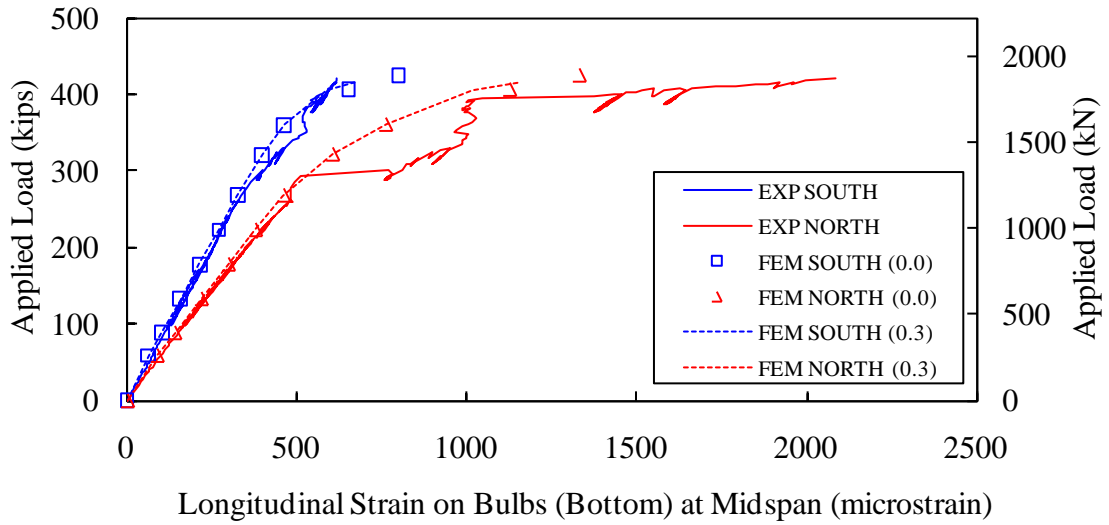


Figure 238. Graph. Effect of coefficient of friction on the longitudinal strain on the bottom surfaces of the bulbs at midspan.

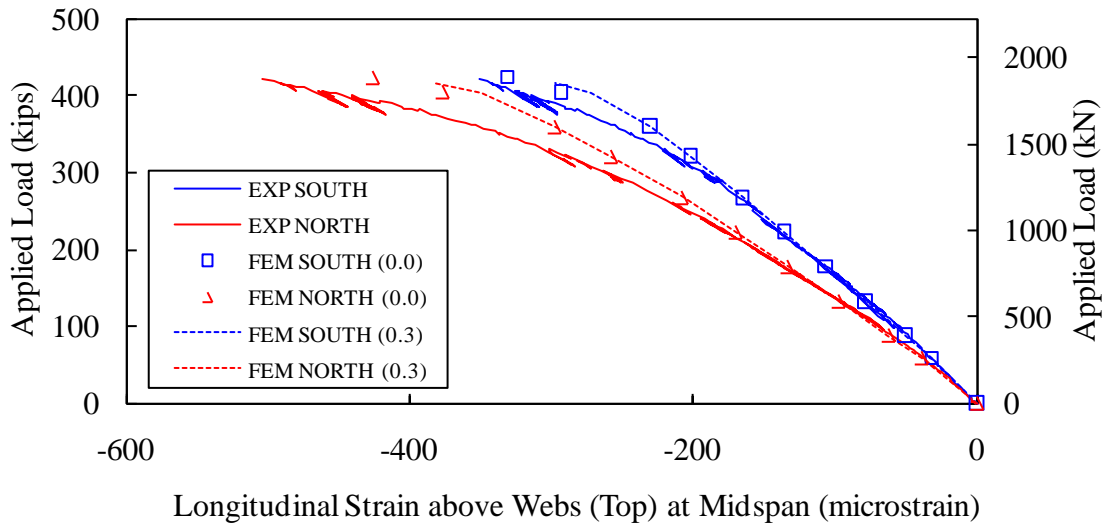


Figure 239. Graph. Effect of coefficient of friction on the longitudinal strain on the deck immediately above the webs at midspan.

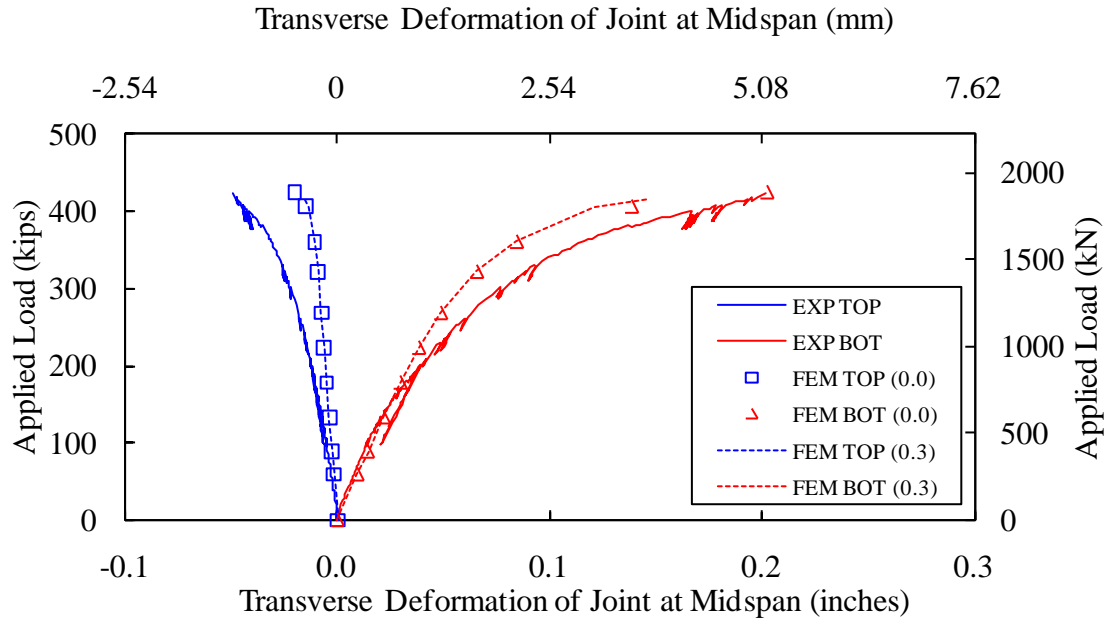


Figure 240. Graph. Effect of coefficient of friction on the transverse deformation of the joint at midspan.

Diaphragms

The impact of the diaphragm was investigated by considering three cases wherein both increased and decreased transverse restraint was provided to the bulbs. Figure 241 through Figure 248 present a comparison among the as-tested case, an upper bound case, and a lower bound case. In the upper bound, four diaphragms of almost infinite stiffness brace the girder legs at the end supports and at the existing quarterspan diaphragm locations. In the lower bound case, no diaphragms are provided at all. Compared with the tested case, infinite diaphragm stiffness and additional diaphragms at the supports can significantly increase diaphragm force and reduce the bulb lateral spreading after an applied load of 150 kips (667 kN) as illustrated in Figure 243 and Figure 244. The bulb lateral spreading would be severe if no diaphragms are provided. Figure 241 and Figure 242 show that the vertical displacements at the bulbs at midspan and the midspan middeck positions are only slightly reduced in the 4-rigid-diaphragm case and slightly increased in the no-diaphragm case. Figure 245 and Figure 246 demonstrate that the longitudinal strains on the surfaces of the bulbs and on the top surfaces immediately above the webs, areas primarily associated to the longitudinal bending, are not been significantly affected by the diaphragms. Figure 247 also shows that only a slight reduction of transverse deformation of the joint was observed on the bottom of the joint in the 4-rigid-diaphragm case. Without diaphragm constraint, the transverse deformation of the joint becomes much larger. The additional restraint on the girder ends provided in the 4-rigid-diaphragm case can significantly reduce the longitudinal bending on the north web. The axial strains in the dowel bars also increase or decrease corresponding to the transverse deformation of the joint as shown in Figure 248.

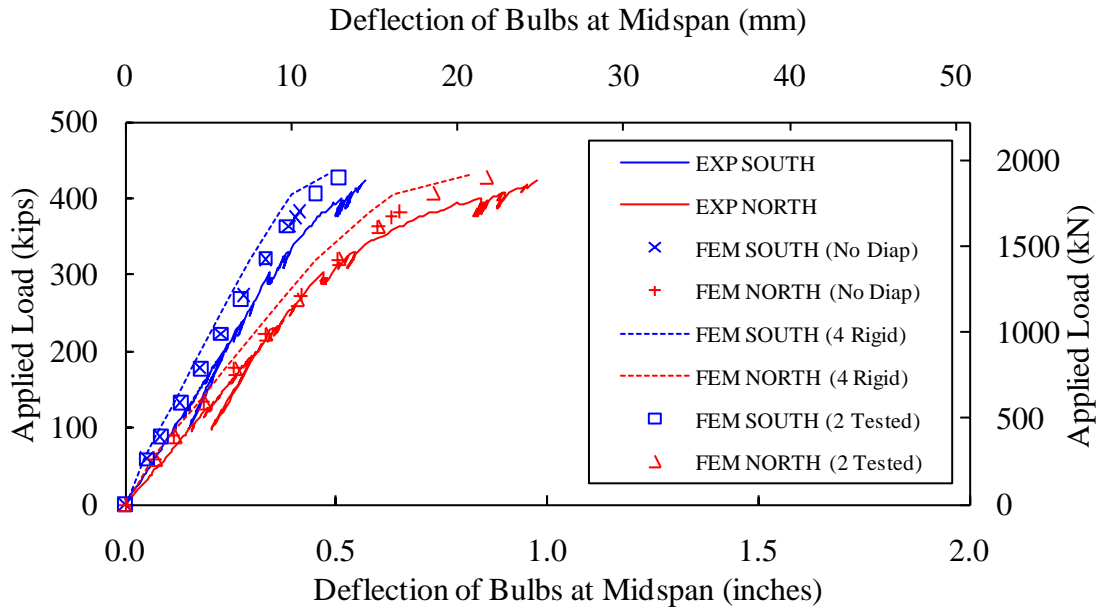


Figure 241. Graph. Effect of diaphragm on the vertical deflection of the bulbs at midspan.

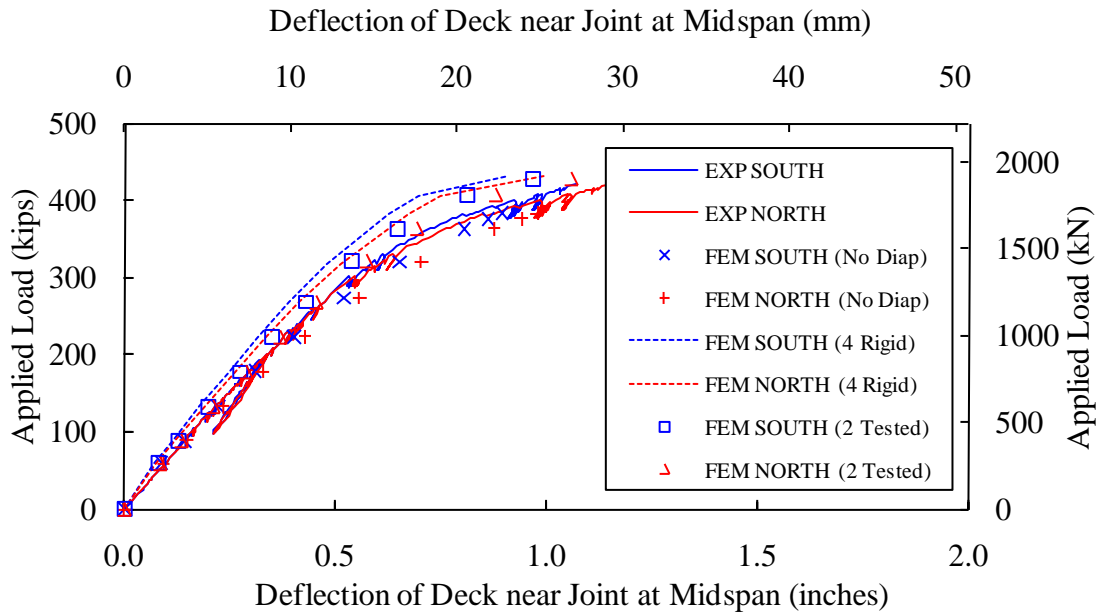


Figure 242. Graph. Effect of diaphragm on the vertical deflection of the deck near the joint at midspan.

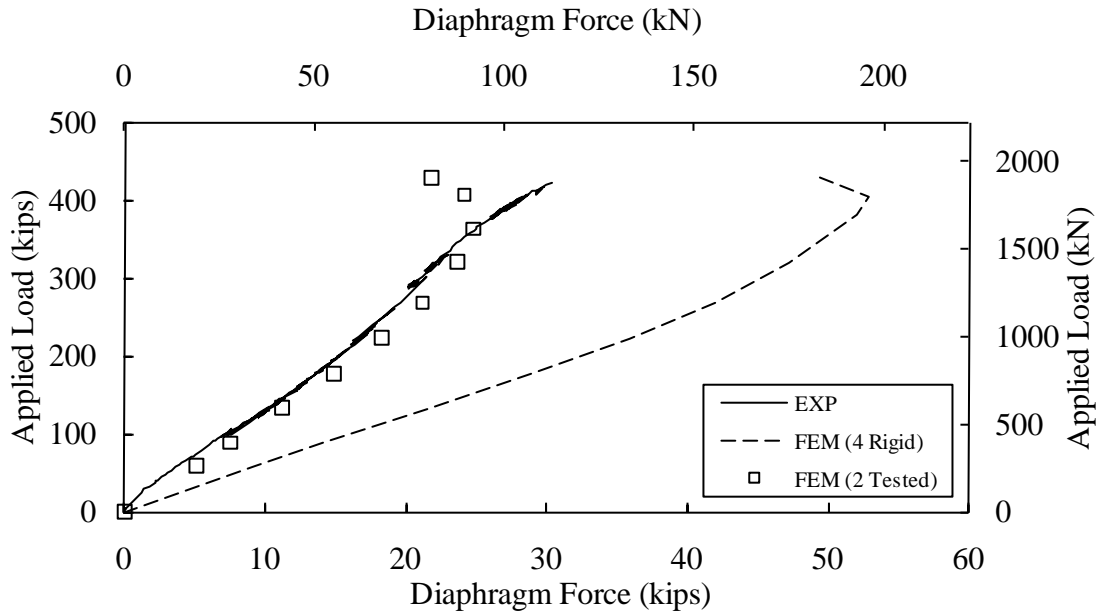


Figure 243. Graph. Effect of diaphragm on the diaphragm force.

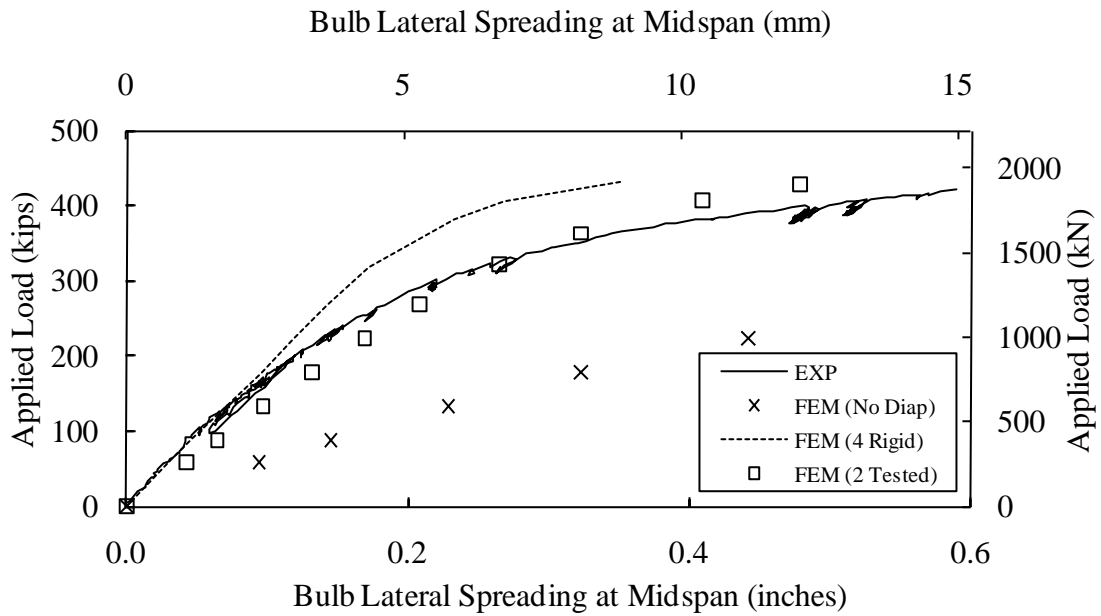


Figure 244. Graph. Effect of diaphragm on the bulb lateral spreading at midspan.

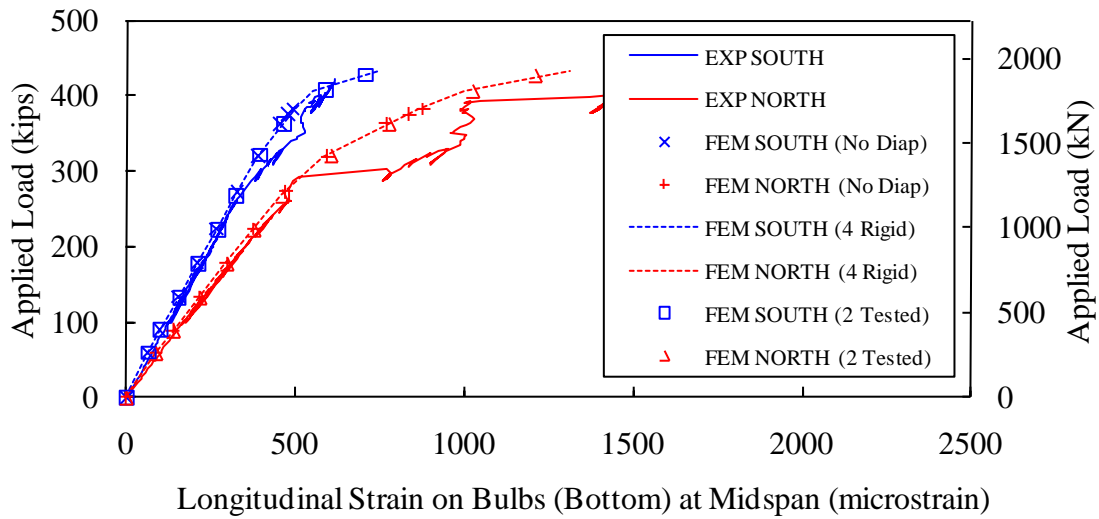


Figure 245. Graph. Effect of diaphragm on the longitudinal strain on the bottom surfaces of the bulbs at midspan.

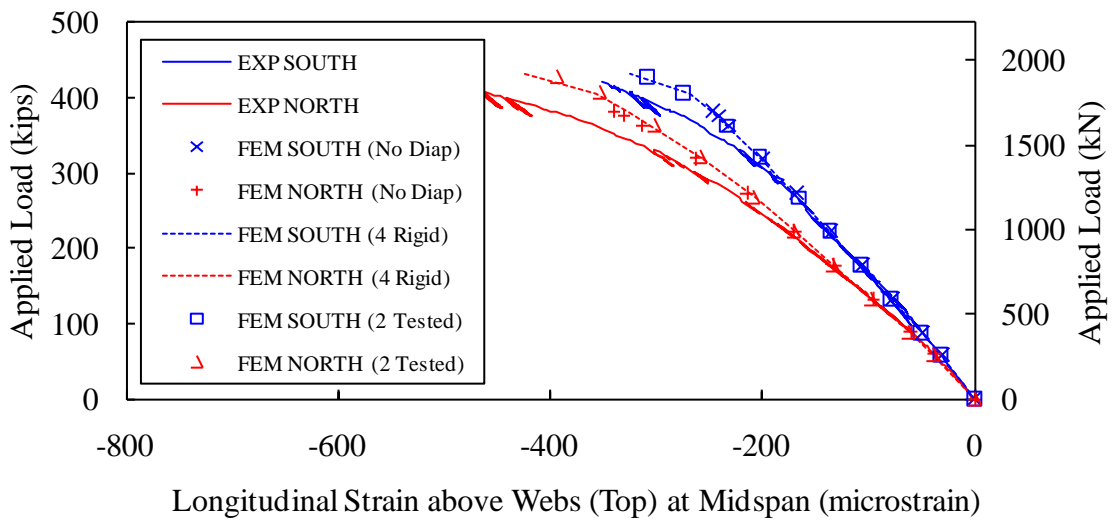


Figure 246. Graph. Effect of diaphragm on the longitudinal strain on the deck immediately above the webs at midspan.

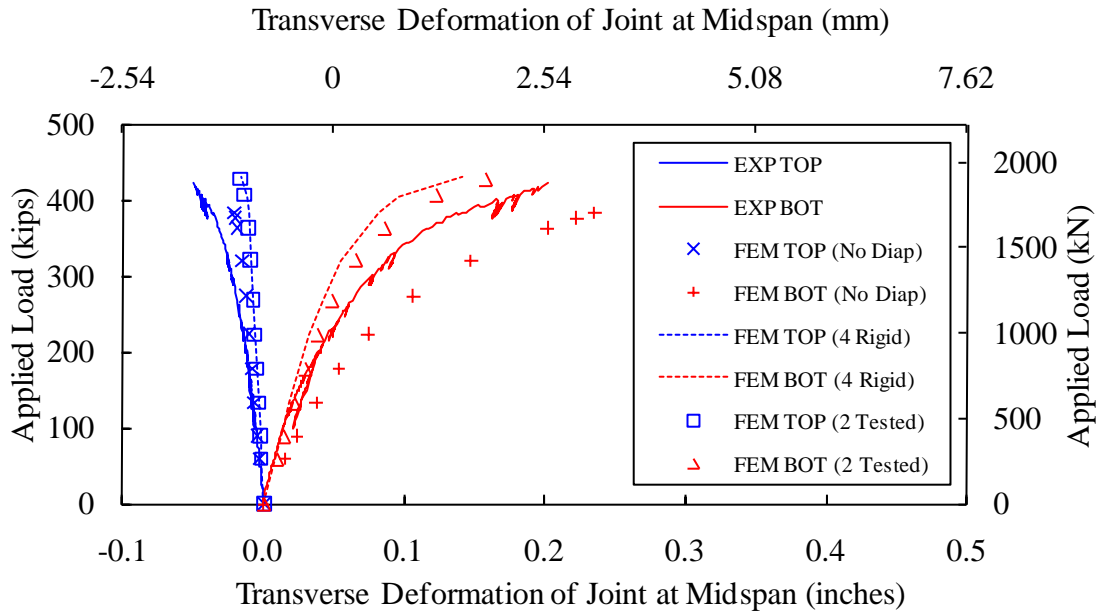


Figure 247. Graph. Effect of diaphragm on the transverse deformation of the joint at midspan.

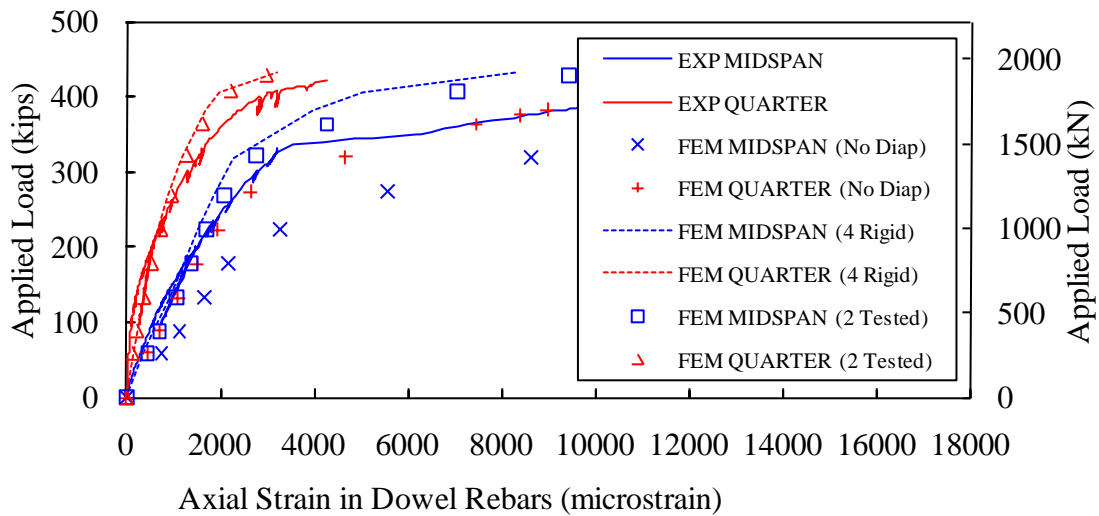


Figure 248. Graph. Effect of diaphragm on axial strains in the dowel bars at midspan and quarterspan.

CONCLUSIONS

Based on the results of the above parametric studies compared to the experimentally observed flexural responses of the UHPC pi-girders in Tests T2J and T1J, the following conclusions are presented.

1. The proposed UHPC material parameters of the CDP model in Table 4 are reconfirmed as reasonable in the pi-girder with joint.
2. Automatic stabilization assisted in stabilizing the model and allowed it to converge at higher applied load levels than were possible in its absence. This stabilization algorithm also did not impact the model response at lower load levels as compared to a similar model without stabilization.
3. Using contact to model the interaction between joint and deck is feasible. Introduction of a small coefficient of friction may facilitate convergence as compared to frictionless or rough contact.
4. Unlike the diaphragms included in the pi-girder results presented in Chapter 6, the structural capacity of pi-girder with joint was not significantly influenced by nonlinear behaviors of the implemented diaphragms. This difference in response was due to the comparatively stiffer behavior inherent in the diaphragm system implemented for the pi-girder with joint tests.
5. In the models, the joint structural detail was simplified such that only the diamond-shaped shear key and dowel rebar were retained. Hard contact with a coefficient of friction equal to 0.1 and no cohesion was assumed along the whole longitudinal joint. The simplified joint intensifies the local stress concentration by reducing the transition area used to transfer the engaging force between the half-girders. This treatment works relatively well in the case of Test T1J because the field-cast UHPC as grouting material has a high compressive strength allowing for resistance to localized compressive crushing between the joint and adjacent UHPC deck. This modeling concept was somewhat less successful for Test T2J where the local compressive stress concentration in the joint exceeds a relatively lower compressive strength of the magnesium phosphate grout.

CHAPTER 8. CONCLUSIONS

INTRODUCTION

This computational investigation focused on finite element modeling and analyzing the behavior of existing UHPC structural components including a prestressed UHPC I-girder and UHPC 2nd generation pi-girders. Both a concrete smeared cracking model and a concrete damaged plasticity model were tailored to model UHPC within a commercially available finite element analysis package. The detailed modeling and analysis were presented. Conclusions resulting from this study are presented below. A brief discussion of ongoing and potential future research related to this topic is presented immediately thereafter.

CONCLUSIONS

The following conclusions are presented based on the research presented in this report.

1. In terms of modeling the constitutive behaviors of UHPC, the concrete damaged plasticity model replicates the observed strain and deflection responses better than the concrete smeared cracking model in the prestressed UHPC I-girder and the prestressed UHPC 2nd generation pi-girders. The concrete damaged plasticity models using appropriate parameters in any of the three types of tension stiffening definitions can capture both linear and nonlinear behavior of the girders reasonably well.
2. Comparison between the experimental and model results confirmed that the assumed elastic perfectly plastic tensile stress-strain relationship for UHPC used in the concrete damaged plasticity models is reasonable. The assumed UHPC properties such as maximum tensile stress of 2.3 ksi (15.9 MPa) and Young's modulus of 8000 ksi (55 GPa) correlated the I-girder's finite element model to the experiment very well. Maximum tensile stress of 1.4 ksi (9.7 MPa) and Young's modulus of 7650 ksi (53 GPa) worked well for the pi-girder and the pi-girder with longitudinal joint. The mesh sensitivity is low and a 2-inch (51-mm) seeded mesh is acceptable.
3. The diaphragms in the pi-girders can be modeled as nonlinear springs. The diaphragms play a significant role in maintaining structural integrity and allowing the cross section to carry the applied loads. The reduced thickness end plates of the diaphragms adversely influenced the overall structural capacity of the pi-girder in Test T2D. The as-designed diaphragms with the original end plates used in Tests T1J and T2J performed well.
4. The interfaces between the precast component flange tips and the field-cast grout at the longitudinal joint in the pi-girder can be modeled as contact surfaces with little friction. The model-based structural performance of the pi-girders was not greatly affected by differences in the mechanical properties of the two grouts tested, namely the magnesium phosphate and the field-cast UHPC. Convergence of the model at high loading levels may be affected by the lower compressive strength of the magnesium phosphate grout.
5. An ultimate tensile plastic strain as large as 0.025 was defined in pi-girder with joint models generated herein in order to facilitate model convergence. These strain values are

significantly larger than the strains which were observed to cause strain localization in the associated experimental investigations. The use of an extended tensile strain range allowed for the generation of longer nonlinear structural responses which otherwise would not have been possible. The models only engaged these higher strain values in local regions subjected to modeling constraints which were not indicative of the physical test constraints.

6. The failure mechanics in the physical tests has been investigated with additional information provided by the models. The I-girder failed by combination of initial UHPC strain localization and steel fiber pullout which was followed by strand yielding and rupture. The model predicts that the UHPC ultimate tensile strain at the failure load approached 0.009, a value consistent with experimental observations. The pi-girder failed by the weakened diaphragms which could not prevent the excessive leg spreading and the resulting transverse flexure of the deck and increased tensile stress on the underside of the deck. These behaviors were replicated in the model. The pi-girder with joint failed by combination of joint crushing and separation, dowel bars' yielding, excessive negative bending on top of the deck of the south half girder as well as significant transverse bending of the web of the north half girder as the bulb rotates inward. These behaviors were also replicated in the model.

ONGOING AND FUTURE RESEARCH

The research presented herein has spurred the initiation of a series of follow-on research studies. These ongoing and future studies include:

1. Further calibrate the concrete damaged plasticity model in terms of damage and recovery functionalities for unloading and cyclic loading cases.
2. Develop a family of UHPC pi-girder cross sections applicable to a range of span lengths and configurations. These girders will be developed to meet appropriate bridge design requirements through use of the concrete damaged plasticity models calibrated herein.
3. Model other full-scale UHPC structural component tests in order to gain a greater understanding of the performance of precast UHPC components and field-cast UHPC connections.

REFERENCES

1. Association Française de Génie Civil, Interim Recommendations for Ultra High Performance Fibre-Reinforced Concretes, 2002.
2. Zienkiewicz, O.C., R.L. Taylor, and J.Z. Zhu, “The Finite Element Method: Its Basics and Fundamentals”, 6th edition, Butterworth-Heinemann, 2005.
3. Zienkiewicz, O.C., R.L. Taylor, “The Finite Element Method for Solid and Structural Mechanics”, 6th edition, Butterworth-Heinemann, 2005.
4. Hughes, J.R.T., “The Finite Element Method”, Prentice-Hall International, Inc., 1987.
5. Cook, R.D., “Concepts and Applications of Finite Element Analysis”, 2nd edition, John Wiley & Sons, 1981.
6. Reddy, J.N., “Finite Element Method”, John Wiley & Sons Inc., 1993.
7. Chen, W. F., “Plasticity in Reinforced Concrete,” McGraw-Hill, Inc., 1982, 474 pp.
8. ABAQUS Software and Documentation, Version 6.9-1. © Dassault Systèmes, SIMULIA, 2009.
9. Hillerborg, A. M. Modeer, and P. E. Petersson, “Analysis of Crack Formation and Crack Growth in Concrete by Means of Fracture Mechanics and Finite Elements,” *Cement and Concrete Research*, V. 6, 1976, pp. 773-782.
10. Lee, J., and G.L. Fenves, “Plastic-Damage Model for Cyclic Loading of Concrete Structures,” *Journal of Engineering Mechanics*, V. 124, No.8, 1998, pp. 892–900.
11. Lubliner, J., J. Oliver, S. Oller, and E. Oñate, “A Plastic-Damage Model for Concrete,” *International Journal of Solids and Structures*, V. 25, No.3, 1989, pp. 229–326.
12. Graybeal, B., “Structural Behavior of Ultra-High Performance Concrete Prestressed I-Girders,” Federal Highway Administration, Report No. FHWA-HRT-06-115, August 2006, 104 pp.
13. Graybeal, B., “Flexural Performance of an Ultrahigh-Performance Concrete I-Girder,” *ASCE Journal of Bridge Engineering*, V. 13, No. 6, November 2008, 602-610.
14. Graybeal, B., “Structural Behavior of a 2nd Generation Ultra-High Performance Concrete Pi-Girder,” Federal Highway Administration, NTIS Accession No. PB2009-115496, 2009, 102 pp.
15. Graybeal, B., “Structural Behavior of a Prototype Ultra-High Performance Concrete Pi-Girder,” Federal Highway Administration, NTIS Accession No. PB2009-115495, 2009, 145 pp.
16. Graybeal, B., “Compressive Behavior of Ultra-High Performance Fiber-Reinforced Concrete,” *ACI Materials Journal*, V. 104, No. 2, March-April 2007, pp. 146-152.

17. Chuang, E., "Ductility Enhancement of High Performance Cementitious Composites and Structures," Massachusetts Institute of Technology, 2002, 319 pp.
18. Park, H., "Model-Based Optimization of Ultra High Performance Concrete Highway Bridge Girders," Massachusetts Institute of Technology, 2003, 139 pp.
19. Soh, M., "Model-Based Design of a Ultra High Performance Concrete Prototype Highway Bridge Girder," Massachusetts Institute of Technology, 2003, 64 pp.
20. Chuang, E., and F. Ulm, "Two-Phase Composite Model for High Performance Cementitious Composites," *Journal of Engineering Mechanics*, V. 128, No. 12, 2002, pp. 1314-1323.
21. Graybeal, B., "Material Property Characterization of Ultra-High Performance Concrete," Federal Highway Administration, Report No. FHWA-HRT-06-103, August 2006, 186 pp.
22. Pansuk, W., H. Sato, Y. Sato, and R. Shionaga, "Tensile Behaviors and Fiber Orientation of UHPC," Proceedings of Second International Symposium on Ultra High Performance Concrete, Kassel, Germany, March 05-07, 161 pp.
23. ASTM C39, "Standard Test Method for Compressive Strength of Cylindrical Concrete Specimens," American Society for Testing and Materials Standard Practice C39, Philadelphia, PA, 2001.
24. ASTM C469, "Standard Test Method for Static Modulus of Elasticity and Poisson's Ratio of Concrete in Compression," American Society for Testing and Materials Standard Practice C469, Philadelphia, PA, 2002.

NTIS DISCLAIMER



This document has been reproduced from the best copy furnished by the sponsoring agency.